Preliminary Development of a Microfluidic Tool for the Characterization of Molecular Machines

by

Zachary Aaron Charles Strike

A thesis
presented to the University of Waterloo
in fulfilment of the
thesis requirement for the degree of
Master of Applied Science
in
Electrical and Computer Engineering (Nanotechnology)

Waterloo, Ontario, Canada, 2021

Author's Declaration

I hereby declare that I am the sole author of this thesis. This is a true copy of the thesis, including any required final revisions, as accepted by my examiners.

I understand that my thesis may be made electronically available to the public.

Abstract

Transmembrane proteins cross the membranes of biological cells and perform integral cell functions that often must be described using quantum mechanics. Developing a better understanding of these quantum mechanical behaviours of transmembrane proteins (i.e., their quantum biology) can enable the development of novel materials and devices, such as more efficient solar cells or chemical sensors. Studies of these behaviours are typically performed in environments that are not biologically representative, like outside of cell membranes and at cryogenic temperatures, leading to possible mischaracterizations. The objective of this thesis was to develop a microfluidic device to facilitate the study of transmembrane proteins and their quantum biology in a biologically representative environment. Laser-cut polymer microfluidic droplet generators were designed and tested to generate water-in-oil droplets and create artificial cell membranes using droplet interface bilayers (lipid bilayers formed by two contacting droplets, "DIBs"). Droplet trapping structures were incorporated into the droplet generators, which held two droplets stationary and in contact, forming a DIB. The devices reliably generated droplets with less than 5% volume variance suitable for forming DIBs that were stable for up to 24 minutes. However, inconsistent DIB lifetimes and unwanted droplet splitting were significant issues. While this work did not apply a microfluidic device to the study of transmembrane proteins, it laid the groundwork for the eventual design and fabrication of such a device. A better understanding was developed of the fluidic resistance of laser-cut microfluidic channels and the resistive effects of droplets occupying those channels. Improvements to the droplet trap design process were made by adapting models of microfluidic droplets splitters to the design of droplet traps. With these lessons, a laser-cut polymer microfluidic device capable of generating DIBs to study transmembrane proteins may be effectively designed in the near future.

Acknowledgements

Many people have helped and supported me through this degree and thesis. I would like to thank my supervisors, Christopher Backhouse and Derek Wright, who offered me support and guidance throughout my journey. In particular, I would like to thank Christopher Backhouse for his work fabricating devices for this project and Derek Wright for his exceptional help editing this thesis. I would also like to thank my family and friends who always supported me and kept me sane. I want to extend a special thank you to my parents, brother, and housemates during the Covid-19 pandemic.

Table of Contents

List of Figures

List of Tables

List of Abbreviations

CB	– Christopher Backhouse
DI	– Deionized
DIBs	– Droplet Interface Bilayers
DRIF	– Droplet Resistance Increase Factor
HDPE	– High-Density Polyethylene
ID	– Inner Diameter
PC	– Polycarbonate
PCR	– Polymerase Chain Reaction
PDMS	– Poly(dimethylsiloxane)
PMMA	– Poly(methyl methacrylate)
TPU	– Thermoplastic Polyurethane

Chapter 1
Introduction

This thesis aimed to create a microfluidic chip that facilitates the study of transmembrane proteins and their quantum biology. The resulting device generates and traps droplets to form droplet interface bilayers (DIBs). This provides a biologically representative environment in which transmembrane proteins can be studied in an automated and relatively simple manner without sacrificing the types of analyses that can be performed.

Transmembrane proteins cross cell membranes and perform important functions, like energy transfer, signalling, and nutrient uptake. Their behaviour often cannot be explained solely using classical physics and must also include quantum mechanical effects. The field of quantum biology studies quantum mechanical behaviours in biological molecules and has important implications in various fields, such as solar energy collection and magnetic field sensing [1]–[3].

It is essential to study transmembrane proteins in biologically representative environments, like cell membranes, because the membrane itself dramatically influences the shape of the proteins, and the protein's shape dictates its function. Studying them in isolation may result in their mischaracterization [4].

Transmembrane proteins have a hydrophobic center and two hydrophilic ends, resulting in a minimum energy position in the middle of the membrane with their hydrophilic ends extending past either side of the membrane surface. The hydrophobic protein center contacts the hydrophobic center of the cell membrane, and the hydrophilic protein ends contact the hydrophilic membrane walls and aqueous exterior. Figure 1-1 shows this structure.

There are two options to study a transmembrane protein accurately: (1) *in vivo* in a cell membrane; or (2) *in vitro* in an artificial cell membrane. Cell membranes are lipid bilayers that separate the aqueous interior from its aqueous exterior [4], [5]. Each lipid in this bilayer is amphiphilic, composed of a hydrophilic head and a hydrophobic tail. The hydrophobic tails are interior to the bilayer, and their hydrophilic heads face outwards on either side. Studying a specific transmembrane protein *in vivo* in a cell membrane can be complicated due to the vast number of other proteins present in the cell and cell membrane. They may generate obscuring optical and electrical signals, particularly in the case of quantum biology, where quantum mechanical behaviours can be difficult to detect [2], [3]. On the other hand, studying an isolated

transmembrane protein *in vitro* in an artificial cell membrane eliminates competing signals from other proteins. Artificial cell membranes are lipid bilayers that mimic natural cell membranes.

There are various artificial cell membrane types and methods to create them, but DIBs stand out as particularly appealing structures because they are simpler to create, easier to manipulate, and smaller to fabricate than other types. When a droplet of water (the "dispersed phase") is placed into oil (the "continuous phase") with a surfactant (an amphiphilic molecule, e.g., most lipids), a surfactant monolayer forms on the surface of the droplet. The surfactant orients itself with its hydrophilic end contacting the water and its hydrophobic end contacting the oil. When two of these droplets are brought together, a surfactant bilayer forms that mimics a cell membrane. Transmembrane proteins can be studied *in vitro* by inserting them into this artificial cell membrane (Figure 1-1).

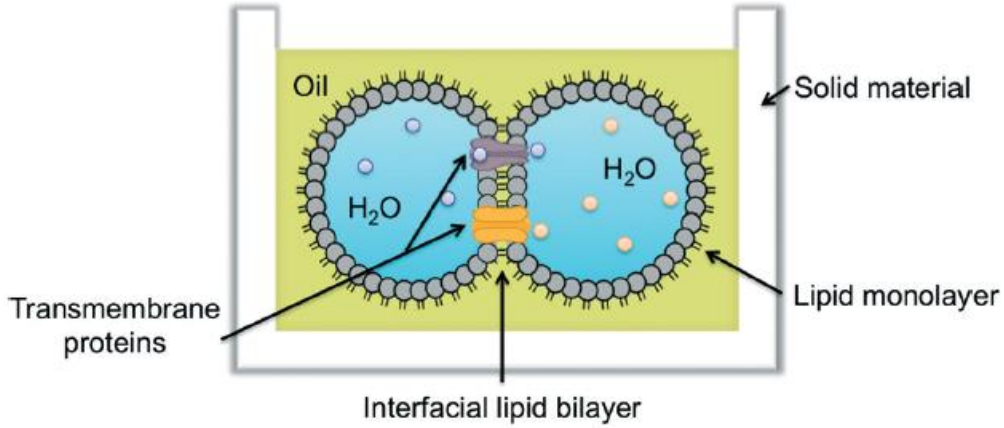

Figure 1-1 – An example schematic of a droplet interface bilayer with transmembrane proteins spanning the bilayer [6].

Microfluidic technologies offer a high degree of control over droplet positions, which is required to form DIBs. Microfluidic devices manipulate pico- to millilitre volumes of fluids within micrometre-scale channels with remarkably high levels of precision. These devices can be designed to perform a wide range of functions, including the production of water-in-oil droplets and their positioning to form DIBs.

Therefore, a microfluidic device that forms DIBs by generating and trapping droplets could be a vital tool in studying transmembrane proteins and their quantum biology. Such devices have been reported in the literature but have not been broadly applied to the study of transmembrane proteins beyond simple pore-forming proteins. There are many opportunities to improve and apply microfluidically-generated DIBs, such as large-ordered arrays of DIBs applied to study complex transmembrane proteins and their quantum biology.

1.1 Background Literature Review

1.1.1 Quantum Biology

Quantum biology is a relatively young but growing field, primarily focused on characterizing quantum mechanical effects in proteins [1]–[3]. Topics in this field range from magnetoreception in the eyes of birds to creating a better model of how human noses process scents [1], [3], [7]. Perhaps one of the most promising topics is the study of electron transfer processes in transmembrane proteins.

Transmembrane proteins facilitate interactions between the interior and exterior of cells, often involving energy and electron transfer [4]. For example, light-harvesting transmembrane proteins that exhibit 100% efficient electron transfer during photosynthesis are being vigorously studied with an eye on improving the efficiency of solar energy systems [3], [7]–[12]. Quantum biological electron transfer processes are challenging to study because they often require cryogenic temperatures and advanced optical techniques [8], [9], [11]–[15]. Available observation methods are very advanced and include ultrafast detection (femtosecond time periods), optically detected magnetic resonance, and enhanced Raman spectroscopy [11], [16]–[20]. The low population numbers or short lifetimes of the observed quantum biological behaviours necessitate such advanced techniques and arise from the spin coherence or excited triplet states of the biological molecules [16], [21]–[29]. In addition, most of these studies occur in non-biologically representative environments: at cryogenic temperatures, outside of a lipid bilayer, or both.

This thesis aims to address the challenges of studying transmembrane proteins in biologically relevant environments by creating a microfluidic device to form lipid bilayers. Transmembrane proteins can be studied in the lipid bilayers, and, given either a sufficiently sensitive detection mechanism or a sufficiently large sample of DIBs, quantum biological behaviours may be observed at physiologically relevant temperatures. Microfluidic devices permit a wide range of sensitive detection mechanisms to be used and high throughput such that many DIBs can be observed sequentially or simultaneously. The first step in achieving these aims is to create an artificial cell membrane (lipid bilayer).

1.1.2 Artificially Constructed Lipid Bilayers

Numerous methods have been used to construct lipid bilayers, including mechanically supported lipid bilayers, DIBs, and microfluidically generated DIBs. The first methods used to create lipid bilayers to study transmembrane proteins were black lipid membranes and Montal-Mueller membranes [30], [31]. These types of membranes involve forming a lipid bilayer across a pore in

a partition dividing two compartments of aqueous fluid [4], [30]–[33]. The resulting membranes are only stable for a few hours, which may not be suitable for all experiments, and are subject to limited observation methods [4], [34]. Other techniques using membranes supported directly on solid surfaces have improved membrane stability [4], [30]. However, these membranes are less popular because only one side of the membrane is in contact with an aqueous solution, which is not biologically representative and limits interactions with the membrane.

Due to the physical structures required to support black lipid and Montal-Mueller membranes, large volumes of membrane-forming reagents are needed. Further, it is challenging to form asymmetric bilayers, where each side of the bilayer is composed of different lipids or proteins [4], [30], [34]. Asymmetric lipid bilayers are essential to creating biologically representative membranes, as these are common cellular structures (e.g., the membranes of mitochondria) [34]–[37]. Furthermore, the options for studying these membranes are limited – optically, because of the interference from the partition containing the pore for the membrane, and electrochemically because only basic detection systems can be used [4], [30], [38], [39].

Efforts have been made to improve the functionality of black lipid and Montal-Mueller membranes [34], [40]. Notably, Tsuji *et al.* developed a microfluidic device to enable solution exchange into droplets to form a black lipid membrane for rapid protein studies [41]. Their device used two droplets to form a black lipid membrane through a partition with several small pores in it. One of the droplets was situated on top of two microfluidic channels, which allowed for solution exchange with the droplet (Figure 1-2). While Tsuji *et al.*'s work effectively addressed some issues with black lipid membranes and Montal-Mueller membranes, DIBs provide additional functionality as will be discussed [41].

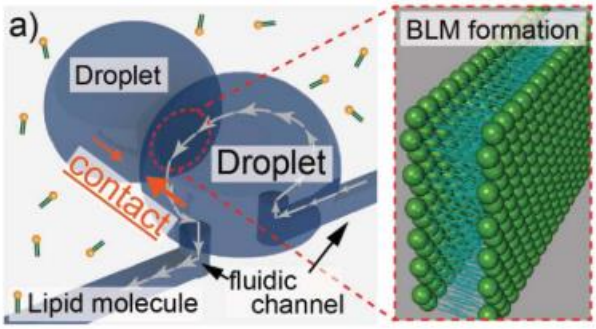

Figure 1-2 – A schematic of the operating principle used by Tsuji et al. to create a DIB-like system with microfluidic solution exchange [41].

1.1.3 Droplet Interface Bilayers

As previously described, DIBs are lipid bilayers formed between two adjacent droplets held in close contact (Figure 1-1). The droplets are a dispersed phase (typically aqueous, e.g., water) suspended in a surrounding immiscible continuous phase (typically an oil). An amphiphilic lipid dissolved in one of the phases forms a monolayer on the droplet surface so that a bilayer is formed when two droplets are in contact. These droplets are generally formed by pipetting and then manipulated via pipettes or micromanipulators into close contact.

Bayley *et al.* developed DIBs in 2008 to address the shortcomings of black lipid and Montal-Mueller membranes and have been used often since then [34], [42]. Compared to earlier bilayer formation techniques, DIBs have improved physical and chemical properties and stability [30], [43]. Some DIBs have been reported to be stable for several days [44].

DIBs also require much less reagent than black lipid and Montal-Mueller membranes, as the volumes of the droplets are typically much smaller than the volumes of the fluid reservoirs used to form these types of membranes. In addition, the interfacial area of the bilayer tends to be much larger for DIBs than in traditional bilayer formation techniques [40]. The interfacial area of the bilayer can also be modulated by moving the droplets closer together or further apart, providing additional control over bilayer properties not found in earlier methods [34].

DIBs are more versatile than traditional bilayer formation techniques because the fluid contents on each side of the bilayer can be more easily altered, forming droplets with different contents [45]. This enables the formation of asymmetric bilayers and offers a simple method to introduce specific chemicals to each side of the formed bilayer by sequentially changing the droplets used to form them [46], [47]. This capability allows the study of specific transmembrane proteins naturally found in asymmetric lipid bilayers that respond to chemical signals from one side of a bilayer.

Asymmetric bilayers can be easily formed with DIBs, depending on how lipids are introduced to form the droplet monolayers [35], [36]. There are two methods of introducing lipids to the droplet-oil interface as a bilayer is formed between two water-in-oil droplets: lipid-out and lipid-in. Lipids are mixed with the oil phase in the lipid-out technique, whereas lipids are dispersed within the droplets before formation in the lipid-in technique (Figure 1-3). The lipid-in technique forms asymmetric bilayers by loading different lipids into different droplets [42], [43], [48]. Therefore, a lipid-in DIB approach can simulate reasonably representative asymmetric biological membranes.

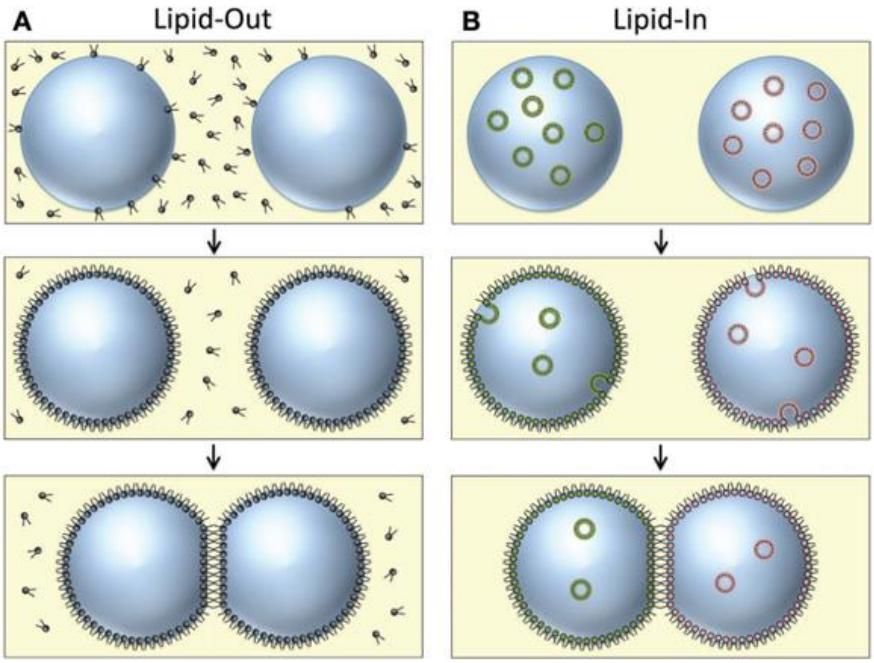

Figure 1-3 – The lipid-out (A) and lipid-in (B) techniques. The lipid-out technique involves dissolving lipids in the continuous phase, while the lipid-in technique dissolves lipids in the dispersed phase [42].

Furthermore, interacting with DIBs is more flexible compared to earlier bilayer formation techniques. Each droplet can be externally accessed by inserting a pipette tip, micromanipulator tip, or electrode into a droplet of sufficient size, allowing for droplet positioning or electrical interrogation of the bilayer and its contents [34], [42], [43]. This capability led to complex systems with automated droplet movement to sequentially form many different bilayers and the formation of DIB arrays where multiple bilayers can interact [49]. These capabilities cannot be readily achieved with black lipid or Montal-Mueller membranes.

DIBs have been created and used in various non-microfluidic applications, typically formed by placing two droplets of a dispersed phase (typically water) into a container filled with a continuous phase (typically an oil, e.g., hexadecane). The DIBs are then manually assembled using pipettes or electrodes to position and hold droplets in contact with each other within the continuous phase [42], [43]. Such DIBs have been studied for a wide variety of applications, like studying the bilayer capacitance and transmembrane protein behaviour, including the transmembrane protein cytochrome c [5], [30], [31], [42]. However, most notable amongst these applications is the use of DIBs to form complex arrays that are functional networks of interacting bilayers [42], [44], [48], [50]. DIB arrays can be as simple as three contacting droplets in a row to form two interacting DIBs or as complex as three-dimensional networks of DIBs to mimic tissue behaviour, such as that shown in Figure 1-4. DIB arrays have been used to make functional networks where different bilayers contain different transmembrane proteins that interact with each other [42], [51].

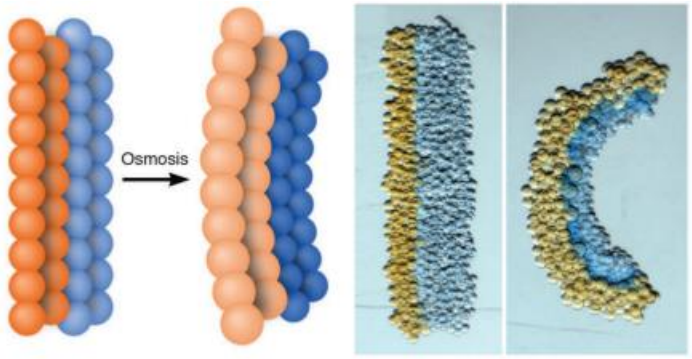

Figure 1-4 - A 3D printed droplet network with droplets of different osmolarities. The different osmolarities cause the network to fold [51].

The structure in Figure 1-4 shows an example of a functional droplet network where droplets of different osmolarity are used to create a "3D-printed" droplet structure that folds [42], [51]. More complex droplet networks have been made by Holden *et al.*, such as a light-sensing DIB network based on the proton pump bacteriorhodopsin [44].

These array structures are most readily formed by positioning droplets using a micromanipulator or a 3D droplet printer, which is essentially a micromanipulator directing a nozzle that dispenses droplets [42], [44], [49]. However, these methods have several shortcomings in that they do not form droplets, and they can take relatively long periods to place droplets in position. A typical droplet placement rate for 3D droplet printers is 0.5 Hz [42]. Booth *et al.* suggest that producing large 3D printed droplet arrays could be accelerated by integrating microfluidic droplet generation techniques, which are known to be more rapid (faster than 0.5 Hz production rate) and produce droplets with little size variability (< 5% variation in droplet volume) [42], [52]. While this may be a valuable extension of existing 3D droplet printers, unless a 3D array of droplets is specifically required, microfluidic devices have efficiently produced, positioned, and interrogated droplets in DIBs and formed ordered 2D arrays of droplets.

1.1.4 Microfluidic Methods for the Production of Droplet Interface Bilayers

Recently, microfluidic devices have been used to generate and improve the functionality of DIBs. These devices can provide an automated way to create and interrogate DIBs with low reagent consumption, high control and reproducibility, and minimal specialized training.

Most devices used to demonstrate the microfluidic generation of DIBs have been fabricated using soft lithography, but some have been fabricated by micromilling polycarbonate (PC). Soft lithography is a fabrication process of creating a mold through photolithography, typically out of the photoresist SU-8, and then casting microfluidic channels of the mold in poly(dimethylsiloxane)

(PDMS) [53]–[57]. This fabrication method is popular within microfluidics and generally results in channels with a rectangular cross-section and uniform height across the device. Micromilling involves mechanically engraving channels that are typically rectangular in cross-section and allows for variable channel dimensions. The process is limited by the resolution of the engraving tool and the surface roughness of the resulting channels. Microfluidic devices fabricated with both methods and others have been used to create and interrogate DIBs.

Perhaps the simplest of these devices was demonstrated by Barlow *et al.*, which required the manual positioning of two moveable pieces of poly(methyl methacrylate) (PMMA) to form multiple DIBs simultaneously [58]. The two moveable pieces of laser-cut PMMA slid together and had matching semicircular cuts along their peripheries (Figure 1-5) [58]. While this system did not use microfluidic channels, it created DIBs with 200 nL droplets and was more like microfluidic methods than forming DIBs through pipetting or by using micromanipulators. Droplets were pipetted into the semicircular cut droplet chambers while the chambers were not aligned (Figure 1-5a). When the PMMA pieces were pushed together, DIBs were formed when the droplet chambers aligned (Figure 1-5b). The formed DIBs were stable for at least 25 minutes (lifetime after 25 minutes was not reported) and were used to study the diffusion of a fluorescent dye across the DIBs. The device allowed for the rapid and controllable formation of multiple DIBs with a single motion but had the disadvantage of requiring more continuous phase than other microfluidic approaches to DIB formation. Additionally, each droplet had to be pipetted manually, which limited the throughput of the device.

Wong and Ren developed a microfluidic droplet generator for forming DIBs. Advanced fluid input controls enabled water-in-oil droplet pairing and immediate trapping at the droplet generation location [59]. The device was fabricated from PDMS using soft lithography (discussed further in Section 1.1.6), had square channels with a 50 μm cross-section, and produced droplets that occupied the full channel width (i.e., droplets were plugs and not spheres). A camera and image processing system tracked droplet positions and adjusted the continuous (oil) and dispersed (water) phase pressure pumps to control droplet positions within the channels. This system could control droplet position and pair two successive droplets. While this system was not explicitly used to make DIBs, it can be considered a method of DIB formation due to its ability to bring two droplets into close contact.

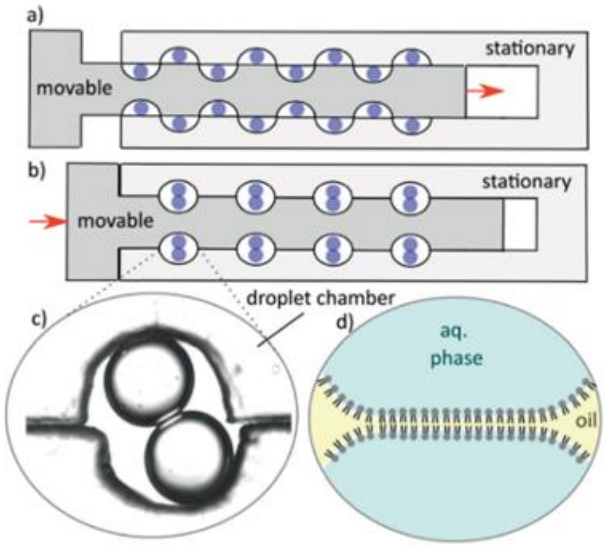

Figure 1-5 - A schematic diagram of the DIB forming device by Barlow et al. (a), how it is used (b), a DIB formed in a droplet chamber (c), and a schematic of the bilayer formed at the droplet interface (d) [58].

A similar method was demonstrated by Elani *et al.* using two syringe pumps to form DIBs between four droplets at an intersection (Figure 1-6) [48]. Droplets were produced by a separate droplet generating device and fed into a microfluidic junction using two syringe pumps. Different combinations of DIBs were made depending on which syringe pump in Figure 1-6 was used to pull droplets from the junction point. The device used by Elani *et al.* was fabricated using soft lithography with PDMS and had square channels with a 400 μm cross-section [48].

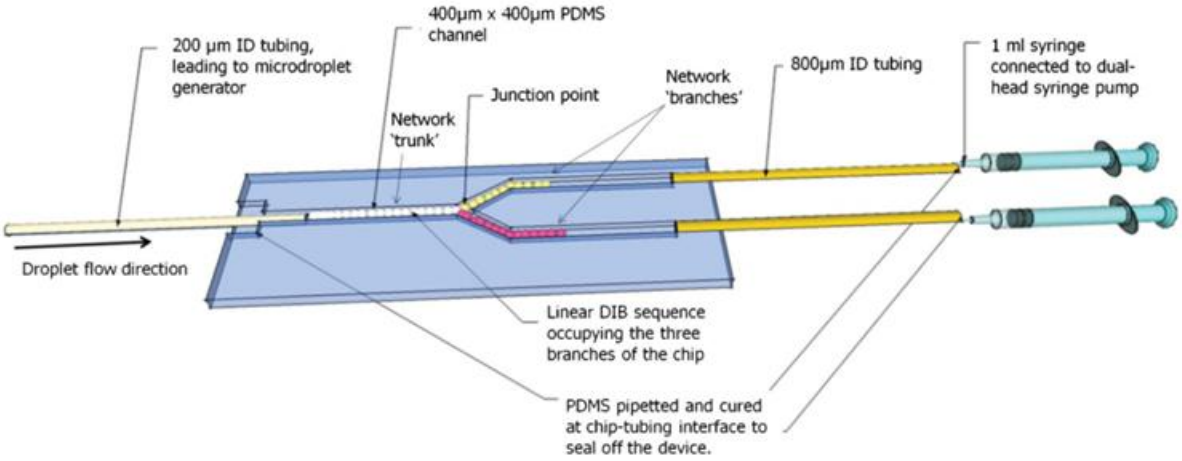

Figure 1-6 - A schematic of the branched channel system used by Elani et al. to create DIBs at a specific junction [48].

The methods of Wong and Ren and Elani *et al.* produce ordered DIBs in specific locations but require a high level of device control and interaction through pressure pumps or syringe pumps [48], [59]. Another more straightforward but less sophisticated approach has been to stack many droplets in a channel larger than the size of a single droplet and remove the continuous phase

between them or produce droplets with almost no continuous phase separating them [48], [60]–[63]. In the case of removing the continuous phase, the droplets initially formed spheres within the channels that did not contact the channel walls. When the continuous phase was removed from between them, they formed arrays of droplets in close contact, becoming ordered as they were packed into the channel. These arrays had limited patterning ability and size in two and three dimensions. The droplets produced with little continuous phase achieved the same effect but without removing excess continuous phase from between droplets. In both cases, droplets would either be ordered randomly or retain the order in which the droplets were produced.

If droplets made of different solvents were produced and the channel was designed correctly, patterned packings of droplets could be formed to control the structure of the DIBs (Figure 1-7) [48]. This capability allows for the formation of asymmetric bilayers in a microfluidic DIB generator. However, these devices required complex structures and operating conditions, like low amounts of continuous phase fluid while maintaining small droplet sizes, which can be challenging to achieve and limit their widespread adoption.

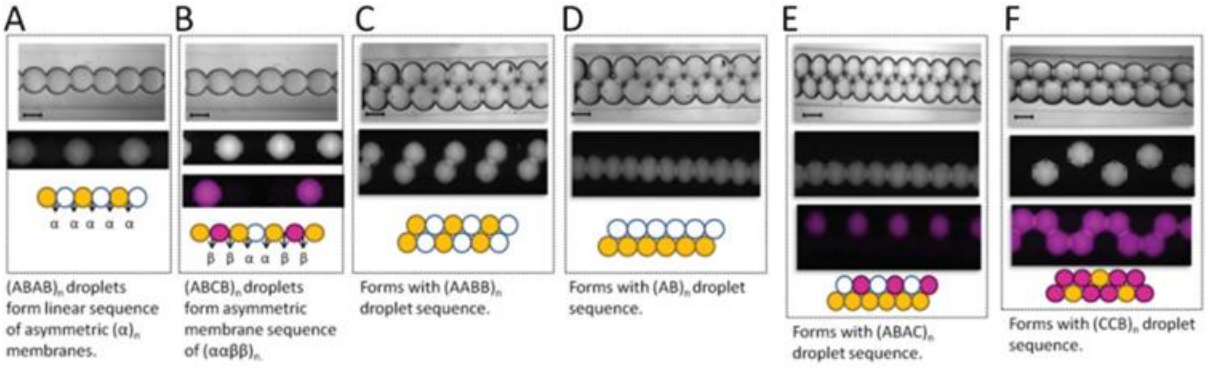

Figure 1-7 - The different droplet patterns Elani et al. could produce in a single channel. The patterns were based on the order in which the different droplet types were made [48].

1.1.4.1 Microfluidic Droplet Traps to Produce Droplet Interface Bilayers

Microfluidic droplet traps are passive channel structures for forming DIBs that aim to avoid manual droplet positioning and production. Droplet traps are designed to hold droplets in place without any active intervention, like syringe pumps or applied electrostatic forces. The traps rely on spatial changes in microfluidic channel dimensions to keep droplets in place while allowing the continuous phase fluid to flow around them. Many channel structures can trap droplets and generally include combinations of pillars and rails.

Pillar-based droplet traps have a series of smaller constricted channels leading away from an input channel so that the continuous phase is selectively removed through the smaller channels [64]–[68]. The droplets cannot enter the smaller channels and are therefore held in place.

Rail-based droplet traps have a deepened channel area – the rail – where droplets will preferentially flow. The working principle is that droplets change their conformation within channels to minimize their surface area, which in turn minimizes their surface energy as *surface energy* = γ × *droplet surface area*, where γ = interfacial tension = interfacial energy (Figure 1-8) [65]. Unless sufficient forces are applied to overcome the droplets' tendencies to minimize their surface energy, they will preferentially be held by the rails.

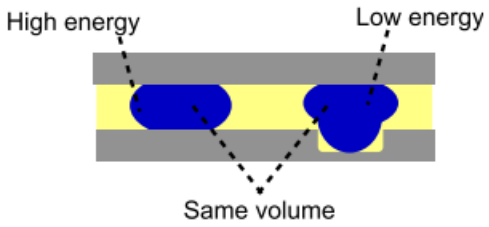

Figure 1-8 - A schematic made by Carreras et al. to describe the difference in surface energy of a droplet in a regular channel and along a guiding rail [65].

King *et al.* built a millifluidic device using PDMS and the droplet trap design, as shown in Figure 1-9. The device used both a series of pillars and a central guiding rail to trap droplets [64]. As droplets arrive in the droplet trap, the continuous phase (yellow) flows through the constricted channels of the trap, while the droplets (red and green) do not. The authors created linear and 1.5D arrays of DIBs in their trap, which were stable for up to six hours. The DIBs could be patterned by setting the order, types, and volumes of the droplets produced. Droplets flowed preferentially along the central guiding rail of the droplet trap, which is why the green droplet in Figure 1-9 is in the center of the droplet trap and does not touch any of the pillars. Droplets could be removed from the trap by increasing the continuous phase flow rate through the device, which pushed the droplets through the constricted channels. The physics behind this behaviour is discussed in Section 2.6.

Carreras *et al.* designed a droplet trap similar to that of King *et al.* using pillars and a central guiding rail [65]. Carreras *et al.* created an array of traps in a very wide channel so that the produced droplets could be sorted into any one of four droplet traps using an auxiliary flow [65]. The device was made of PDMS using soft lithography and had rectangular channels 50 μm deep and 100 μm wide. The produced droplets were spherical but bound by the top and bottom of the channels. The authors sorted droplets into specific traps with this system and formed linear arrays of up to 21 droplets (20 DIBs), stable for at least 1.5 minutes [65].

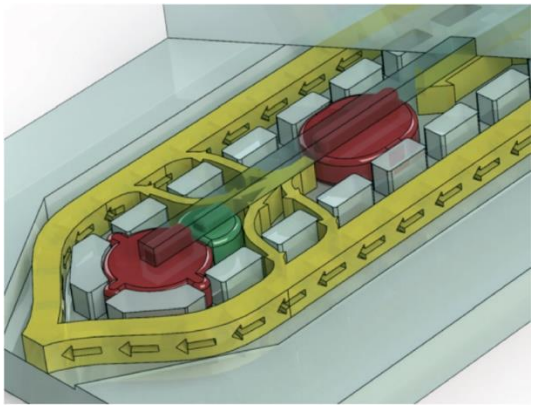

Figure 1-9 - A model of the droplet trap designed by King et al. using a pillar design and a central rail [64].

Schlicht and Zagnoni reported a pillar-based trap where droplets could be ejected in order through one specific set of pillars. The authors referred to this structure as a shift register, but it was also a droplet trap used to form DIBs [68]. Linear arrays of alternating droplets were made in these traps and were stable for at least two hours. Once a series of pillar traps were filled with droplets, the first droplet entered into the trap would be ejected. Therefore, the size of the linear array of droplets could be adjusted by setting the number of channels between pillars. The devices were fabricated using soft lithography with PDMS and produced droplets that formed cylindrical plugs in the microfluidic channels [68].

Korczyk *et al.* developed a rail-based droplet metering module that used a rail as the entire metering and trapping structure [69]. A droplet metering module is a set of channels that takes a droplet and splits it into a specific volume. As droplets entered the metering module, they were held after being split or if they were below the module holding volume. The module used a "normally-sized" channel surrounded by a shallow droplet-trapping region, as in Figure 1-10. The shallow "bypass" region allowed the continuous phase to flow around the trapped droplet. Although this was a droplet metering module, it could form DIBs by sending two smaller droplets into the channel structure. The droplet trap was micromilled from polycarbonate (PC). The device dimensions were not reported, but the bypass region was noted as being one-quarter the depth of the trapping channel.

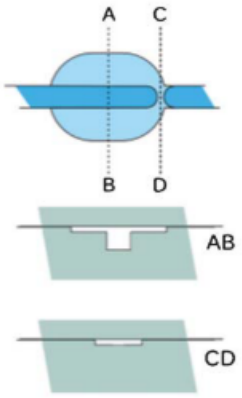

Figure 1-10 - A droplet metering and trapping module designed by Korczyk et al. The design was based on a regular channel surrounded by a shallow venting channel [69]. The cross-sections of the channel structure along the lines A-B and C-D are also shown.

Czekalska *et al.* designed two devices similar to Korczyk *et al.* [46], [47]. However, they positioned droplets in deepened circular holding traps surrounded by shallow bypass regions rather than guiding droplets on a rail. The circular holding traps were close enough that adjacent droplets contacted to form DIBs. Droplets in these positions could be cycled so that a single droplet could be used to create DIBs with several other droplets sequentially. The droplets were formed as cylindrical plugs in the microfluidic channels but expanded into spheres in the holding traps and were stable for at least 1.5 minutes. These devices were micromilled from PC and used rectangular channels 400 μm deep and 200 μm or 400 μm wide.

Czekalska *et al.* also reported a second type of droplet trap based on a guiding rail system that moved droplets from the main flow path and into a deepened holding cell where the droplets' surface energy was minimized [45]. The droplets used in these traps were initially cylindrical plugs but adopted spherical conformations as they entered the deepened holding cells. These droplet traps were paired with droplet metering modules that controlled the trapped droplet volume but complicated the device operation. The DIBs formed in the traps were stable for at least one hour but were not observed beyond that. The devices required complex geometries developed by thermally bonding micromilled PC sheets.

Several droplet traps that used hydrodynamic effects to trap droplets instead of pillars or rails have been reported [6], [70]. These traps sorted droplets at junctions based on channel resistance, guiding them to predetermined trapping positions. Once droplets had filled the trapping positions, the channel resistances changed to divert the continuous phase flow and subsequent droplets around the trap.

The design of Nguyen *et al.* is an example of a hydrodynamic trapping structure, shown in Figure 1-11 labelled with its equivalent electrical circuit elements [6]. In Figure 1-11, R_T represents the fluidic resistance of the trapping region, R_a and R_b represent the resistances of the different channels that comprise the trapping region, and R_M represents the resistance of the channel bypassing the trapping region. Two droplets enter the hydrodynamic trap, which has a total fluidic resistance of R_T, then block the narrow "bleed valves" leading from the trap, increasing the trap resistance. The trap's fluidic resistance becomes much larger than the channel resistance flowing around the trap, R_M. Therefore, subsequent droplets flow around the filled trap as the bleed valves are blocked.

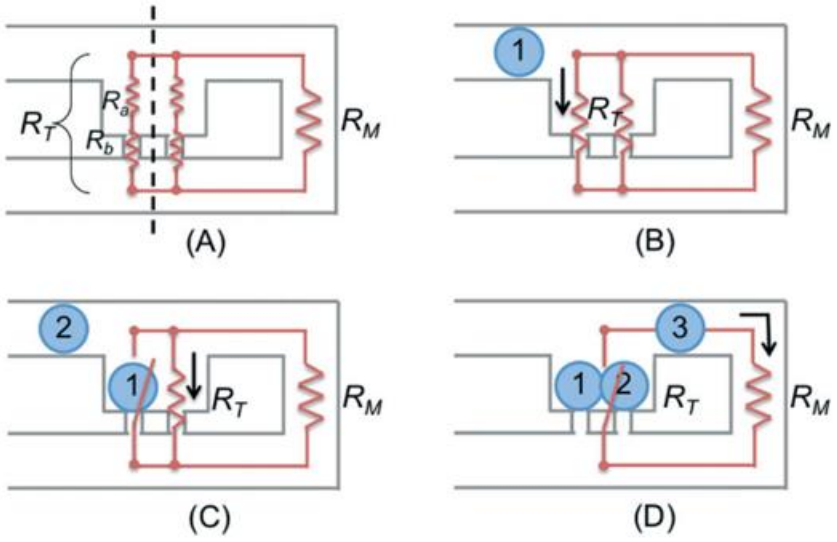

Figure 1-11 - A hydrodynamic droplet trap designed by Nguyen et al. to create DIBs [6]. (A) displays the trap resistance when no droplets are present each path in the trap has a resistance of $R_a + R_b$, (B) shows the trap and the primary path of fluid flow with a droplet entering the trap as $R_T < R_M$, (C) shows one of the trap "bleed valves" being blocked by the first droplet (switch is open). However, the primary flow path is through the trap as $R_T < R_M$ and (D) after a second droplet enters the trap, the third droplet bypasses the trap as $R_T > R_M$.

The device was fabricated from PDMS using soft lithography and had square channels with 125 μm sides [6]. The trap itself was much larger than the channels to hold droplets in place without blocking the flow of subsequent droplets, and the bleed valves were much narrower than the other channels. The trap could be altered to form linear arrays of trapped droplets and DIBs by lengthening the trap area and including more bleed valves. Trapped droplets formed as elongated plugs in the channels and expanded into spheres in the widened trapping areas.

Bithi *et al.* also created a hydrodynamic trap similar to that of Nguyen *et al.*, but with a less sophisticated design that could not form a linear array of DIBs [6], [70]. Their device operated in much the same manner as the device of Nguyen *et al.* but only had a single trapping chamber to

hold droplets, which meant that often only one droplet was trapped. The device was also fabricated out of PDMS and used rectangular channels 80 μm deep and 200 μm wide [70].

The droplet traps described above have only been used to trap pairs of droplets or form linear or 1.5D arrays of droplets. 1.5D arrays are arrays of droplets where there is limited ability to pattern droplets in a second dimension; however, creating a grid of droplets is not possible.

To the best of the author's knowledge, no microfluidic droplet trap has been reported that forms ordered 2D or 3D arrays of DIBs with similar complex ordering as can be achieved using 3D droplet printers. Elani *et al.* do report a device that is capable of producing limited 2D and 3D arrays with limited complexity in channels with specific dimensions [48]. However, their device requires difficult to achieve operating conditions and has a limited array size. Achieving the complexity of a 3D droplet printer would require advanced control over droplets and their flow paths which hasn't been observed in the literature to date. Additionally, the ability to create large microfluidic chambers to house the droplet arrays would be required. However, microfluidic devices have been used to produce 2D droplet arrays, which could be used as a foundation to develop ordered arrays of DIBs in microfluidic devices.

1.1.4.2 Microfluidics to Produce Arrays of Droplet Interface Bilayers

To date, most microfluidic devices for forming DIBs have focused on successfully trapping droplets to form limited numbers of DIBs instead of creating large arrays of DIBs. Linear and 1.5D arrays of droplets have been reported both with (Figure 1-7) and without droplet traps [6], [48], [64], [65], [68]. The droplets in an array can be patterned by adding multiple droplet types in a given order.

While 2D and 3D networks of DIBs can act as functional droplet networks, they can also characterize proteins where signals with low strength are of interest, like optical and electrical signals in quantum biology. Many DIBs can be simultaneously observed to collect the cumulative signals from all proteins in all DIBs. This collection of many proteins in a single location could enable techniques like Raman spectroscopy to be applied to the study of quantum biology.

To the best of the author's knowledge, there have been no attempts to produce large 2D or 3D arrays of droplets in microfluidic devices explicitly for the study of DIBs and their contents. The one exception being the work of Elani *et al.* however, their DIB arrays were limited in their 2D and 3D size and patterning [48]. Efforts have been made to create arrays of individual droplet traps to allow for the study of several individual DIBs or arrays of DIBs simultaneously to take advantage of examining the cumulative signals of multiple DIBs [6], [45], [65], [68]–[70].

While efforts have not been directed toward fabricating sizeable 2D DIB arrays, several notable efforts have constructed large-scale 2D arrays of droplets for other applications. Schmitz *et al.* reported a microfluidic device, Dropspots, designed for the large-scale storage and retrieval of individual droplets in a 2D array of droplet traps [71]. Droplets were stored too far apart to form DIBs, but a similar approach could be taken to form large arrays of individual DIBs. The storage in the Dropspots device appeared to be random but could potentially become ordered depending on the order in which droplets were to be introduced to the storage area. As with the droplet trap of King *et al.*, droplets could be retrieved from their storage areas by simply increasing the flow rate through the device [64], [71].

Of even more interest to the creation of large 2D arrays of DIBs is the work of Hatch *et al.*, which created a microfluidic device to make an array of 1-million droplets for large-scale fluorescence imaging for digital polymerase chain reaction (PCR) applications (Figure 1-12) [63]. This device was not intended to create DIBs but could be adapted into a large DIB array due to the droplet contact. However, droplets in this device could not be ordered selectively, which would prevent forming patterned arrays.

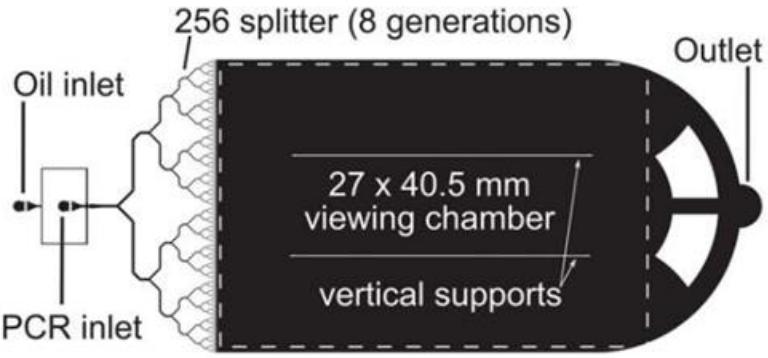

Figure 1-12 - The device design used by Hatch et al. to produce a one million droplet array for wide-field fluorescence measurements of droplets containing polymerase chain reaction (PCR) reagents [63].

These examples demonstrate that large 2D arrays of droplets packed close together can be created, and these technologies could be adapted to study large arrays of DIBs. However, forming DIBs and DIB arrays is only advantageous if there are means of interacting with the DIBs and their contents. Fortunately, microfluidic devices have been used to perform a wide variety of assays and measurements, which can be, and in some cases have been, adapted to measure DIB and transmembrane protein behaviours.

1.1.5 Interaction with Microfluidically-Generated Droplet Interface Bilayers

Many of the droplet traps described above were used to study DIB and transmembrane protein behaviours using electrical, optical, and chemical interrogations. Most studies of transmembrane proteins in microfluidically-generated DIBs have focused on the pore-forming protein α-hemolysin and the molecular transfer rate through the protein in a bilayer [6], [45]–[47], [64], [68]. α-hemolysin is a relatively simple transmembrane protein in that it simply forms an opening in the bilayer. However, the methods used to study its behaviour could be applied to more complex transmembrane proteins.

The most popular method for studying microfluidically-generated DIBs is through electrical interrogation by contacting each droplet forming the DIB with electrodes. This method has been used to confirm the formation of bilayers between droplets and measure the transfer of ions through those containing α-hemolysin [6], [46], [47], [64]. Both King *et al.* and Czekalska *et al.* used agar-coated silver wires inserted through the top layer of their devices to contact trapped droplets [46], [47], [64]. This style of electrode integration can be seen schematically represented in Figure 1-13. Czekalska *et al.* developed a trap to hold four droplets in a row, forming three DIBs containing α-hemolysin between them [46]. Agar-coated silver wire electrodes were inserted into the end droplets to study the center DIB, but neither was directly inserted into the droplets forming the center DIB. Due to the presence of α-hemolysin in the bilayers and ions in the aqueous droplets, it was possible to send signals between the electrodes and relate specific electrical behaviours to the center DIB based on the concentration of α-hemolysin in each bilayer. These measurements demonstrated that it is possible to study particular bilayers within a network of DIBs without directly contacting the droplets involved in those bilayers. This capability may be significant for studying specific transmembrane proteins if they are sensitive to electric potentials or if there is concern about the bilayer stability since electric potentials have been linked to droplet coalescence. The process also removes the risk of cross-contamination of the electrodes when cycling several droplets through the droplet trap [46].

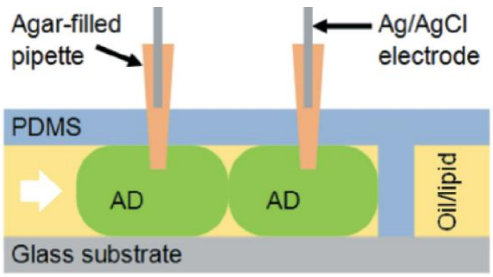

Figure 1-13 – The style of electrodes used by King et al. to interface with trapped droplets (AD), which form a DIB [64].

Nguyen *et al.* also performed electrical interrogation of DIBs formed in droplet traps but used planar silver electrodes patterned on channel walls rather than wire electrodes [6]. They used their electrodes to study the formation dynamics of DIBs, specifically the removal of oil from between DIBs and the bilayer areas, and the simultaneous study of voltage-dependent pore formation of the alamethicin peptide in eight DIBs [6].

Microfluidically-generated DIBs have also been characterized optically, mainly focusing on measuring the transfer rate of analytes across lipid bilayers with and without a pore-forming protein such as α-hemolysin. These measurements have primarily been accomplished by introducing fluorescent dyes to the DIB through one droplet and measuring the change in fluorescence over time of the other droplet forming the DIB [45], [64], [65], [68], [72]. Such behaviours have been observed for single and linear arrays of DIBs. King *et al.* also related the transfer of fluid between droplets to changes in the sizes of trapped droplets over time [64]. Aside from these fluorescence studies, there has been little work in the optical characterization of transmembrane proteins in or lipid bilayers of microfluidically-generated DIBs.

Some effort has been made to chemically interrogate transmembrane proteins, specifically α-hemolysin, in microfluidically-generated DIBs. Czekalska *et al.* studied α-hemolysin by measuring the electric current through a bilayer containing the pore-forming protein while sequentially replacing one DIB droplet with others containing various pore-blocking chemicals [46], [47]. This capability is essential for studying transmembrane proteins, as they often require a chemical stimulus from one side to perform their specific functions. Successfully cycling droplets in and out of DIBs to provide chemical stimuli sequentially would control when the proteins perform particular functions and give more options for studying their behaviours.

The methods of interacting with microfluidically-generated DIBs enable complex studies of transmembrane proteins to be performed with high levels of control that would otherwise be difficult to achieve. It may be possible to combine all of the discussed interrogation methods – electrical, optical and chemical – so that all three methods can be used simultaneously. The ease of integrating these interrogation methods and other advantages of microfluidic systems provide many opportunities for microfluidic devices to be used to form and study DIBs and their contents.

1.1.6 Summary of the State of the Art of Microfluidics for Droplet Interface Bilayers

Numerous microfluidic devices have been used to form and study DIBs by holding droplets in contact, relying both on advanced control of the fluid flow (e.g., advanced control over pressure pumps or syringe pumps) [48], [59]–[63] and using passive droplet traps [6], [45]–[47], [64]–[69].

The majority of these devices were fabricated using soft lithography of PDMS [6], [46], [57]–[67], [70], although some have been made using micromilling of PC [45]–[47]. The DIBs formed in these devices were stable for at least several minutes, with some stable for up to six hours [64] [65] [68] [46], [47].

The most complicated DIB structures formed by microfluidic devices are linear or 1.5D arrays of droplets in channels or droplet traps [6], [64], [65], [68]. The work of Elani *et al.* is the one notable exception where 2D and 3D arrays of limited size and complexity were demonstrated by closely packing droplets in a single channel [48]. These arrays could also be ordered if heterogeneous droplet types were introduced into the array.

These DIB and droplet trap arrays allowed multiple DIBs to be studied either rapidly or simultaneously depending on the observation method used [6], [45], [65], [68]–[70]. Additionally, droplets could be cycled in and out of these arrays without destroying the DIB structures, allowing for the sequential introduction of chemicals to specific DIBs [46], [47]. To the best of the author's knowledge, no 2D arrays of DIBs have been explicitly formed. However, microfluidic devices capable of creating large 2D arrays of closely packed droplets have been reported and could be adapted to form large 2D arrays of DIBs [63], [71].

To date, microfluidically-generated DIBs have been used primarily for studying the pore-forming transmembrane protein α-hemolysin by detecting the diffusion of ions or other molecules through the lipid bilayer via electrical or fluorescent signals [6], [45]–[47], [64], [68].

The use of microfluidically-generated DIBs is still relatively new; however, some significant advancements have been made. The devices reviewed appear to be capable of reproducibly forming DIBs and have been applied to studying a relatively simple transmembrane protein (α-hemolysin). However, several challenges affect the implementation of microfluidically-generated DIBs and opportunities to advance the field further.

1.1.6.1 Challenges for Microfluidics for Droplet Interface Bilayers

Most devices used to form DIBs have been made from PDMS, the most popular fabrication material for microfluidic devices. However, several challenges are associated with using PDMS, including its reduced optical signal strength for some optical detection methods, high flexibility, and ability to absorb fluids.

PDMS has been found to reduce the signal strength of some optical detection techniques. For example, Raman signals are reduced by a factor of approximately four when passing through a

PDMS layer [73]. However, signal enhancement techniques can mitigate the reduction in signal strength, meaning that PDMS is still a viable material for microfluidic devices.

The high flexibility of PDMS can reduce the definition of microfluidic channels and requires extra supports to make sizeable 2D droplet arrays [53], [63]. Additionally, it is challenging to make channels with non-uniform depths on a single device using soft lithography, complicating droplet trap design [74], [75].

The most challenging aspect of using PDMS for the study of DIBs is its high fluid absorption. A careful choice of operating fluids and other preventative measures can mitigate this property, but regardless, reduced DIB lifetimes are observed [6], [43]. PDMS can absorb water from the droplets forming the DIBs, disrupting the DIB structure, eventually leading to the merging of the droplets comprising the DIB [6], [43]. To mitigate this behaviour, Schlicht and Zagnoni soaked their PDMS devices in water for one hour before testing to reduce this effect. Still, they observed a 16% reduction in the top-down area of droplets forming DIBs over 40 minutes [73]. Mruetusatorn *et al.* showed that aqueous droplets used to form DIBs merged within three to five minutes without any device soaking due to PDMS water absorption [43]. This result indicates that PDMS will absorb water from droplets in DIBs and reduce DIB lifetimes even with preventative measures.

DIB lifetime is also affected by the microfluidic device operating conditions but has not been extensively studied or reported in the literature. The speed at which droplets come together to form DIBs and their compression or rarefaction affect their lifetime [68], [72], [76]. Therefore, careful control over the fluid velocities and pressures within microfluidic devices can avoid conditions that minimize DIB lifetimes.

Finally, the electrical interrogation of DIBs can be challenging because of the risk of electrocoalescence [60], [77]. If a sufficient voltage is applied to a lipid bilayer, the bilayer will begin to form pores, and eventually, the droplets forming the bilayer will merge, a process termed electrocoalescence [60]. This problem has already been addressed by indirectly contacting droplets or incorporating electrodes into droplets adjacent to the DIBs of interest [6], [46].

Many of these challenges can reasonably be addressed by choosing a different material for microfluidic devices and careful design. Opportunities for microfluidically-generated DIBs lie in addressing these challenges.

1.1.6.2 Opportunities to Advance Microfluidics for Droplet Interface Bilayers

New materials and fabrication methods for microfluidic droplet traps would avoid the problems associated with soft lithography of PDMS. Of particular interest is finding materials and fabrication techniques for creating large droplets chambers.

To the best of the author's knowledge, a droplet holding chamber for creating large ordered 2D arrays of DIBs has not yet been demonstrated. These would be useful for studying DIBs and transmembrane proteins optically, allowing for many DIBs to be observed simultaneously. Weak quantum biological signals could be observed resulting from a larger observation population. Additionally, ordered 2D arrays could produce complex droplet arrays faster than 3D droplet printers.

One challenge of creating ordered 2D arrays of DIBs is the inability to sequentially cycle droplets to introduce new chemicals to one side of the DIB. This issue is partly addressed by creating an ordered array of DIBs in advance so that each necessary droplet type is queued for use. Electrodes could be placed in specific DIBs to perform controlled and selective electrocoalescence to introduce new chemical species [60]. While this first requires an ordered 2D array, adding selective electrocoalescence capabilities would provide a level of control over DIB arrays that has not been demonstrated to date.

Another opportunity for the use of microfluidically-generated DIBs is their application to study complex transmembrane proteins. The microfluidic capabilities described in Section 1.1.5 regarding the study of α-hemolysin using DIBs would help in studying other transmembrane proteins. For example, a transmembrane transfer protein (i.e., a protein that actively moves molecules from one side of a bilayer to the other) could be observed electrically or optically both before and after introducing a chemical signal to trigger its behaviour in a highly controlled manner.

1.2 Research Objectives and Project Plan

This thesis aimed to design, build, and test a microfluidic system capable of facilitating the study of transmembrane proteins and their quantum biology. This would require a device capable of forming DIBs to create biologically representative environments to study transmembrane proteins.

Specifically, it was intended to study a transmembrane protein in the cytochrome family. These proteins are involved in electron transfer processes, vital to mitochondrial functions and integral to a cell's life. They are significantly more complex than α-hemolysin, can respond to chemical

stimuli, and have spin effects related to quantum biological behaviours. These behaviours were to be observed using Raman spectroscopy which can detect these spin effects [20], [78]–[82]. The signal strength of quantum biological behaviours can be boosted using signal-enhancing techniques, like surface-enhanced Raman spectroscopy and resonance Raman spectroscopy. It was hypothesized that the signal could be detected at physiologically relevant temperatures rather than cryogenic temperatures. Compared to the typical application of fluorescence detection to microfluidically-generated DIBs, such detection methods would represent a more advanced optical detection technique that has not been reported to date.

Time permitting, creating large ordered 2D arrays of droplets and integrating electrodes into the device was to be pursued. Large ordered 2D arrays of droplets would apply directional chemical stimuli to transmembrane proteins and multiple DIBs to be simultaneously observed. This increased number of observed DIBs would enhance the received optical signals, providing more complicated analyses of transmembrane proteins such as Raman spectroscopy. Implementing Raman spectroscopy would be even more feasible if the devices were made from Raman compatible materials.

Integrating electrodes would allow the DIB electrical behaviours to be monitored and possibly allow the selective electrocoalescence of specific DIBs, enabling a sophisticated form of control over introducing chemicals to specific DIBs, which has not previously been demonstrated.

The microfluidic devices developed in this thesis were fabricated using a CO_2 laser cutter to engrave microfluidic channels into PMMA to explore using a different material and fabrication method for making microfluidic droplet traps. Previously, the author built microfluidic droplet generators using integrated peristaltic micropumps in laser engraved microfluidic channels in PMMA [83], discussed in Section 3.3.

Rather than focusing on device fabrication, this thesis is concerned with the design and application of pressure-driven microfluidics. Device fabrication was performed by the author's supervisor, Dr. Christopher Backhouse. The fabrication process was very similar to the one used previously by the author [83]. Design and testing of the devices were the primary focus of the author.

To the best of the author's knowledge, no microfluidic droplet trapping devices fabricated from PMMA using laser-cutting have been reported. Laser-cut microfluidic channels have a different channel profile than the typically used rectangular channels of devices made through soft lithography with PDMS. While laser fabrication provides some advantages, designs demonstrated

to date in the literature would require adaptation due to the unique channel profile of laser-cut channels.

The goals of this thesis were achieved according to the following project plan:

First, a reliable microfluidic droplet generator was required. Based on the design criteria of the droplet traps using the chosen fabrication method, the droplets had to be approximately twice as long as they were wide and could vary in volume by no more than 10%. The reasoning for these requirements is detailed in Section 4.3.1.

Next, a droplet trap had to be designed and integrated into the droplet generator to allow DIBs to form. The DIBs were intended to be stable for at least 1.5 minutes because this was the minimum lifetime reported in the literature to perform a typical DIB experiment. However, more complex analyses of transmembrane proteins could be performed more stable DIBs.

Then two capabilities had to be developed: A droplet generator capable of producing heterogeneous droplet types and an expanded droplet trap to make a large DIB array. A means of ordering droplets within the array would then be developed. Transmembrane proteins could be studied at any point once DIBs had been successfully made, but it was thought to be most beneficial to begin once heterogeneous droplets could be produced.

Time permitting, incorporated electrodes could be used to study electrical signals from transmembrane proteins or perform selective electrocoalescence within a DIB array.

The combination of electrical, optical, and chemical stimuli for studying microfluidically-generated DIBs has not been demonstrated and would represent a significant advancement in the state of art.

These were ambitious but achievable goals, but the project faced numerous challenges that prevented several from being completed. This thesis covers the work performed towards achieving these goals and provides an overview of how future work may make further progress.

1.3 Thesis Organization

The following chapters describe the relevant physics, theoretical models, fabrication methods, evaluation methods, and iterative design approaches for microfluidic droplet traps.

Chapter 2 provides an overview of the relevant theory of microfluidics used in the device design process. Microfluidic physics and the design principles for T-junction droplet generators and droplet traps are reviewed.

Chapter 3 describes the selected fabrication method and materials. The verification methods applied to the material and device properties used in the device design and the analyzed test results are presented. The verified properties include the device substrate surface properties and the densities and viscosities of the chosen fluids: Deionized (DI) water and mineral oil loaded with 2 wt% Span 80. Lastly, an empirical model of the fluidic resistance of the uniquely shaped laser-engraved microfluidic channels is developed.

Chapter 4 describes the design and test principles for microfluidic droplet generators using pressure-driven flow. Their development uses an equivalent circuit model along with specific design parameters and constraints. The operating and test methods for the resulting droplet generators are also detailed.

Chapter 5 builds on the design and test principles, including microfluidic droplet traps and their integration into droplet generators. The designs of two droplet traps, the Primary Droplet Trap and Alternate Droplet Trap, are detailed, along with their operating procedures and test methods.

Chapter 6 summarizes the numerical design and test results of a droplet generator, the base device into which the subsequently designed droplet traps were integrated. The droplet generator produced reliable and reproducible droplet streams. However, the model underwent several adjustments to bring its predicted behaviour in line with the observed behaviour.

Chapter 7 describes the design and test of several droplet traps: three iterations of the Primary Droplet Trap and one version of the Alternate Droplet Trap. The test results and a droplet-splitting model to describe their behaviour are also discussed.

Chapter 8 discusses the final designs of the Primary and Alternate droplet traps and how the deficiencies of their previous versions are addressed. The droplet trap model is applied to understand and address problems observed in earlier iterations of the droplet traps.

Chapter 2
Microfluidics Theoretical Background

2.1 Introduction

This chapter provides an overview of the physics required to design and predict the behaviour of microfluidic devices, specifically droplet generators and traps. This includes the electric circuit analogy for microfluidics, channel resistance and Laplace pressure. Models for the design of a T-junction droplet generator and passive droplet trapping are also discussed.

2.2 Electric Circuit Analogy for Modelling Microfluidics

The interactions between fluid flow and the device's channels must be understood to effectively design a microfluidic device, such as a droplet generator. The design of a microfluidic device often requires complex modelling, which in many cases, can be accomplished through the use of an electric circuit analogy [6], [70], [84], [85].

A common analogy used in teaching electronic circuits courses is that electric current can be thought of like water flowing through a hose. The fluid flow rate (Q) is analogous to electric current (I), the fluid pressure (P) is equivalent to voltage (V), and the resistance of the hose ($R_{fluidic}$) is analogous to the resistance of an electric circuit element ($R_{electric}$). This analogy is helpful to provide a physical understanding of electric circuit principles but can also be applied to the design of microfluidic devices. A microfluidic device can be thought of as an electric circuit that runs on fluid rather than electricity. However, this becomes more complicated in droplet microfluidics, as will be discussed later in Section 2.5.2.

With this in mind, a fluidic version of Ohm's law ($V = IR$) can be written to describe fluid flow through a microfluidic channel. In Equation (2-1), P is fluidic pressure [Pa], Q is fluid flow [$m^3\ s^{-1}$], and R is the fluidic resistance of the microfluidic channel [Pa s m^{-3}] [84], [85]. This relationship can also be derived from Hagen-Poiseuille's law for fluid flow applied to a steady-state pressure-driven fluid flow in a channel [84]. This analogy allows for electric circuit design principles, such as Kirchoff's Current and Voltage Laws, to be applied to the design of microfluidic devices using equivalent fluidic circuits and Equation (2-1).

$$P = QR \tag{2-1}$$

Understanding two of the three parameters in Equation (2-1) is necessary to determine the third parameter. The method used to drive fluid flow within microfluidic channels will determine the pressure (P) or the fluid flow rate (Q). The fluidic resistance (R) of channels can be modelled based on their dimensions and fluid properties.

2.2.1 Driving Fluid Flow in Microfluidic Devices

The microfluidic channel structure of a device is mainly immutable after fabrication. Therefore, control over how fluids are driven through the channels of a device is the primary method to influence device behaviour. Depending on the method used to drive fluid flow in the microfluidic channels, the pressure or the flow rate can be determined. There are a variety of means available for driving fluid flows in microfluidic channels. These range from syringe pumps to on-chip peristaltic pumps and electrically driven fluid flows [84], [86]–[91].

The most commonly used methods to drive fluids through microfluidic devices are syringe pumps and constant pressure-driven sources. A syringe pump operates by gradually depressing a plunger on a syringe filled with fluid and connected to the microfluidic device (Figure 2-1). The syringe's plunger is depressed at a programmable rate such that a constant flow rate of fluid is applied to the microfluidic channels [84], [86], [92].

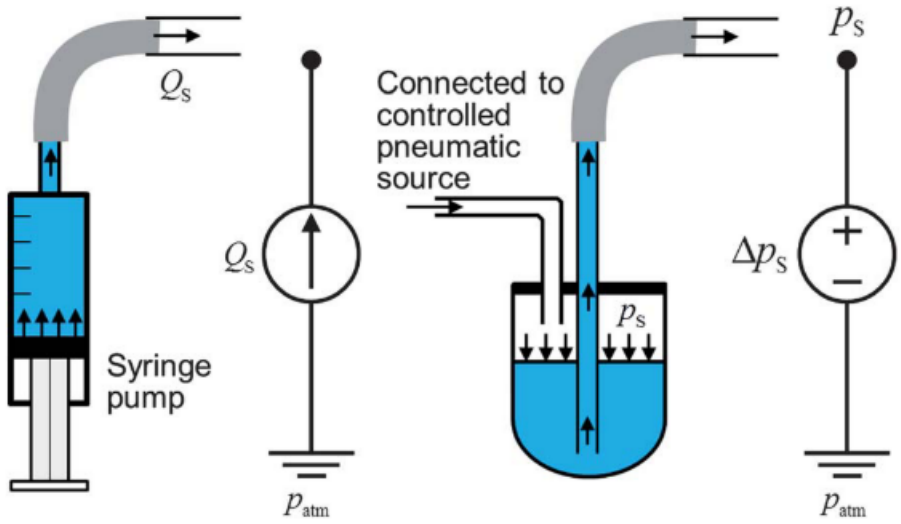

Figure 2-1 - A schematic of a syringe pump, a constant pressure-driven fluid source, and their analogous electronic circuit components [84].

A constant pressure-driven source generates a pressure difference between a fluid reservoir and the microfluidic channels of the device. The most common method to accomplish this is to apply pressure to a sealed container holding a fluid with a tube leading to the microfluidic device (Figure 2-1). As the container is pressurized, the fluid is driven through the tubing and into the microfluidic channels [84], [85], [92].

Alternatively, a pressure difference between a fluid reservoir and a microfluidic device can be generated by elevating the fluid reservoir above the microfluidic device. The pressure generated in this way can be calculated according to Equation (2-2). In Equation (2-2), where P is the pressure [Pa], ρ is the density of the fluid [kg m^{-3}], g is the acceleration due to gravity [m s^{-2}], and Δh is the height difference between the fluid reservoir and the output of the microfluidic device [m] [65], [84].

$$P = \rho g \Delta h \tag{2-2}$$

Combining a known fluid flow rate or pressure with a known fluidic resistance allows the remaining variable in Equation (2-1) to be determined. Therefore, the behaviour of the device can be predicted.

In this thesis, gravity-generated pressure-driven fluid flows were used. This required fluid reservoirs to be suspended at certain heights above the microfluidic devices. The fluid pressures generated using this method were calculated using Equation (2-2).

2.2.2 Channel Hydraulic Resistance

The microfluidic channel's hydraulic or fluidic resistance is determined by the channel's cross-sectional perimeter and area, length, and fluid viscosity. The fluidic resistance can be calculated based on the channel dimensions, channel profile and fluid properties. It can be determined independently from the means used to operate the microfluidic device as it is an intrinsic property of the channel.

Relationships between a channel's parameters and its hydraulic resistance have been determined analytically for some standard channel cross-sections. These include channels with circular, rectangular, elliptical, equilateral triangle cross-sections. For example, the hydraulic resistance of a channel with a circular cross-section has been well studied and can be calculated analytically using Equation (2-3) [84], [93]. In Equation (2-3), R is the hydraulic resistance [Pa s m^{-3}], η is the viscosity of the fluid [Pa s], L is the length of the channel [m], and r is the radius of the channel [m]. Equation (2-3) is derived from the Hagan-Poiseuille law. It is only valid for laminar flow in circular channels [93].

$$R = \frac{8\eta L}{\pi r^4} \tag{2-3}$$

Several assumptions are made in the derivation of the laminar flow profile from the Navier-Stokes equation, which describes the flow of incompressible fluids (Equation (2-4)) [93]. In Equation (2-4), ρ is the fluid density [kg m^{-3}], v is the velocity vector field [m s^{-1}], t is time [s], k represents volume forces that create momentum (e.g., gravity, etc.) [N], p is the pressure [Pa], and η is the fluid's dynamic viscosity [Pa s]. The assumptions required to derive the laminar flow profile include that fluid flow is constant with respect to time, parallel throughout the channel, driven by a pressure drop and is not-convective. This last assumption requires that the convection term $\left[\left(\vec{v}\cdot\vec{\nabla}\right)\vec{v}\right]$ of the Navier-Stokes equation can be ignored [93]. If these assumptions are not met, Equation (2-3) cannot be used.

$$\rho\left(\frac{\delta\vec{v}}{\delta t} + \left(\vec{v}\cdot\vec{\nabla}\right)\vec{v}\right) = \vec{k} - \vec{\nabla}p + \eta\Delta\vec{v} \tag{2-4}$$

These assumptions are typically met in microfluidic flow except for the convective flow assumption. Therefore, it is essential to check that the flow is not convective. The Reynolds number can be used to determine whether the convective term of the Navier-Stokes equation can

be ignored. The Reynolds number describes the relationship between viscous and inertial forces in a fluid flow and can be calculated according to Equation (2-5) [93]. In Equation (2-5), ρ is the fluid density [kg m^{-3}], v is the flow velocity [m s^{-1}], L is the characteristic linear dimension [m], and η is the fluid's dynamic viscosity [Pa s]. In a circular channel, the characteristic length is the diameter of the channel. If the value of the Reynolds number is below ~1500, then the flow is likely laminar. There is some debate in the literature about the limit of the Reynolds number for laminar flow. However, the Reynolds number provides a simple method to determine if laminar flow occurs and whether Equation (2-3) can be applied [93].

$$Re = \frac{\rho v L}{\eta} \tag{2-5}$$

Even if the fluid flow is laminar, not all microfluidic channels have circular cross-sections, and only some channel cross-sections have analytical solutions for their resistance. For non-standard channel cross-sections, solutions for their resistance must be either determined numerically through complex calculations or approximated.

A standard approximation uses a hydraulic radius (r_H) to describe a circular channel roughly equivalent to a non-circular channel with respect to hydraulic resistance [93]. The hydraulic radius of the channel, r_H, can be calculated according to $r_H = 2A/U$, where A and U are the cross-sectional area [m^2] and wetted perimeter [m] of the non-circular channel, respectively [84]. Substituting r_H into Equation (2-3) results in an approximation of fluidic resistance for a non-circular channel. This approximation is shown in Equation (2-6) [94]. More precise equations for the hydraulic resistance of some non-circular channels have been developed. However, these are more complicated to use [6], [70], [84], [93]. When possible, the analytically determined equations for the exact hydraulic resistance of microfluidic channels should be used, as Equation (2-6) can produce significant errors [93].

$$R = \frac{2\eta L U^2}{A^3} \tag{2-6}$$

Henrik Bruus also proposed a generalized formula for the resistance of a channel which depends on a geometrical correction factor α that is unique to the geometry of the channel (Equation (2-7)) [95]. Bruus developed this equation based on solving Poiseuille flow for a channel with an arbitrary cross-section. The geometrical correction factor is related to how surface phenomena affect fluid flow through the channel. It depends on both the perimeter and area of the channel.

$$R = \alpha \frac{\eta L}{A^2} \tag{2-7}$$

This geometric correction factor was related to a compactness factor (C) that described a microfluidic channel's surface-to-volume ratio. Relationships between C and channel dimensions and between α and C could be determined analytically for some cross-sections. However, for

non-standard channel cross-sections, these relationships had to be determined numerically. These relationships required the assumption that the fluid flow through the channel is laminar and obeys the Hagen-Poiseuille Law [95]. The geometrical correction and compactness factors for an arbitrary channel cross section were linked as: $\alpha = C = U^2/A$ as an approximation [96]. Using this relationship in Equation (2-7) results in a different approximation for the resistance of a non-circular channel. This approximation is smaller by a factor of two compared to Equation (2-6). This difference in the common approximations of fluidic resistance highlights the difficulty in determining the resistance of a microfluidic channel with a non-standard cross-section.

While Equation (2-6) and Equation (2-7) may serve as rough approximations of channel resistance, it is necessary to verify that their use is appropriate through computations and experiments. The presence of droplets is known to affect the resistance of microfluidic channels making determining channel resistance even more complicated [85], [97]–[99].

2.3 Microfluidic Droplet Generation

The physics described above is sufficient to model the behaviour of a single fluid phase flowing through a microfluidic device, but not the behaviour of droplets. Two immiscible phases need to be driven into a single channel to form droplets in a microfluidic device. This process creates segments of one phase (i.e., droplets of a dispersed phase) within the other phase (i.e., a continuous phase). State-of-the-art microfluidic droplet generators can typically produce droplets that vary in volume by less than 5% [83], [85], [100].

The most common microfluidic channel geometries used to make droplets in a microfluidic device are T-junctions and flow-focusing structures [41]-[43]. A T-junction is simply an intersection of two microfluidic channels that are perpendicular to each other. One channel is filled with a continuous phase, and the other is filled with a dispersed phase (Figure 2-2). For this thesis, a T-junction droplet generator was chosen because of the author's previous experience with T-junction droplet generators and their simple channel geometry.

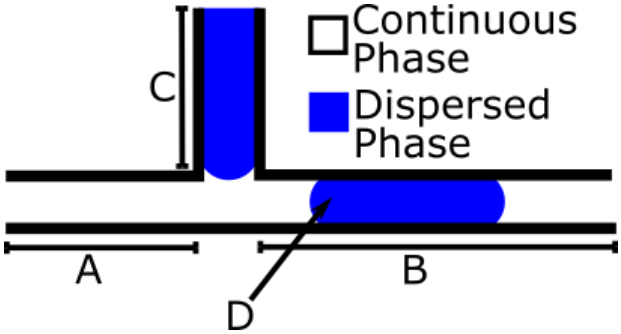

Figure 2-2 – A simple depiction of a T-junction droplet generator. Black lines define channel walls, the dispersed phase is denoted by blue regions, and the continuous phase constitutes any non-blue region within the channel boundaries.

T-junction droplet generators function as follows: as the dispersed phase flows, it enters the channel containing the continuous phase. The dispersed phase gradually blocks the flow of the continuous phase, which then shears off segments of the dispersed phase to form droplets. This process can be classified into the following three regimes: squeezing, dripping or jetting, as

illustrated in Figure 2-3 [100]–[102]. Depending on the intended use of the produced droplets, it may be preferable to create droplets by using a specific regime.

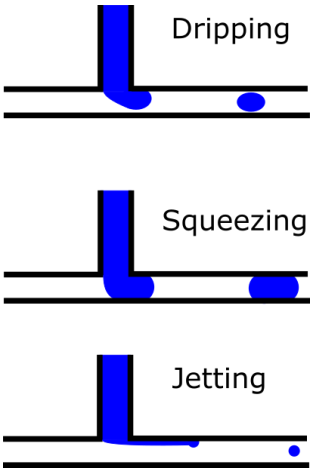

Figure 2-3 - The three typical droplet formation modes for continuous flow microfluidic droplet generation.

These regimes are often defined in literature based on the Capillary number (*Ca*) of the continuous phase flow (Equation (2-8)) [100]–[102]. The Capillary number describes the ratio between interfacial and shear forces in droplet formation. In Equation (2-8), η is the dynamic viscosity of the continuous phase [Pa s], u is the average velocity of the continuous phase [m s^{-1}], and γ is the interfacial tension between the continuous and dispersed phases [N m^{-1}] [100]. These regimes can be challenging to identify optically and are often subjectively categorized. Some droplets cannot be characterized into one of these three regimes. Instead, they belong to transitional regimes and pose an additional challenge to correctly identifying the droplet formation regime.

$$Ca = \frac{\eta u}{\gamma} \tag{2-8}$$

Differences between regimes are related to the balance between interfacial forces and pressures generated by the continuous phase. The squeezing regime produces droplets that are longer than the width of the channel in which they are made. This regime occurs at low values of the Capillary number for the continuous phase (Figure 2-3) [100], [101]. The dripping regime is characterized by slightly smaller droplets with widths smaller than the channel width and occurs at higher Capillary numbers (Figure 2-3) [100], [101]. The jetting regime is rarer in a T-junction geometry and only occurs at very high Capillary numbers. It is characterized by a short section of co-flow between the dispersed and continuous phases (Figure 2-3) [100]–[102].

The classifications of droplet formation regimes are not often reported in the literature on microfluidic droplet trapping and DIB formation. However, based on images of the produced droplets, microfluidic devices that form DIBs typically use the squeezing regime. They may also use a transitional regime between the squeezing and dripping regimes. This regime is most often used because droplets occupy the majority of the droplet forming channel. Therefore, their shapes depend on channel geometry, and they can be more predictably trapped.

The literature has reported few models of pressure-driven droplet generation using the electric circuit analogy [85]. From the few reported models, it is known that an additional pressure, the Laplace pressure, must also be considered. This pressure is vital to droplet generation and behaviour in microfluidic devices and accounts for interfacial forces affecting the droplets.

2.4 Laplace Pressure

Forming droplets by forcing two immiscible fluids into a single microfluidic channel creates interfaces between the two fluid phases. These curved interfaces have pressure drops between the inside and outside of the interfaces, characterized by the Laplace pressure (P_{LP}). The Laplace pressure can be calculated using Equation (2-9), where γ is the interfacial tension (also known as the interfacial energy) [N m^{-1}], and r_{d1} and r_{d2} are the radii of the two principal curvatures of the interface [m] [103]. These two principal radii are orthogonal to each other. If the interface has a circular cross-section, then $r_{d1} = r_{d2} = r$, and Equation (2-9) can be simplified [70], [85]. This pressure can also be thought of as a capillary pressure or pressure source that pushes into the curved surface to flatten it.

$$P_{LP} = \gamma\left(\frac{1}{r_{d1}} + \frac{1}{r_{d2}}\right) = \frac{2\gamma}{r} \tag{2-9}$$

In most microfluidic channels, the principal radii of curvature are defined by, or assumed to be defined by, the channel geometry. The relevant parameters include a channel's cross-section, depth and width. In a rectangular channel, the fluid interface is defined by two principal radii, one defined by the channel depth (H) and the other defined by the channel width (W) (Equation (2-10)) [85], [104]. In a wide and shallow rectangular channel, the Laplace pressure is defined primarily by the channel depth, which represents the tightest radius of curvature. When the channel width and depth are of comparable size, the relationship between the radius of curvature and the channel geometry is more complicated.

$$P_{LP} = 2\gamma\left(\frac{1}{H} + \frac{1}{W}\right) \tag{2-10}$$

The ability to control the dimensions of microfluidic channels provides control over the Laplace pressure of droplets and the dispersed fluid phase at the droplet generation point. The works of Satoh *et al.* and Glawdel and Ren state that the Laplace pressure plays a role in the formation of droplets by defining a lower bound on the pressure required to generate droplets [85], [104]. While the Laplace pressure plays a relatively minor role in droplet generation, it is more important in designing passive droplet traps to produce DIBs. The role of the Laplace pressure in droplet trapping will be discussed further in Section 2.6.

2.5 Theory of Microfluidic T-junction Droplet Generators

As mentioned in Section 1.2, this project will use a T-junction droplet generator to create droplets to form DIBs. It is common practice to operate T-junction droplet generators using pressure-driven

flow [85], [97], [105]. The use of gravity is a simple and cost-effective way to generate pressure-driven flow in a microfluidic device, as described previously (see Section 2.2.1) [65], [105]. The droplet generators designed for this thesis will use gravity-generated pressure-driven flow. This was accomplished by suspending fluid reservoirs above the device at certain heights. Given a known fluid flow source and the resistance of the microfluidic channels in a device, the behaviour of a T-junction droplet generator can be predicted.

A T-junction droplet generator is a standard design, which is schematically shown in Figure 2-2. In Figure 2-2, the channel left of the junction is referred to as the continuous phase input channel (Figure 2-2A), the channel right of the junction is referred to as the main channel (Figure 2-2B). The channel entering the junction from the top of the image is the dispersed phase input channel (Figure 2-2C). If the dispersed phase flows towards the junction and the continuous phase flows towards the junction, droplets of the dispersed phase will be formed in the main channel. The droplet will be surrounded by the continuous phase (Figure 2-2D).

The physics in the electric circuit analogy represents a T-junction geometry as a resistive network. This includes a pressure drop in the dispersed phase input channel due to the Laplace pressure of the dispersed phase fluid front at the T-junction (Figure 2-4). In Figure 2-4, P_d is the pressure applied to the dispersed phase, R_d is the resistance of the dispersed phase input channel (channel C in Figure 2-2), and Q_d is the volumetric flow rate of the dispersed phase. P_c is the pressure applied to the continuous phase, R_c is the resistance of the continuous phase input channel (channel A in Figure 2-2), and Q_c is the volumetric flow rate of the continuous phase. P_{LP} is the Laplace pressure of the dispersed phase fluid front at the T-junction; this is the curved dispersed phase fluid front in channel C of Figure 2-2. R_m is the resistance of the main channel (channel B in Figure 2-2), and P_j is the pressure at the T-junction.

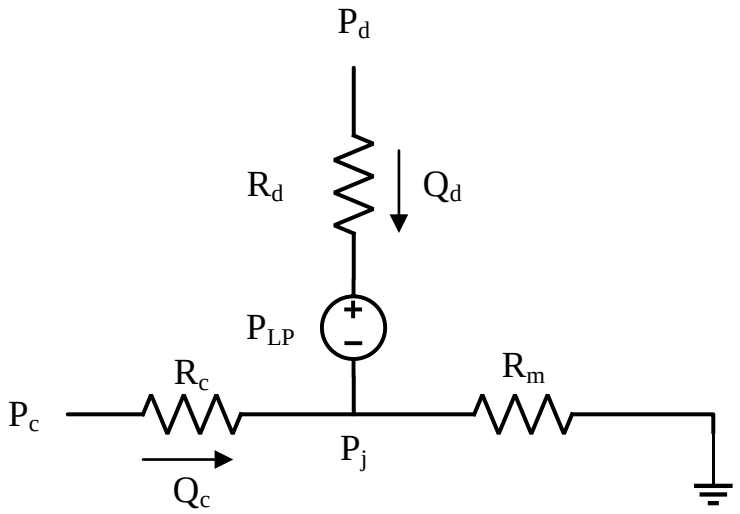

Figure 2-4 – An equivalent resistive network for a T-junction droplet generator. The Laplace pressure is thought to behave similarly to a constant pressure source.

A value that can be derived from this diagram is the fluid flow rate in the main channel, Q_m. This flow rate is equal to the sum of Q_d and Q_c: $Q_m = Q_d + Q_c$. This resistive network model can be used to predict the behaviour of T-junction droplet generators and design them to create stable

streams of uniform droplets. Specifically, the model can predict the operating pressure range of a pressure-driven T-junction droplet generator to avoid backflow. Backflow is when the continuous or dispersed phase flows into the other phase's input channel rather than through the main channel. Preventing backflow ensures the constant production of droplets during the operation of the droplet generator.

2.5.1 Defining an Operating Range to Prevent Backflow

Avoiding backflow in a T-junction droplet generator is imperative to producing a reproducible stream of droplets. T-junction droplet generators function by forcing two immiscible fluids into a single microfluidic channel. Therefore, to form droplets in the main channel, both Q_d and Q_c should be positive values. Such values would indicate flow in the direction of their corresponding arrows in Figure 2-4. If either of these flow rates is a negative value, droplets will not be formed. In this case, fluid from one of the fluid sources will flow into the input channel leading to the other fluid source, through R_c or R_d. This undesired flow during operation - Q_d or Q_c flowing in the opposite direction to the arrows in Figure 2-4 - is defined as backflow. Not only does backflow stop droplet production, but it was observed in the initial testing of droplet generating devices to cause fluid source contamination. This contamination created unwanted emulsions of the dispersed and continuous phases. Such emulsions led to unpredictable device performance as their fluidic properties (e.g., viscosity) were unknown. Additionally, contamination of the fluid sources requires a lengthy recovery period, estimated at 15 minutes or more, to return the device to regular operation. Avoiding backflow is therefore of the utmost importance to ensure reliable device operation and timely droplet formation.

Appropriate operating pressures for generating pressure-driven flow must be chosen to prevent backflow. Two limiting cases can be considered to define a normal operating range. Case (1) – $Q_d < 0$, fluid flows through the dispersed phase input channel (R_d) and away from the T-junction. Case (2) – $Q_c < 0$, fluid flows through the continuous phase input channel (R_c) and away from the T-junction. These cases are the same as considered in the T-junction droplet generator model proposed by Glawdel and Ren [85].

The dispersed phase flow rate, Q_d, can be calculated according to Equation (2-11). In Equation (2-11), Q_d, P_d, P_j, P_{LP} and R_d are defined above for the resistive circuit model shown in Figure 2-4.

$$Q_d = \frac{P_d - P_j - P_{LP}}{R_d} \tag{2-11}$$

The continuous phase flow rate, Q_c, can be calculated according to Equation (2-12). In Equation (2-12), Q_c, P_c, P_j, and R_c are defined above for the resistive circuit model shown in Figure 2-4.

$$Q_c = \frac{P_c - P_j}{R_c} \tag{2-12}$$

The pressure at the T-junction (P_j) is dependent on several factors, including the input pressures of both the dispersed phase (P_d) and the continuous phase (P_c) (Equation (2-13)). In Equation

(2-13), P_d, R_d, P_c, R_c, R_m and P_{LP} are defined above for the resistive circuit model shown in Figure 2-4. The derivation of this equation is provided in Appendix A.

$$P_j = \frac{(P_d - P_{LP})R_m R_c + P_c R_m R_d}{R_d R_c + R_m R_c + R_m R_d} \tag{2-13}$$

By considering a constant continuous phase input pressure (P_c), an acceptable operating pressure range for the P_d of the Droplet Generator can be defined (Equation (2-14)). The limits of this inequality are determined by solving for P_d in Equation (2-11) and Equation (2-12), wherein Q_d and Q_c are equal to zero, respectively. The derivation of these limits can be found in Appendix A. In Equation (2-14), P_d, P_c, R_d, R_c and P_{LP} are the same as defined for Figure 2-4. R_{mcp} and R_{mdp} refer to the resistance of the main channel (R_m) when filled with only continuous phase and dispersed phase, respectively.

$$P_c\left(\frac{R_{mcp}}{R_c + R_{mcp}}\right) + P_{LP} < P_d < P_c\left(1 + \frac{R_d}{R_{mdp}}\right) + P_{LP} \tag{2-14}$$

The lower limit of Equation (2-14) corresponds to the case when the fluid flow in the dispersed phase input channel is equal to zero. Dropping P_d below the lower limit would result in Case (1), $Q_d < 0$ (i.e., backflow). The upper limit of Equation (2-14) corresponds to the case when the fluid flow in the continuous phase input channel is equal to zero. Raising P_d above the upper limit would result in Case (2), $Q_c < 0$ (i.e., backflow). By operating within these limits, backflow can be avoided. Operating near the lower limit of Equation (2-14) corresponds to lower fluid flow rates and smaller droplet volumes, which are easier to manipulate. Therefore, the droplet generator devices designed in this thesis were intended to be operated near this lower limit.

Equation (2-14) allows for the operation range of a T-junction droplet generator to be determined based on appropriate operating conditions and device properties. These include choosing P_c, a flow rate ratio (Q_d/Q_c), channel resistances and the value of P_{LP}. Therefore, the operating range of a droplet generator can be defined by Equation (2-2) to determine the input pressures, the LaPlace Pressure (P_{LP}) and fluidic resistances. However, Equation (2-14) does not account for changes in main channel resistance which can occur due to droplets being made or leaving the main channel. These processes may affect the operating range of the Droplet Generator.

2.5.2 Resistance Variations

Droplets in the main channel of a T-junction droplet generator are the primary source of resistance variations [85]. Fluidic resistance corresponds to the average pressure-driven flow of a viscous fluid with a known viscosity through a filled channel of known geometry. This can be determined analytically for some well-known geometries but not for all channel geometries, as discussed in Section 2.2.2. However, it has not been solved when considering channels filled with two immiscible phases, e.g., droplets of a dispersed phase in a continuous phase. Droplets are expected to affect the resistance of a microfluidic channel as they drastically reduce the area of the channel through which the continuous phase can flow and disrupts the laminar flow. With a reduced cross-

sectional area, the resistance would increase. Operational rules of thumb to manage the resistance irregularities of droplets have been developed.

The resistance of a droplet is dependent on many factors, including droplet length, droplet width, channel dimensions, and it can be difficult to predict [85], [98], [99]. The work of Glawdel and Ren on a T-junction network model suggested that the resistance of a droplet in a rectangular microfluidic channel was two to five times greater than the resistance of the same microfluidic channel filled with only a continuous phase [85]. This increase was the case despite the droplet, composed of water, having a much lower viscosity than the ongoing phase. Understanding the resistive effects of droplets is vital to determining the main channel resistance. Depending on how many droplets are present, the main channel resistance could be much higher than when filled with just the continuous phase.

The main channel resistance, R_m, is based on its fluid content and depends on both the continuous phase resistance and the resistance of droplets surrounded by the continuous phase. Droplets in the channel cause an increase in the main channel resistance and variability in R_m. The resistance can increase or decrease as a droplet is formed in or leaves the main channel. R_m can be calculated, accounting for the presence of droplets using Equation (2-15). In Equation (2-15), where δ represents the fraction of the main channel filled only with droplets, n represents the number of droplets, and R_{drop} represents the resistance of one droplet. n can be determined by multiplying the length of the main channel by δ and then dividing by the length of a single droplet. It should also be noted that δ is equivalent to the ratio of the dispersed phase flow rate to the total main channel flow rate (Q_d/Q_m).

$$R_m = (1-\delta)R_{mcp} + nR_{drop} \pm R_{drop} \tag{2-15}$$

As seen in Equation (2-15), the main channel resistance varies by as much as $\pm R_{drop}$ when filled with droplets. This variation in resistance affects the operating pressure range to prevent backflow. However, it can be minimized by choosing a suitably high value for R_m, such that the effect of one droplet entering or leaving the channel is minimal (i.e., R_{drop}/R_m is small). While a specific number of droplets may be desired, unless the number of droplets is large, it is helpful to create more droplets than required. Creating more droplets requires a longer main channel, increasing R_m and minimizing the variation in main channel resistance.

The acceptable pressure range for P_d for a given P_c can then be extended to account for the presence of droplets and accompanying variability. All that is required to extend the model is to replace R_{mcp} in the lower limit with R_m as calculated using Equation (2-15) for the desired droplet forming conditions. This adaptation should be performed considering the highest possible value for R_m. The adjusted acceptable pressure range for P_d can be seen in Equation (2-16). R_{mdp} need not be replaced with R_m in the upper limit because, at that limit, the main channel would be filled entirely with the dispersed phase. At the upper limit, the main channel would look like a single droplet occupying the entire length of the channel.

$$P_c\left(\frac{R_m}{R_c+R_m}\right) + P_{LP} < P_d < P_c\left(1+\frac{R_d}{R_{mdp}}\right) + P_{LP} \tag{2-16}$$

Equation (2-16) allows for the calculation of acceptable values of the dispersed phase input pressure (P_d) for a given continuous phase input pressure (P_c). It also accounts for the presence of droplets in the main channel of a T-junction droplet generator. This equation can be used to define the operating parameters of a T-junction droplet generator once the resistances of the three channels have been determined. It is the same as the operating pressure range equation proposed by Glawdel and Ren in their droplet generator model [85].

2.6 Microfluidic Droplet Trap Design Theory

The effective formation of DIBs in a microfluidic device requires that droplet trapping behaviours are well understood. Perhaps the most important consideration in passive droplet trapping is the Laplace pressure.

The curved fluid interfaces of droplets, typically bound by the channel they occupy, have principal radii dependent on the channel dimensions. If the channel dimensions were to change suddenly, the Laplace pressure would also change. For example, if a channel were to constrict suddenly, then the curved interface of a droplet would become much smaller. The principal radii of curvature would also decrease, resulting in a higher Laplace pressure. Droplet traps generally rely on a rapid change in channel dimensions, and therefore, this becomes important in droplet trapping applications. The pressure required to displace trapped droplets is often quantified by the difference in Laplace pressure of the droplets when in trapping positions and in constricted channels leaving a droplet trap [6], [69], [70].

As a droplet approaches a constriction in a channel, e.g., a constricted channel leaving a droplet trap, the front fluid interface of the droplet becomes constricted. This constriction results in a higher Laplace pressure and the exertion of a greater force on the droplet, preventing it from entering the constricted channel. In comparison, the Laplace pressure exerted at the rear interface of the droplet is smaller. Therefore, the difference in the droplet's Laplace pressures at the front and rear fluid interfaces needs to be overcome to force a droplet into a constricted channel. This difference can be described by Equation (2-17). In Equation (2-17), r_r is the radius of the rear fluid interface (i.e., the fluid interface at the back of the droplet), and r_f is the radius of the front fluid interface (i.e., the fluid interface at the leading end of the droplet) [6], [70].

$$\Delta P_{LP} = 2\gamma\left(\frac{1}{r_f} - \frac{1}{r_r}\right) \tag{2-17}$$

Equation (2-17) assumes fluid fronts each have only one principal radius or two principal radii, but one remains constant during the channel transition. It also assumes a constant interfacial tension. However, Equation (2-17) may change depending on the conformation of the droplet, changes in the channel dimensions or changes in contact with the channel walls.

If this pressure barrier (i.e., the trapping pressure, ΔP_{LP}) is overcome, the droplet will enter the constricted channel. This pressure barrier is commonly used for passive droplet trapping. Specific

constrictions in channels are added, which will hold droplets in place when the device is operated such that the pressure across a constriction does not exceed its ΔP_{LP} value.

The Laplace pressure difference effectively determines the pressure required to push a droplet through a channel transition. Equation (2-17) is most easily applied to channels with standard geometries like circular, rectangular or elliptical channels because their principal radii can be determined based on known relationships. In some cases, the principal radii can even be directly measured. However, for non-standard channel geometries with less well-known relationships between the principal radii and channel geometry, determining the Laplace pressure of a droplet can be more complicated.

The principal radii of droplets in microfluidic channels can typically only be observed from above and are therefore difficult to measure in channels with non-standard geometries. At most, one principal radius can be measured from a top-down view. The second principal radius can be approximated by assuming the droplet has hemispherical ends. However, Musterd *et al.* have shown that this is not a wise assumption based on modelling the 3D shape of droplets in microfluidic channels [106].

To further complicate this issue, as droplets are transitioned into a smaller channel, the droplet shape may change, and possible direct contact with channel walls also needs to be considered. Contact with the channel walls can be challenging to determine when only observing droplets from above. Additionally, wall contact is not strictly addressed with the Laplace pressure approach (Equation (2-17)). Therefore, using Equation (2-17) based on the principal radii of droplets as measured from above can only provide approximate values of the Laplace pressures of droplets, particularly in the context of droplet trapping.

2.6.1 Effects of Channel Geometry

It may be possible to obtain a value of the principal radii of a droplet by considering the shape of droplets in microfluidic channels. It is accepted that droplets will largely conform to a channel's cross-section, except in the corners of the channel. The droplets will be surrounded by a sheath of the continuous phase separating them from the channel walls [106]–[108]. It is typically assumed that the continuous phase sheath surrounding droplets has a negligible thickness, and therefore, droplets occupy the channel's entire cross-section. The degree to which droplets fill a channel's cross-section has implications for both the Laplace pressure and channel resistance, as will be discussed in Section 6.3.2.

Droplets will attempt to minimize their surface energy within a channel, and therefore, their shape can be predicted with complex mathematics. Conveniently, Musterd *et al.* have examined this complex mathematical problem and created a general model to describe the shape of a droplet in a channel given the channel's depth (H), width (W), top corner angle (β) and bottom corner radius (r_c) [106]. These features can be seen labelled in Figure 2-5 and can be measured by examining the cross-section of a channel and directly measuring these dimensions. These cross-sections were obtained following the method described in Section 3.3.2.

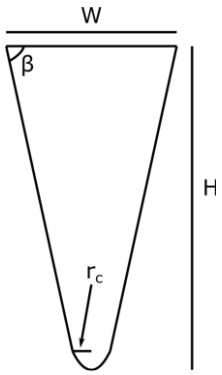

Figure 2-5 – A typical cross-section of a laser-cut channel with key features labelled. The features include the top corner angle (β), the bottom corner radius (r_c), the channel width (W) and channel depth (H).

The method of Musterd *et al.* is summarized in Figure 3 of their work (reference [106]). This figure directs the reader to select a set of equations that describe the droplet shape based on different channel cross-sections. Selecting the correct set of equations is accomplished through a series of calculations based on β, W, H and r_c.

The set of equations for each channel geometry describes the top corner radius of a droplet (r_t), the cross-sectional area of the body of a droplet (A_{bd}) and the length of the rounded end caps of a droplet (L_{cap}). The top corner radius describes the radius of curvature of a droplet in the top corners of a channel (i.e., the corners described by the angle β). The cross-sectional area of the body of a droplet describes the cross-section in the droplet center, away from the rounded end caps. These values rely on other geometric values that can allow for the perimeter of droplets to be calculated.

In this thesis, most channels (those cut with a laser speed of 0.5% as discussed in Section 3.3) fit into one category of Musterd *et al.*'s model (Figure 3c in their work) [106]. Some channels cut with different laser settings (i.e., some channels cut with a laser speed of 1%) are described by a different category of Musterd *et al.*'s model (Figure 3b in their work) [106]. In both cases, all channel parameters were measured in the same manner and correspond to the dimensions labelled in Figure 2-5. However, by following Musterd *et al.*'s model, different sets of equations are used to describe the different channel types based on these parameters. For simplicity, only the equations for the majority of channels will be discussed. The same values can be calculated but are governed by different geometric relationships in all cases.

The top corner radius of the droplets (r_t) could be calculated with Equation (2-18), where W and β are as defined above.

$$r_t = \frac{W\left(\sin\left(\frac{\beta}{2}\right) + \sin\left(\frac{3\beta}{2}\right) - 2\sqrt{\pi}\sin^{\frac{3}{2}}\frac{\beta}{2}\sqrt{\cos\left(\frac{\beta}{2}\right) + \cos\left(\frac{3\beta}{2}\right)}\right)}{2\pi\left(\sin\left(\frac{\beta}{2}\right) - \sin\left(\frac{3\beta}{2}\right)\right) + 8\cos^3\frac{\beta}{2}} \tag{2-18}$$

The cross-sectional area of the body of droplets (A_{bd}) could be calculated with Equation (2-19), where W, β, and r_t are as defined above.

$$A_{bd} = \frac{1}{4}tan\beta\left(W^2 - 8r_t^2 - \frac{2r_tW}{\tan\left(\frac{\beta}{2}\right)}\right) + \frac{r_t^2}{\tan\left(\frac{\beta}{2}\right)}\left(\frac{1}{\cos(\beta)} - 3\right) + \pi r_t^2 + \frac{Wr_t}{2cos\beta} + \frac{Wr_t}{2} \quad (2\text{-}19)$$

The length of the end caps of the droplets (L_{cap}) could be calculated with Equation (2-20), where W, β, and r_t are as defined above.

$$L_{cap} = \frac{W}{2} - \frac{r_t}{\tan\left(\frac{\beta}{2}\right)} + r_t \quad (2\text{-}20)$$

It should be noted that the bottom corner radius is only used in the criteria which determine the set of equations to use for a given channel type. The bottom corner radius is not used to calculate any properties of droplets in the channels.

Additionally, the laser-cut channels are approximated as isosceles triangular when calculating the channel resistance. This approximation does not account for the bottom corner radius, hence why it is an approximation of the channel cross-section. When considering droplet shape using Musterd *et al.*'s model, the rounded bottom corner of the laser-cut channels should be considered [106]. Similarly, the top corner angle of the channels could be calculated considering the approximation of an isosceles-triangular channel cross-section. However, the actual top corner angle varies slightly from this approximation because of the rounded bottom of the laser-cut channels. Therefore, a measured top corner angle was used whenever using the model of Musterd *et al.* [106].

The method described by Musterd *et al.* allows for droplet shape to be determined based on measurements taken only from above [106]. The values described above could then be used to calculate droplet volume, as discussed in Section 6.3.2, and their Laplace pressures.

If the droplet is sufficiently long, longer than twice the end cap length (L_{cap}), then the Laplace pressure of a droplet in a channel can be determined using the top corner radius of the droplet, r_t. Close to the center of the droplet, at a point on the curved upper corner, one principal radius would be the top corner radius (r_t), and the other would be nearly infinite as the center of the droplet would be flat along its length. Considering this case, according to Equation (2-9), the Laplace pressure of the droplet would be $P_{LP} = \gamma/r_t$. This method provides an alternate way to calculate the Laplace pressure of a droplet and the Laplace pressure difference of a droplet trap. It is more accurate than assuming that the droplet end caps are hemispherical. The use of Musterd *et al.*'s method was verified, as will be discussed in Section 6.3.2 [106].

2.6.2 Ensuring Successful Droplet Trapping During Droplet Generator Operation

Droplets are held in passive droplet traps based on a pressure barrier due to a difference in Laplace pressure. The droplets will remain held in place as long as the pressure applied to the trapped droplets does not exceed the Laplace pressure difference (ΔP_{Trap} or ΔP_{LP}) required to push droplets into the constricted trapping channels. This requires that the pressure drop across the droplet trap

must be smaller than the ΔP_{Trap} value for the droplet trap to hold droplets. The pressure drop across the trap can be calculated by multiplying the fluid flow rate through the trap (Q_{Trap}) by the resistance of the trap (R_{Trap}). The trap resistance should be considered when it contains the desired number of trapped droplets. This pressure drop must be less than $\Delta P_{Trap,}$ which is shown as the inequality in Equation (2-21). This requirement limits the operating conditions of a T-junction droplet generator when a droplet trap is integrated into its main channel.

$$\Delta P_{Trap} > Q_{Trap} R_{Trap} \tag{2-21}$$

The presence of droplets in a microfluidic channel has been found to increase the fluidic resistance of the channel. This is why R_{Trap} is considered the fluidic resistance of the droplet trap containing the desired number of trapped droplets. In some droplet trap designs, the presence of droplets can significantly alter R_{Trap} by acting like switches, completely blocking fluid flow through the constricted channels. Nguyen *et al.* used this to their advantage in designing a droplet trap to form DIBs and schematically showed this switching effect for their trap design in Figure 1-11 [6]. As droplets entered the trapping region of the droplet trap, they blocked bleed valves which then acted as switches forcing subsequent fluid flow around the trapping region.

The flow rate through or around the trap can be increased sufficiently to break the inequality shown in Equation (2-21). Breaking this inequality would evacuate droplets from the trap. The ΔP_{Trap} value of a droplet trap is based on the trap's geometry and interfacial tensions of the fluids. These are relatively constant, although they can change depending on channel wall contact. The resistance of a droplet trap will vary as droplets become trapped; however, these changes can be predicted and are limited in magnitude. Increasing the flow rate through or around a droplet trap can be achieved by increasing the dispersed phase or continuous phase input pressures of a T-junction droplet generator.

An effective droplet trap can be designed, and its behaviour can be predicted using Equation (2-17) and Equation (2-21).

This thesis used two droplet trap designs, the "Primary Droplet Trap" and the "Alternate Droplet Trap". Chapter 5 will discuss the application of the trapping principles outlined here to the design of these droplet traps.

2.7 Model of Droplet Splitting

In this project, an issue not often discussed in droplet trapping literature was droplet splitting at channel junctions. Typical advice on operating droplet traps is generally limited to following Equation (2-21) [6], [64], [69]. However, droplet traps, whether hydrodynamic traps with a bypass channel or pillar-based traps, typically involve channel junctions (i.e., intersections between two or more channels), and droplets may split at these junctions. Over the course of this project, droplet splitting was observed at channel junctions. Therefore, it became necessary to consider the physics of microfluidic droplet splitting devices to understand how this behaviour could be predicted.

Droplet splitting microfluidic devices typically consist of a single channel entering a junction with multiple channels. A droplet approaches the junction from the single channel and leaves in parts

through each of the outgoing channels [105], [109]–[113]. These devices often use T-junction and cross-junction channel geometries to split droplets. Such channel geometries are also commonly used in droplet sorting devices [97], [114]. Within the droplet traps used in this thesis, bypass channel junctions are intended to function as droplet sorters and direct droplets towards constricted trapping channels without splitting them. These junctions have similar design structures to droplet splitters and sorters. Therefore, models for droplet splitting devices could be reasonably applied to understand and overcome the droplet splitting issues observed during testing droplet traps in this thesis.

The majority of droplet splitting devices reported in the literature use channel junctions in which all channels have the same dimensions [105], [109], [112]. Typically, empirical relationships between the Capillary number and droplet splitting have been developed for specific junctions. These relationships are not widely applicable and do not provide much predictive ability for droplet splitting unless specific channel geometries are used. The bypass channel junctions used in this thesis are comprised of channels with different dimensions, and therefore a different model of droplet splitting is required to describe their behaviour.

Liang *et al.* proposed a model of droplet splitting based on channel resistances, applied pressures and Laplace pressure differences. However, they only applied this to channel junctions with symmetric dimensions [105]. This work referred to the droplet approaching the junction as the mother droplet, and the droplet split from the mother droplet as the daughter droplet. The model suggested that the volume of the mother droplet will be proportional to the volume of the daughter droplet in one of the channels leaving the junction. This assertion is also supported by the work of Link *et al.* on droplet splitting [109]. The ratio of these volumes was equivalent to the flow rate ratio through the outgoing channel and the channel leading to the junction. This relationship can be expressed as Equation (2-22). In Equation (2-22), $V_{daughter}$ is the volume of the daughter droplet, V_{mother} is the volume of the mother droplet. $Q_{daughter}$ is the flow rate through the outgoing channel containing the daughter droplet, and Q_{mother} is the flow rate through the incoming channel, which contained the mother droplet.

$$\frac{V_{daughter}}{V_{mother}} = \frac{Q_{daughter}}{Q_{mother}} \tag{2-22}$$

If the value of Equation (2-22) is less than zero, then no daughter droplet would be formed. If the value of Equation (2-22) is greater than zero and less than one, then a daughter droplet would be formed. If the value of Equation (2-22) is equal to one, then the entire mother droplet would travel through that single outgoing channel.

For example, consider the equivalent circuit of a cross-junction (Figure 2-6) where a droplet approaches the junction through a resistance R_s driven by a pressure P_j and a flow rate of Q. To determine whether a daughter droplet would be formed in the channel corresponding to the resistance R_1, the ratio of Q_1/Q would predict the volume of any formed daughter droplets. However, the flow rate of the droplet itself would need to be considered, not the bulk fluid flow rate.

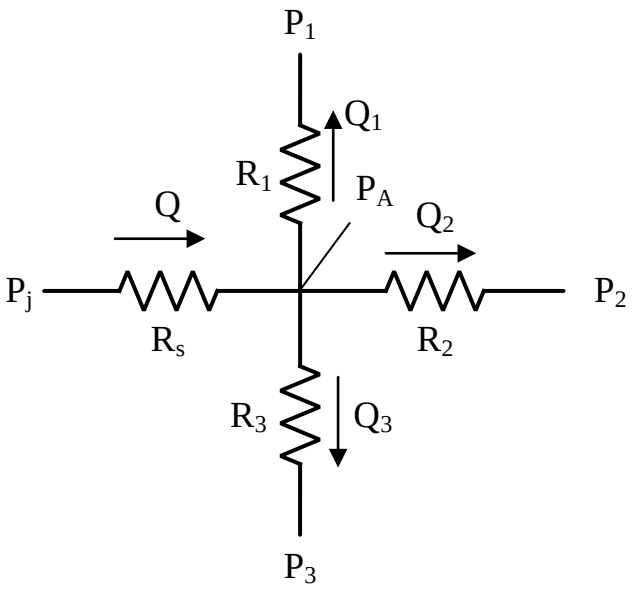

Figure 2-6 – An equivalent fluidic circuit diagram of a cross-junction assuming fluid only flows into the junction from the left channel.

If the droplet needs to flow between channels with different dimensions, the flow rate of the droplet is different from the flow rate of the continuous phase. As established in Section 2.6, droplets face a pressure barrier, the trapping pressure, when entering a constricted channel. This barrier needs to be accounted for when considering the flow rate of a droplet. To determine whether a daughter droplet would form in the channel corresponding to R_1 in Figure 2-6, the ratio of $Q_{1,droplet}/Q$ would need to be determined. This ratio can be calculated using Equation (2-23) using the pressures and resistances marked in Figure 2-6, where $\Delta P_{LP,1}$ represents the trapping pressure of R_1.

$$\frac{Q_{1,daughter}}{Q} = \frac{R_s}{R_1}\frac{P_a - P_1 - \Delta P_{LP,1}}{P_j - P_a} \tag{2-23}$$

As long as the droplet flow rate through an outgoing channel and the flow rate entering a channel junction can be determined, Equation (2-22) can predict the daughter droplet volume relative to the mother droplet volume. Based on Equation (2-23), this leads to a simple rule that the pressure drop across an outgoing channel should not exceed the trapping pressure of that channel to avoid droplet splitting. This requirement is the only way to get a negative value of Equation (2-23). It should be noted that Equation (2-23) cannot be used for channel junctions with symmetric channel dimensions, as no trapping pressure would be expected for outgoing channels. Liang *et al.* avoid this problem in their work by manually controlling the pressure drop across an outgoing channel (i.e., $P_a - P_1$ in Equation (2-23)). They developed an empirical relationship based on their test results [105]. Without control over the pressure drop across an outgoing channel in a junction with symmetric dimensions, empirical relationships must be used to describe droplet splitting, such as those developed by Liang *et al.* and Link *et al.* [105], [109].

This model was not implemented in the design of droplet traps for this thesis until the final droplet trap designs described in Chapter 8. However, the droplet splitting model was used to verify the behaviour observed when testing droplet traps (Section 7.6).

2.8 Summary

The physics described in Chapter 2 can be used to predict the behaviour of microfluidic devices. Specifically, the physics behind driving fluid through microfluidic channels, e.g., pressures, flow rates and channel resistances, and their electric circuit equivalents, were discussed. The Laplace pressure was also discussed as it describes the pressure drop at a fluid interface. These concepts were then used to discuss models of T-junction droplet generators, droplet traps and droplet splitting at channel junctions. A summary of the most important equations used in this project and their purposes is provided in Table 2-1.

These system properties, including the pressure, flow rate, Laplace pressure, channel resistance, depend on the properties of the fluids being driven through the microfluidic devices and the dimensions of the microfluidic channels. They are dependent on both the fluids chosen for the operation of a device and how the device was fabricated. Input pressures generated by gravity for T-junction droplet generators in this project are dependent on the density of the fluids being used (Equation (2-2)), and channel resistance is dependent on both the viscosities of the fluid being used and the channel dimensions (see Section 2.2.2). These fluid and device properties need to be well understood to effectively model and predict the behaviours of droplets in microfluidic devices. The fabrication method used to build devices in this project, the testing fluid and resulting device properties will be detailed and verified in Chapter 3.

Table 2-1 – A summary of the key concepts used in this project to design and test microfluidic devices for droplet generation and trapping applications.

Concept	Equation Number	Description
Poiseuille's Equation	(2-1)	Poiseuille's Equation is analogous to Ohm's Law for the electric circuit analogy of microfluidics [84], [85]. It links pressure, flow rate and fluidic resistance together.
Gravity-generated Pressure	(2-2)	This project uses gravity-generated fluid pressure to operate microfluidic devices [65], [84]. The pressure is defined by density, acceleration due to gravity and fluid height.
Reynold's Number	(2-5)	Reynold's number is a measure of turbulence in fluid flow [93]. A value less than 1500 indicates that a fluid flow is laminar.
Fluidic Resistance	(2-7)	The fluidic resistance corresponds to the average pressure-driven flow of a viscous fluid with a known viscosity through a filled channel of known geometry [95]. It is vital for modelling device behaviours using the electric circuit analogy.
Laplace Pressure	(2-9)	The Laplace pressure describes the pressure across a curved fluid interface [103]. This value is important in droplet generation and trapping.
T-junction Operating Range to Prevent Backflow	(2-16)	The operating pressure range of a T-junction droplet generator describes the range of pressures that can be used to make droplets [85]. This operating range is also the range where backflow will not occur.
Laplace Pressure Difference	(2-17)	The Laplace pressure difference determines the pressure barrier produced by a change in channel dimensions [6], [70]. This difference is equivalent to the trapping pressure of a droplet trap.
Droplet Trapping Condition	(2-21)	The basic droplet trapping condition states that a droplet trap will hold a droplet(s) as long as the pressure across the trap does not exceed the trapping pressure.
Droplet Splitting Ratio	(2-22)	The droplet splitting ratio describes the ratio in droplet volume between a daughter droplet and the mother droplet from which it is split [105], [109].

Chapter 3
Microfluidic Device Fabrication and System Properties Testing

3.1 Introduction

Chapter 2 provided an overview of the physics required to support using a microfluidic device to generate and trap droplets. Chapter 3 discusses the fabrication method selected for this thesis and the process to verify that devices were fabricated to the specified values. The fluids (i.e., dispersed and continuous phase) chosen to test chips for this project are also discussed. The various properties required for designing microfluidic devices given these choices are verified. These include the fluid density and viscosity and the resistances of the microfluidic channels used.

3.2 Microfluidic Implementation Details

Based on the author's previous experience and the information presented in Chapter 2, a microfluidic T-junction droplet generator fabricated from PMMA using a laser cutter was chosen for use in this project. A T-junction droplet generator was chosen due to the author's familiarity with the system and its simple design. Fabricating devices from PMMA using a laser cutter was chosen because of the author's familiarity with the technology and its ability to prototype devices rapidly with low-cost materials. These devices were to be operated using gravity-generated pressure-driven fluid flows. Gravity-generated pressure-driven fluid flows enable the devices to be operated without specialized equipment or extensive training. This simplicity allows the devices to be more accessible to researchers who wish to study DIBs and their contents.

A relatively simple dispersed phase and continuous phase were chosen to allow the microfluidic devices in this thesis to be tested before studying proteins. These more advanced tests may require expensive specialized fluids. The selected "Dispersed Phase" consisted of blue-dyed DI water (500 µL blue liquid tracer dye (ID: 106005) from BrightDyes in 50 mL DI water) and the chosen "Continuous Phase" consisted of mineral oil (M5904, Sigma-Aldrich, Oakville, ON, Canada) mixed with 2 wt% Span 80 (S6760, Sigma-Aldrich, Oakville, ON, Canada).

The blue dye in the dispersed phase was chosen because it had been used previously in a surface contact experiment of water on PMMA performed by Trinavee *et al.* [115]. It was not found to have any apparent effect on the interaction of the Dispersed Phase and the PMMA surface compared to undyed DI water.

The Continuous Phase was chosen because it is a commonly used oil and surfactant combination for generating droplets in microfluidic channels. It was also used by the author previously [70], [83], [116]. All references to DI water, blue dye, mineral oil, Span 80, Dispersed Phase or Continuous Phase throughout this thesis refer to the fluids described here unless stated otherwise.

The densities and viscosities of DI water, the blue dye, mineral oil and Span 80 are reported in Table 3-1. These parameters can be used to predict the behaviour of the designed microfluidic devices.

Table 3-1 – The densities and viscosities of the fluids used to test the microfluidic devices in this project. The temperatures corresponding to these properties are specified below each reported value.

Fluid	Density [g mL^{-1}]	Viscosity [mPa s]
DI Water	0.997 – 0.998 (20°C to 25°C) [117]	0.89 – 1 (25°C to 20°C) [117]
Blue Dye	1.04 ± 0.03 (25°C) [118]	1.8 (25°C) [118]
Dispersed Phase	0.998 (25°C)	0.90 (25°C)
Mineral Oil	0.840 (25°C) [119]	14.2 – 17.2 (40°C) [119]
Span 80	0.99 (25°C) [120]	-
Continuous Phase	0.843 (25°C)	-

The Dispersed Phase consisted of DI water with a 1% loading of blue dye by volume. Therefore, the Dispersed Phase was expected to have a density and viscosity approximately equal to the values reported in Table 3-1.

The Continuous Phase consisted of mineral oil loaded with 2 wt% Span 80. Therefore, the Continuous Phase was expected to have a density approximately equal to the value reported in Table 3-1. However, it should be noted that the density of the mineral oil reported in Table 3-1 is that from the material safety data sheet from Sigma-Aldrich [119]. The specification sheet for the mineral oil reports a wider range of densities (0.839-0.859 g mL^{-1}) and therefore, the actual density may vary slightly from the expected value.

The only important parameter not reported in Table 3-1 is the interfacial tension. The interfacial tension between the Dispersed Phase and Continuous Phase was expected to be between 4.5 to 5 mN m^{-1} as reported in the literature by Bashir *et al.* and Bithi *et al.*, respectively [70], [116]. This will be discussed further in Section 3.6.3.

A surfactant, Span 80, was used in place of an amphiphilic lipid in the initial demonstrations of the microfluidic devices in this project. Span 80 is amphiphilic and will still form a monolayer at the surface of the produced droplets. However, it has been found to have no adhesion forces between monolayers. Therefore, droplets with Span 80 monolayers will not create DIBs between two droplets [40]. With no adhesion force between the Span 80 monolayers, when two droplets are brought into close contact, they will not "zip" together and remove the oil separating the monolayers. However, if a lipid is included in a Span 80 monolayer, it will displace the Span 80 molecules and form a bilayer with an adjacent droplet [40]. In such monolayers, the Span 80 was found to increase the bilayer stability such that the bilayers were stable for several days [40]. Therefore, it was decided first to demonstrate the ability to hold droplets in close contact to form

apparent DIBs. Once that was established, a lipid would be incorporated into the Continuous Phase to form actual DIBs.

Several fluid properties denoted above are specified as a range or at temperatures beyond the intended operating temperature (i.e., room temperature, 22 ± 0.5°C). Therefore, these properties needed to be verified at room temperature before being used to design microfluidic devices effectively.

The following sections describe the tests performed to verify the fluid, material and device properties necessary to design devices. Equation (2-2) can predict the fluid pressures applied to the microfluidic devices. However, this requires that the fluid density be well known. Calculation of the fluidic resistance of a microfluidic channel depends on the viscosities of the fluid flowing through the channels (see Section 2.2.2). Therefore, the fluid viscosities need to be verified. Additionally, as laser-cut microfluidic channels are not commonly used, an appropriate equation to calculate their hydraulic resistance must be determined.

Tests were performed first to verify the wetting characteristics of PMMA to ensure that water-in-oil droplets would be formed in the designed devices (Section 3.5). Then the densities and viscosities of the Dispersed and Continuous Phases were verified as described in Section 3.6. The densities and viscosities of DI water and mineral oil were also measured to determine the effects the blue dye and Span 80 had on these properties. The interfacial tension was not verified before device construction, but instead, once a droplet trap was designed and fabricated. Therefore, verification of this value will be discussed later in this thesis (see Section 7.6). However, a brief overview of all possible interfacial tensions in the device is provided in Section 3.6.3. Finally, a method of calculating the resistance of laser-cut microfluidic channels was determined (Section 3.7).

3.3 Laser-cut Microfluidic Fabrication Method

For this project, the fabrication method chosen to make the microfluidic devices was laser engraving microfluidic channels in layers of PMMA. This choice was made because of the author's familiarity with the process, its ease of design, and the lab group's goals. This method allowed polymer devices to be rapidly produced without needing significant processing steps or highly specialized equipment, aside from the laser cutter. Furthermore, PMMA is a material compatible with mass production techniques such as injection moulding, allowing the devices designed for this project to be more easily translated to commercial applications [54]. Additionally, to the best of the author's knowledge, no microfluidic droplet trapping devices used to form DIBs have been reported using this fabrication method.

The basics of laser cutter fabrication of microfluidic devices are described here using the author's previously published work, "CO_2 Laser-Based Rapid Prototyping of Micropumps" [83]. Dr. Christopher Backhouse ("CB") fabricated all microfluidic devices for this project, and therefore, some specific variations and minute details of the process may not be identified here. CB also provided characterization data for some standard laser parameters. The author's role was to develop designs to be fabricated and test them.

The main steps are laser cutting and thermal bonding. Microfluidic channels are engraved into sheets of 1.5 mm thick PMMA, and then the different device layers are cut from the sheets. Instructions for the laser cutter are provided as vector graphics files designed with the Asymptote vector graphics programming language [121]. In the vector graphics files, different colours of lines are linked to different laser cutter settings and therefore channels with different dimensions.

Once all of the layers have been laser cut, they are thermally bonded. In "CO_2 Laser-Based Rapid Prototyping of Micropumps", only the top two layers of the device are thermally bonded [83]. The thermal bonding process was achieved by clamping together two pieces of PMMA and placing them in an oven for about two hours (30 minutes at 115°C, 1 hour at 80°C and then allowed to cool in the deactivated oven until a temperature of 60°C, which took approximately 30 minutes) [83]. This laser-cut PMMA fabrication process is similar to the work of Shaegh *et al.* [83], [122], [123].

The fabrication method used in this thesis is similar to that described above. However, the fabricated devices use only two layers of PMMA which are thermally bonded and have no thermoplastic polyurethane (TPU) layer. One PMMA layer contains the input/output wells, and the other PMMA layer contains the microfluidic channels. No on-chip microvalves were used in this thesis, and therefore, no TPU membrane was required.

3.3.1 Predicting Laser-Cut Channel Dimensions

A method for predicting channel dimensions based on laser parameters was required to design microfluidic devices in this project effectively. This method allowed the dimensions of new types of channels required by new designs to be predicted before fabricating complete devices. This saved time and material as it allowed fabricated devices to have dimensions closer to those intended.

A method for predicting channel dimensions based on laser parameters was developed using data gathered by examining the cross-sections of channels of microfluidic devices (see Section 3.3.2 for the data gathering method). The laser parameters that primarily affected channel dimensions were laser power and laser speed. The other parameters, laser frequency and focus level were constant at 1000 Hz and z = 0 (i.e., focused on the PMMA surface).

A series of test channels were cut using a variety of laser powers and laser speeds, and CB measured their dimensions. Sets of test channels cut with three different laser speeds were tested: 0.5%, 1% and 2% speed. Five test channels were cut at a laser speed of 0.5%, with powers ranging from 2.5% to 6%. Eight test channels were cut laser speeds of 1% and 2%, with powers ranging from 2.5% to 8%. All test channels were cut with two passes of the laser line to minimize variability in channel dimensions and were not bonded. The unbonded channel depths as they relate to laser power for these test channels can be seen in Figure 3-1. The lines of best fit in Figure 3-1 were then used to predict the laser power required to achieve a certain unbonded channel depth. These lines also allowed for the ablation threshold of PMMA (i.e., minimum laser power needed to engrave a channel) to be determined given a specific laser speed. For example, Equation (3-1) was used to predict the laser power required for a given channel depth using a laser speed of 0.5%. It indicates an ablation threshold of ~1.8% laser power. The formulae for the other two laser speeds are provided in Figure 3-1. They are written in the colours corresponding to their data on the graph.

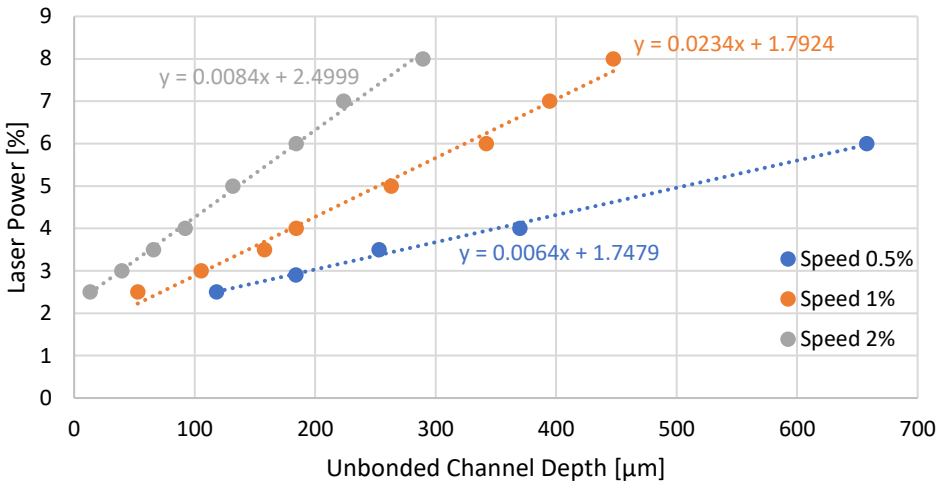

Figure 3-1 – The relation between known unbonded channel depths and the laser power used to cut channels with two passes at a speed of 0.5%, 1% or 2% at 1000 Hz and focused on the chip surface (z = 0). Data was gathered from test pieces fabricated and measured by CB. Equations for the lines of best fit are shown written in the colour corresponding to the data on the graph.

$$Laser\ Power\ [\%] = \frac{Unbonded\ Channel\ Depth\ [um] + 273.11}{156.2} \qquad (3\text{-}1)$$

A similar graph was made for channel width (Figure 3-2). For a laser speed of 0.5%, channel width was constant regardless of laser power and was not plotted. Additionally, only two laser powers with a laser speed of 0.5% were used, 3.1% and 3.5%, and both had the same channel width. Therefore, variations in channel width for the laser speed of 0.5% were not considered.

It was observed that bonded channel dimensions were slightly smaller than unbonded channel dimensions. On average, the depth of a bonded channel was ~96% of its unbonded depth, and the width of a bonded channel was ~83% of its unbonded width for the channel types considered in this thesis. This average included channels cut at 0.5% and 1% laser speeds with powers ranging from 2.7% to 3.5%. These conversions were approximate values because the relationships between the bonded and unbonded dimensions varied between channels with different dimensions and between fabrication runs.

On average, the depth of a bonded channel cut with a laser power of 3.5% and a laser speed of 0.5% was 94% of its unbonded depth. The width of these bonded channels was 82% of their unbonded width. The depth of a bonded channel cut with a laser power of 3.3% and a laser speed of 1% was 90% of its unbonded depth, and the bonded width was 89% of its unbonded width. The depth of a channel cut with 3.1% laser power and 1% laser speed was 97% of its unbonded depth, and its width was 93% of its unbonded width. These relationships between bonded and unbonded dimensions were highly variable and could not be determined until at least one fabrication run was performed using the settings. Therefore, the bonded channel depth was assumed to be ~96% of the unbonded channel depth, and the bonded channel width was assumed to be ~83% of the bonded channel width for all channel types as a first approximation.

Using the relationships between the unbonded channel dimensions and the adjustments for bonded channel dimensions, reasonably accurate channel dimensions for a given microfluidic device design could be estimated based only on laser parameters.

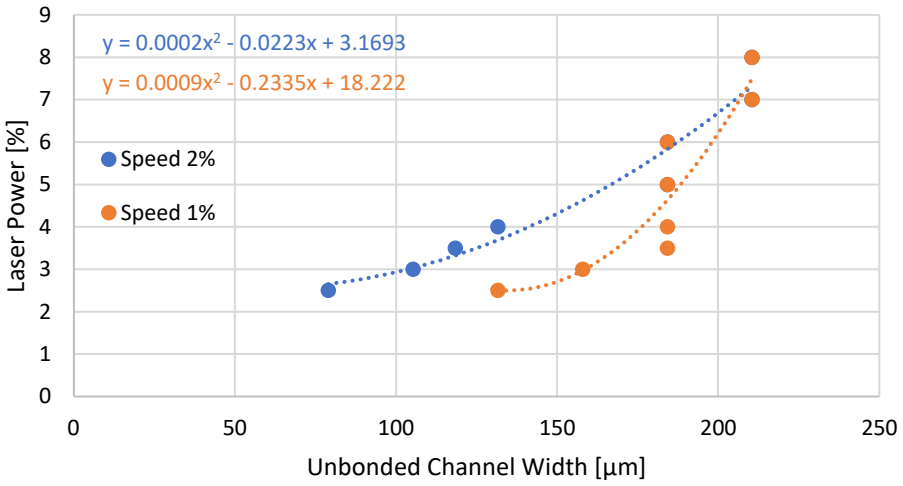

Figure 3-2 - The relation between known unbonded channel widths and the laser power used to cut channels with two passes at speeds of 1% and 2% at 1000 Hz and focused on the chip surface (z = 0). Data was gathered from test pieces fabricated and measured by CB. Equations for the second-order polynomial of best fit are shown in the colour corresponding to the data on the graph.

3.3.2 Fabrication Verification Testing Procedure

The channel profile in a microfluidic device is vital to understanding fluidic resistance and, therefore, the device's operating conditions. A quality control test was developed to examine channel profiles and verify that the fabrication processes were performed as intended. This test involved cutting a series of test channels and selected throughcuts into a piece of PMMA. The throughcuts were parallel or perpendicular to the test channels, such that the piece of PMMA could be cracked along the lines created by the throughcuts. These throughcuts resulted in cracks along or across the test channels. Channel cross-sections were then examined and measured using a microscope to observe the cracked face of the PMMA test piece. This test was referred to as a "crack test", and the piece of PMMA with the test channels a "crack test chip".

An example of an early crack test chip designed for the fabrication process can be seen in Figure 3-3. Blue and green lines denote test channels, red lines are throughcuts, and the bounding red rectangle is the outline of the piece of PMMA (dimensions of 76.2 mm by 25.4 mm). The crack test chip was designed to measure channel depth variation along a test channel and the depth and width of a channel. Additionally, it could determine how proximate channels could be cut before they began interfering with adjacent channel geometry.

Cracking the test chip along a crack line parallel with the test channel provided a channel profile such as the one shown in Figure 3-4. This allowed channel depth to be measured at multiple points along the length of a test channel. This type of crack line was rarely used when measuring channel dimensions and only to examine depth variation along the length of the channel. When used, the crack would be examined from above to ensure that it followed the center of the channel.

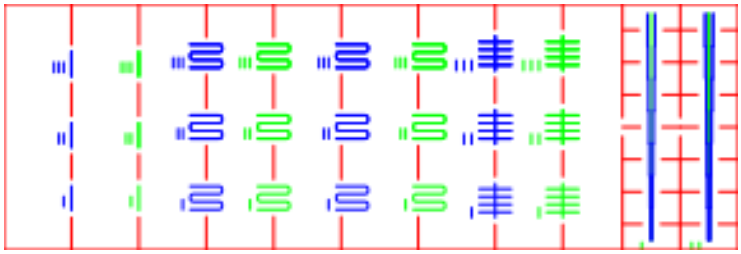

Figure 3-3 – An early crack test chip design for the thesis fabrication process.

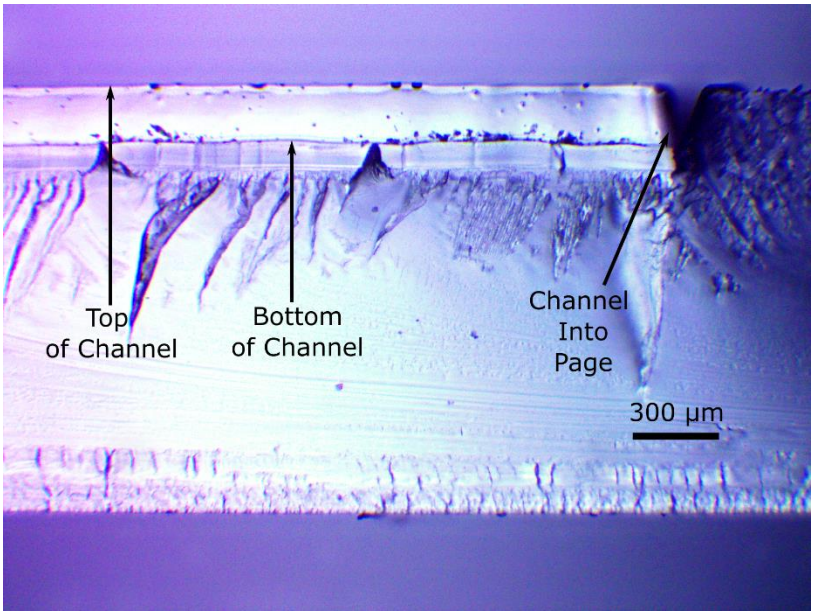

Figure 3-4 - A parallel cross-section of a channel cut with two passes of the green laser line in the zig-zag region of the unbonded crack test chip blank.

Examinations of channel profiles by cracking the test channels along perpendicular crack lines resulted in cross-sections like the one shown in Figure 3-5.

The procedure for performing crack tests was relatively simple. First, the crack test chip was cleaned with a water and detergent solution (five drops Palmolive detergent in 100 mL water) and allowed to dry completely. Drying the chip could be accelerated by drying with the laboratory's clean, dry air supply. The crack test chip was then placed flat on a benchtop with the test channels facing upwards. The crack line to be cracked was then aligned with the edge of the benchtop. This resulted in part of the chip being on the benchtop and another section extending past the benchtop edge. While holding the chip on the benchtop, a pressure was applied to the region extending past the benchtop. A clean break along the crack line aligned with the edge of the benchtop was then created. The cracked edge was then positioned under a stage microscope equipped with a USB camera, and test channel cross-sections were photographed (the microscope is defined in detail in Section 4.4). This procedure was performed on all crack test chips made for this thesis and evaluated the fabricated devices.

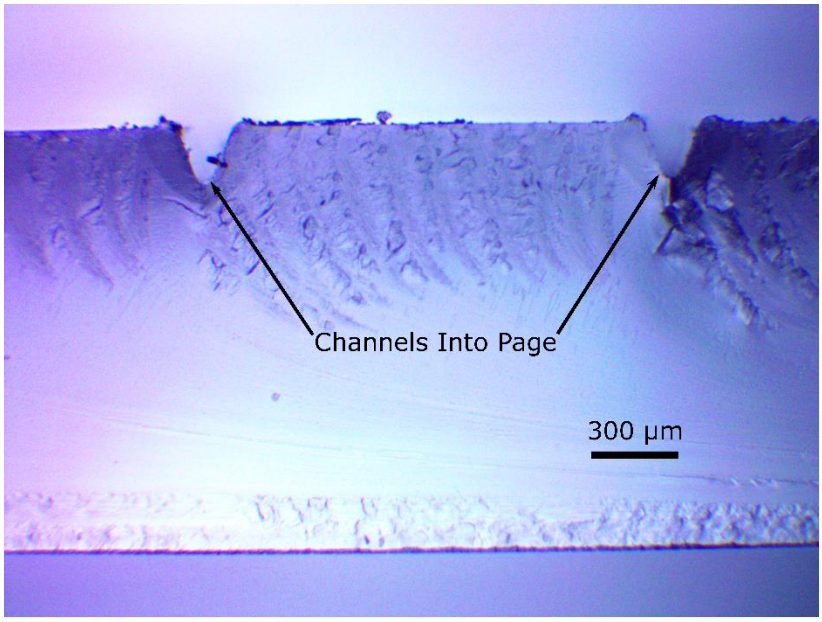

Figure 3-5 - A perpendicular cross-section of two channels cut with two passes of the green laser line in the zig-zag region of the unbonded crack test chip blank.

The dimensions of the crack test channels observed were then measured and compared to either previous fabrication runs or the predicted channel dimensions for a specific fabrication run. When analyzing crack test chips, the primary concern was consistency between dimensions for channels cut with the same laser settings. However, crack test chips were also used diagnostically to determine if a problem occurred with fabricating a particular design.

3.3.3 Crack Test Chip Results

There were four fabrication runs performed as part of this thesis. The first fabrication run produced droplet generating devices without an integrated droplet trap. Every subsequent fabrication run produced droplet generating devices with integrated droplets traps of varying designs (discussed in Chapter 7). For the first three fabrication runs, at least one crack test chip was produced and examined in each fabrication run.

Regardless of whether it had an integrated droplet trap, every droplet generating device used the same channels for the main channel, dispersed phase input channel and continuous phase input channel as defined in the droplet generator model described in Section 2.5. These channels were all cut with the same laser line, with 3.5% laser power and 0.5% laser speed settings. All channels cut with these settings were expected to have the same channel dimensions. These channels were considered the standard channels for this thesis.

Examining the crack test chips from the initial design and fabrication run (Fabrication Run 1), it was found that channels cut in a horizontal orientation and channels cut in a vertical orientation had different channel cross-sections and dimensions. An example of the channel cross-section of a horizontally-oriented channel, with the channel dimensions labelled, is shown in Figure 3-6. An example of the channel cross-section of a vertically-oriented channel, with the channel dimensions

labelled, is shown in Figure 3-7. Comparing these two cross-sections shows that channels cut in a horizontal orientation were deeper and narrower than channels cut in a vertical orientation.

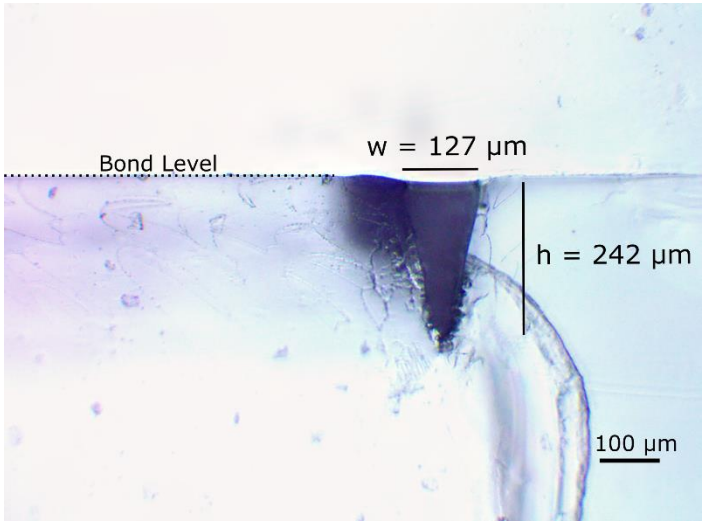

Figure 3-6 – Cross-section of a horizontally-oriented channel of a Droplet Generator with channel width (w) and channel depth (h) labelled. The cross-section is of the main channel in a long, straight and isolated position.

The difference in channel dimensions between horizontally-oriented and vertically-oriented channels does introduce a minor problem in predicting channel dimensions. Due to this difference, Figure 3-1 and Figure 3-2 can only approximate the channel dimensions before fabrication. As more data was gathered, the dimensions of specific laser settings used to cut channels in specific orientations were understood and used to predict channel dimensions before fabrication.

It can also be seen in Figure 3-6 and Figure 3-7 that the roofs of the channel were slightly lower than the division between the two thermally-bonded PMMA layers. This behaviour was determined to be a side effect of the thermal bonding process and did not significantly affect the channel dimensions.

Based on 12 measurements of vertically-oriented channels and six measurements of horizontally-oriented channels from the first fabrication run of devices, the average channel dimensions for both channel orientations were determined. Channels cut in a horizontal orientation had an average depth of 242 ± 6 µm and an average width of 127 ± 8 µm. Channels cut in a vertical orientation had an average depth of 221 ± 17 µm and an average width of 147 ± 9 µm. The increased uncertainty in the depth of the vertically-oriented channels was attributed to difficulties in obtaining a clean crack through these channels. These represented the dimensions of the standard channels used in all devices.

Based on these dimensions, vertically-oriented standard channels had a 6% larger area and a 0.7% larger perimeter. These differences were not a significant issue as the resistances of channels cut in each orientation could be calculated. Therefore, the difference in resistances could be accounted for in the modelling of devices once the issue was identified.

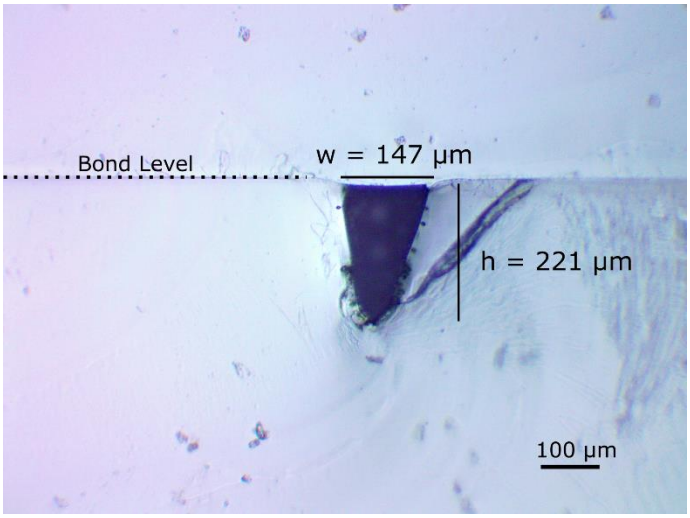

Figure 3-7 – A cross-section of a vertically-oriented channel of a Droplet Generator with the channel width (w) and channel depth (h) labelled. The cross-section is of the dispersed phase input channel in a long, straight and isolated position.

Subsequent fabrication runs of the devices with integrated droplet traps also had slightly different standard channel dimensions, but these variations were not significant. The average dimensions of standard channels across all fabrication runs – including devices with integrated droplet traps – are reported in Table 3-2. It should be noted that some measured channel dimensions were not characterized by their orientation and therefore were not included in the average channel dimensions for specific orientations. It can be seen in Table 3-2 that vertically-oriented channels were, on average, shallower and wider than horizontally-oriented channels.

Table 3-2 – The average depths and widths of the standard channels across all fabrication runs. The "All Channels" group includes both horizontally-oriented and vertically-oriented channels.

Channel Orientation	Sample Number	Depth [µm]	Width [µm]
All Channels	72	240 ± 17 (± 7.1%)	132 ± 20 (± 15%)
Horizontally-Oriented	28	253 ± 12 (± 4.7%)	119 ± 22 (± 18%)
Vertically-Oriented	30	236 ± 10 (± 4.2%)	138 ± 13 (± 9.4%)

There was some variability in channel dimensions from fabrication run to fabrication run. However, channel dimensions were consistent between devices in the same fabrication run. Therefore, devices made in the same fabrication run were expected to behave similarly but showed varied behaviour compared with devices from a different fabrication run.

Table 3-3 summarizes key channel types used during this project and their unbonded and bonded channel dimensions measured using crack test chips. These channel types were used for different purposes, such as bypass channels or trapping channels for a droplet trap. More channel types were used but not examined, and their use will be discussed in more detail in Chapter 7.

Another critical observation was made with crack test chips and bonded devices before testing. When observing the channels from above, it was noted that they had a speckled appearance. This speckled pattern was present in both unbonded and bonded devices. Figure 3-8 shows an example of the speckled appearance of the laser-cut channels in a set of channels in an as-received bonded droplet trap. These speckles were thought to be minor imperfections in the surface finish of the channel walls and can be seen on the channel sidewall in Figure 3-4.

Table 3-3 – A summary of the unbonded and bonded channel dimensions of different key channels used throughout this thesis. All channels were cut with the additional settings of 1000 Hz and focused on the chip surface (z = 0).

Channel Purpose	Laser Power [%]	Laser Speed [%]	Orientation	Unbonded Channel Depth [µm]	Unbonded Channel Width [µm]	Bonded Channel Depth [µm]	Bonded Channel Width [µm]
Standard Channel	3.5	0.5	Horizontal Vertical	268 ± 13 244 ± 10	153 ± 9 170 ± 7	253 ± 12 236 ± 10	119 ± 22 138 ± 13
Bypass Channel	3.1	0.5	Horizontal Vertical	187 203 ± 10	151 156 ± 4	190 ± 5 180 ± 11	141 ± 15 139 ± 6
Bypass Channel	3.3	1	Horizontal Vertical	114 ± 1 110	124 ± 6 149 ± 2	103 ± 8 94 ± 11	110 ± 1 131 ± 1
Trapping Channel	3.1	1	Horizontal Vertical	98 ± 2 91 ± 9	120 ± 1 138	95 ± 3 85 ± 6	111 ± 4 137 ± 6

The speckled channel appearance could not be removed by flowing fluids through the channels, including DI water, mineral oil and 70% ethanol. They were not observed to change during device operation or significantly affect the performance of devices. The literature suggests that they might be removed through treatment with chloroform during the fabrication process [122]–[124]. As the speckled appearance of the channels was not found to affect device performance, no corrective action was taken during this thesis.

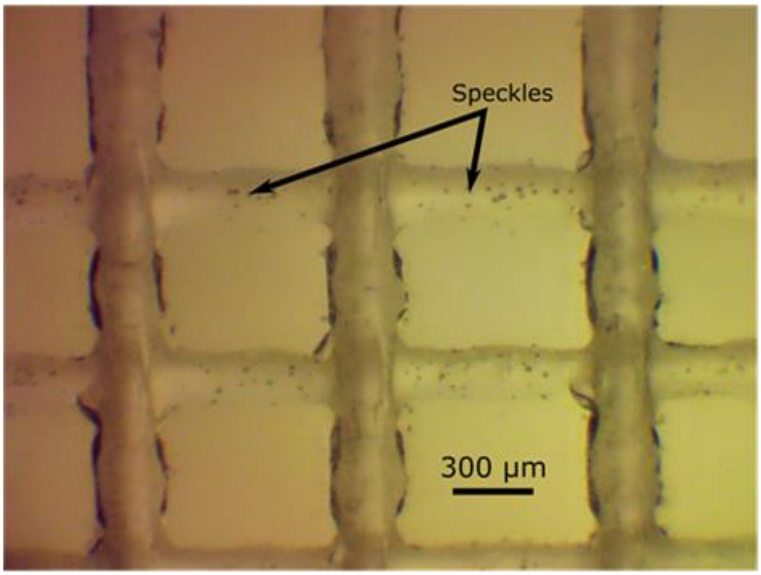

Figure 3-8 – A picture of bonded channels of a droplet trap taken with 10x magnification of the Microscope. The photograph was taken of the chip as received after the fabrication process.

3.4 Fabrication Considerations

The fabrication process for the microfluidic devices (i.e., chips) made in this thesis was standardized on PMMA substrates with dimensions of 3 cm x 4.7 cm, with each chip having three wells. Two well configurations were used: a configuration where two wells had radii of 0.84 mm and one well had a radius of 3.5 mm; and a second configuration where all three wells had radii of 0.84 mm. In all chip designs, parallel channels were spaced at least 1.6 mm apart, unless they were part of a droplet trap, and were no shorter than 1 cm in length. The minimum channel length was imposed to help prevent contamination should backflow occur. It also allowed droplet formation at the T-junction to be examined with a stage microscope during operation.

The main channels of the droplet generators were designed in a zig-zag configuration (i.e., a series of parallel lines with connections at alternating ends) so that several droplets could be optically observed simultaneously. The minimum channel length to implement a zig-zag shaped main channel while maintaining a stable channel profile was ~4.5 cm.

The specifications described in the preceding paragraph, restricted channel density, and the lengths and orientations of the channels that could form a T-junction influenced the design of the droplet generators. The nature of these restrictions was difficult to quantify in a limit on the total length of channels that could fit on a device. It was estimated that the total length of channels used in a single device could not be larger than 38 cm and have the device fit onto the 3 cm x 4.7 cm PMMA chips being used in the fabrication process. These limits were considered when designing the microfluidic devices, as discussed in Chapter 6 and Chapter 7.

3.5 Verification of PMMA Surface Properties

When designing microfluidic droplet generating devices, particularly those involving droplet trapping, understanding which channel surfaces will contact the Dispersed Phase helps predict droplets' shape and interfacial tension. Furthermore, ensuring the Dispersed Phase does not contact the channel walls ensures droplets of the Dispersed Phase will be formed.

In the devices used in this thesis, droplets are formed and flow through microfluidic channels laser cut into PMMA. The effects of laser cutting on the wetting behaviour and contact angle of water and PMMA has been the subject of some research.

PMMA is normally hydrophobic but has a contact angle of ~70^{o} for water with no other competing fluids present and may demonstrate some hydrophilic behaviours [125]. Various lasers used to ablate the surface of a piece of PMMA have been shown to affect the contact angle of the PMMA [125]–[130]. However, these changes are not consistent between different lasers, and it is unclear if they represent a microchannel environment. Most of the tests on this subject have been performed with a roughened wide surface of PMMA, not a microchannel, and it is known that surface roughness plays a role in the contact angle of a surface. Therefore, it was necessary to perform additional testing to verify the surface properties and contact angle of PMMA using the Dispersed Phase and Continuous Phase chosen for this thesis.

Measurements of the contact angle of Dispersed Phase on a PMMA surface submerged in Continuous Phase were performed to determine whether the oil submerged PMMA surface would be hydrophobic (contact angle of > 90°) or hydrophilic (contact angle of < 90°). A piece of uncut PMMA was immersed in the Continuous Phase to create an environment more representative of a droplet in a channel. A 50 µL droplet of the Dispersed Phase was then pipetted onto the PMMA surface and observed periodically over a duration of 10 minutes. Photographs of the contact surface were taken, and the contact angle was measured from these (Figure 3-9). The contact angle was then measured on the photographs using the angle function of ImageJ, an image processing software [131].

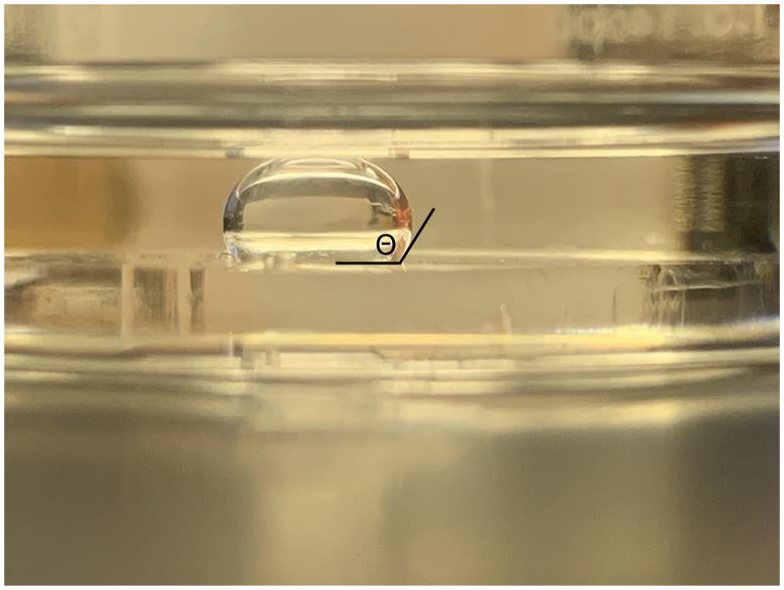

Figure 3-9 - A droplet of DI water resting on an uncut PMMA surface submerged in mineral oil after one minute. The measured contact angle (Θ) is marked on the figure.

Four conditions were tested: a droplet of DI water on a PMMA surface submerged in mineral oil, a droplet of DI water on a PMMA surface submerged in Continuous Phase, and these same two conditions but using droplets of Dispersed Phase. These different fluid combinations were tested to understand better the effects that the blue dye in the Dispersed Phase and Span 80 in the Continuous Phase had on the behaviour of droplets.

The contact angle of each test droplet was measured five times per test over a duration of 10 minutes: (1) immediately after the droplet was placed on the PMMA surface, (2) 30 seconds after droplet placement, (3) one minute after droplet placement, (4) five minutes after droplet placement and (5) 10 minutes after droplet placement. Each condition was tested three times to verify that the results were reproducible.

The average contact angle over the 10 minutes for each condition tested can be seen in Table 3-4. The contact angle appeared to decrease slightly over the 10 minutes (Figure 3-10). However, the slopes of each line of best fit were not statistically significant within a 95% confidence interval, except the DI water in Continuous Phase test. This test suggests that over time, in the case of DI water in Continuous Phase, the PMMA surface becomes more hydrophilic. However, at the rate indicated by the slope of the line of best fit (-0.0057 degrees per second), it would take

approximately 2 hours and 15 minutes for this to occur. This behaviour may or may not occur in a microfluidic channel due to the use of moving fluids. However, it should be noted as it may affect droplet and device lifetimes, particularly in the case of stationary (or trapped) droplets.

Averaging all values over the 10 minutes was deemed acceptable in all cases except for the DI water in Continuous Phase test because there was no statistically significant change in contact angle. Based on the data in Table 3-4, the presence of blue dye in the DI water did not significantly affect the contact angle between the water and the PMMA. However, the presence of Span 80 in the mineral oil did significantly increase the contact angle.

*Table 3-4 - The average contact angle for each test case over the 10 minutes of observation. Values denoted with a * denote the range of contact angles over the 10-minute test period as there was a statistically significant change in the contact angle for these test conditions.*

Test Case	Number of Measurements	Average Contact Angle [º]	Standard Deviation of the Contact Angle [º]
DI Water in Mineral Oil	15	117.7	6.1
DI Water in Continuous Phase	15	132.5 - 137.1*	2.5
Blue Dyed DI Water in Mineral Oil	15	116.8	3.2
Blue Dyed Water in Continuous Phase	15	136.2	4.0

It should be noted that a decrease in contact angle occurred in the conditions where the PMMA was submerged in mineral oil between the one-minute and five-minute observation points (Figure 3-10). A similar decrease was seen in the conditions where the PMMA was submerged in Continuous Phase, but only after five minutes of contact between the droplet and the PMMA surface (Figure 3-10). These decreases were slight and not statistically significant, except in the case of the DI water in Continuous Phase test, as discussed above.

The contact angle test measurements summarized in Table 3-4 demonstrate that the uncut PMMA surface, when submerged in mineral oil or Continuous Phase, presents a hydrophobic surface to a water droplet. Therefore, minimal contact between a water droplet and an uncut PMMA channel surface was expected. Tests of non-submerged PMMA suggested that laser-cut PMMA surfaces and uncut PMMA surfaces had similar contact angles for DI water (data not shown). Therefore, a laser-cut PMMA surface would also be expected to be hydrophobic when submerged in mineral oil or Continuous Phase for an extended period. However, over time the PMMA surface may become more hydrophilic.

As water-in-oil droplets are formed in oil-filled microfluidic channels, channel surfaces in a microfluidic device can be considered “submerged” in Continuous Phase. The droplets are expected to be separated from the channel walls by a sheath of Continuous Phase, preventing wall contact. Therefore, the Dispersed Phase droplets should show minimal direct contact with the channel walls, particularly when in motion. However, this may change over time, especially if droplets are held stationary. Inclusion of a surfactant, Span 80, into the Continuous Phase increases

the contact angle, further minimizing any channel wall contact a Dispersed Phase droplet may have. Therefore, to design the microfluidic devices for this thesis, channel walls were considered preferentially contacted by Continuous Phase while droplets moved.

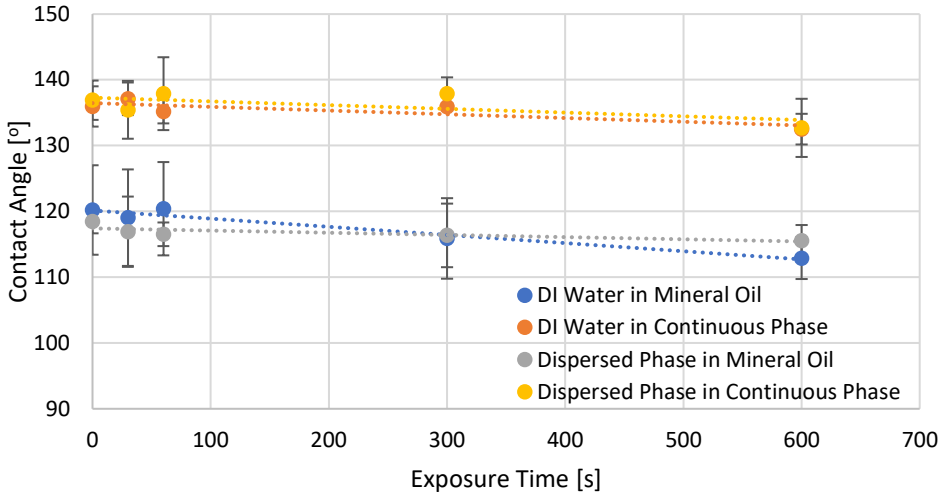

Figure 3-10 - A comparison of the DI water contact angle for each test condition over the 10-minute observation (exposure) period. Each point on the graph represents an average of three measured values, and the corresponding error bars are equal to one standard deviation of that average.

3.6 Verification of Fluid Properties

The relevant fluid properties for operating a gravity-fed microfluidic droplet generator are density, viscosity and interfacial tension. The densities of the fluids are used only to determine the input pressures of fluids using Equation (2-2). Of more importance are the viscosities of the fluids, which are used to calculate the hydraulic resistance of channels and the Capillary number of fluid flows (Equation (2-7) and Equation (2-8), respectively). The interfacial tension is also a crucial parameter in calculating the Laplace pressure and trapping pressure of a droplet trap.

3.6.1 Verification of Fluid Density

The microfluidic devices used in this thesis use fluid reservoirs held at specific heights above the devices to generate fluid pressures on-chip. Fluid pressures generated in this way can be calculated using Equation (2-2). They can only be determined accurately if both the density of the fluids and the height of the fluid reservoirs are known with precision. The density of three fluids of interest - DI water, mineral oil and the Continuous Phase - were measured for this project. The density of the Dispersed Phase was not measured, as the loading of blue dye in DI water was low (~1% by volume), and the density of the dye was similar to that of DI water (Table 3-1) [118]. Therefore, the dye was expected to have little to no effect on the density of the Dispersed Phase (Table 3-1).

The mass of a known volume of each of the three fluids identified above was measured to within 0.1 mg. Density was then calculated by dividing the measured mass by the known volume (i.e., mass/volume = density). To accurately measure the volume of each weighed fluid, each fluid was in turn drawn into a different 1 mL syringe with 0.1 mL major gradations and 0.01 mL minor gradations. Different syringes were used for the DI water, mineral oil and Continuous Phase,

respectively, to avoid cross-contamination of the fluids. It was estimated that the volume could be accurately measured to within ±0.005 mL in the 1 mL syringe. Care was taken to ensure that no air bubbles were present in the fluid in the syringe.

When filled with fluid, the syringe was weighed when it contained 0.8 mL of fluid by placing it into a tared beaker on a digital scale. The syringe was weighed again in the same manner after expelling the fluid from the syringe. The difference between these two measurements was determined to be the mass of the known fluid volume. The syringe mass and the mass dead volume in the syringe were eliminated from the measurement by taking this difference.

Each fluid was measured separately six times, with each syringe being emptied and refilled for each measurement. The exterior of each syringe was cleaned after drawing fluid to minimize unintended fluid volume. All fluids were measured at a temperature of 22 ± 0.5°C.

The density measurements for DI water, mineral oil, and the Continuous Phase are presented in Table 3-5. Error in the measurement system was primarily related to the uncertainty in measuring the volume of the fluid samples and is also included in Table 3-5. The measured density of DI water (0.996 ± 0.001 g mL^{-1}) was found to agree with the density of water at 22°C reported in the literature (0.997 g mL^{-1}, [117]). As stated above, the Dispersed Phase was expected to have the same density as unaltered DI water.

The measured density of mineral oil (0.852 ± 0.003 g mL^{-1}) was far from the value reported by Sigma-Aldrich on its material safety data sheet (0.840 g mL^{-1}) but within the reported range (0.839-0.859 g mL^{-1}) on its specification sheet [119]. This range confirmed that the mineral oil had the expected density.

Table 3-5 – The measured density results for DI water, mineral oil, and Continuous Phase. The standard deviation of the average value represents the non-systematic error in the measurement, and the error in the measurement system represents systematic sources of error.

Fluid	Sample Size	Average Density [g mL^{-1}]	Standard Deviation of Average [%]	Error in Measurement System [%]
DI Water	6	0.996	0.17	0.62
Mineral Oil	6	0.852	0.42	0.62
Continuous Phase	6	0.855	0.38	0.62

Assuming that the measured density of mineral oil was correct, then the density of the Continuous Phase would be 0.854 g mL^{-1} considering the reported density of Span 80 of 0.99 g mL^{-1} [120]. The measured density of the Continuous Phase (0.855 ± 0.003 g mL^{-1}) agreed with this theoretical value. Therefore, to design microfluidic devices, the Continuous Phase density was 0.855 ± 0.003 g mL^{-1}.

The fluid density verification described above indicated that the values of 0.996 g mL^{-1} and 0.855 g mL^{-1} were appropriate values for the density of Dispersed Phase and Continuous Phase in the microfluidic design procedures, respectively.

3.6.2 Verification of Fluid Viscosity

Determining the viscosity of the fluids used in the microfluidic devices for this project was important as a critical parameter in predicting channel resistance, which is vital in modelling droplet generation and trapping behaviour. A purpose-built capillary viscometer was used to measure the viscosities of DI water, mineral oil, the Continuous Phase and the Dispersed Phase. The viscometer was based on the viscosity measurement technique described by Peiris and Tennakone [132].

The viscometer was comprised of a 10 cm length of tubing (with an estimated nominal 570 μm inner diameter (ID)), a 16-gauge needle, a 10 mL syringe with its plunger removed, and a wooden dowel attached to a plumb wall in a vertical orientation. A 2 cm length of the tubing was inserted in the 16-gauge needle and then glued in place using Gorilla Glue Gel Super Glue, sealing the needle aside from the hole in the tubing. The needle was attached to the 10 mL syringe, which was then attached to the wooden dowel 10 cm above the benchtop with the open end of the syringe directed upwards. The syringe was secured at a height where the open end of the tubing was just above the benchtop. The open end of the tubing was then placed in an empty 100 mL beaker filled with just enough test fluid to submerge the open tubing end. The beaker was used to collect fluid running through the viscometer. During set up, special care was taken to ensure that the syringe and tubing were exactly vertically-oriented. A schematic representation of the viscosity measurement system can be seen in Figure 3-11.

The viscometer was operated by filling the open 10 mL syringe with fluid until the tubing and syringe were filled to just above the 3 mL mark while fluid was flowing through the tubing. This mark was 16.6 cm above the open lower end of the tubing. Then, the time for 1 mL of fluid to drain from the syringe was recorded. This was a measurement of the time required for the fluid level to fall from the 3 mL mark to the 2 mL mark, 16.0 cm above the lower end of the tubing. The recorded time was used to calculate the volumetric flow rate through the tubing: 1 mL/time difference (seconds). By measuring the fluid flow through the viscometer once the tubing was full and having the lower end submerged in a thin layer of test fluid, capillary/wetting forces and Laplace pressures were expected to have negligible effects on the measurement of the fluid flows. All tests were performed at room temperature (22 ± 0.5 ^{o}C).

The viscometer was cleaned using a 70% ethanol solution when switching from measuring a water phase (DI water or Dispersed Phase) to measuring an oil phase (mineral oil or Continuous Phase). After cleaning, the next test fluid was run through the tubing twice to remove any trace amounts of ethanol left in the tubing after cleaning. Test runs were only performed after completion of these cleaning steps to minimize cross-contamination between test fluids.

The volumetric flow rate was then used to calculate the viscosity of the test fluids (η) using Equation (3-2). Equation (3-2) uses the volumetric flow rate (Q) [m^3 s^{-1}], the density of the fluid (ρ) [kg m^{-3}], the radius of the tubing (r) [m], the length of the tubing (L) [m], the average height of the fluid above the benchtop (h) [m], and the acceleration due to gravity (g) [m s^{-2}] [132]. The height of the fluid and length of the tubing were both measured to within ± 1 mm. This system assumed that fluid flows were laminar and thus followed the equation for Poiseuille flow used to

derive Equation (3-2). The Reynold's number was calculated for each test case and never exceeded 100, far below the 1500 limit where flow is no longer laminar [93]. Therefore, the flows through the viscometer were expected to be laminar.

$$\eta = \frac{\pi r^4 \rho g h}{8QL} \tag{3-2}$$

By taking the derivative of Equation (3-2) with respect to each of the measured variables (tubing inner radius, fluid height, tubing length and volumetric flow rate), it was found that the largest source of error would be in the measurement of the inner radius of the tubing. Therefore, particular attention was paid to determining the tubing radius used in the viscometer, which was 285 ± 4.79 µm. This value was determined using a stage microscope by examining the tubing cross-section at five points along its length. The tubing diameter was then measured at five locations for each cross-section. The average of all measurements was then determined and divided by two.

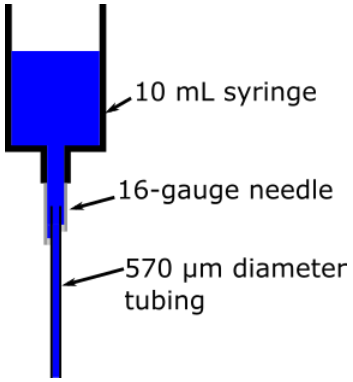

Figure 3-11 – A schematic drawing of the purpose-built viscosity measurement system.

For calculations using Equation (3-2) and the measured inner radius, error propagation calculations predicted an error of 6.72% due to the uncertainty in the tubing's inner radius. Errors due to uncertainty in fluid height or tubing length were estimated to be on the order of 1% for a cumulative 1.2% error for both parameters. Table 3-6 presents all measured parameters involved in calculating viscosity, their known measurement uncertainties and resulting uncertainties in the calculated viscosity.

Table 3-6 – The measurement uncertainty of the measured parameters involved in calculating the viscosity and the resulting uncertainty in the viscosity calculation.

Measured Viscosity Parameter	Measurement Uncertainty [%]	Resulting Uncertainty in Viscosity [%]
Tubing Radius (*r*)	± 1.68	± 6.72
Fluid Height (*h*)	± 0.61	± 0.61
Tubing Length (*L*)	± 1	± 1

The results of viscosity testing performed with the viscometer are shown in Table 3-7. The standard deviations of the average viscosity values represent non-systematic (random) errors in

measurements. Errors due to uncertainty in the tubing radius represent the most significant systematic error in the measurement system and are also shown. No trends were observed between runs for any of the tested fluids.

Table 3-7 – The measured viscosity results using the purpose-built capillary viscometer. The standard deviation of the average value represents the non-systematic error in the measurement system. The error due to the tubing's inner radius represents the largest source of systematic error in the measurement system.

Fluid	Sample Size	Average Viscosity [mPa s]	Standard Deviation of Average [%]	Error due to Measurement System Uncertainty [%]
DI Water	5	0.97	1.11	6.72
Dispersed Phase	5	1.01	1.62	6.72
Mineral Oil	5	26.58	2.25	6.72
Continuous Phase	5	28.51	0.42	6.72

The viscosity of DI water is well known to be between 0.89 mPa s at 25°C and 1 mPa s at 20°C, and a value within that range was expected [117]. Therefore, the values determined by measurements made with the viscometer for the DI water and Dispersed Phase agreed with the literature (0.97 mPa s and 1.01 mPa s, respectively).

The viscosity of the mineral oil used was only reported at 40°C, far from the temperature at which these viscosity measurements were performed (Table 3-1) [119]. However, a value of 30 mPa s has been reported for two different varieties of mineral oil in literature at room temperature (between 20°C and 25°C) [70], [112], [133]. As mineral oil is typically a mixture of different length hydrocarbons, it is not expected that different mineral oils will have precisely the same viscosity. However, it appears that a value of 30 mPa s is a representative viscosity of similar mineral oil products. Therefore, a similar viscosity could be expected for the mineral oil being used in this thesis at the testing temperature (22 ± 0.5°C). The values determined by measurements made with the viscometer for the mineral oil and Continuous Phase agreed with a representative viscosity of similar mineral oil products.

However, the measured viscosities may have been influenced by the large systematic error of the viscometer. Because water is such a well-studied fluid, it can be used as a calibration standard for the viscometer, allowing for the removal of systematic errors from the measured values. A theoretical value for the viscosity of water at the conditions tested (e.g., fluid temperature) needed to be determined to use such a calibration standard.

The Vogel equation (Equation (3-3)) can be used to determine the viscosity of a fluid based on temperature [134]. In Equation (3-3), a, b and c are constants dependent on the fluid, and T is the temperature of the fluid in Kelvin (K). The Dortmund Data Bank has reported the constants required for the Vogel equation with DI water as a = -3.7188, b = 578.919 and c = -137.546 [134]. It determined these parameters by fitting the Vogel equation to collected viscosity data between T = 273 K and T = 373 K for DI water. Therefore, the reported parameters are only valid to predict viscosities in this temperature range.

$$\eta = e^{a+\frac{b}{T+c}} \quad (3\text{-}3)$$

For the Vogel Equation to be accurately used (i.e., to predict a viscosity within a 95% confidence level) with DI water, the fluid temperature must be stable to within ± 2°C. In the experiment described above, the temperature of the DI water was measured to be 22 ± 0.5°C (295 ± 0.5 K). Therefore, the parameters for the Vogel equation detailed above could be used, and the calculated viscosity was expected to be accurate.

A viscosity of 0.958 ± 0.011 mPa s for DI water can be determined using the Vogel equation with the parameters provided by Dortmund Data Bank and a temperature of 22 ± 0.5 °C. This value agreed with the measured value for DI water (0.97 mPa s). It is within the combined uncertainty due to the measurement error and the standard deviation of the average measured value (combined systematic and random errors). Therefore, it was reasonable to believe that the measured values were correct.

The uncertainty in measuring the inner radius of the capillary tubing represented a systematic error and was primarily due to measurement difficulties. These measurement challenges included anomalies in the tubing structure (i.e., not perfectly circular cross-sections) and difficulties ensuring a perfectly perpendicular view of the tubing cross-section. As the measurements appeared to be successful, it was possible to refine the estimate of the tubing inner radius based on the calculated value of DI water viscosity using the Vogel equation. In other words, the known value of DI water viscosity was used as a calibration standard for the viscometer system. The effective tubing radius for the measured viscosity to match the calculated viscosity would be 284 μm to the nearest micrometre. Using the effective tubing radius eliminated the systematic error in the measurement system due to the uncertainty in the inner radius measurement.

The measured viscosities calculated with an effective inner radius of 284 μm are shown in Table 3-8. Using the effective inner radius to calculate the values shown in Table 3-8, the largest error from the measurement system is much lower, originating only from uncertainty in the measurement of fluid height and tubing height. This uncertainty represented a combined error of ~1.2%. While the temperature does affect the viscosity of the fluid being tested, it was not included in the error due to measurement system uncertainty. All fluids were tested on the same day at the same temperature, and there was no clear linkage between fluid temperature and its effects on Equation (3-2).

The measurements of the viscosities of mineral oil and Continuous Phase took far longer test (~310 seconds compared to ~24 seconds for each of the water phases) as could be reasonably expected. Except for two values for mineral oil, the viscosity measurements provided much more precise values for the average viscosities. The explanation of why two measured values (the second and final values) of the viscosity testing of mineral oil deviated by ~0.6 mPa s (corresponding to ~10 seconds of measurement time) compared to the average value is unclear.

The viscosity measurements performed for this project found that a viscosity of 0.96 ± 0.02 mPa s was appropriate for DI water, and a viscosity of 0.99 ± 0.02 mPa s was appropriate for the

Dispersed Phase. A viscosity of 26.39 ± 0.96 mPa s was appropriate for mineral oil, and a viscosity of 28.31 ± 0.52 mPa s was appropriate for the Continuous Phase. These values were used in the design and modelling of microfluidic devices for this thesis.

Table 3-8 – The measured viscosities using the viscometer considering the effective tubing radius of 284 μm. The standard deviation of the average value represents the non-systematic error in the measurement system.

Fluid	Sample Size	Average Viscosity [mPa s]	Standard Deviation of Average [%]	Error due to Measurement System Uncertainty [%]
DI Water	5	0.956	1.11	1.2
Dispersed Phase	5	0.993	1.62	1.2
Mineral Oil	5	26.393	2.25	1.2
Continuous Phase	5	28.313	0.42	1.2

3.6.3 Interfacial Tension

The tests described above indicate that channels preferentially fill with oil rather than water (i.e., the channel walls are hydrophobic, see Section 3.5). Therefore, droplets in microfluidic channels will be surrounded by a sheath of the Continuous Phase. This conformation indicates that the interfacial tensions that should be considered are those for the Dispersed Phase - Continuous Phase interface. However, some evidence of contact between stationary droplets and the channel walls was found (see Section 6.3.2). Therefore, understanding all possible interfaces a droplet could form may be essential to understand droplet behaviour in the devices.

The possible interfacial tensions involved in the behaviour of Dispersed Phase droplets are listed in Table 3-9. Interfacial tensions could not be found in the literature for the exact fluids being used in this project. Therefore, as a starting point, interfacial tensions that were thought to be representative were assumed to be true for the fluids being used and were later verified.

The reported values in Table 3-9 assume that Span 80 plays no role in the PMMA-Continuous Phase interactions and assume that mineral oil behaves similarly to a silicone oil with a viscosity of 48.1 mPa s [115]. The interfacial tension between 2 wt% Span 80 in mineral oil and DI water was measured using a mineral oil with a viscosity of 30 mPa s and a density of 0.875 g mL^{-1} [70], [133]. The value of the interfacial tension between mineral oil and DI water was measured using a mineral oil with a viscosity of 30 mPa s and a density of 0.84 g mL^{-1} [112].

*Table 3-9 – The possible interfacial tensions that could be involved in the surface energy of a droplet. The * denotes an estimate of the surface energy assuming mineral oil behaves similarly to silicone oil.*

Interface	Interfacial Tension [mN m^{-1}]
PMMA – DI Water	22.04 [115]
PMMA – Mineral Oil	4* [115]
2 wt% Span 80 in Mineral Oil – DI Water	5 [70], [133]
Mineral Oil – DIW	46.28 [112]

A Continuous Phase-sheathed droplet in a PMMA channel has two interfaces (PMMA-Continuous Phase and Continuous Phase-Dispersed Phase) with a combined interfacial tension of approximately 9 mN m^{-1}. In contrast, a direct droplet-PMMA interface has an interfacial tension of just over twice as large. This variability might lead to erratic droplet pressure behaviours due to the uncertainty of the presence of the Continuous Phase sheath, mainly when the droplet is stationary (see Section 6.3.2). As discussed in Section 3.2, the interfacial tension of the Dispersed Phase and Continuous Phase interface was not verified before device testing. Instead, a value of 5 mN m^{-1}, as reported by Bithi *et al.*, was assumed when designing microfluidic devices [70]. However, the interfacial tension of the interface was verified when testing the designed droplet traps, as will be discussed in Section 7.6. This verification found the assumed value to be appropriate. The interfacial tension was verified by fitting the droplet splitting model described in Section 2.7 and a form of Equation (2-17) to the observed behaviours in droplet traps fabricated for this project.

3.7 Laser Cut Channel Resistance

As discussed in Section 2.2.2, understanding the fluidic resistance of microfluidic channels is imperative when using the electric circuit analogy to design microfluidic devices. The fluidic resistance of channels with standard cross-sections (e.g., circular, rectangular) are well understood and can be described by analytical solutions. However, the laser-cut channels used in this thesis have non-standard cross-sections with no available analytical solution. Therefore, the resistance of the laser-cut channels had to be determined experimentally.

The approximation of channel resistance based on a channel's cross-sectional area and perimeter proposed by Bruus (Equation (2-7)) was used as a starting point to determine a method of predicting channel resistance for this project's laser-cut channels. A typical cross-section of these channels can be seen in Figure 3-12. A difference in contrast can be seen between the top and bottom layers due to a difference in the quality of the cracked PMMA surface and the lack of channels in the top layer.

Initially, the cross-sections of the laser-cut channels were approximated as isosceles triangular cross-sections when bonded (Figure 3-12(B)). Later, the cross-sections of the laser-cut channels were described more precisely as a trapezoid with a rounded bottom end (Figure 3-12(C)). While these approximations do not precisely represent the cross-sections of the channels, they provided a means of quickly calculating channel perimeters and cross-sectional areas without having to make complex measurements for each channel type.

A series of tests were performed to determine an accurate model for the prediction of channel resistance in laser-cut microfluidic channels. These tests used microfluidic chips inscribed with a channel connecting two wells. Each well was connected to an open 10 mL syringe using a brass fitting, Tygon tubing (with a 1.59 mm ID) and a 16-gauge needle. The chip was placed flat on a lab benchtop. Fluid was loaded into one syringe (the "input syringe"), which was affixed above the chip at a minimum height of 20 cm, using gravity to flow fluid through the channel. The input syringe height defined the pressure applied to the fluid and thereby determined its flow rate through the channel (see Equation (2-2) and Equation (2-1)).

The fluid flowed to the other well, through its attached Tygon tubing and into an open 1 mL "output syringe". The output syringe was positioned such that its bottom was level with the benchtop. The time elapsed to transfer 0.2 mL of fluid from the input syringe to the output syringe was measured. This time was then related to the volumetric flow rate of the fluid through the microfluidic channel. This method of measuring volumetric flow rate was thought to remove or reduce any possible capillary effects on the fluid flow rate, providing a more accurate measurement than measuring the fluid velocity in the outflow tubing. The diameter of the output syringe was much larger than the diameter of the output tubing, and therefore, Laplace pressure effects were not expected to be significant.

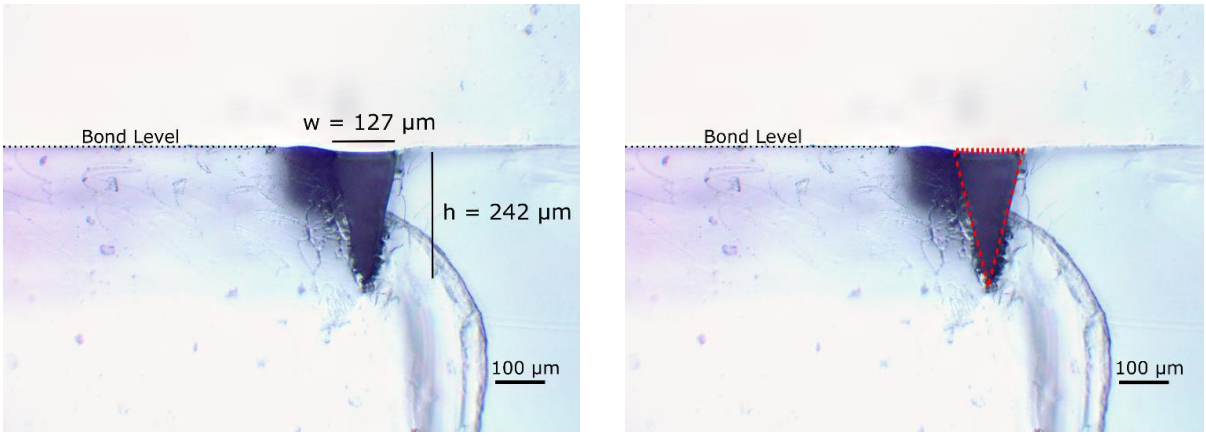

(A) (B)

Figure 3-12 – (A) A typical cross-section of a bonded laser-cut channel taken using 10x magnification. (B) The channel cross-section fit with an isosceles triangle.

The 0.2 mL mark of the output syringe was 1 cm above the benchtop. Fluid reaching this height would only introduce a maximum 5% height difference to the measured input syringe height over the testing period. This height difference represented a minimal change in input pressure during testing, particularly at higher input syringe heights. During testing, the fluid level in the input syringe was maintained at a constant level at the 2 mL mark of the input syringe.

The microfluidic chip used to test channel resistance had the design shown in Figure 3-13. The input syringe was connected to the input well, and the output syringe was connected to the output well. The input and output wells are defined in the third sub-chip from the left in Figure 3-13. The channel left of the T-junction was sealed at the droplet trap, marked by the blue area length of the channel. Consequently, no fluid flowed in that direction, creating a channel with a single fluid flow path suitable for channel resistance testing. The resulting channel connecting the input and output wells had a total length of 3.524 cm, a depth of 202 ± 9.35 µm, a width of 110 ± 7.57 µm and an approximately isosceles triangular cross-section. The value of DI water and Dispersed Phase viscosity used to calculate channel resistance was 0.96 ± 0.02 mPa s, as determined by the fluid viscosity measurements established in Section 3.6.2. It was assumed that the direction in which the channel was cut and the rounded channel corners had no effect on the fluidic resistance of the system. No differences in horizontally-oriented and vertically-oriented channels had been found

at the time of this experiment. These differences were discovered later in the project and are discussed in Section 3.3.3.

Following error propagation analysis of the methods for calculating channel resistance, it was found that the largest source of error was due to the uncertainty in the value of the fluid's viscosity. The viscosity was only known to be within 2.51% of the measured value. Thus, resistance measurements had a source of error of at least 2.51%.

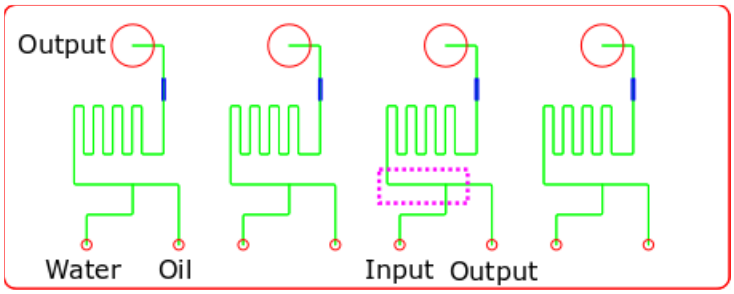

Figure 3-13 – The master chip (set of four chips) design fabricated as an early test fabrication run. A pink dashed box surrounds the T-junction region. On this fabrication run, the blue region was sealed.

The sealed channel halfway along the test channel may have acted as a fluidic capacitor [95]. However, the calculated time constant of the sealed channel acting as a fluidic capacitor was low, only ~0.1 s. Therefore, it was not predicted to affect channel resistance measurements as the experiments took much longer than 0.1 s to perform (>120 s, data not shown).

The resistance of the laser cut channel connecting the input and output wells was measured using DI water and Dispersed Phase. The input syringe was placed at six heights: 20 cm, 40 cm, 60 cm, 80 cm, 100 cm, and 120 cm. Channel resistance was measured three times at each height. The applied fluid pressure was calculated using the density of DI water and Dispersed Phase, input syringe height and Equation (2-2).

The measured volumetric flow rate obtained from the tests was plotted against the applied fluid pressure, and a line of best fit was applied (see Figure 3-14). The slope of the line of best fit can be related to the channel resistance using Equation (2-1) which indicated that the inverse of the slope was equivalent to channel resistance.

Two different models of the channel resistance were considered: (1) Bruus' equation to approximate the resistance of a channel with an arbitrary cross-section (Equation (2-7) with $\alpha = C = U^2/A$) and (2) the commonly used approximation for channel resistance based on the hydraulic radius (Equation (2-6)). Models were considered assuming the channel had an isosceles-triangular cross-section.

Equation (3-4) and Equation (3-5) were used to calculate the perimeter and cross-sectional area of the tested channels. These equations approximated the channels with isosceles-triangular cross-sections (Figure 3-12(B)). In Equation (3-4) and Equation (3-5), w represents channel width, and h represents channel depth.

$$U = w + 2\sqrt{\frac{w^2}{4} + h^2} \tag{3-4}$$

$$A = \frac{wh}{2} \tag{3-5}$$

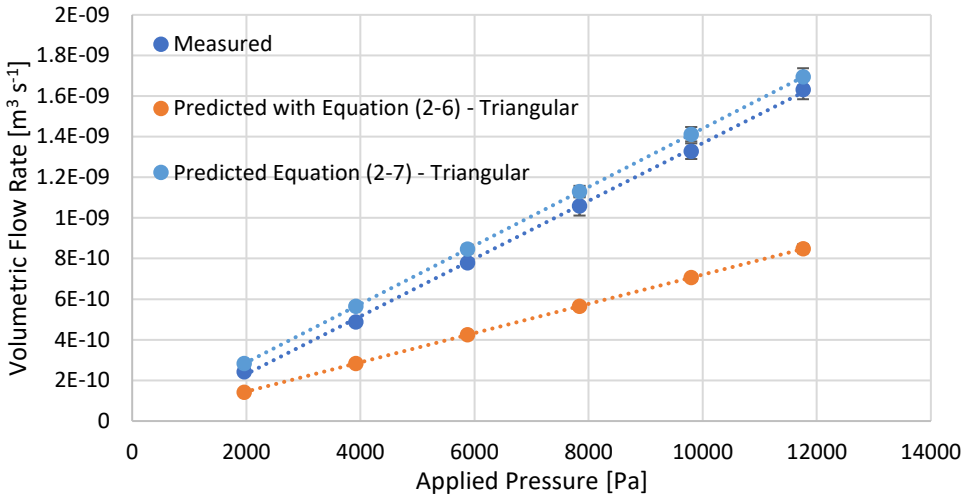

Figure 3-14 – The volumetric flow rate results of channel resistance testing compared to two channel resistance models. The channel cross-section was approximated in two ways: as isosceles-triangular. Results indicated that measured channel resistance was much lower than expected, as the volumetric flow rate was higher than expected. The measured data points have error bars of one standard deviation, while the predicted data points have error bars of 2.51%.

The measured cross-sectional area of a microfluidic channel with the dimensions listed above was ~10370 μm^2. This was measured from a cross-sectional image of a channel using the image processing software ImageJ [131]. Assuming an isosceles-triangular profile for the channel results in a calculated cross-sectional area of 11110 μm^2 according to Equation (3-5). This represents a ~7% difference between the measured and calculated cross-sectional areas. Therefore, approximating the channel cross-sections as isosceles-triangular was deemed suitable as an approximation when calculating the channel resistance.

The measured volumetric flow rate was found to be within a 10% error of the predicted volumetric flow rate using Equation (2-7) when assuming the channels had isosceles-triangular cross-sections.

Analysis of the fluidic resistance calculated at each applied pressure indicated a statistically significant (within a 95% confidence interval) dependency of resistance on applied pressure (Figure 3-15). This result was unexpected as no mention of a dependence of fluidic resistance on applied pressure has been seen in any literature to date. Additionally, any change in input pressure due to the output syringe being filled with fluid was insignificant and could not account for the observed behaviour. This same behaviour was found on the second day of testing, which produced the same results (data not shown). The cause of this behaviour is unknown but may be related to either the capacitance of the Tygon tubing or a cumulative change in pressure over time affecting the channel resistance (i.e., the filling of the output syringe over time). There may also be some

form of turbulent fluid flow occurring. However, at all settings tested, the Reynold's number indicated laminar fluid flow was expected.

The results shown in Figure 3-15 show that Equation (2-7) assuming isosceles-triangular channel cross-sections produced the closest predictions to the measured results, particularly as the applied pressure was increased. At low pressures, the measured resistance varied from the predicted resistance by up to 17%. However, at higher pressures, particularly at 11.8 kPa, the measured resistance was in close agreement with the predicted value, within 4%. As discussed later, the devices in this project are intended to be operated with pressures of about 8 kPa. The results shown in Figure 3-15 indicate that the measured channel resistance agrees with the predicted channel resistance to within ~6.8% at this pressure.

These results indicated that Equation (2-7) was the most appropriate method for calculating the resistance of a laser-cut channel. However, an additional adjustment factor could further improve its predictive ability. Equation (2-7) is rewritten below as Equation (3-6), with $\alpha = C = U^2/A$ and an adjustment factor of 1.088. This adjustment factor accounts for the channel profile not being perfectly isosceles-triangular and minor variations in channel dimensions along the channel length.

This additional adjustment factor was determined by fitting the channel resistance calculated using Equation (2-7), with $\alpha = C = U^2/A$ to the average measured resistance over the tested pressure range. This adjustment meant that the expected difference in the measured and predicted channel resistance at pressures of about 8 kPa was reduced to only ~1.9%. This closer agreement between the predicted and the measured resistance demonstrates an improvement in the predictive ability of Equation (3-6). An adjustment factor that would result in even more accuracy at the anticipated operating pressure was not chosen because it was suspected that operating at lower pressures may be required to facilitate droplet trapping. Therefore, it was beneficial to choose an adjustment factor that improved the predictive ability at lower pressures.

For all design aspects in this thesis, laser-cut channel resistance was calculated using Equation (3-6) and assuming that bonded channels have isosceles-triangular cross-sections. It was assumed that this equation was valid for channels of every dimension to expedite the project. This assumption was thought to be reasonable because the resistance of standardized channels dominated all devices.

$$R = 1.088\frac{\eta L U^2}{A^3} \tag{3-6}$$

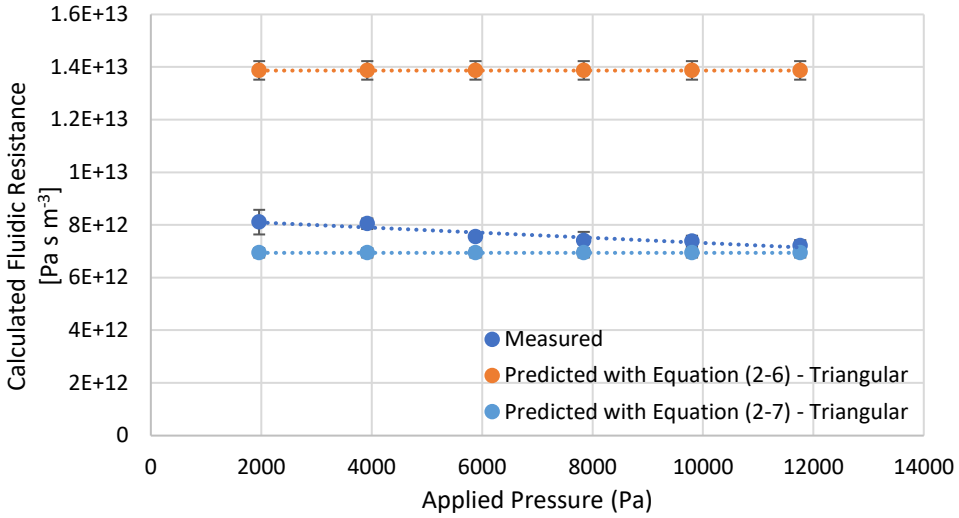

Figure 3-15 – Channel resistance calculated at each data point from Figure 3-14. The measured data points are averages of three measured values and have error bars corresponding to one standard deviation of that average. The predicted data points have error bars of 2.51%.

3.8 Summary

The details of the general microfluidic implementation and the chosen fabrication method for this thesis – laser cutting microfluidic channels in PMMA – were discussed. A method for predicting the dimensions of channels based on laser parameters before fabrication was described, including a verification procedure for ensuring the cut channels met their designed dimensions. Then, the material and device properties relevant to designing a microfluidic droplet generator were discussed and verified. These properties included the surface properties of PMMA, the densities and viscosities of the chosen Dispersed Phase and Continuous Phase, and the resistance of the laser-cut channels. The properties used in the design of the microfluidic devices in this thesis are summarized in Table 3-10.

Table 3-10 – The fluid properties of the Dispersed Phase and Continuous Phase used to design microfluidic devices in this thesis.

Fluid Property	Dispersed Phase	Continuous Phase
Density [g mL^{-1}]	0.996 ± 0.001	0.855 ± 0.003
Viscosity [mPa s]	0.96 ± 0.02	28.31 ± 0.52

A new method of calculating the resistance of laser-cut channels was determined based on their observed behaviours. For this project, all channel resistances were calculated using Equation (3-6) while approximating the channel cross-section as isosceles-triangular. The fluid and device properties described and verified in Chapter 3 can be applied to the effective design of microfluidic droplet generators and droplet traps using the models discussed in Chapter 4.

Chapter 4
Microfluidic Droplet Generator Design and Operational Methods

4.1 Introduction

Chapter 2 discussed the physics and framework required to design a T-junction droplet generator and droplet trap. Chapter 3 then established the material and device properties required to implement those design frameworks. This chapter seeks to lay out the refinements to the design framework of a T-junction droplet generator (a "Droplet Generator") made specifically for this project. Then various design considerations used when designing a Droplet Generator will be detailed. Finally, the operational methods used to test the fabricated Droplet Generators will be discussed.

4.2 Refinements to the Droplet Generator Design Framework

The design of the Droplet Generators in this project was conducted by closely following the framework outlined in Section 2.5. Variation in device performance due to droplets in the main channel was minimized through appropriate design choices. These choices balanced the dispersed phase input channel resistance (R_d), the continuous phase input channel resistance (R_c) and the main channel resistance (R_m).

Minimizing variations in the main channel resistance was essential to maintain consistent droplet volumes and production rates in the Droplet Generator. This optimization was necessary for the formation of DIBs using droplets traps because droplet size is vital in the function of a droplet trap that relies on changes in channel dimensions. Should droplets be too small, they may not contact neighbouring droplets in the droplet trap. In the most extreme case, they may be unaffected by the changes in channel dimensions meant to trap the droplets and flow through the droplet trap. Either of these scenarios would prevent DIBs from being formed. Therefore, it is crucial to ensure that the Droplet Generator will produce droplets of consistent size, such that they will always come into contact when in a droplet trap. The acceptable droplet volume variation depends on channel placement and channel dimensions used to form the droplet trap. For this thesis, droplet volumes consistent to within 10% were deemed suitable; this is explained in more detail in 4.3.1. Therefore, the Droplet Generators were designed to have minimal operational sensitivity to main channel resistance variations to minimize variations in droplet volume.

4.2.1 Operational Sensitivity to Resistance Variation

Instabilities in the operation of the Droplet Generator that might cause variability in droplet size and production rate are thought to arise from fluctuations in flow rate ratio (Q_d/Q_c). The flow rate ratio has been linked to both droplet volume and production rates [85]. These instabilities might also cause unexpected periods of backflow. The only parameter of the droplet trap that is known to fluctuate during the regular operation of a Droplet Generator is the resistance of the main

channel, R_m. These fluctuations are caused by droplets being formed in and leaving the main channel and affect the pressure at the T-junction (P_j) (see Equation (2-13)). The fluctuations affect both the dispersed phase input flow rate (Q_d) (see Equation (2-11)) and the continuous phase input flow rate (Q_c) (see Equation (2-12)). Therefore, minimizing the fluctuations in Q_d and Q_c is of the utmost importance to produce droplets with consistent volumes.

This project targeted smaller droplet volumes, specifically those with a flow rate ratio of about 0.2 ($Q_d/Q_c \sim 0.2$). The dispersed phase flow rate is much lower than the continuous phase flow rate in this targeted regime. Therefore, the dispersed phase flow rate variability was deemed the most important factor in droplet production stability and minimized. This variability can be quantified by the derivative of Q_d with respect to R_m, Equation (4-1). The derivation of Equation (4-1) is provided in Appendix A. Minimizing $\delta Q_d/\delta R_m$ will minimize variations in the dispersed phase flow rate and can be accomplished by choosing appropriate values of R_d, R_c and R_m for given operating pressures.

$$\frac{\delta Q_d}{\delta R_m} = \frac{\delta Q_d}{\delta P_j}\frac{\delta P_j}{\delta R_m} = -\frac{\big((P_d - P_{LP})R_c + P_c R_d\big)R_c}{[(R_c + R_d)R_m + R_d R_c]^2} \tag{4-1}$$

Glawdel and Ren took a similar approach to minimize variations in droplet size and spacing, and through experimentation and simulation, found the guideline: $R_d > R_m > R_c$, or at the least $R_d = R_m > R_c$ [85]. By inspection of Equation (4-1), the value of $\delta Q_d/\delta R_m$ cannot equal zero, but one way of minimizing it is by using Glawdel and Ren's guideline. Numerical analysis with sample designs (see Section 4.3.7) confirmed that Equation (4-1) was minimized by following the rule of thumb $R_d > R_m > R_c$. However, a wide range of values can be chosen for R_d and R_m without making significant sacrifices in the variability of Q_d.

It should also be noted that the dispersed phase fluid flow rate is dependent on the Laplace pressure of the dispersed phase fluid front. As mentioned previously in Section 2.4, the Laplace pressure is dependent not only on the fluids being used but also on the dimensions of the channels and the contact of the fluids with channel walls. Variations in channel dimensions will lead to variations in Laplace pressure and, consequently, the dispersed phase flow rate. Variations due to the Laplace pressure can largely be addressed by using symmetric channel dimensions at the T-junction for the dispersed phase input channel, the continuous phase input channel and the main channel. Symmetric channel dimensions are channels with the same depth, width and cross-section for every channel. This approach is also consistent with the work of Glawdel and Ren [85].

The resistive network model described in Section 2.5 has been used to design a robust microfluidic Droplet Generator capable of producing stable streams of droplets suitable for the formation of DIBs when a droplet trap is incorporated into its main channel. The actual design and results demonstrating this conclusion can be seen in Chapter 6.

4.3 Droplet Generator Design Considerations

There were several additional considerations used to guide the design of the Droplet Generator. The primary goal of the Droplet Generator design was to produce droplets that would be

approximately twice as long as they were wide, which varied in volume by no more than 10%. Droplets would be created using gravity-generated pressure-driven fluid flows of the Dispersed Phase and the Continuous Phase, as described in Section 3.2. The Droplet Generator was designed following the theoretical model described in Section 2.5 and considered the effects of droplet resistance and Laplace pressure. Practical considerations related to the height of the fluid reservoirs, operating pressure ranges and length of the main channel were also taken into account.

4.3.1 Droplet Size

Droplet size was a crucial element in the design of the Droplet Generator as it was a critical element in the eventual design of droplet traps. For the droplet traps to function correctly, each trapped droplet had to entirely block the constricted channel intended to hold it in place. This requirement follows the droplet trap design of Nguyen *et al.* (Figure 1-11) [6]. Additionally, to form a DIB, droplets in the droplet trap had to be of sufficient lengths to contact an adjacent trapped droplet. Therefore, in the design of a droplet trap, both the spacing of adjacent parallel constricted channels and the length of the trapped droplets were crucial and related parameters.

To maintain well-defined channel dimensions with the chosen fabrication method, the minimum distance between two parallel channels, measured from the centers of each channel, should be slightly more than one channel width. However, in most droplet traps in this project, parallel channels were used with a spacing of one to two channel widths between them. The increased distance between parallel channels significantly reduced the risk of distortion of channel dimensions. However, this required that droplets be approximately twice as long as the standard channel width to span the gap between two parallel constricted trapping channels. Spanning this gap would result in droplet contact and the formation of a DIB. Additionally, droplets needed to be of a consistent size such that they would always be expected to make contact in the droplet trap. A consistent size was defined as a droplet volume variation of no more than 10%.

From the author's previous work with droplet generators, and considering similar work by Glawdel and Ren, it was known that (1) droplets that were approximately twice as long as they were wide could be easily produced and that (2) the widths of the laser-cut channels were largely constant [85]. Droplets were also observed in the author's previous work to occupy the entire width of the devices' main channel width. Therefore, the Droplet Generator was designed to produce droplets that were approximately twice as long as they were wide.

Glawdel and Run suggest in their work that droplets of the same size will be produced if the flow rate ratio between the dispersed phase and continuous phase remains the same [85]. In the author's previous work (see Appendix B), droplets were formed with a flow rate ratio (Q_d/Q_c) of 0.2 in channels with widths of 118 μm and depths of 181 μm. Droplets had lengths of 280 ± 38 μm (± 14%), appeared to occupy the full width of the microfluidic channels (i.e., droplets were ~118 μm wide) and had spacings of 1.19 ± 0.11 mm (± 10%). These droplets were determined to be suitable for forming DIBs because they were about twice as long as the channels were wide. Therefore, they could be held in place at two parallel channels while blocking those channels and contacting adjacent droplets. This droplet length would allow multiple parallel channels in a droplet trap design without extensive channel overlap (discussed in Chapter 7). However, it was

observed that the formation of these droplets was unstable and had an unacceptable degree of size variability (i.e., >10% variation in droplet volume).

For Chapter 4, the term "Standard Channels" refers to laser-cut channels with widths of 118 μm and depths of 181 μm, as above. "Standard Droplets" refers to droplets formed with a Flow Rate Ratio of 0.2 and with the lengths, widths and spacing noted in the preceding paragraph.

In the author's previous work, the instability in production of the Standard Droplets was attributed to (1) handling/operational issues and (2) variation in flow resistance resulting in backflow and variability in droplet size and production rate. These could both result in (3) contamination issues. The instabilities caused by issues (1) and (3) were addressed by improved handling/operation and better control of flow resistance. As described in Section 2.5.2, variations in flow resistance arise from the creation of droplets in the device's main channel. The design of the Droplet Generator was created to address the issues of backflow and contamination specifically. This design requirement was accomplished by ensuring the device operated far from the limits where these phenomena occur, and produced droplets deemed suitable for the production of DIBs.

4.3.2 Droplet Resistance

Equation (2-15) was refined to account for the fluidic resistance of Standard Droplets. In the author's previous work, the resistance of the Standard Droplets was measured to be $3.30R_{norm} \pm 0.45R_{norm}$, where R_{norm} is the resistance of a 1 cm length of Standard Channel filled with the Dispersed Phase. R_{norm} was calculated to be 2.13 x 10^{12} ± 4.44 x 10^{10} Pa s m^{-3} using Equation (3-6). This measured droplet resistance corresponded to an increase of approximately four times in channel resistance compared to a Standard Channel of the same length as a Standard Droplet filled only with the Continuous Phase.

The droplet resistance can be described as an increase in the resistance of a channel filled with the continuous phase. This increase can be quantified by a droplet resistance increase factor (*DRIF*), which describes how the resistance of a channel filled with the continuous phase is increased by when containing a droplet. In the case described above, standard channels had a *DRIF* of four. Therefore, the resistance of the main channel filled with droplets can be calculated by determining the channel portion filled with droplets and multiplying that by the *DRIF*. Therefore, nR_{drop} in Equation (2-15) can be rewritten as *DRIF* x δ x R_{mcp} where δ is the total flow rate ratio (Q_d/Q_m). This approach allows Equation (2-15) to be rewritten accounting for droplet resistance with a *DRIF* of four to reflect the behaviour of Standard Droplets in Standard Channels more specifically. Equation (2-15) has been rewritten as Equation (4-2) to incorporate this refinement. Thus, Equation (4-2) was the equation used to calculate the resistance of the main channel in the design of the Droplet Generator.

$$R_m = (1-\delta)R_{mcp} + nR_{drop} \pm R_{drop} = (1-\delta)R_{mcp} + 4\delta R_{mcp} \pm R_{drop} \qquad (4\text{-}2)$$

4.3.3 Laplace Pressure

In the author's previous work on droplet formation, the radius of curvature of the fluid interface between the Dispersed Phase and the Continuous Phase in Standard Channels was measured to be

50 ± 8 μm from a top-down view of the channels. This radius of curvature was observed to be constant throughout the previous devices, regardless of the fluid front. The fluid fount in the dispersed phase input channel and the droplet fluid fronts were found to have the same radius of curvature. As a constant channel geometry was used in the previously tested devices, the same radius of curvature was expected for every fluid front in the Standard Channels.

The radius of curvature was not constant during the droplet formation process as multiple fluid fronts with different radii of curvature were present. During droplet formation, multiple fluid fronts develop and change rapidly over the course of droplet formation. This level of modelling was not required to design an effective Droplet Generator. This dynamic edge case is not considered in the droplet generator model, and describing the dynamics of the Laplace pressures during droplet formation is beyond the scope of this thesis. Although, this has been addressed in part in literature [135].

The radius of curvature discussed was measured as the length of the end caps of the produced droplets, which were assumed to be hemispherical. It is known that this assumption could lead to errors in calculating the Laplace pressure (see Section 2.6.1). However, it was deemed a suitable approximation to design the Droplet Generator using the available materials and data at the time of design.

The interfacial tension between the Dispersed Phase and the Continuous Phase has been reported by Bithi *et al.* as 5 mN m^{-1} and was assumed to be representative (Table 3-9) [70]. This result was verified and will be discussed in Section 7.6. The measured radius of curvature in the Standard Channels and interfacial tension were used to calculate a Laplace pressure of 200 ± 38 Pa as a first approximation using Equation (2-9). Some deviation in the fluid interface during droplet formation was expected. While this value may have been an adequate approximation for creating the first design, variations in the Laplace pressure could have contributed to instabilities in the droplet formation process. However, no such instabilities of significance were observed.

4.3.4 Fluid Reservoirs

An additional practical consideration for the design of the Droplet Generator was that the heights used to generate the fluid input pressures needed to be convenient for its operation. The input pressure flows of the Droplet Generator were intended to be generated using fluid reservoir heights of 1 m. This height was determined based on the heights found convenient for use in the author's previous work. Heights ranging from 0.7 m to 1.3 m were considered convenient for the operation of the device. This height range corresponded to dispersed phase input pressures from 6.84 kPa to 12.7 kPa.

The fluid reservoir heights could be set to within ± 2 mm. Therefore, the minimum acceptable P_d or the required P_d were not allowed to correspond to a height within 2 mm of the acceptable operating height limits. Additionally, the required P_d was designed to correspond to a height at least 5 mm higher than the minimum acceptable P_d. This requirement represented a height difference of 2.5 times the resolution with which the fluid reservoir heights could be set. This 5 mm translated into a 50 Pa pressure difference and avoided backflow caused by errors in setting the height of the dispersed phase fluid reservoir. The limits of the dispersed phase input pressure

to create backflow were determined in the design of the Droplet Generator. As long as these were avoided using the requirements defined above, an error in setting the height of the continuous phase reservoir within the specified ± 2 mm was not anticipated to produce any significant issues.

4.3.5 Operating Pressures and Stability

The design of the Droplet Generator centred around the use of Equation (4-1), as this was the main factor in determining its operational stability. Equation (4-1) is quite complex to discuss in an analytical framework, and it is helpful for further discussions based on numerical values. Several Droplet Generator designs that can produce Standard Droplets were considered and evaluated based on several performance metrics. These performance metrics included (1) the required P_d value to achieve a Flow Rate Ratio (Q_d/Q_c) of 0.2, (2) the acceptable P_d range calculated using Equation (2-16), and (3) the variability in the dispersed phase flow rate. The required P_d value needed to be at least 50 Pa higher than the minimum acceptable P_d value.

Furthermore, the required P_d value and minimum acceptable P_d value should be between 6.84 kPa and 12.7 kPa (see Section 4.3.4). Preferably these P_d values would be at least 1 kPa away from either of these limits. These requirements were determined by the practical use of the fluid reservoirs used to generate pressure via gravity needed to operate devices in this thesis, as described in Section 4.3.4.

The dispersed phase flow rate variability was determined by multiplying Equation (4-1) by R_{drop}, as R_m may vary as much as ± R_{drop}. This calculation determined the value of δQ_d, which can be divided by Q_d to calculate the variability in Q_d. As previously discussed in Section 4.2.1, the relationship between the dispersed phase flow rate variability and droplet size variability is unclear. Therefore, the percent variability in the dispersed phase flow rate was designed to be comparable, within 1%, to that predicted for the Droplet Generator used in the author's previous work (±1.64 %).

4.3.6 Length of Main Channel

To quantify droplet size, spacing and behaviour in the main channel of the device, the Droplet Generator was designed such that multiple droplets could be observed optically at one time. For simplicity and the stability of the droplet generation (as discussed in 3.4), the Droplet Generator's main channel was specified to be 6.78 cm in length. This channel length was slightly shorter than the main channel used in the devices in the author's previous work. A main channel of this length could be incorporated into the design of the Droplet Generator in a similar geometry, allowing for an existing design to be adjusted rather than begin a new design. The chosen length also made for easier observation of droplets with a stage microscope, as was discussed in Section 3.4. Furthermore, choosing a longer channel length resulted in more stable droplet production than shorter lengths, as discussed later in Section 4.3.7.

This main channel length, 6.78 cm, was predicted to contain 40 Standard Droplets made at a Flow Rate Ratio of 0.2. The resistance of the main channel, made as a Standard Channel and filled with Standard Droplets, would be $R_m = 300R_{norm}$.

4.3.7 Flow Rate Variability

Eight theoretical designs were considered, and their calculated performance metrics can be seen in Table 4-1. Each design is described by its ratio of the three channel resistances: R_d:R_m:R_c. Every resistance is normalized to $R_m = 300R_{norm}$. The designs were evaluated considering a continuous phase input pressure of 8.38 kPa, corresponding to a fluid reservoir height of 1 m. Standard Channels and Standard Droplets were assumed for every design. In this state, a Laplace pressure of 200 Pa can represent pressure drops due to interfacial tension within the device, and a R_{drop} value of $3.30R_{norm}$ can be used.

Table 4-1 – A design performance evaluation table for several of the evaluated designs. All resistance values are normalized to $R_m = 300R_{norm}$. The design R_d:R_m:R_c = 0.004:1.47:0.012 describes the droplet generating devices used in the author's previous work.

Design R_d:R_m:R_c	**Performance Metric**		
	Acceptable P_d Range [kPa]	**Required P_d for Q_d/Q_c = 0.2 [kPa]**	$\frac{\delta Q_d}{Q_d}$ **[%]**
R_d:R_m:R_c = 0.004:1.47:0.012	8.48 < P_d < 10.1	8.50	±1.64
R_d:R_m:R_c = 1:1:1	4.41 < P_d < 379	5.53	±0.88
R_d:R_m:R_c = 0.1:1:1	4.41 < P_d < 45.6	4.85	±2.19
R_d:R_m:R_c = 10:1:1	4.41 < P_d < 3710	12.4	±0.13
R_d:R_m:R_c = 1:0.442:1	2.81 < P_d < 846	4.20	±2.01
R_d:R_m:R_c = 1:1.47:1	5.20 < P_d < 260	6.16	±0.53
R_d:R_m:R_c = 1:1:0.1	7.82 < P_d < 379	9.22	±0.37
R_d:R_m:R_c = 1:1:10	0.97 < P_d < 379	1.25	±0.25

Several key observations were made by comparing the theoretical behaviour of the designs shown in Table 4-1. While the devices previously used by the author (i.e., R_d:R_m:R_c = 0.004:1.47:0.012) showed a reasonably low variability in the dispersed phase flow rate ($\delta Q_d/Q_d$), Standard Droplets produced using these devices were much more variable in length and therefore volume (±14% variability in droplet length). This variability was attributed to the slight difference between the minimum acceptable P_d (8.48 kPa) and the required P_d (8.50 kPa). Changes in R_m would change the minimum acceptable P_d value, which could result in significant changes in droplet sizing, spacing and even backflow.

Designs with main channel lengths of (1) 3 cm (R_d:R_m:R_c = 1:0.442:1), (2) 6.78 cm (R_d:R_m:R_c = 1:1:1) and (3) 9.98 cm (i.e., the main channel length of the device used previously by the author, R_d:R_m:R_c = 1:1.47:1) were compared with the same dispersed phase input channel and continuous phase input channel. Comparing these three designs showed that while increasing the main channel length reduced variability in the dispersed phase flow rate, the separation between the minimum acceptable P_d and required P_d was reduced. This reduced separation could also lead to instabilities in droplet production. Therefore, choosing a longer main channel length was beneficial to reduce variability in the dispersed phase flow rate. Increasing the main channel length was a viable option as long as the increased length did not compromise the lower operating pressure limit of the device.

This method may seem counter-intuitive, and it might be assumed that minimizing the number of droplets in the channel, and therefore the length of the main channel, would minimize the variation in R_m. However, Equation (4-1) shows that R_m is only present in the denominator, and consequently, a larger value of R_m will result in a smaller value of $\delta Q_d/\delta R_m$ and hence a smaller $\delta Q_d/Q_d$ value. Longer channels have large resistances, and therefore, a longer main channel results in a larger R_m. Furthermore, the more droplets that are present in the main channel, the less variability will occur in R_m, as a change of $\pm R_{drop}$ represents less of the overall resistance produced by droplets. Therefore, a single droplet entering or leaving the main channel represents less of a change in R_m.

The recommended guideline of $R_d > R_m > R_c$ mentioned in Section 4.2.1 was confirmed by comparing the designs evaluated in Table 4-1. It can also be seen that adhering to this guideline tended to reduce the dispersed phase flow rate variability and separated the minimum acceptable P_d and the required P_d. Increasing this separation can help prevent backflow issues and minimize the dispersed phase flow rate variability. The design of the Droplet Generator was created using the main channel resistance detailed above and the recommended guideline of $R_d > R_m > R_c$.

4.4 Device Operating Protocol

The Droplet Generator devices were designed according to the theoretical model described in Section 2.5 while accounting for the considerations detailed in Section 4.3. After the devices were fabricated, they needed to be tested to verify that they behaved as predicted. This section describes the operating procedure of the Droplet Generator devices used to test their behaviour and validate that they could produce droplets suitable for droplet trapping applications.

4.4.1.1 System Setup

The operation of the Droplet Generator was relatively simple and required the device be set up in a manner shown schematically in Figure 4-1.

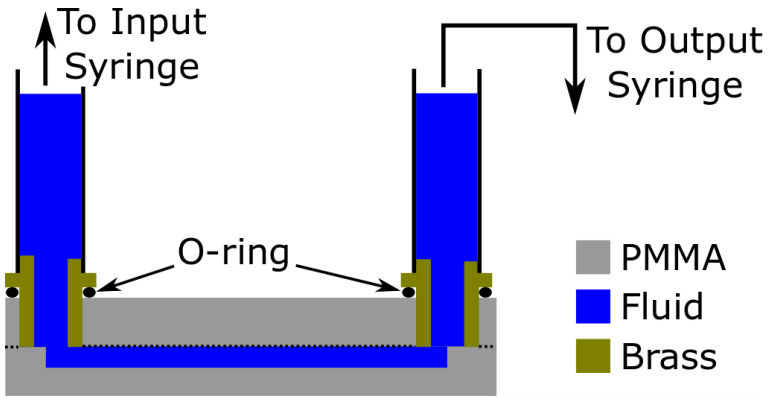

Figure 4-1 - A schematic showing the general setup for operating a microfluidic device using gravity-generated pressure-drive flow.

First, 3-56 to 1.59 mm barbed brass fittings (Clippard Instrument Laboratory Inc., Cincinnati, OH, USA) were attached to the two input and one output wells, with 3-56 Viton O-rings to seal the connections. Brass fittings were attached while looking at the O-rings from the backside of the device, the side of the device opposite to the PMMA layer containing the wells. This method

allowed for the compression of the O-rings to be seen, preventing overtightening of the brass fittings. Overtightening the fittings could result in delamination of the device.

The Droplet Generator was then secured to a glass microscope slide jig using double-sided tape to allow it to sit in a stage microscope.

4.4.1.2 Preparing the Input Fluid Reservoirs

Two 10 mL Input Syringes (BD 303134) were attached to their corresponding 140 cm lengths of 1.59 mm ID Tygon tubing using gauge 16 needles inserted into one end of the tubing. A 60 mL output syringe ("Output Syringe") was connected to an 80 cm length of Tygon tubing with an ID of 1.59 mm through a gauge 16 needle inserted into one end of the tubing. The Output Syringe was secured to a position such that its bottom was level with the Droplet Generator. The plungers were removed from all syringes, and the Tygon tubings of the Input Syringes were closed using plastic clamps (Bel-Art Acetal Mid-range Plastic Tubing clamps for 1/8 to 7/16 in. O.D. Tubing, F18228-0000, SP Scienceware).

The Dispersed Phase Input Syringe was then filled with 5 mL of Dispersed Phase and secured to a vertical dowel attached to the lab wall using bulldog clips. Before the Tygon tubing of the Dispersed Phase Input Syringe was connected to the input brass fittings, the open ends of the tubing were placed into a beaker, and the clamp was loosened so that the Tygon tubing could be filled with the fluid from the Input Syringe. Filling the Tygon tubing required approximately 3 mL of fluid to run through the device. As soon as the tubing was full, the clamp was closed, and the fluid level was adjusted so that there was 2 mL of Dispersed Phase in the Dispersed Phase Input Syringe. This process was repeated for the Continuous Phase Input Syringe.

The heights of the Input Syringes were then adjusted to ensure the fluid levels were in line with the appropriate heights for the test.

4.4.1.3 Priming the Droplet Generator

The Continuous Phase Input Syringe tubing and the Output Syringe tubing were then attached to their corresponding brass fittings on the Droplet Generator. The Continuous Phase input tubing clamp was released, allowing all device channels to be filled with the Continuous Phase. Before the Continuous Phase filled the dispersed phase input channel, the Dispersed Phase input tubing was connected to its brass fitting. Its tubing clamp was released, allowing the dispersed phase input channel to be filled with the Dispersed Phase. Once the continuous phase input channel and main channel were filled with the Continuous Phase, and the dispersed phase input channel was filled with the Dispersed Phase, the chip was in a testable state. This process took about an hour to complete using a dispersed phase input pressure of P_d = 8.45 kPa and a continuous phase input pressure of P_c = 8.38 kPa.

4.4.1.4 Device Operation and Observation

During the operation of the Droplet Generator, the formation of droplets on-chip was observed, and photographs and videos were recorded using a laboratory stage microscope equipped with a 9-megapixel USB camera (Model MU900, AmScope, Chino, CA, USA) and Toupview software

(the “Microscope”). If multiple pressure settings, and hence Input Syringe heights, were being tested, the device would be reset between testing each pressure setting. The reset process involved lowering the Dispersed Phase Input Syringe such that backflow into the dispersed phase input channel occurred for a brief time. While this occurred, the main channel was cleared of droplets and filled with only the Continuous Phase. In doing so, care was taken that no Continuous Phase reached the brass fitting of the dispersed phase input channel to avoid the formation of an emulsion of the Dispersed Phase and Continuous Phase. The heights of the Input Syringes for inducing this controlled backflow varied with each Continuous Phase Input Syringe height tested. For example, when testing a device using P_c = 8.38 kPa (Continuous Phase Input Syringe height = 100 cm), P_d would be set to 6.98 kPa to induce a slow and controlled backflow (Dispersed Phase Input Syringe height = 71.5 cm).

This method resulted in reproducible device operation, and every device could be operated successfully in this manner. However, air bubbles were observed occasionally in the dispersed phase input channel. Formation of air bubbles was possible when attaching the dispersed phase input tubing to its brass fitting. These air bubbles sometimes required manual intervention but were usually naturally cleared during the priming stage of setting up the device.

4.4.1.5 Storage of the Droplet Generator

Between tests, Droplet Generators were stored with the Continuous Phase filling all channels. Brass fittings were left attached to the devices; their openings were covered with Scotch Tape. During repeated testing, no indication of device failure was found due to the storage method. Before their subsequent use, the surfaces of the devices required cleaning with a paper towel dampened with water to remove adhesive residue from the Scotch Tape.

4.4.2 Test Methods

A variety of properties of each iterative fabrication of the Droplet Generator were tested using the methods described in Section 4.4. Fabrication quality, channel dimensions and droplet generation capabilities were all evaluated.

The fabrication quality of the Droplet Generators was determined by: (1) visual inspection before operation and (2) examining crack test chips. Crack test chips were included in several fabrication runs to ensure that there were no flaws in the devices and that channel dimensions appeared to be consistent. The channels of every received chip were examined from above using the Microscope set at 4x magnification before any other action was taken using the device. This examination was performed before fluid was put into channels and fittings attached to wells to determine if any channel blockages were present. An accompanying video of this process was taken so that if any issues arose when testing a device, any observed blockages could be compared to the device's state before testing. This process took approximately three minutes to examine every channel of a device.

Devices were fabricated in batches of four. In most fabrication runs, the left-most chip of a set of four devices for fabrication contained a series of crack lines allowing for the analysis of channel dimensions after the chips were bonded. The analysis of crack test chips followed the method

described in Section 3.3.2. In brief, the device was cracked along the red crack lines by placing the bonded chip on a benchtop with the crack line aligned with the edge of the benchtop. With the cut side of the crack line facing up, pressure was applied to the chip section hanging over the edge of the benchtop. This pressure snapped the chip into pieces along the crack line. The chip was then held in the Microscope such that the cross-sections of channels could be examined. The channel cross-sections were examined with the Microscope set at 10x magnification, and pictures of the cross-section were taken. The dimensions of the channel cross-sections were then measured in pixels using the line tool in the image process software ImageJ [131]. Pixel measurements were converted into real dimensions by multiplying by the ratio of the field of view to the pixel dimension of the photograph. Photographs of channel dimensions were 1744 pixels by 1308 pixels, and the Microscope had a field of view of 1166 μm by 873 μm when set at 10x magnification. The channel width was measured across the widest point of the channel, and channel depth was measured from the bottom of the channel bond level.

4.4.2.1 Droplet Generation Studies

For all testing, the Droplet Generators were operated following the method described in Section 4.4. These tests evaluated basic droplet generation by measuring the lengths, spacings and volumes of the produced droplets. Several droplet forming conditions defined by the Dispersed Phase and Continuous Phase input pressures were tested. This work primarily focused on pressures similar to the targeted pressure settings of P_d = 8.06 kPa and P_c = 8.38 kPa, which were thought to produce droplets suitable for droplet trapping applications (see Section 6.2). Other pressure settings were tested but primarily in the context of determining suitable droplet trapping operating conditions. These will be discussed in more detail in Chapter 7.

All devices were tested with a Continuous Phase input pressure of P_c = 8.38 kPa, corresponding to a Continuous Phase Input Syringe height of 1 m above the device. The Dispersed Phase input pressure was then varied between 7.83 kPa and 8.31 kPa (Dispersed Phase Input Syringe heights of 80.10 to 85.00 cm) to determine the range of a device's droplet forming capabilities. Specifically, at minimum, all devices were tested with P_d = 7.83 kPa, P_d = 7.94 kPa and P_d = 8.06 kPa. The P_d = 8.06 kPa setting was tested most frequently. If a pressure setting was tested multiple times, each test was performed consecutively, resetting the device between each test run.

The Droplet Generator was operated at the chosen pressure combination for a minimum of five minutes. Videos of droplet production focused on the main channel immediately past the T-junction were taken using the Microscope set at 4x magnification. A representative frame of such a video can be seen in Figure 4-2. Each video was a minimum of one minute in length. If the video did not last for five minutes and record the entire test run, at least three videos were taken at times: t = 0 minutes, t = 3 minutes and t = 5 minutes.

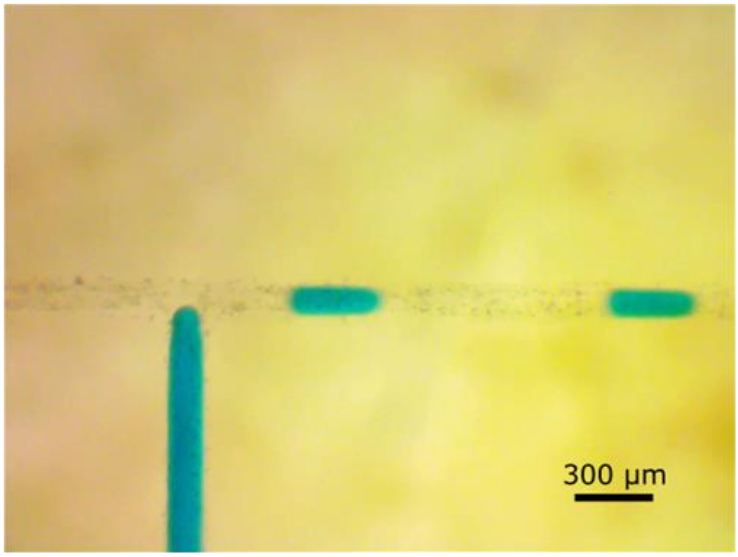

Figure 4-2 – A frame from a video of droplets being produced at the T-junction of a Droplet Generator using Pd = 8.06 kPa and Pc = 8.38 kPa. Droplets appear blurry, as they were captured in motion and flowing towards the frame's right. The channel has a naturally speckled appearance as verified before testing and device operation.

After testing was completed, data processing was performed as follows: videos were reviewed using the VLC media player program, and the lengths and spacings of droplets were measured on the screen with a ruler calibrated in millimetres. The droplet lengths were measured from tip-to-tip for each droplet, and the spacing between droplets was measured from the rear tip of one droplet to the leading tip of a second droplet. The dimensions of the video on the screen were also measured using the same ruler. Then, using both the dimensions of the video frame (172 mm x 128 mm) and the field of view of the Microscope set at 4x magnification (2.81 mm x 2.03 mm), the length of the droplet on the screen was converted to its real length. Measurements were converted to real lengths by multiplying the measured values by the ratio of the Microscope field of view to the video frame dimension.

The lengths of two to three groups of six consecutive droplets were measured in the first minute of production, the third minute of production and the fifth minute of production. This method was used to gather a representative amount of data from each test. Each group was measured at different times within these minute long periods at approximately equal time intervals. This data was considered representative of the droplet population observed in that test. The entire duration of all videos was observed to ensure that there were no anomalous droplets (i.e., overly short or long droplets) that were not included in the gathered data. If anomalous droplets were observed, they were either measured individually and included in the gathered data or included in one of the groups of six measured droplets.

The method described above was used for almost all studies of droplet generation. However, some tests were performed to examine more specific characteristics, including the droplet shape in laser-cut channels and varied from the method described above. In these cases, the methodologies for these special tests are described alongside their results.

4.5 Summary

Chapter 4 described the refinements made to the droplet generator model regarding how to ensure minimal variability in the produced droplet volume during the operation of the device. Then an overview of the various considerations taken into account when designing a Droplet Generator was discussed. This process included a preliminary estimate of droplet resistance in the microfluidic channels intended for use in the Droplet Generator and numerical verification of guidelines on channel design to improve the droplet generator stability (i.e., $R_d > R_m > R_c$). Finally, the operational methods used to test the designed and fabricated Droplet Generators were detailed. The numerical design and results of testing the Droplet Generators in this project will be discussed in Chapter 6.

Chapter 5
Droplet Trap Design and Operational Methods

5.1 Introduction

The critical feature in a passive droplet trap is the Laplace pressure barrier (ΔP_{LP} or ΔP_{Trap}) that holds droplets in place (Equation (2-17)). The general guiding theory in trap design is to ensure that the pressure drop across the droplet trap is smaller than this pressure barrier to hold droplets in place. The literature has few examples of passive droplet trap design processes to determine whether this pressure barrier will be exceeded. The notable exceptions are Nguyen *et al.* and Bithi *et al.*, who discuss resistive models of their droplet traps [6], [70]. This chapter seeks to describe the resistive models used to predict the behaviour of the two droplet traps used in this thesis, the Primary Droplet Trap and the Alternate Droplet Trap. These models also describe how they are integrated into Droplet Generator designs. After describing these resistive models, the changes to the operating procedure of the Droplet Generator devices with integrated traps are detailed.

5.2 Surface Energy Approach to the Laplace Pressure Difference

Before discussing the design of droplet traps used in this project, a means of calculating the Laplace pressure accurately in laser-cut microfluidic channels is required. In literature, most droplet trapping devices use rectangular channels for which the Laplace pressure of a fluid front is well known (Equation (2-10)). However, this requires the assumption that droplets fully fill the channel but are separated from the channel walls by a negligibly thin layer of the continuous phase. This assumption makes calculating the Laplace pressure difference between two rectangular channels relatively easy using Equation (2-17). However, this cannot be said for all channels. The Laplace pressure is known to be dependent on the channel geometry (Section 2.6.1), and the contact with channel walls may change as droplets transition between channels with different dimensions. Therefore, a better means of calculating the Laplace pressure difference for channels with non-standard geometries (e.g., laser-cut microfluidic channels) that also accounts for potential changes in interfacial tension is required.

Another way to think about the Laplace pressure difference is through the surface energy of a droplet. Droplets always seek to minimize their surface energy and move along deeper parts of microfluidic channels to minimize their surface energy by adopting more spherical conformations [65]. Droplets will therefore avoid entering constricted channels, as they would need to adopt smaller cross-sections. Smaller cross-sections result in smaller fluid front radii, increasing their surface energy and Laplace pressure. The energy required to make such a channel transition can be determined and used to calculate the pressure barrier to a droplet entering a constricted channel.

The difference between the surface energy of an infinitesimally short length of a droplet moving into a constricted channel from an unconstricted channel is equivalent to the Laplace pressure

difference between the two channels. Therefore, a surface energy approach provides a means of calculating the trapping pressure of a channel constriction based on a droplet's dimensions rather than the principal radii of its fluid interfaces. Consider a droplet with an arbitrary cross-sectional area A_1 and perimeter (of that area) of U_1 that is being forced into a smaller channel to have an area A_2 and perimeter U_2. The pressure required for the droplet to make the transition can be related to the droplet's surface area using Equation (5-1). In Equation (5-1), γ_1 and γ_2 are the corresponding interfacial energies at the droplet perimeters. Therefore, the behaviour of a droplet will be determined by the dimensions and geometries of the respective channels and the droplet's interfacial energies. A full derivation of Equation (5-1) is provided in Appendix C.

$$\Delta P_{SALP} = \left(\frac{\gamma_2 U_2}{A_2} - \frac{\gamma_1 U_1}{A_1}\right) \tag{5-1}$$

Equation (5-1) can derive the same equations for the trapping pressure commonly applied to circular and rectangular channels (i.e., Equation (2-17), see Appendix C). The most important difference about this approach is that it does not rely upon knowing the principal radii of curvature, which are difficult to determine in a microfluidic system. This approach allows for the Laplace pressure to be determined based on the more easily measured perimeter and cross-sectional area of a channel rather than the difficult to measure radii of curvature. While some channels have well-known relationships between the channel dimensions and radii of curvature, Equation (5-1) allows for a more accurate calculation of the Laplace pressure for channels where this is not the case.

The derivation of Equation (5-1) is similar to thermodynamic derivations of the Laplace pressure equation based on energy minimization [136]. However, to the best of the author's knowledge, this specific equation has not been used to calculate the trapping pressure of a microfluidic droplet trap.

This method of calculating the Laplace pressure difference of a channel transition was used to calculate the trapping pressures for all droplet traps designed in this project. It was initially assumed that droplets fully filled the channel cross-section. Therefore, the droplet perimeter and cross-sectional areas were considered the same as the channel perimeter and cross-sectional areas. The droplet perimeter and cross-sectional areas were calculated with Equation (3-4) and Equation (3-5).

With this revised method of calculating the Laplace pressure difference of a channel transition, the trapping pressure of a droplet trap could be determined, and resistive models of the traps could be generated.

As the project progressed and new data was acquired, it was realized that this resulted in minor inaccuracies of the estimated trapping pressure of droplet traps. As the model of Musterd *et al.* was beginning to be used, it was realized that the cross-sectional area and perimeter of droplets were different from their initial estimates [106]. These differences could lead to inaccuracies in the trapping pressure of droplet traps. It became simpler to calculate the Laplace pressure using the model of Musterd *et al.* [106].

The Laplace pressure differences of droplet traps were recalculated for work verifying the droplet splitting model (Section 7.6). First, the Laplace pressure of a droplet in each channel of the droplet trap was recalculated using the top corner radius of the droplet cross-section (Equation (2-18)) as predicted by the model of Musterd *et al.* as discussed in Section 2.6.1 [106]. Then the difference between these Laplace pressures was taken to determine the Laplace pressure difference of the channel transition of interest.

5.3 Primary Droplet Trap Design and Integration into Droplet Generator

Many droplet trap designs have been reported in the literature and are discussed in Section 1.1.4. One common type of design in literature is to have two or more channels that hold droplets in place via a Laplace pressure barrier (each a "trapping channel"), with another channel that bypasses the trapping channels (a "bypass channel") [6], [70]. Once the trapping channels have been blocked with droplets, subsequent droplets flow around the trapped droplets through the bypass channel. The Primary Droplet Trap designs followed this general method, with some adaptations.

The Primary Droplet Trap designs had channel layouts similar to Figure 5-1, except for the first iteration (Section 7.2.1). In Figure 5-1, green lines represent standard channels with dimensions equivalent to those of the main channel of a Droplet Generator. Cyan lines represent constricted trapping channels that will hold droplets in place at their upstream ends, and blue lines represent the bypass channels that will allow subsequent droplets to flow around the two trapped droplets. The trapping channels (cyan) are constricted relative to the standard channels (green) and therefore provide a Laplace pressure barrier to entry for a droplet (a trapping pressure, ΔP_{Trap}). As long as the pressure drop across the trapping channels does not exceed the trapping pressure (ΔP_{Trap}), trapped droplets will remain held in place. The droplet traps were designed to be integrated into the main channel of the Droplet Generator such that droplets would enter the trap from part of the main channel connected to the T-junction. They would then leave the trap and flow towards the device outlet through the remainder of the main channel.

Designs with the channel layout shown in Figure 5-1 can be described, at a high level, by the equivalent circuit shown in Figure 5-2, which is composed of a main channel contributing a larger resistance R_s through which a pressure P_{Tot} generates a fluid flow (Q). When integrating a droplet trap into a Droplet Generator, R_s is equivalent to the main channel resistance, R_m, and P_{Tot} is equivalent to the T-junction pressure, P_j. The droplet trap is composed of a trapping region defined by an unconstricted channel with resistance R_{Tu}. It also has two constricted trapping channels with resistances of R_{Tc} in series with Laplace pressure barriers at the constrictions (represented as ΔP_{Trap}). Lastly, the trap has N bypass channels with a total resistance of R_B/N in series, with pressure barriers if the bypass channels are constricted compared to R_s (represented as ΔP_{Vent}). Each bypass channel has a resistance of R_B.

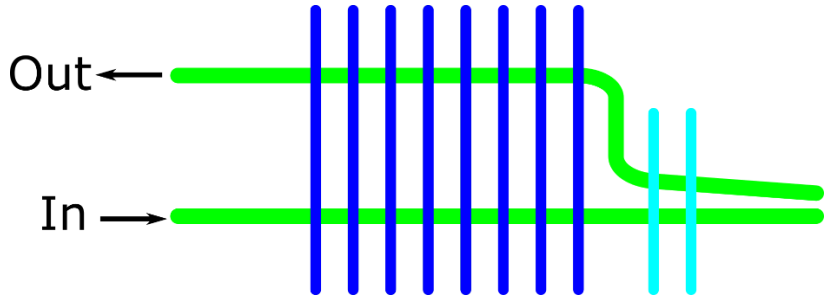

Figure 5-1 – A typical channel layout of a Primary Droplet Trap design. Green lines represent the standard channels with dimensions equivalent to those of the Droplet Generator, blue lines represent bypass channels and cyan lines represent trapping channels.

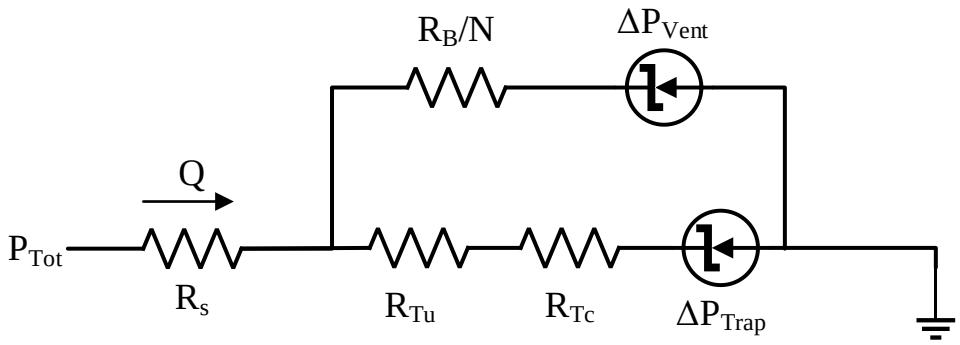

Figure 5-2 – A simple equivalent circuit for a typical Primary Droplet Trap design using electrical components to represent fluidic elements.

The equivalent circuit shown in Figure 5-2, although used in early iterations of the design process for the Primary Droplet Trap, is an idealization of this droplet trap design. It assumes that either all bypass channels are connected at the same junction or that the resistances of channels connecting parallel bypass channels are negligible. These assumptions may lead to significant errors.

A revised, more accurate equivalent circuit diagram is shown in Figure 5-3. This circuit considers the connections between each of the N bypass channels with resistances $R_{Tu,con}$. The channels connecting the bypass channels had the same dimensions as the R_{Tu} channel.

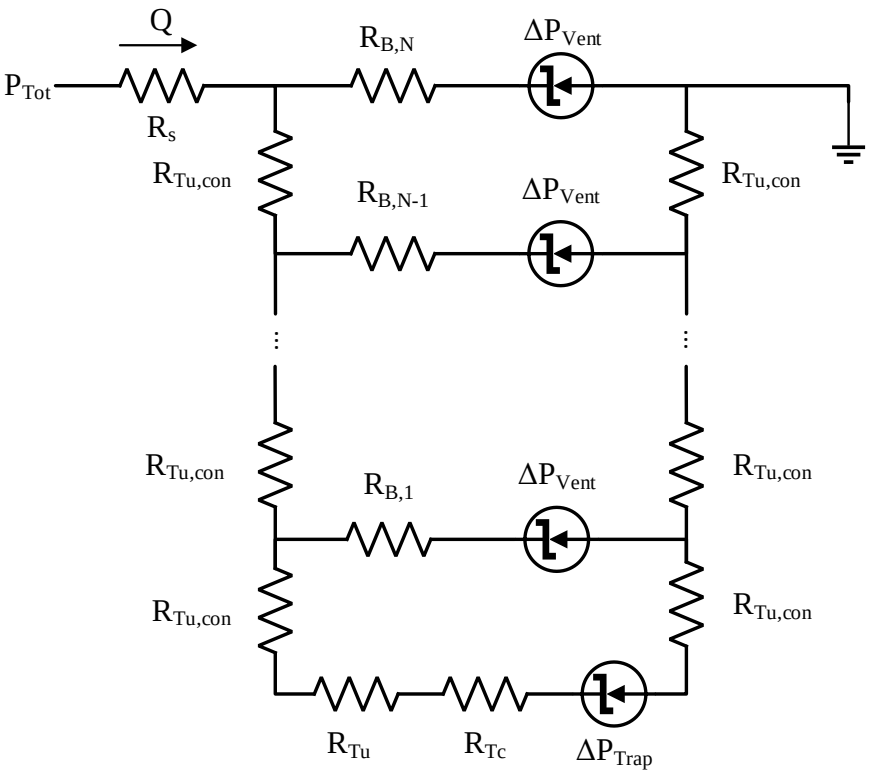

Figure 5-3 – A revised, more accurate equivalent circuit for a typical Primary Droplet Trap design using electrical components to represent fluidic elements.

5.3.1 Primary Droplet Trap Design Process

For simplicity, Primary Droplet Traps were designed with the requirement that R_B and R_T (the series combination of R_{Tu} and R_{Tc}) were small compared to R_s. Droplet traps were designed to have the T-junctions upstream by P_{Tot}.

The flow rate would always be stronger towards the trapping channels (R_{Tc}) as droplets passed bypass channels to sort droplets to the trapping channels. This sorting was accomplished by making each bypass channel resistance greater than the unoccupied trap resistance. This method is commonly used for droplet sorting in the literature and can be described by Equation (5-2) for the Primary Droplet Trap [97], [110], [114].

$$R_B > R_{Tu} + R_{Tc} \tag{5-2}$$

Once the droplet trap was filled with droplets and fluid flow through the trapping channels was blocked, the total flow (Q) needed to bypass the droplet trap. The flow also needed to bypass the trap without leading to a pressure drop greater than the trapping pressure of the droplet trap. The pressure drop could not exceed the trapping pressure (ΔP_{Trap}) of the transition from R_{Tu} to R_{Tc}. This requirement can be represented by the inequality in Equation (5-3) (Section 2.6 provides a more detailed discussion).

$$Q\left(\frac{R_B}{N}\right) < \Delta P_{Trap} \tag{5-3}$$

If the dimensions of bypass channels are constricted relative to the main channel of the droplet trap, they will contain pressure barriers. This pressure barrier, ΔP_{vent}, represents the trapping pressure of the transition from R_s to R_B. Once the droplet trap is filled with droplets, subsequent droplets will flow through the bypass channels, or droplets held in the droplet trap will eventually be displaced. This behaviour requires the inequality shown in Equation (5-4) so that droplets can enter the bypass channels once the trap has been filled. However, droplet traps were initially still expected to function (i.e., trap droplets) if the condition was met prematurely. Later on, it was found that droplet splitting may occur if this is the case. Equation (5-4) necessitated another easily met requirement that ΔP_{Vent} is smaller than ΔP_{Trap}, so bypass channels would not act as trapping channels.

$$Q\left(\frac{R_B}{N}\right) > \Delta P_{Vent} \tag{5-4}$$

Equation (5-3) and Equation (5-4) work well when considering the idealized equivalent circuit shown in Figure 5-2. However, they are not adequate when the revised, more accurate equivalent circuit shown in Figure 5-3 is considered. In the latter case, Equation (5-5) should be substituted for Equation (5-3) as it calculates the pressure drop across the closest, parallel bypass channel with the trapping channels. In Equation (5-5), Q_{B1} and R_{B1} refer to the volumetric flow rate through and the fluidic resistance of the closest, parallel bypass channel to the trapping channels (see Figure 5-3).

$$Q_{B1}R_{B1} < \Delta P_{Trap} \tag{5-5}$$

Equation (5-4) stipulates that the pressure drop across all bypass channels must be greater than ΔP_{Vent}. However, it was reasonable only to require that the pressure drop across some bypass channels be greater than ΔP_{Vent}. This revised requirement still allowed droplets to travel through some bypass channels while still directing droplets towards the droplet trap via the resistance sorting requirement (Equation (5-2)).

It is convenient to discuss the design of droplet traps in terms of resistivities (r_s, r_{Tu}, r_{Tc} and r_B) rather than resistances (R_s, R_{Tu}, R_{Tc}, and R_B). Using resistivities gives $R_x = r_x \times L_x$ where L_x is the length of the respective channel and x is s, Tu, Tc, or B. Values chosen for r_s, r_{Tu}, $r_{Tc,}$ and r_B have to represent attainable and suitable laser parameters. Whether a resistivity was suitable was determined by finding out whether the corresponding channel perimeter (U) and cross-sectional area (A) (and hence a channel's depth and width) were attainable using the fabrication method described in Section 3.3.

Requirements for channel lengths can be generated by discussing the droplet trap design in terms of resistivities. By direct substitution, Equation (5-2) can be rewritten as Equation (5-6) to provide a lower limit on the lengths of the bypass channels.

$$L_B > \frac{L_{Tu} * r_{Tu} + L_{Tc} * r_{Tc}}{r_B} \tag{5-6}$$

The design process generally began by choosing appropriate values of r_{Tc} and r_{Tu} to maximize the trapping pressures of the trapping channels, ΔP_{Trap}. Then a suitable value of r_B was chosen to create an appropriate value of $\Delta P_{Vent,}$ and the lengths of the bypass channels were determined. A suitable number of bypass channels was then determined, and a geometry was designed in which all of the required channel lengths could be accommodated. This design process was often under-constrained, as many of the above parameters could be controlled and required reasonable choices to be made. Therefore, some numerical design was required to determine the optimal values of several parameters based on other reasonable choices. This numerical design process will be discussed in Chapter 7.

5.4 Alternate Droplet Trap Design and its Integration into the Droplet Generator

As discussed in Section 1.1.4, droplet traps reported in literature often use pillar-based designs. A pillar-based droplet trap uses a series of short constricted channels to remove continuous phase from between droplets that are then held stationary in a droplet trap. The design of the Alternate Droplet Trap drew inspiration from these droplet trap designs. The channel geometry of the first design iteration of the Alternate Droplet Trap is presented in Figure 5-4. In Figure 5-4, green lines represent unconstricted input and output channels, grey lines represent bypass channels, and cyan lines represent constricted trapping channels.

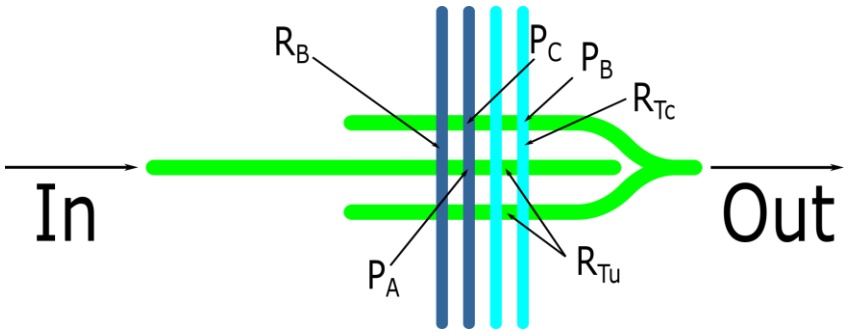

Figure 5-4 - The channel geometry of the first design iteration of the Alternate Droplet Trap with key design features labelled. Green lines represent unconstricted input and output channels, grey lines represent bypass channels, and cyan lines represent constricted trapping channels. Relevant equivalent circuit elements are noted.

The operating principle of the Alternate Droplet Trap design is relatively simple and similar to that of the Primary Droplet Trap design. As droplets enter through the unconstricted input channel of the droplet trap from the left of Figure 5-4, they are always directed towards the trapping channels (cyan lines). This sorting is accomplished by making the flow rate towards the trapping channels is the largest at any given channel intersection. Constricted trapping channels provide pressure barriers (ΔP_{Trap}) to the entry of droplets, and therefore droplets will not flow through trapping channels until those pressure barriers are overcome. Bypass channels (grey lines) and unconstricted output channels are included such that once both trapping channels hold droplets in place and the trap is full, subsequent continuous phase and droplets can flow around the trapped droplets. This bypass prevents increased pressures across the trapped droplets and their displacement from the trap.

The behaviour of the Alternate Droplet Trap is more challenging to model compared to the Primary Droplet Trap design. It can be described by the equivalent circuit shown in Figure 5-5. The circuit in Figure 5-5 is composed of a main input channel contributing a large resistance R_s through which a pressure P_{Tot} generates a fluid flow (Q). The droplet trap is composed of a trapping region defined by unconstricted channels with resistance R_{Tu1} and constricted trapping channels with resistance R_{Tc}. Each constricted channel is in series with pressure barriers represented as ΔP_{trap}. Multiple bypass channels are parallel to the trapping channels, each with a resistance of R_B, and connect to two unconstricted output channels. These output channels are comprised of channel lengths with resistances of R_{Tu1} and then proceed through channels with resistances of R_{Tu2} to exit the droplet trap. Several resistances and key pressure locations are marked on the droplet trap channel layout shown in Figure 5-4. The fluid flow direction is noted by the in and out arrows.

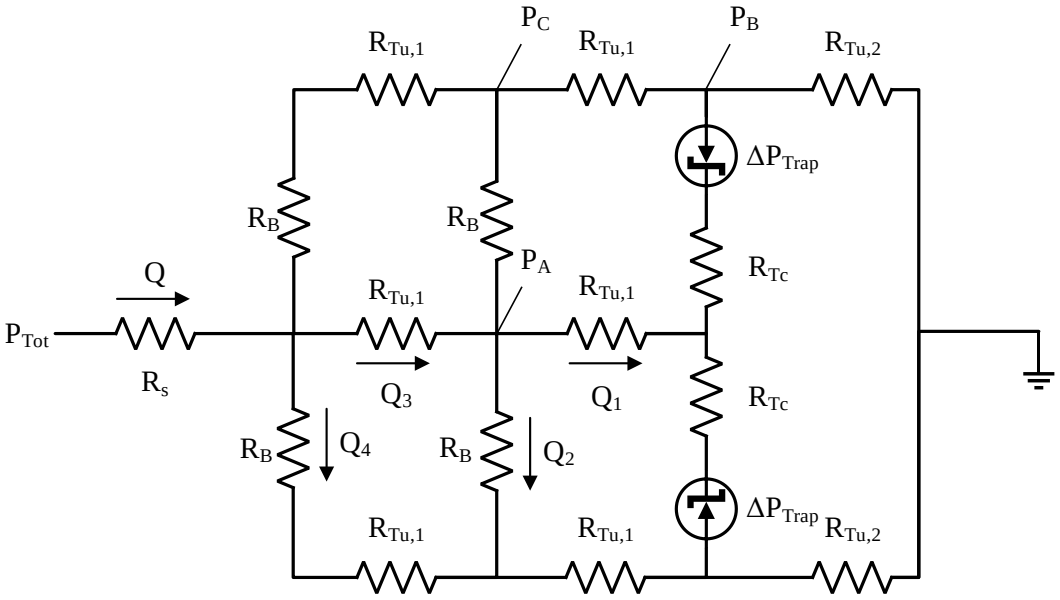

Figure 5-5 – An equivalent circuit depiction of the Alternate Droplet Trap using electrical components to represent its fluidic elements. This circuit would represent the channel geometry shown in Figure 5-4 if it only had two constricted trapping channels and held one trapped droplet.

The Alternate Droplet Trap provides a trapping pressure (ΔP_{trap}) at each of two constricted trapping channels. After droplets are held stationary at each trapping channel, subsequent droplets and continuous phase are diverted around the droplet trap. They flow through bypass channels to the output channels so that the pressure of the droplet trap does not exceed the trapping pressure (ΔP_{trap}). The pressure drop across the trap can be described by the pressure difference between P_A and P_B in Figure 5-5. This design requires a balance of fluid flows before and after trapping. The equivalent circuit in Figure 5-5 is drawn with only one constricted trapping channel. This circuit represents the droplet trap state with the highest resistance due to the constricted trapping channels, excluding the trap containing two droplets. In addition to the pressure barriers at the constrictions of the trapping channels (R_{Tc}), there are pressure barriers of ΔP_{vent} at each of the bypass channels (not shown in Figure 5-5).

5.4.1 Alternate Droplet Trap - Design Process

Although similar to the design process for the Primary Droplet Trap described in Section 5.3.1, the design process for the Alternate Droplet Trap used less specific equations due to the complexity of its equivalent circuit.

For simplicity, all design iterations of the Alternate Droplet Trap required that R_B, $R_{Tu,1}$, $R_{Tu,2}$ and R_{Tc} were small compared to R_s and their T-junctions upstream by P_{Tot}. As droplets approach the droplet trap, the fluid flow rate towards the constricted trapping channels is always strongest. This behaviour is represented by the inequalities in Equation (5-7) and Equation (5-8), where Q_1, Q_2, Q_3 and Q_4 are defined as in Figure 5-5. In Figure 5-5, Q_1 is the fluid flow rate towards the trapping channels at the rightmost bypass channel intersection with the input channel, and Q_2 is the fluid flow rate through the rightmost bypass channels. Similarly, Q_3 is the fluid flow rate towards the constricted trapping channels at the leftmost bypass channel intersection with the input channel, and Q_4 is the fluid flow rate through the leftmost bypass channels.

These inequalities need to be met when the droplet trap holds one trapped droplet, as this represents the state where Q_1 is at its minimum before the droplet trap is filled with two trapped droplets. This state represents the most extreme design criterion.

$$Q_1 > Q_2 \tag{5-7}$$
$$Q_3 > Q_4 \tag{5-8}$$

Once the droplet trap holds two droplets in place, all trapping channels are blocked by droplets. The flow of subsequent droplets and continuous phase (Q) must bypass the two trapped droplets without leading to a pressure drop greater than the trapping pressure of the droplet trap. Equation (5-9) shows the inequality describing this behaviour, where P_A and P_B are the pressures at the points indicated in Figure 5-4 and Figure 5-5.

$$P_A - P_B < \Delta P_{Trap} \tag{5-9}$$

If the bypass channels are constricted relative to the input channel, they too would have pressure barriers, ΔP_{Vent}. Once the droplet trap is filled fully, subsequent droplets have to flow through the bypass channels, or the trapped droplets in the droplet trap will eventually be displaced. This requires the inequality shown in Equation (5-10), where P_A and P_C represent the pressures at the points indicated in Figure 5-4 and Figure 5-5. Ideally, this condition would only be met once the droplet trap holds two trapped droplets. However, the droplet trap should still function if the condition is met prematurely (i.e., trap droplets). It was later found that droplet splitting may occur if this is the case. This behaviour necessitates another easily met requirement that ΔP_{Vent} is smaller than ΔP_{Trap} so that the bypass channels do not become trapping channels.

$$\mathrm{P_A} - \mathrm{P}_C > \Delta P_{vent} \tag{5-10}$$

As with the Primary Droplet Trap design process (see Section 5.3.1), the design can be more easily in resistivities rather than resistances. All chosen resistivities were verified to ensure that they represented channel dimensions capable of construction using the fabrication method described in Section 3.3. Resistivities were chosen to maximize the trapping pressure of the constricted trapping channels and to create suitable trapping pressures for the bypass channels. This process was often under-constrained because of the almost complete control over many of the parameters involved (e.g., resistivities and channel lengths).

5.5 Droplet Trap Operation and Testing

The Primary Droplet Traps and the Alternate Droplet Trap were integrated into Droplet Generators described in Chapter 6. The droplet traps acted as passive elements in the Droplet Generators and could not be controlled directly. Droplet Generators with integrated droplet traps were operated much in the same way as described in Section 4.4. The only significant differences in the operating protocol were that (1) the behaviour of the droplet traps was observed using the Microscope when droplets arrived at the droplet traps, and (2) procedures were introduced to remove trapped droplets from the droplet trap.

During droplet production testing of Droplet Generators with integrated droplet traps, the Microscope was initially focused on the T-junction to observe the droplet formation process. As droplets arrived at the droplet trap, it was then moved to focus on the droplet trap. It was observed that droplets typically required ~45 seconds to travel from the T-junction to the droplet trap when operating the Droplet Generator with P_c = 8.38 kPa. The behaviour at the droplet trap was typically observed for one to two minutes before returning the focus of the Microscope to the T-junction. Upon returning to the T-junction, the characterization of the droplet production process would be continued until droplets had been continuously produced for approximately five minutes. Depending on the droplet trap design being tested, the framing of the droplet trap with the Microscope varied but was typically focused on the trapping channels.

After testing was completed, clearing the trapped droplets from the droplet trap required manual intervention. The main channel was allowed to fill with the Continuous Phase, and the dispersed phase input channel was partially filled with the Continuous Phase. The dispersed phase input channel was not allowed to be filled enough to create contamination issues. On occasion, this would generate a small number of minuscule droplets of the Dispersed Phase in the Continuous Phase. The tubing leading to the Output Syringe was then disconnected from the Output Syringe and reconnected to a 10 mL syringe with an intact plunger that had first been fully depressed. The plunger on the intact syringe was then retracted to apply significant negative pressure to the Output Well of the Droplet Generator. This negative pressure increased the pressure drop across the droplet trap and ejected any trapped droplets. Immediately after all trapped droplets were cleared from the droplet trap, the tubing was disconnected from the intact syringe and reconnected to the Output Syringe.

One specific fabrication run of Droplet Generators with integrated Primary Droplet Trap Iteration 2 included several devices with a specific purge line with a permanently connected 10 mL syringe

with an intact plunger. Therefore, the Output Syringe did not need to be disconnected and reconnected after every test. This design will be discussed further in Section 7.3.2.

5.5.1 Droplet Traps: Specific Test Methods

Several tests were performed specifically on Droplet Generators with integrated droplet traps in addition to the regular droplet production tests described in Section 4.4.2. The test methods described in Section 4.4.2 were intended primarily to confirm that continuous streams of droplets could be reliably produced and observed. Droplet Generators with integrated droplet traps were also tested by examining the behaviour of single droplets and isolated pairs of consecutively-produced droplets when they entered the area of the droplet trap.

A Droplet Generator was operated largely following the operating protocol described in Section 4.4 but with several minor changes to create single or isolated pairs of droplets. Once a single droplet or an isolated pair of droplets was produced, the height of the Dispersed Phase Input Syringe was immediately lowered. This action decreased the dispersed phase input pressure to a point where a small controlled amount of backflow into the dispersed phase input channel occurred. The height for the Dispersed Phase Input Syringe to induce backflow into the dispersed phase input channel was determined before testing for a given pressure setting. As an example, for tests with P_c = 8.38 kPa, it was calculated that the Dispersed Phase Input Syringe had to be lowered to a height of 71.5 cm, corresponding to a dispersed phase input pressure of 6.99 kPa.

When performing tests with single or isolated pairs of droplets, the Microscope was focused on the droplet(s) from the point in time when they were generated to when they arrived within the droplet trap. For every test, videos that were five minutes in length were recorded, allowing droplets to be observed in the droplet trap after being trapped. If the trapped droplets did not merge within the five-minute duration, they were continually observed (but not recorded) until they merged or they had been under observation for 25 minutes. The time between two droplets being trapped in contact with each other and their merging was defined as “droplet lifetime”. Droplet lifetime was manually recorded using a stopwatch. This process was also performed for droplets produced as part of a continuous droplet stream. However, only the first one to two minutes of the droplets within the droplet trap were directly observed and recorded in this case. The droplets were observed again after five minutes of being trapped. The droplets were not observed in the droplet trap between the two-minute and five-minute marks of the droplet production tests. Measuring the trapped droplet lifetime was not performed until the third design iteration of the Primary Droplet Trap and the first design iteration of the Alternate Droplet Trap. Construction of both such devices occurred in the same fabrication run.

The Droplet Generators with integrated droplet traps were tested at the pressure settings defined in Section 4.4.2 for regular droplet generation studies, specifically P_d = 7.83 kPa, 7.94 kPa and 8.06 kPa in each case with P_c = 8.38 kPa. Other pressure settings with lower values of P_c were also tested as needed to determine if the droplet trap behaviour changed with changes in pressure. These lower P_c settings included P_c = 2.51 kPa, 3.35 kPa and 6.70 kPa, with values of P_d that were predicted to produce droplets at the same relative droplet volume as the pressure setting P_d = 8.06 kPa and P_c = 8.38 kPa. These values were P_d = 2.51 kPa, 3.22 kPa and 6.45 kPa,

respectively. Other pressure settings close to these values were also tested to observe the behaviour of the droplet trap with droplets with different volumes.

Whenever a Droplet Generator with an integrated droplet trap was tested multiple times with a given pressure setting, all tests were performed consecutively. The Droplet Generator was reset between each test run by clearing, filling the main channel of the device with Continuous Phase and purging any trapped droplets from the droplet trap as described in Section 5.5. Occasionally small droplets became trapped in the dead-end channels of the droplet traps, but these did not affect the performance of the Droplet Generator or droplet trap. These could not be readily removed when purging the droplet trap and, therefore, can be seen in images of droplet trapping presented in Chapter 7.

Aside from the changes and new tests described here, all other testing methods (e.g., data processing techniques) were otherwise the same as described in Section 4.4.2.

5.6 Summary

The method of calculating the Laplace pressure difference described in this chapter, combined with the resistive network models of droplet traps, provides a robust framework to design droplet traps. The resistive network models for two droplet traps, the Primary Droplet Trap and the Alternate Droplet Trap were described and the design process to integrate them into Droplet Generators. The operational changes to Droplet Generators with integrated droplet traps were also detailed. The design and performance of the droplet traps used in this thesis will be described in Chapter 7.

Chapter 6
Gravity Driven Microfluidic Droplet Generator Design and Testing

6.1 Introduction

Chapter 6 describes the design process undertaken to design a Droplet Generator using the theoretical model described in Section 2.5 and the design considerations and model refinements discussed in Chapter 4. The Droplet Generator was designed to reliably produce droplets that were twice as long as they were wide, varied in volume by no more than 10% and could be generated with reasonable operating pressures. These criteria were determined by several constraints of the fabrication method, droplet generator model and operation method, which are discussed in detail in Section 4.3.

Following these criteria, a Droplet Generator was designed and tested. Droplet traps were also designed and integrated into the main channel of the Droplet Generator (as will be discussed in Chapter 7). These were designed in such a way that they minimally impacted the behaviour of the Droplet Generator. Therefore, Droplet Generators, both with and without integrated droplet traps, were tested to ensure that they could reliably and reproducibly produce droplets that met the criteria stated above over multiple test runs and devices.

The success of the Droplet Generators was judged based on the lengths, spacings and volumes of the produced droplets. However, to enable this, a suitable method for calculating the shape and volume of droplets in laser-cut microfluidic channels was determined. This method for calculating droplet volume was applied to validate the droplet generator model described in Section 2.5. Following these experiments, the Droplet Generators were found to reproducibly produce droplets that met the specified size criteria and were suitable for droplet trapping applications.

6.2 Numerical Design of Droplet Generator

The final Droplet Generator device design was focused on minimizing variability in the dispersed phase flow rate. This minimization was accomplished through appropriate choices of the dispersed phase input channel resistance (R_d), the continuous phase input channel resistance (R_c) and the main channel resistance (R_m). The final numerical design and optimization of the Droplet Generators was performed similarly to the comparison of flow rate variability in Section 4.3.7 but focused on the other design considerations outlined in Section 4.3. The final design process for the Droplet Generator will be described in reference to the ratio of R_d:R_m:R_c and normalized to the main channel resistance of $R_m = 300R_{norm,}$ where R_{norm} is as defined in Section 4.3.2. The design was initially standardized on the Standard Channels defined in Section 4.3.1. However, as will be discussed later, these were not the resulting dimensions of the channels of the Droplet Generators.

As shown in Table 4-1, the Droplet Generator design with R_d:R_m:R_c = 1:1:1 using Standard Channels shows a lower dispersed phase flow rate variation than the device design used in the

author's previous work (R_d:R_m:R_c = 0.004:1.47:0.012). Therefore, it was a good starting point to consider the practical limitations imposed on the design for fabrication.

With a main channel length of 6.78 cm (as chosen in Section 4.3.6), this design corresponded to channel lengths of L_d:L_m:L_c = 44.2:1:1.5, normalized to the length of the main channel. This conversion from channel resistance to length was performed using Equation (3-6). L_d, L_m, and L_c correspond to the length of the dispersed phase input channel, length of the main channel and length of the continuous phase input channel, respectively. Considering L_m = 6.78 cm, then L_d = 300 cm, and L_c = 10.17 cm, the sum of which was much greater than the maximum acceptable 38 cm (as determined in Section 3.4). The required P_d was 5.53 kPa, far outside the acceptable pressure range based on the heights of the dispersed phase and continuous phase reservoirs in the design (Section 4.3.5). While this design was effective in terms of stability and showed minimal variation in Q_d, it could not be practically fabricated.

The R_d:R_m:R_c = 1:1:1 design was adjusted, following the recommendation of $R_d > R_m > R_c$ as closely as possible. This method was thought to result in the best performing Droplet Generator with a main channel length of 6.78 cm. To make this adjustment, the continuous phase input channel resistance was minimized, and the dispersed phase input channel resistance was maximized. With a minimum acceptable channel length of 1 cm, R_c was minimized by setting L_c = 1 cm. Consequently, $L_c + L_m$ = 7.78 cm, so approximately 30.22 cm of channel could be used to form the dispersed phase input channel while not exceeding the 38 cm limitation for the length of the three channels. Due to several geometry constraints involved in implementing the Droplet Generator's design, related primarily to well placement and optical paths to a stage microscope, the longest possible dispersed phase input channel was 26 cm long. This resulted in the following chip design: L_d:L_m:L_c = 3.83:1:0.15, normalized to L_m = 6.78 cm and corresponded to R_d:R_m:R_c = 0.087:1:0.098, normalized to $R_m = 300R_{norm}$ (as defined in Section 4.3.2). The layout of this design can be seen in Figure 6-1. The performance metrics for the design can be seen in Table 6-1, wherein they have been compared to those of the devices used in the author's previous work.

The design shown in Figure 6-1 could be operated using the Dispersed Phase and Continuous Phase to form a steady stream of droplets in the main channel with similar dimensions to Standard Droplets. This behaviour could be accomplished by using only Standard Channels to ensure symmetric channel dimensions at the T-junction. Standard Droplets were predicted to form with the operating conditions of P_c = 8.38 kPa (corresponding to a continuous phase reservoir height of 1 m), P_d = 8.06 kPa (corresponding to a dispersed phase reservoir height of 82.5 cm), at a Flow Rate Ratio of Q_d/Q_c = 0.2. These operating conditions were accessible practically by using convenient heights to place fluid reservoirs to generate appropriate pressure-driven fluid flow. The device was expected to produce droplets suitable for the formation of DIBs and was determined to be the most stable design that could fit on a standard PMMA chip.

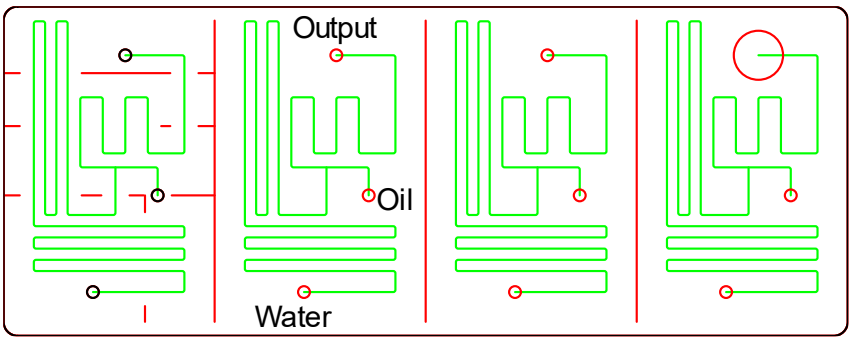

Figure 6-1 - An overlay of all chip layers and crack line patterns in the Droplet Generator design. The input and output wells are labelled in the second chip from the left.

Table 6-1 shows that the performance metrics of the R_d:R_m:R_c = 0.087:1:0.098 design passed all of the requirements identified previously. The required P_d (8.06 kPa) was greater than both the minimum acceptable P_d for the design (7.84 kPa) and the minimum acceptable P_d for an operating height (6.84 kPa). The variability of the dispersed phase flow rate of the Droplet Generator design (2.26%) was within 1% of the variability of the dispersed phase flow rate of the devices used in the author's previous work (1.64%). While this was a larger variability, the separation between the required P_d and the minimum acceptable P_d was much greater in the Droplet Generator design. This increased separation was expected to help minimize droplet size variations. It also allowed the fine-tuning of the dispersed phase operating pressure to create a broader range of low Flow Rate Ratios.

Table 6-1 – A design performance evaluation table for the starting design of R_d:R_m:R_c = 0.087:1:0.098 and R_d:R_m:R_c = 0.004:1.47:0.012 (the device used previously) normalized to R_m= 300R_{norm}.

Performance Metric	**Design**	
	R_d:R_m:R_c = 0.004:1.47:0.012	**R_d:R_m:R_c = 0.087:1:0.098**
Acceptable P_d Range [kPa]	8.48 < P_d < 10.1	7.84 < P_d < 40.7
Required P_d for Q_d/Q_c = 0.2 [kPa]	8.50	8.06
$\frac{\delta Q_d}{Q_d}$ [%]	±1.64	±2.26

The Standard Channels were intended to have widths of 118 µm and depths of 181 µm. CB approximated the laser settings shown in Table 6-2 to provide the specified channel dimensions. The channels cut with these settings were standardized, and all devices, including those in the first fabrication run of Droplet Generator devices, used these settings and their resulting dimensions.

Table 6-2 – The laser settings used to cut the Standard Channels in the Droplet Generator devices for the first fabrication run.

Channel Type	**Standard Channels**
Laser Line Colour	Green
Number of Passes	2 Pass
Laser Power [%]	3.5
Laser Speed [%]	0.5

6.3 Testing Results

6.3.1 Crack Test Chip Results

There was a total of five fabrication runs performed as part of this thesis. The first fabrication run produced Droplet Generators without an integrated droplet trap. Every subsequent fabrication run produced Droplet Generators with integrated droplets traps of varying designs (discussed more in Chapter 7). For the first three fabrication runs, at least one crack test chip was produced and examined.

Every Droplet Generator device, regardless of whether it had an integrated droplet trap, used the same channels for the main channel, dispersed phase input channel and continuous phase input channel (see Figure 6-1). These channels were all cut with the same laser line and were therefore expected to have the same channel dimensions. However, as noted in Section 3.3.3, channels with different orientations (i.e., horizontally-oriented versus vertically-oriented) were found to have different dimensions.

As discussed in Section 3.3.3, the channels used for all channels in the Droplet Generators, had on average, depths of 240 ± 17 μm (± 7.1%, n = 72) and widths of 132 ± 20 μm (± 15%, n = 72). Horizontally-oriented channels were on average 253 ± 12 μm (± 4.7%, n = 28) deep and 119 ± 22 μm (± 18%, n = 28) wide and vertically-oriented channels were on average, 236 ± 10 μm (± 4.2%, n = 30) deep and 138 ± 13 μm (± 9.4%, n = 30) wide. There were variations in the channel depth and width between devices and, more significantly, between fabrication runs.

The variations in channel dimensions resulted in minor changes to the predicted operating range of the Droplet Generator. However, no significant differences between the predicted and actual behaviour were observed due to variations in channel dimensions. No single set of channel dimensions could be used to describe the channels for every fabrication run accurately. Therefore, the specific channel dimensions of the device used to form droplets are reported when discussing droplet lengths or droplet spacing distances.

It is, however, much more convenient to discuss the Droplet Generator test results in terms of droplet volumes, thereby eliminating the need for channel dimension consistency. To do so requires a good understating of droplet shape in the channels so that the droplet volumes can be accurately calculated from the top-down measured droplet length. Therefore, tests were performed to determine the droplet shape in the laser-cut microfluidic channels.

6.3.2 Droplet Shape in Microfluidic Channels

As discussed in Section 2.6.1, droplets were initially expected to conform to the channel cross-section but are separated from the channel walls by a thin sheath of Continuous Phase. Droplets in laser-cut channels were initially expected to have cross-sections similar to Figure 6-2. This was later found not to be the actual cross-section of a droplet in a laser-cut channel, as discussed later in this Section.

The Continuous Phase sheath thickness surrounding the droplets has been reported to be proportional to the channel width and dependent on the droplet speed through the channel. The

thickness is also often quantified by the Capillary number of the fluid flow [106], [107]. Therefore, to begin determining the shape of the droplets, the thickness of the Continuous Phase sheath was measured for both moving and stationary droplets.

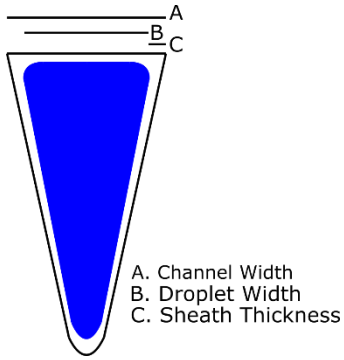

Figure 6-2 – A rough sketch of the expected droplet cross-section in a horizontally-oriented laser-cut channel. The blue area denotes the droplet cross-section.

6.3.2.1 Measurement of Continuous Phase Sheath Thickness

A series of droplets were created using a Droplet Generator with a pressure setting of P_d = 8.06 kPa and P_c = 8.38 kPa. The Capillary number for this pressure setting was expected to be 0.006. Musterd *et al.* suggest that the continuous phase sheath is negligibly thick if the capillary number is less than 0.001 [106]. This was not the case for the droplets that were considered and therefore, a non-negligible continuous phase sheath was expected and measured.

Photographs of stationary droplets were taken using the Microscope set at 10x. Videos were taken of these droplets transitioning to and from stationary positions using the Microscope set at the same magnification. Droplets were made stationary by changing the applied Dispersed Phase and Continuous Phase input pressure by lowering the Input Syringes such that the fluids were level with the Droplet Generator being used. The droplets were observed in a vertically-oriented channel with an average depth of 238 ± 11 μm (± 4.6%, n = 18) and an average width of 140 ± 10 μm (± 7.1%, n = 18) as determined by examining channel cross-sections using crack test chips. A representative frame of a video of a droplet transitioning to a stationary position can be seen in Figure 6-3. A representative photo of a droplet in a stationary position can be seen in Figure 6-4.

Droplet lengths and widths and the widths of the channels containing the droplets were measured. The difference between the droplet width and the channel width could be used to determine the thickness of the continuous phase sheath (Figure 6-2). As a first approximation, half of the difference between the two widths was used as the thickness of the continuous phase sheath. A more accurate value can be determined considering the slope of the channel walls. However, due to the large top corner angle of the channels being used and the measured widths, this would introduce a maximum of a 3% error in calculating the continuous phase sheath thickness. This error represented was a similar level of uncertainty to the measurement uncertainty in the widths (2%) and therefore was not significant.

A summary of the results of this testing can be seen in Figure 6-5. The measured droplet dimensions were gathered from nine stationary droplets, and 28 moving droplets from three

different test runs on two days using the same Droplet Generator device. All stationary droplets were examined after being held in stationary positions for 20 minutes. All droplets were observed in the same location on the device. The lengths of the moving droplets measured from videos have a higher measurement error (± 12 μm) compared to the droplet lengths of stationary droplets measured from still photographs (± 3 μm).

The average droplet length of moving droplets was not within ± 12 μm of the average droplet length of stationary droplets, suggesting a change in the droplet length when transitioning from moving to stationary. Specifically, the moving droplets appeared slightly longer than the stationary droplets. Moving droplets were slightly narrower and, therefore, slightly elongated to maintain constant volumes.

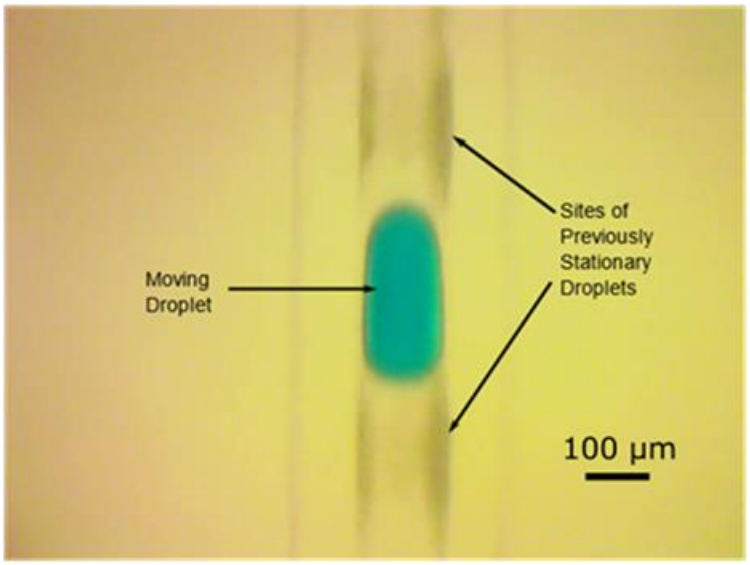

Figure 6-3 – A frame from a video taken at 10x magnification of droplets transitioning to moving after being held stationary for 20 minutes. The "droplet shadows" indicate where two droplets were previously in stationary positions.

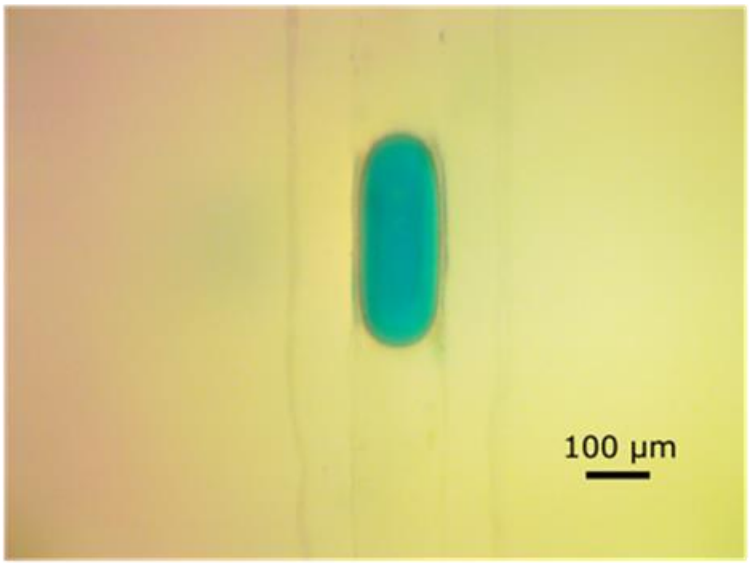

Figure 6-4 – A representative photograph of a stationary droplet after being held stationary for 20 minutes taken with 10x magnification.

The results shown in Figure 6-5 demonstrate significant differences in the average widths of droplets and the channel width when the droplets were moving and stationary. The average droplet width was determined to be 129 ± 2.83 µm after droplets had been stationary for 20 minutes and 120 ± 2.11 µm when in motion. The channel width was a constant 147 ± 2.84 µm, agreeing with channel widths measured from channel cross-sections. These results indicated that there was a sheath of Continuous Phase around the droplets with an average width of 8.88 µm when the droplets were stationary for 20 minutes and 13.38 µm when they were in motion. Based on a 10-minute period with photographs taken every 30 seconds using the Microscope set at 10x magnification, the widths of droplets broadened as soon as they became stationary. After the initial broadening, their lengths and widths remained constant for as long as they were stationary (data not shown). The presence of a Continuous Phase sheath around droplets both when stationary over 20 minutes and in motion indicated that the droplets did not touch the channel sidewalls. Therefore, the droplet shape shown in Figure 6-2 was thought to be a reasonable estimate of the actual cross-sectional shape of droplets in laser-cut channels.

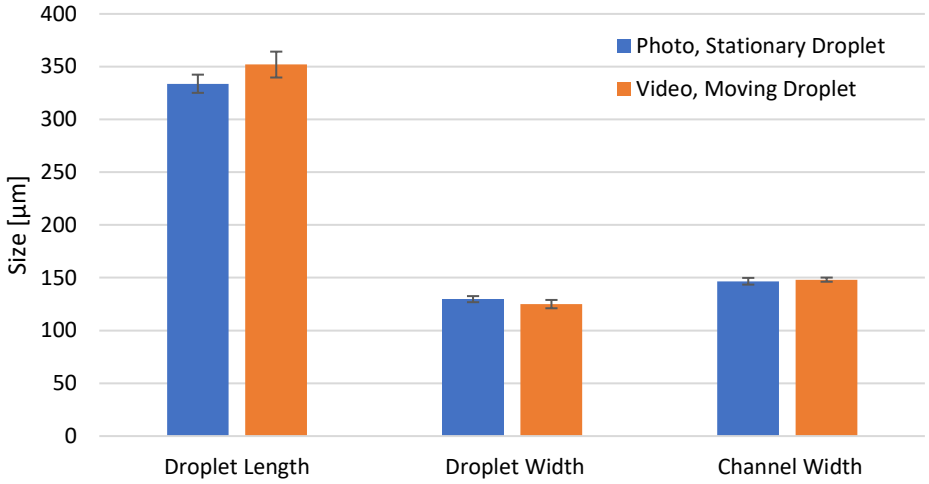

Figure 6-5 – A comparison of average droplet length, average droplet width, and channel width of droplets made with the same settings when stationary and in motion. Data was gathered from photographs and videos taken at 10x magnification. Nine stationary droplets and 12 moving droplets were measured. Error bars represent one standard deviation of the average values or one measurement error in the case of droplet lengths measured for moving droplets.

6.3.2.2 Changes in Stationary Droplet Shape Over Time

As the thesis aims to create a droplet trap that would hold droplets in stationary positions for extended periods, it is essential to understand changes in stationary droplet shape over time. Accordingly, during the 20 minutes that droplets were held stationary in this test, timelapse photographs of droplets were taken.

Droplets were produced with two Droplet Generator devices fabricated in the same fabrication run, with the same integrated droplet trap and at the same pressure settings of P_d = 8.06 kPa and P_c = 8.38 kPa. One of these Droplet Generators was the same device used in the experiments in the preceding section. The droplets produced by the two Droplet Generators were held in stationary positions for periods of 20 minutes. Series of time-lapse photographs were taken of the stationary droplets using different Microscope magnifications - 2x and 4x magnification. The lengths and

widths of droplets were measured in both vertically-oriented channels and horizontally-oriented channels. The vertically-oriented channels had an average depth of 238 ± 11 μm (± 4.6%, n = 18) and an average width of 140 ± 10 μm (± 7.1%, n = 18) and horizontally-oriented channels had an average depth of 260 ± 11 μm (± 4.2%, n = 14) and an average width of 113 ± 26 μm (± 23%, n = 14).

An example of a typical time-lapse photograph using 2x magnification is shown in Figure 6-6. The first feature of note was that the stationary droplets in vertically-oriented channels appear shorter and broader than those in horizontally-oriented channels. Droplets in vertically-oriented channels were ~150 μm shorter and ~30 μm wider than those in the horizontally-oriented channels. However, their volumes were determined to be highly similar (see Section 6.3.4). Droplets in the wider vertically-oriented channels were expected to widen and therefore shorten. Droplets would elongate in the narrower horizontally-oriented channels to maintain constant volumes. This change in length was dependent on the change in channel width and the change in channel depth. Therefore, to estimate the change in droplet length, the shape of droplets in laser-cut channels needed to be better understood.

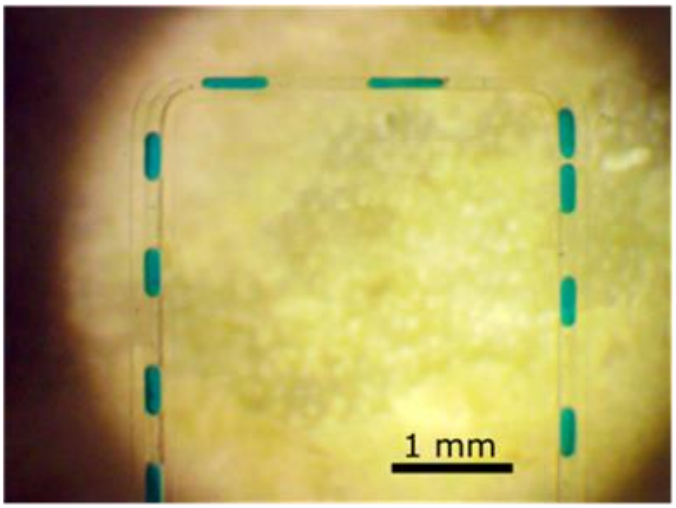

Figure 6-6 – An example of a typical stationary droplet time-lapse photograph using 2x magnification; all droplets were produced with the same setting and should have had constant volumes. The horizontally-oriented and vertically-oriented channels had different dimensions, leading to different droplet dimensions and shifts in droplet spacing in the near channel corners due to the difference in Laplace pressure at each of the droplet's fluid fronts.

The second feature of note in Figure 6-6 is that droplet spacing was offset in the upper right corner of the image. This change in droplet spacing was not observed when the droplets were moving before they became stationary.

Differences in droplet spacing were caused by changes in the position of droplets that became stationary in a bend of the channel. A droplet in a corner had one fluid front in a horizontally-oriented channel and the second in a vertically-oriented channel. Because these two channels had different width and depth dimensions, each of its two fluid fronts would be expected to have different Laplace pressures (as discussed in Section 2.4). Therefore, any droplets that became stationary in a bend in the main channel of the Droplet Generator moved into positions

that minimized this difference in Laplace pressure. This movement changed the droplet spacing, as is the case in Figure 6-6.

It was found that stationary droplets in a channel for 20 minutes maintained essentially constant lengths and widths over that period. Figure 6-7 shows the measured lengths of individual droplets generated by two different Droplet Generators. Droplet lengths were measured over 20 minutes from five sets of time-lapse photographs using the Microscope set at 2x magnification. Each point in Figure 6-7 represents the measured length of a single droplet and includes error bars equivalent to the estimated measurement error of ± 30 μm. Droplets measured in horizontally-oriented channels comprised the upper band in Figure 6-7, while droplets measured in vertically-oriented channels comprised the lower band. There was no significant change in droplet lengths and, therefore, droplet volume over the 20 minutes. This stability indicated that droplets could be held in a droplet trap for at least 20 minutes without significant loss in volume or integrity.

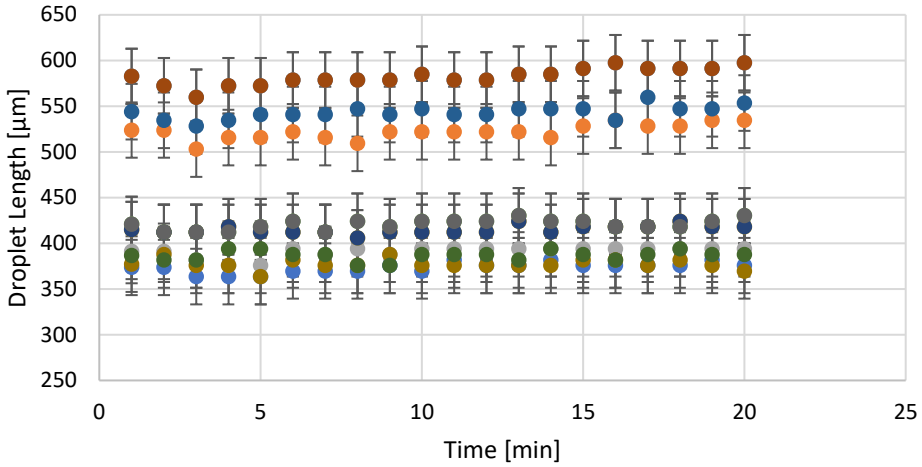

Figure 6-7 – Measured lengths of stationary droplets observed over 20 minutes from time-lapse photographs obtained with the Microscope at 2x magnification. Both droplets in horizontally-oriented and vertically-oriented channels were measured, resulting in 2 distinct bands of droplet lengths. Each point represents the measured length of a droplet and has error bars corresponding to the estimated measurement error (± 30 μm).

Similar results can be seen in droplet width measurements that were performed at the same time (see Figure 6-8). However, it should be noted that the widths of droplets measured in horizontally-oriented channels comprised the lower band of Figure 6-8. In contrast, the widths of droplets measured in vertically-oriented channels comprised the upper band. Again, no significant change in droplet width was observed over the 20 minutes.

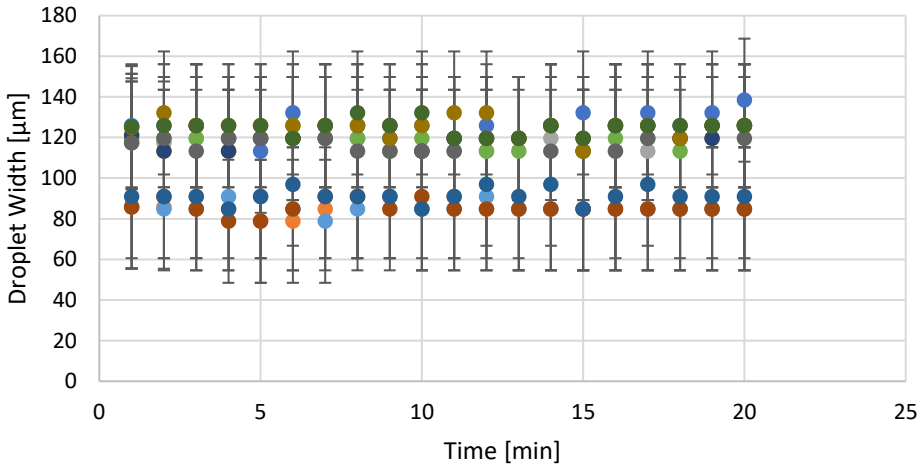

Figure 6-8 – Measured widths of stationary droplets observed over 20 minutes from time-lapse photographs obtained with the Microscope at 2x magnification. Both droplets in horizontally-oriented and vertically-oriented channels were measured, resulting in 2 distinct bands of droplet widths. Each point represents the measured width of a droplet and has error bars corresponding to the estimated measurement error (± 30 µm).

The stationary droplet time-lapse photographs were retaken using 4x magnification to reduce measurement error in droplet dimensions. Figure 6-9 and Figure 6-10 show the results of four different 20-minute photographic timelapse tests using one of the Droplet Generators used over two consecutive days. All droplets were measured in a vertically-oriented channel. Although droplet dimensions were slightly lower than those measured from the 2x magnification photographs, the same trends are present. This difference in length was attributed to the higher resolution at the higher magnification. Droplet dimensions did not change significantly over the 20 minutes.

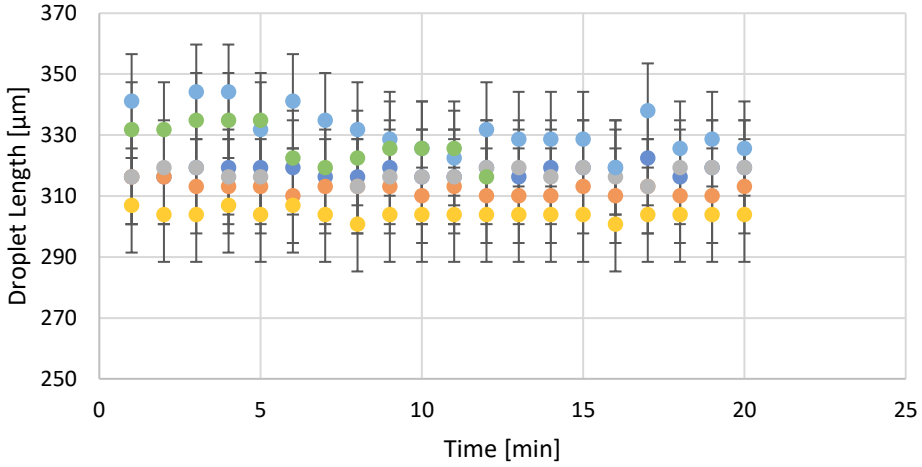

Figure 6-9 – Measured lengths of stationary droplets observed over 20 minutes from time-lapse photographs obtained with the Microscope at 4x magnification. Only droplets in vertically-oriented channels were measured. Each point represents the measured length of a droplet and has error bars corresponding to the estimated measurement error (± 15 µm).

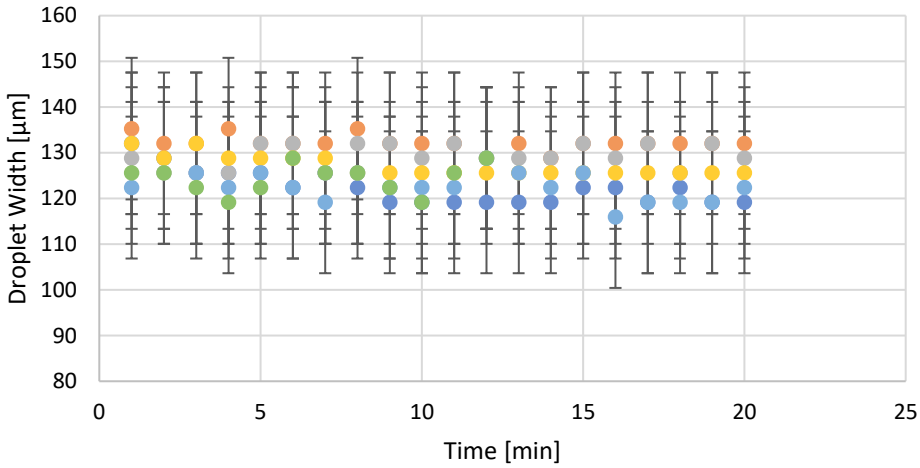

Figure 6-10 – Measured widths of stationary droplets observed over 20 minutes from time-lapse photographs obtained with the Microscope at 4x magnification. Only droplets in vertically-oriented channels were measured. Each point represents the measured width of a droplet and has error bars corresponding to the estimated measurement error (± 15 µm).

It was observed that after being stationary for 20 minutes, droplets that were then moved had deposited a residue on the area of the channel walls where they were held stationary. This phenomenon can be seen in Figure 6-3, where "droplet shadows" have been marked. Figure 6-3 was obtained by focusing on the location of two stationary droplets immediately after a 20-minute time-lapse. The Dispersed Phase and Continuous Phase input pressures were reapplied to the Droplet Generator to resume droplet motion in the main channel shortly before taking this photograph. The stationary droplets moved from their stationary positions and left a dark residue on the channel walls. This residue was present on both the sidewalls and the top wall of the channel. These positions are marked by the "droplet shadows" in Figure 6-3. A third droplet then moved through the channel and can be seen between the two "droplet shadows" in Figure 6-3. The "droplet shadows" were observed to disappear within five minutes of subsequent operation of the Droplet Generator.

The origin of these shadows is unknown but is likely due to channel wall contact or precipitates forming from the droplets. They were observed to begin forming 30 seconds after droplets became stationary and indicate that droplets make some form of contact with the channel walls when stationary.

A continuous phase sheath was measured between the channel's sidewalls and the stationary droplets as described above. Therefore, if the stationary droplets contacted any channel walls, the contact point would have to be the top channel wall as a continuous phase sheath was measured between the droplet and the side walls over 20 minutes. The shadow material would have migrated from the top channel surface to the side walls if the shadows were related to droplet wall contact.

Channels were illuminated from below while obtaining Figure 6-3, and the shadows only occurred at positions in the channel where droplets were known to be stationary. No reasonable explanation of this shadow effect due to the illumination of the channel or a quirk in the illumination system of the Microscope could be determined. This observation, combined with the known conditions

that make the shadows appear and disappear, clearly indicated that the shadows are caused by residue on the channel walls.

6.3.2.3 Determining the Droplet Shape and Volume in the Microfluidic Channels

The data presented in the preceding two sections provide the following findings: (1) measurements of the thickness of the Continuous Phase sheath between droplets and channel walls when stationary and moving, and (2) that there is no significant change in droplet shape when droplets are held stationary for extended periods. The first finding provides valuable information that enables the prediction of the cross-sectional droplet shape when droplets are both moving and stationary. The cross-sectional shape of a droplet in motion was of great interest because it allowed for the calculation of droplet volume based on top-down measurements of droplet length and the dimensions of the channel the droplet occupied. The ability to accurately calculate the volume of droplets allowed for the performance of the Droplet Generators to be compared between fabrication runs in which channel dimensions may have varied. It also allows the data obtained from the videos taken of droplet generation to be accurately compared to the behaviours predicted by the droplet generator model.

In previous work performed by the author, apparent droplet volume (V) was calculated by multiplying droplet length ($L_{droplet}$), as measured from above from tip to tip, by the cross-sectional area of the channel (A_{ch}), as this has been a commonly made assumption in literature (Equation (6-1)) [106], [108]. Furthermore, no mathematical model could be found to describe the volume of droplets confined by laser-cut channels. Therefore, droplets were assumed to fully fill the known channel cross-section over its entire length. This assumption is known to be an inaccurate method of calculating droplet volume, as droplets in microfluidic channels are known to have rounded caps due to surface tension effects. They also do not occupy the full cross-section of the channels due to a Continuous Phase sheath surrounding the droplets.

$$V = L_{droplet} A_{ch} \tag{6-1}$$

As described in Section 2.6.1, the work of Musterd *et al.* examined the physics of droplets confined within a range of different microfluidic channel geometries [106]. They developed equations to describe the expected shapes and volumes of droplets. Using their model, the volume of droplets (V) confined within microfluidic channels can be calculated using Equation (6-2). In Equation (6-2), L_{cap} is the length of the droplet caps, A_{bd} is the cross-sectional area of the droplet body, and $L_{droplet}$ is the length of the droplet measured from tip to tip from above. Both L_{cap} and A_{bd} can be calculated from measured channel dimensions. In these calculations, the thickness of the continuous phase sheath was considered as recommended by Musterd *et al.* as Capillary number indicated a non-negligibly thick sheath [106].

$$V = \frac{4}{3} L_{cap} A_{bd} + \left(L_{droplet} - 2L_{cap}\right) A_{bd} \tag{6-2}$$

The apparent volumes of droplets confined in microfluidic channels were compared to the volumes of the same droplets as spheres outside of the channels. This comparison was performed to determine the best method for calculating the volume of a droplet in a laser-cut microfluidic channel. The apparent volumes of droplets were calculated using Equation (6-1) and the method of Musterd *et al.* (Section 2.6.1) [106].

Droplets were produced using a Droplet Generator with no integrated droplet trap, following the procedure described in Section 4.4 using the pressure settings P_d = 8.06 kPa and P_c = 8.38 kPa. These settings correspond to a Capillary number of ~6 x 10^{-3} and an average droplet velocity of ~1.06 mm/s. The lengths of the produced droplets were measured in a horizontally-oriented channel with an average depth of 242 ± 6 μm, an average width of 127 ± 8 μm, channel top corner angle of 75° and bottom corner radius of 14 ± 2 μm. Droplets in channels with these dimensions could be modelled with one of the sets of equations developed by Musterd *et al.*, specifically, Equations (2-18) to (2-20) [106]. These equations were chosen following the recipe shown in described in the work of Musterd *et al.*, accounting for a continuous phase sheath thickness of 10.5 μm [106].

A continuous phase sheath thickness of 10.5 μm was used because it was proportional to the measured thickness of the continuous phase sheath surrounding droplets detailed above. The same conditions were used to make these droplets. Therefore, they were made with the same average Capillary number but in channels with a different width. The thickness of the continuous phase sheath has been reported to be proportional to channel width [106], [107]. As droplets were made with the same pressure settings in channels with similar dimensions, it was reasonable that the thickness of the continuous phase sheath in the channels was proportional to the previously measured thickness [106], [107].

The diameters of droplets as they entered the output well of the Droplet Generator device, which was not attached to an output syringe, were also measured from above. These droplets were unconstrained by a microfluidic channel and expected to be spherical. Droplet volumes (V) could then be calculated using Equation (6-3), where r is the measured droplet radius (half of the measured droplet diameter). As droplets in the output well may have contacted the bottom of the well, the possible effects of that contact were estimated. Based on the measured contact angle of a droplet of water on a PMMA surface submerged in Continuous Phase (see Section 3.5) and following the method of Sommers and Jacobi, contact with the bottom of the output well introduced a negligible change in volume of ~12.5% [137]. This change was smaller than the measurement error associated with the calculation and therefore was insignificant.

$$V = \frac{4}{3}\pi r^3 \tag{6-3}$$

The apparent volumes and measured volumes of droplets in the output well for the produced droplets can be seen in Table 6-3, alongside the droplet volumes produced at two other pressure settings studied in the same way.

In Table 6-3, $V_{droplet,fully\ filled}$ refers to apparent droplet volumes in channels calculated using Equation (6-1). $V_{droplet,Musterd}$ refers to apparent droplet volumes in channels calculated using Equation (6-2) and the accompanying method of Musterd *et al.* [106]. Finally, $V_{droplet,well}$ refers to the volumes of droplets measured in the output well of the Droplet Generator.

When the droplet volumes shown in Table 6-3 are compared, it is clear that the volumes calculated by assuming droplets fully filled the channels do not agree with the volumes of droplets in the output well. However, volumes calculated according to the method of Musterd *et al.* do agree with volumes of droplets in the output well [106].

It should be noted that uncertainty in the channel dimensions may affect the calculation of droplet volumes in channels. Based on the dimensions of the above-reported channel, in which droplets were observed, droplet volumes would vary by at most ± 0.3 nL, considering the largest possible channel dimension variations. This change was comparable to the measurement uncertainty of droplets in the channels ± 0.24 nL. Therefore, if channel dimensions did vary from their average values, the effect on the calculated droplet volumes would not be significant.

Since the model of Musterd *et al.* was determined to calculate the volume of droplets in the laser-cut channels accurately, droplet cross-sections were expected to occupy approximately half of the channel cross-section (Figure 6-11) [106]. The corners of the droplets were expected to have radii of 23 μm. The cross-sectional area of the droplet body was expected to be 8075 μm^2 which occupied approximately half of the cross-sectional area of the channels containing the droplets. Lastly, the droplet caps were expected to be 44.7 μm long.

Table 6-3 – The droplet volumes calculated with each of the different methods for each tested pressure settings: P_d = 7.83 kPa, P_d = 7.94 kPa and P_d = 8.06 kPa, all with P_c = 8.38 kPa. All values are reported ± their standard deviation or measurement error, whichever was larger. $V_{droplet,\ fully\ filled}$ and $V_{droplet,\ Musterd}$ values had a measurement error of ± 0.24 nL and $V_{droplet,\ well}$ values had a measurement error of ± 0.3 nL.

Pressure Setting [kPa]	$V_{droplet,fully\ filled}$ **[nL]**	$V_{droplet,Musterd}$ **[nL]**	$V_{droplet,well}$ **[nL]**
P_d = 7.83	4.28 ± 0.24 (n = 18)	1.72 ± 0.24 (n = 18)	1.66 ± 0.30 (n = 10)
P_d = 7.94	5.00 ± 0.24 (n = 42)	2.04 ± 0.24 (n = 42)	2.00 ± 0.32 (n = 10)
P_d = 8.06	6.04 ± 0.26 (n = 96)	2.52 ± 0.24 (n = 96)	2.62 ± 0.38 (n = 10)

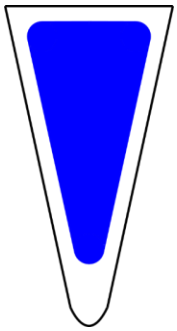

Figure 6-11 – A sketch of the expected droplet conformation in horizontally-oriented Standard Channels predicted by the cross-sectional droplet model of Musterd et al. [106].

Using the method of Musterd *et al.*, droplet volumes can be calculated accurately, and changes in droplet shape can be predicted [106]. These capabilities are important for applications where changes in droplet shape are vital – e.g., droplet trapping applications – and may also provide insight into droplet contact with channel walls over time. However, most importantly, accurately calculating droplet volumes allows for the observed behaviour of the Droplet Generators to be accurately compared to the behaviour predicted by the Droplet Generator model.

6.3.3 Droplet Generator Model Optimization

The droplet generator model described in Section 2.5 cannot be used to directly predict the volume of the produced droplets. However, it can predict the volumetric flow rate ratio of the dispersed phase to the total flow rate through the main channel (Q_d/Q_m) given a specific pressure setting. This predicted flow rate ratio is equivalent to the ratio of the droplet volume to the total fluid volume per droplet ($V_{droplet}/V_{total}$), herein defined as the "relative droplet volume".

As droplets are produced at a regular frequency, f, it would be expected that the volume of droplets could be calculated according to $V_{droplet} = f \times Q_d$. Similarly, the total fluid volume dispensed through the Droplet Generator during the time it takes to form a droplet can be calculated according to $V_{total} = f \times Q_m$. These relationships indicate that relative droplet volume is equivalent to the volumetric flow rate ratio of the dispersed phase to the total flow rate through the main channel, $V_{droplet}/V_{total} = Q_d/Q_m$.

As demonstrated in Section 6.3.2, the method of Musterd *et al.* can be used to accurately calculate the volume of droplets in microfluidic channels, which means that relative droplet volume can also be accurately calculated [106]. Therefore, the relative droplet volume predicted by the droplet generator model can be compared to the observed relative droplet volume with reasonable accuracy.

To compare the observed and predicted relative droplet volumes, droplets produced for the experiment described in the Determining the Droplet Shape and Volume in the Microfluidic Channels Section above were considered. The total volume of fluid per droplet (V_{total}) was calculated according to Equation (6-4), which included both the dispersed and continuous phases. In Equation (6-4), $L_{droplet}$ is the measured droplet length, $L_{spacing}$ is the measured droplet spacing distance, and A_{ch} is the cross-sectional area of the channel. The sum of $L_{droplet}$ and $L_{spacing}$ describes the total length of fluid pushed through the T-junction to form a droplet. The channels are expected

to be fully filled by droplets and surrounding continuous phase. Therefore, the sum of the lengths can be multiplied by the channel cross-sectional area to determine the total fluid volume per droplet. This calculation accounts for the volume of the continuous phase surrounding the droplets, the volume of the droplet and the volume of the continuous phase separating droplets.

$$V_{total} = \left(L_{droplet} + L_{spacing}\right)A_{ch} \quad (6\text{-}4)$$

The observed relative droplet volume was then calculated by dividing droplet volume, calculated according to Equation (6-2) (reported in Table 6-3), by the total fluid volume per droplet calculated using Equation (6-4). When the predicted and observed relative droplet volumes for the settings tested in Table 6-3 are compared, the droplet generator model predicts relative droplet volumes that are ~1.5 times larger than the observed relative droplet volumes (Table 6-4).

Table 6-4 - The predicted and observed relative droplet volumes tested pressure settings: P_d = 7.94 kPa and P_d = 8.06 kPa, all with P_c = 8.38 kPa. The relative droplet volume could not be calculated for the P_d = 7.83 kPa pressure setting because the droplet spacing was too large to be measured. The observed relative droplet volumes are reported with uncertainties considering the standard deviation in the measured droplet and spacing lengths.

Pressure Setting [kPa]	Predicted Relative Droplet Volume	Observed Relative Droplet Volume
P_d = 7.94	0.13	0.082 ± 0.016
P_d = 8.06	0.18	0.12 ± 0.018

The discrepancy in the predicted and observed relative droplet volumes could not be explained by any reasonable variation in channel dimensions, indicating that an underlying assumption of the droplet generator model being used was incorrect. The droplet generator model assumed that the presence of a droplet in a channel increases the resistance of that length of channel by a factor of four compared to the resistance of the same length of channel filled with only the Continuous Phase (see Section 4.3.2). This value is referred to as the "droplet resistance increase factor" (*DRIF*). The *DRIF* was determined by fitting the droplet generator model to a Droplet Generator used in previous work performed by the author with devices with different channel dimensions. This work was also performed assuming that droplets completely filled the main channel cross-section. As shown in Section 6.3.2, droplets were subsequently found not to fill the entire channel cross-section. Therefore, the *DRIF* determined in the author's previous work could not be correct.

If the droplet generator model was adapted to match the observed relative droplet volumes for the tested pressure settings shown in Table 6-4, a *DRIF* factor of 8.2 ± 1.7 would be required. This droplet resistance increase factor is outside of Glawdel and Ren's rule of thumb range of values between two and five [85]. However, it does not seem unreasonable given that their rule of thumb was proposed for rectangular channels, which are not used in this project. To determine whether this fitted value was reasonable, verification by a second method was necessary.

6.3.3.1 Theoretical Verification of Droplet Resistance Increase Factor

The increase in channel resistance due to the presence of a droplet in a channel can be measured using specialized channel structures or instrumentation [98], [99], [138]. These pieces of specialized equipment may not apply to all microfluidic devices and do not provide predictive value before working with the specialized device. Few methods for the theoretical predictions of the *DRIF* have been reported in the literature, except for some qualitative methods for specific channel geometries [99]. These efforts have been focused on determining pressure changes surrounding the droplets and their end caps [99], [108].

An important underlying assumption about the *DRIF* is that it inherently assumes that the flow of droplets through a channel can be described by laminar flow. This assumption is required to model the channel resistance following the linear relationship of Poiseuille's equation (Equation (2-1)) and is a standard assumption when determining droplet resistance [85], [97]–[99], [138]. While it is recognized that the presence of droplets does affect laminar flow in microfluidic channels, the *DRIF* is intended to describe the resistive effects and account for these non-laminar behaviours.

It was hypothesized that the model of Musterd *et al.*, which can be used to accurately predict the cross-sectional area of a droplet in a microfluidic channel, could be extended to approximate the droplet resistance increase factor for a channel with known dimensions [106].

The *DRIF* is simply the resistance ratio of a channel filled with a droplet surrounded by the continuous phase and the channel when filled only with the continuous phase. Section 2.2.2 established that channel resistance depends on fluid viscosity, the wetted channel perimeter, the channel cross-sectional area, and the length of the channel. Channel resistances were calculated using Equation (3-6) for this thesis. Therefore, the *DRIF* can be determined by taking the ratio of Equation (3-6) when considering a channel containing a droplet and when the channel does not contain a droplet. This calculation is the same as taking the ratio of the more generalized Equation (2-7). The resulting equation for the *DRIF* can be seen in Equation (6-5).

$$DRIF = \frac{R_{dropletin}}{R_{nodroplet}} = \frac{A_{ch}^3}{\left(A_{ch} - A_{bd,effective}\right)^3} \tag{6-5}$$

Equation (6-5) only depends upon the area of the channel (A_{ch}) and the effective cross-sectional area of the droplet ($A_{bd,effective}$). The effective cross-sectional area of the droplet would be the cross-sectional area if the droplet had a uniform cross-section along its entire length.

For droplets with known lengths in a channel with known dimensions, $A_{bd,effective}$ can be calculated using Equation (6-6). In Equation (6-6), L_{cap} is the length of the droplet cap, $L_{droplet}$ is the overall length of the droplet, and A_{bd} is the cross-sectional area of the droplet body.

$$A_{bd,effective} = \left(\frac{4}{3}\right)\left(\frac{L_{cap}}{L_{droplet}}\right)A_{bd} + \left(1 - \frac{2L_{cap}}{L_{droplet}}\right)A_{bd} \tag{6-6}$$

When a droplet is present in a channel of the Droplet Generator, testing found that it occupied roughly half of the channel's cross-sectional area (see Section 6.3.2). Therefore, the presence of a droplet reduces the cross-sectional area that should be considered when calculating channel resistance using Equation (3-6).

The viscosity of interest when considering the flow of droplets through a channel is that of the continuous phase. The droplets are carried in the flow of the continuous phase. They do not directly affect the flow of the continuous phase when the ratio of the dispersed phase and continuous phase viscosity is low [108]. Therefore, when calculating the *DRIF*, the only viscosity involved is the continuous phase viscosity. This viscosity does not change when a droplet is present. Therefore, viscosity does not contribute to Equation (6-5).

Similarly, the channel length considered to be filled with a droplet or not filled with a droplet is the same. Therefore, the channel length does not contribute to the *DRIF* or Equation (6-5).

The wetted perimeter of the channel is not affected by the presence of a droplet in the channel. This parameter is involved in calculating channel resistance due to a no-slip boundary condition applied at the channel walls when solving the Navier-Stokes equation. This condition means that the velocity of fluid flowing through the channel is zero at the channel walls. Such a condition does not appear to exist at the droplet interface, and therefore, the wetted perimeter remains unchanged when a droplet is present in the channel. It is known that droplets and their surrounding continuous phase move at different speeds, flow fields within droplets are not coupled to those outside of droplets, and surfactant molecules can be redistributed by these flow fields at the droplet interface [108], [138]. As droplets and the surrounding continuous phase show a net movement in the same direction, it doesn't make sense for the fluid velocity at the droplet interface to be equal to zero.

Additionally, surfactant molecules redistribute themselves at the droplet interface according to flow fields within the droplet. This movement further indicates motion at the droplet interface and that the fluid velocity is not equal to zero [108]. Therefore, the presence of a droplet is not expected to change the wetted perimeter of a channel used in Equation (3-6).

The information presented above supports the hypothesis that *DRIF* is based solely on a droplet changing the cross-sectional area of the channel (Equation (6-5)). However, it should be noted that because of the assumption that the entire fluid flow can be modelled as a laminar flow, Equation (6-5) can only calculate an approximate value of the *DRIF*. Additionally, Labrot *et al.* found that the DRIF depends on droplet spacing and velocity [138]. These are not accounted for in Equation (6-5), further indicating that Equation (6-5) should only be used as an approximation.

The Droplet Generators used in this project had only droplets in their main channels, composed of both horizontally-oriented and vertically-oriented channels. Due to the variation in channel dimensions between horizontally-oriented and vertically-oriented channels (Section 6.3.1), the average *DRIF* needed to be determined. This required consideration of the differences in *DRIF* resulting from differences in the dimensions of horizontally-oriented and vertically-oriented segments of the main channels. The average *DRIF* was determined by taking the weighted average

of the *DRIF* in the horizontally-oriented and vertically-oriented segments of the channels based on their volumetric contributions to the total volume of the entire main channel.

These volumetric contributions need to be considered as droplets had different cross-sectional areas and lengths in each channel orientation. Vertically-oriented channel segments that contained shorter droplets contributed a slightly higher overall increase in channel resistance when filled with droplets because they can hold more droplets. This consideration represented a relatively minor correction.

To determine the droplet resistance increase factor for the Droplet Generator used to generate the droplets described in Table 6-3, droplets produced using the P_d = 8.06 kPa and P_c = 8.38 kPa pressure setting were considered. The dimensions of the channel's segments, both horizontally-oriented and vertically-oriented, dimensions of the droplets contained in each segment and expected *DRIF* in each channel orientation can be seen in Table 6-5. The cross-sectional areas of the channel segments were calculated using Equation (3-5). The cross-sectional droplet areas and cap lengths were calculated using Equation (2-19) and Equation (2-20). The expected *DRIF*s for the horizontally-oriented and vertically-oriented segments of the main channel were calculated according to Equation (6-5).

By calculating the weighted average of the droplet resistance increase factors for the horizontally-oriented and vertically-oriented segments of the main channel of the Droplet Generator, an average *DRIF* of 7.57 was calculated. This calculated value was lower than the 8.2 ± 1.7 predicted by simply fitting the droplet generator model to the observed relative droplet volumes in Table 6-4. However, the calculated value was within the uncertainty of the fitted value. The difference between these two values represents an almost negligible difference in the context of the droplet generator model. If the theoretically predicted value of 7.57 was assumed to be correct, then to produce droplets at the relative droplet volume observed for the P_d = 8.06 kPa and P_c = 8.38 kPa condition in Table 6-4, the actual pressure settings would be P_d = 8.04 kPa and P_c = 8.38 kPa. This difference in the dispersed phase input pressure could be explained by the uncertainty in the estimated Laplace pressure, the uncertainty in the channel dimensions used in the droplet generator model or some combination of those factors. The difference in P_d values represents a 2.6 mm difference in the height of the Dispersed Phase Input Syringe. This difference is slight compared to the total height of that Input Syringe (82.5 cm) and large compared to the estimated measurement error in the syringe height (± 2 mm).

The difference in the predicted *DRIF* and the *DRIF* determined by fitting the droplet generator model to the observed relative droplet volumes was functionally negligible. Therefore, either value would be appropriate to use in the droplet generator model. However, the fitted value is more representative due to the approximate nature of Equation (6-5).

After this discrepancy in droplet resistance increase factor was understood, a value of 8.2 was used as the droplet resistance increase factor in the droplet generator model. This change to the droplet generator model brought the predicted relative droplet volumes in line with those observed. Therefore, the droplet generator model was appropriate and could accurately describe the behaviour of the Droplet Generators.

The method described herein for predicting the *DRIF* represents a valuable extension of the work of Musterd *et al.* [106]. It provides a predictive value of the *DRIF* without the need for specialized testing equipment. This method could be refined further by testing in a simpler channel layout and likely could be improved by considering pressure effects found locally around droplets. To the best of the author's knowledge, a method of approximating the *DRIF* based on a droplet's cross-sectional area and a channel's cross-sectional area such as that described above has not been reported in the literature.

Table 6-5 – The channel dimensions, droplet dimensions, and calculated droplet resistance increase factor for the Droplet Generator device used to produce the droplets whose volumes are detailed in Table 6-3. The length of the droplets in vertically-oriented channels was not directly measured but calculated, assuming the volumes maintained a constant volume. Values are reported ± one standard deviation where applicable.

Parameter	Horizontally-Oriented Channels	Vertically-Oriented Channels
Channel Dimensions		
Depth (H) [μm]	242 ± 6	221 ± 17
Width (W) [μm]	127 ± 8	147 ± 9
Top Corner Angle (β) [°]	75	75
Bottom Corner Radius (r_c) [μm]	14 ± 2	14 ± 2
Cross-sectional Area (A_{ch}) [μm^2]	17978	18333
Percent Volume of Main Channel [%]	0.31	0.69
Droplet Dimensions		
Length ($L_{droplet}$) [μm]	342 ± 15 (n = 96)	268 ± 11*
Cap Length (L_{cap}) [μm]	44.7	51.8
Cross-sectional Area (A_{bd}) [μm^2]	8088	10837
Effective Cross-sectional Area ($A_{bd,effective}$) [μm^2]	7383	9441
Droplet Resistance Increase Factor	4.89	8.77

6.3.4 Droplet Generation Reproducibility

The results discussed in Sections 6.3.2 and 6.3.3 describe the methods required to accurately describe droplet shape in microfluidic channels, calculate the volume of produced droplets and validate specific aspects of the droplet generator model. However, they do not directly describe the reproducibility of the Droplet Generator behaviour and whether it met the required criteria. Specifically, whether the Droplet Generator could reliably create droplets that were twice as long as they were wide with volumes that varied by no more than 10%. As discussed in this section, these criteria were met, and the Droplet Generators were successful.

The performance of the Droplet Generators will be discussed in reference to the Droplet Generator with no integrated droplet trap and the Droplet Generator with an integrated droplet trap. The

droplet trap designs were made to affect the performance of the Droplet Generator minimally. Therefore, the performance of Droplet Generators with integrated droplet traps is discussed here. For clarity, the results of the Droplet Generators with and without integrated droplet traps will be discussed separately.

6.3.4.1 Droplet Generator with No Integrated Droplet Trap

Due to fabrication issues (e.g., well tapping issues) and losses due to early operating protocol development, few Droplet Generators with no integrated droplet traps were tested. Only one such Droplet Generator was tested using the operating protocol described in Section 4.4. Two other devices were tested with earlier operating protocols that affected their performance, so their test results will not be discussed here. The test results from the single Droplet Generator tested are summarized in Table 6-3 and will be discussed in more detail here.

The device was tested at three pressure settings: P_d = 7.83 kPa, P_d = 7.94 kPa and P_d = 8.06 kPa, in each case with P_c = 8.38 kPa. The conditions were tested consecutively on a single day once, twice, and four times, respectively. Each pressure setting that was tested multiple times was tested consecutively. Droplet volumes for each test can be seen in Figure 6-12, where each data point represents the average of, at a minimum, 18 droplet volumes measured over five minutes of production. Each pressure setting produced droplets that had volumes within 5% of one another regardless of when they were produced during the five minutes.

Droplet volumes increased linearly as the dispersed phase input pressure was increased. This behaviour was not unexpected, as Glawdel and Ren suggested in their model that droplet volumes would change linearly with changes in the input pressures of a T-junction droplet generator [85].

These results demonstrate that a Droplet Generator with no integrated droplet trap reliably produced droplets with volumes varying by less than 5% at various dispersed phase input pressures. Droplets produced at P_d = 8.06 kPa and P_c = 8.38 kPa had an average length of 342 ± 15 μm and were ~106 μm wide in the first horizontally-oriented segment of the main channel (see Table 6-5). This result established that the Droplet Generator could create droplets at least twice as long as they were wide using those input pressure settings. An example of this droplet generating performance can be seen in Appendix D, which provides a representative recording of five minutes of droplet production at the settings specified above.

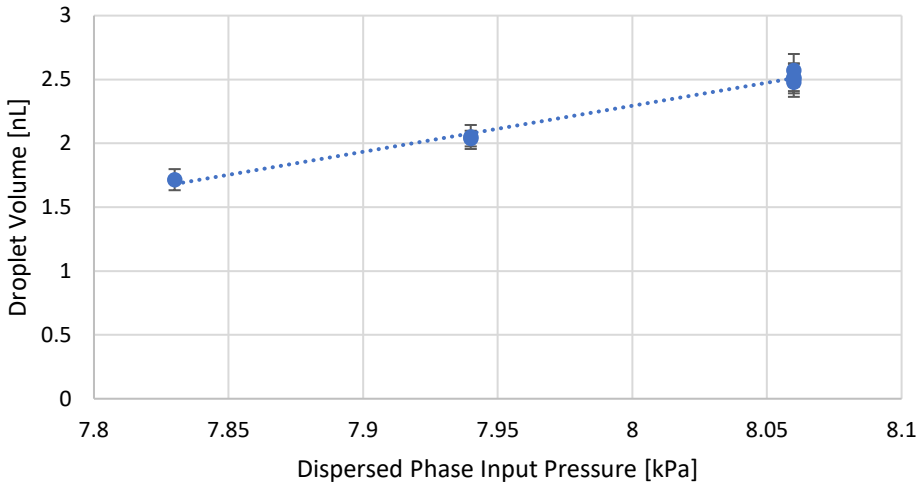

Figure 6-12 – Average droplet volumes produced by a Droplet Generator with no integrated droplet trap at three different dispersed phase pressure settings (P_d = 7.83 kPa, P_d = 7.94 kPa and P_d = 8.06 kPa). Continuous phase input pressure was a constant P_c = 8.38 kPa for all tested settings. Each data point represents the average of at minimum 18 droplets measured over five minutes and is marked with errors bars corresponding to ± one standard deviation.

An interesting nuance of the Droplet Generator's behaviour can be seen if droplet volumes and droplet spacings are examined over time. Figure 6-13 shows droplet volumes produced over five minutes using pressure settings of P_d = 8.06 kPa and P_c = 8.38 kPa. In Figure 6-13, each data point represents the average of six droplet volumes.

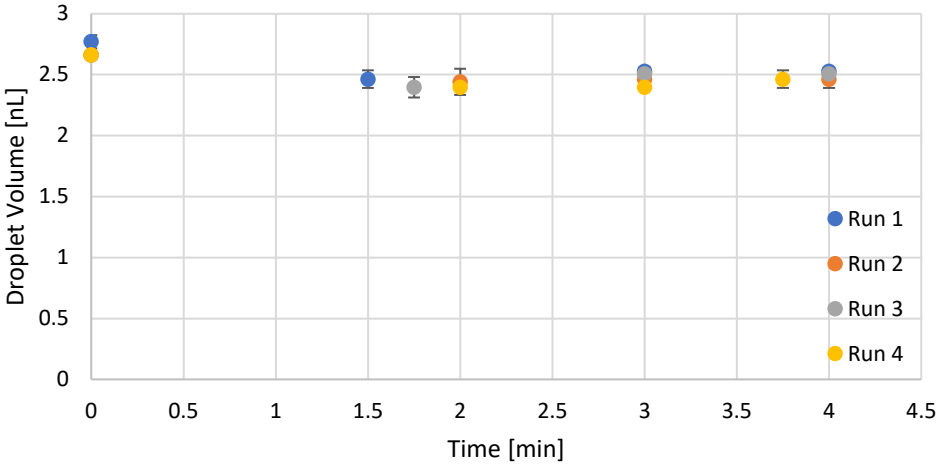

Figure 6-13 – Average droplet volumes at each measurement time for droplets produced by a Droplet Generator with no integrated droplet trap using pressure settings of P_d = 8.06 kPa and P_c = 8.38 kPa. Each data point represents the average of six measured droplet volumes and has error bars corresponding to ±1 standard deviation.

Droplet volumes at the start of the droplet production period are higher than those at any other measurement time. However, the first six droplets only have a volume that is on average 9% larger than the droplets produced later once the Droplet Generator has reached steady-state. Therefore, this difference in droplet volume was not expected to affect the suitability of the produced droplets for trapping applications.

The difference between the initial and steady-state behaviour of the Droplet Generator can be seen more dramatically by examining differences in average spacing distances between droplets. The initial spacing of droplets was much lower than droplet spacing at later observation times (see Figure 6-14).

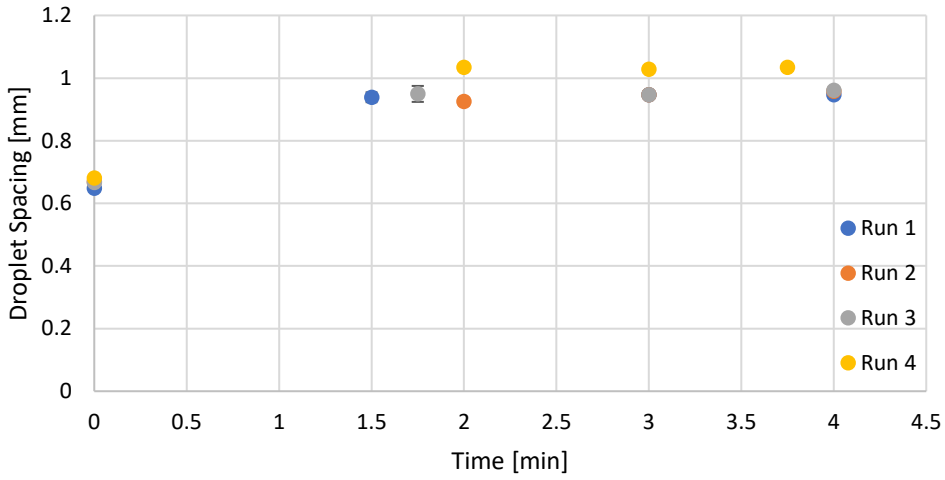

Figure 6-14 - Average droplet spacings at each measurement time for droplet produced by a Droplet Generator with no integrated droplet trap using pressure settings of P_d = 8.06 kPa and P_c = 8.38 kPa. Each data point represents the average of six measured droplet spacings and has error bars corresponding to ±1 standard deviation.

These behaviours were expected. At the start of droplet production, the main channel of the Droplet Generator would not contain any droplets and therefore would not be at its higher steady-state resistance when filled with droplets. Dispersed phase and continuous phase input flow rates would be expected to be different from their steady-state values. Differences in droplet volumes and spacing lengths would therefore be expected. Changes in droplet spacing and volume may impact the behaviour of a droplet trap integrated into a Droplet Generator as the time between droplets entering the droplet trap may or the droplet positions in the trap may vary. However, this behaviour was not expected to significantly impact the behaviour of droplet traps integrated into the Droplet Generator because the differences in volume and spacing were relatively small.

6.3.4.2 Droplet Generator with Integrated Droplet Trap

Droplet Generators with integrated droplet traps were expected to perform similarly to the Droplet Generator without an integrated droplet trap. Droplet Generators with integrated droplet traps were expected to produce droplets with slightly lower volumes, as the integration of a droplet trap was expected to increase the main channel resistance. While the droplet traps were designed to minimize changes in the performance of the Droplet Generator, the exact effect the droplet traps had on the Droplet Generator performance was difficult to quantify. The droplet trap designs significantly extended the residence time of droplets in the main channel and droplet trap. Due to their complexity, the main channel resistance and these residence times were difficult to model, especially how these resistances affected the Droplet Generator itself.

Figure 6-15 shows average droplet volumes of droplets produced using four Droplet Generators with the same integrated droplet trap at pressure settings of P_d = 7.83 kPa, P_d = 7.94 kPa and

P_d = 8.06 kPa in all cases with P_c = 8.38 kPa. All four devices were fabricated in the same fabrication run. Testing was performed on different days with multiple test runs at each P_d setting. At a minimum, each P_d setting had one test run and up to four test runs. Except for Chip UBBOP1.2, all other tested chips showed reproducible droplet production behaviour and produced droplets with volumes that varied by less than 10% at all P_d settings.

The abnormal behaviour of Chip UBBOP1.2 on its first day of testing (Day 1) was attributed to pieces of debris in channels of the device, which impacted channel resistance and, therefore, droplet volumes. On the second day of testing Chip UBBOP1.2 (Day 2), the debris was maneuvered into a dead-end channel of the droplet trap. In this area, it was not expected to impact the channel resistances significantly. Consequently, the device behaved much more similar to the other tested devices (see Figure 6-15).

As with the Droplet Generator with no integrated droplet trap, at the pressure settings of P_d = 8.06 kPa and P_c = 8.38 kPa, droplets were produced with average lengths of 313 ± 28 µm and average widths of approximately 97 µm. These dimensions were deemed suitable for droplet trapping applications, as their lengths were more than twice their widths.

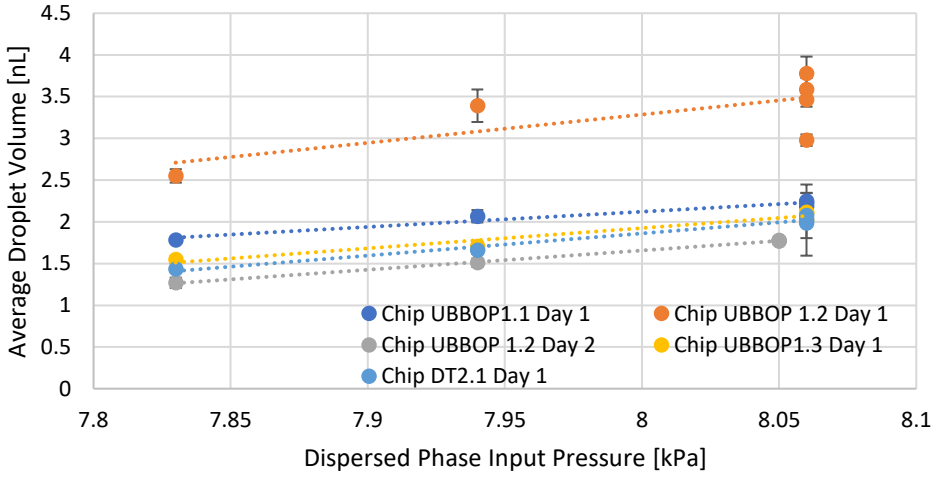

Figure 6-15 – Average droplet volumes produced by four Droplet Generators with the same integrated droplet trap at three different dispersed phase input pressure settings. Continuous phase input pressure was constant at P_c = 8.38 kPa in all cases. Each data point represents the average of a minimum of 36 droplets measured over five minutes and is marked with errors bars corresponding to ±1 standard deviation. Each data series is labelled with its internal chip ID and test date.

Changes in droplet volumes and droplet spacings over time were examined in more detail using the Droplet Generators with integrated droplet traps. Figure 6-16 shows changes in droplet volumes over time for droplets produced with Chip UBBOP1.2 using pressure settings of P_d = 8.06 kPa and P_c = 8.38 kPa. Data was gathered by measuring the length and spacing of three consecutively produced droplets every 15 seconds over a period of five minutes of continuous production, except for Run 1, where measurements were only made at t = 0 minutes, t = 3 minutes and t = 5 minutes. Droplet volumes are only slightly larger by insignificant amounts at the start of droplet production, considering a measurement error of ±0.24 nL; otherwise, droplet volumes were constant.

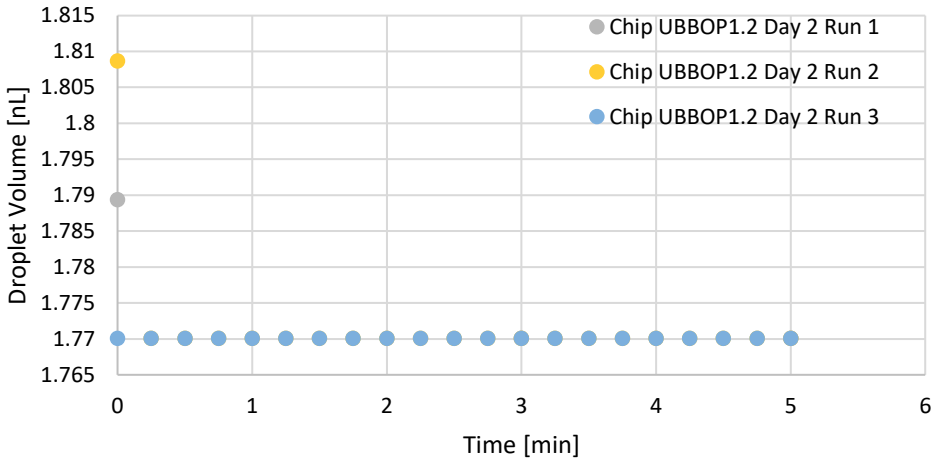

Figure 6-16 – Average droplet volumes measured every 15 seconds for droplets produced by Chip UBBOP1.2 using pressure settings of P_d = 8.06 kPa and P_c = 8.38 kPa. Each data point represents the average volume of three consecutively produced droplets. Every droplet in every group was measured to have the same volume, and therefore no standard deviation could be determined. It should be noted that the measurements have an associated measurement error of ±0.24 nL (that is not shown).

While droplet volumes did not change significantly over time, droplet spacings changed dramatically (see Figure 6-17). Droplet spacings took a significant period (~1-2 minutes) to reach a steady-state but still showed slight oscillations in droplet spacing. The time required to reach a steady-state was approximately the same as the time required to fully fill the main channel with droplets. Droplets were observed to arrive at the droplet trap, positioned near the end of the main channel, after 45 seconds to 1 minute of production. The main channel was observed to be fully filled with droplets after ~1.5 minutes of continuous droplet production. Therefore, the most reasonable cause of the variation in droplet spacing over time was that the main channel did not reach its steady state resistance value until it was filled entirely with droplets.

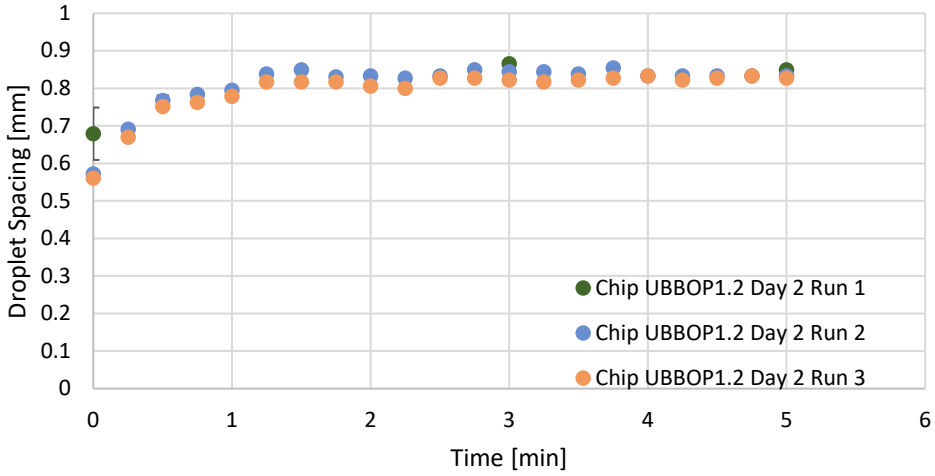

Figure 6-17 – Average droplet spacings measured every 15 seconds of droplets produced by Chip UBBOP1.2 using pressure settings of P_d = 8.06 kPa and P_c = 8.38 kPa. Each data point represents the average volume of three consecutively produced droplets. Each data point is marked with error bars corresponding to ±1 standard deviation, but these values are small. Measurements have an associated measurement error of ±16 μm that is not shown on the graph.

The design of the Droplet Generator was explicitly focused on reducing variability in the dispersed phase flow rate. Therefore, droplet spacing was expected to vary until the main channel attained its steady-state channel resistance. That this was observed indicated that the design of the Droplet Generator was effective, as droplet volumes were consistent over the entire periods of observed droplet production.

The results shown in this Section 6.3.4 demonstrate that the designed Droplet Generator could produce droplets with consistent volumes (< 10% variation) and lengths twice as long as the droplets were wide and suitable for droplet trapping applications. The droplet volumes were consistently within 10% over the entire production period, including before the Droplet Generator reached steady-state.

The designed Droplet Generator devices met the critical success criteria of producing droplets that were twice as long as they were wide and varied in volume by no more than 10%. There was a warm-up period for the Droplet Generators to reach steady-state droplet production; however, this did not significantly affect their performance. They could also operate effectively at various pressures, and the integration of a droplet trap into the main channel of the device did not impact their performance. Therefore, the Droplet Generator devices were suitable for droplet trapping applications which will be discussed in the following chapters.

6.4 Summary

A Droplet Generator device was successfully designed according to the theoretical model described in Section 2.5 and the refinements to that model and various design considerations described in Chapter 4. First, the numerical design of the Droplet Generators was described, and then the test results of their performance were detailed. Several additional refinements were made to the T-junction droplet generator model as a better understanding of the droplet shape and resistance in microfluidic channels was gained. It was found that the Droplet Generators could easily produce droplets that were twice as long as they were wide and varied in volume by no more than 10%. The Droplet Generators were therefore capable of producing reliable streams of droplets suitable for droplet trapping applications. Therefore, droplet traps were designed and integrated into the Droplet Generators, as discussed in Chapter 7.

Chapter 7
Droplet Traps: Design and Testing

7.1 Introduction

As discussed in Chapter 6, testing of the Droplet Generators established that they could reliably produce droplets that were (1) appropriately sized for being held stationary in a droplet trap and (2) were consistent in volume. These droplets were twice as long as they were wide and varied in volume by no more than 10%. Consequently, the Droplet Generators were considered suitable for use in droplet trapping applications, and therefore the design of droplet traps was undertaken.

The design of the droplet traps was an iterative process, with three iterations of trap designs being fabricated and tested. Unsuccessful traps failed principally due to unforeseen fabrication or design issues, which were addressed in subsequent designs. The droplet trap designs can be categorized broadly into two types: the "Primary Droplet Trap" design, which was fabricated more frequently, and the "Alternate Droplet Trap" design. The design of the Primary Droplet Trap followed the method described in Section 5.3.1, while the design method for the Alternate Droplet Trap followed the method discussed in Section 5.4.1. The three iterations for the Primary Droplet Trap will be discussed here. However, only the numerical design of the third iteration will be discussed in detail to provide an example of the design process. The first iteration of the Alternate Droplet Trap will also be discussed as well as its numerical design.

7.2 Primary Droplet Trap – Iteration 1

7.2.1 Design

The first design iteration of the Primary Droplet Trap used the channel layout shown in Figure 7-1, which follows the design method described in Section 5.3.1. In Figure 7-1, green lines represent unconstricted input/output channels, blue lines represent bypass channels, and cyan lines represent trapping channels.

It should be noted that many channels terminate in dead-ends. These dead-end channels were required because the last millimetre of a laser-cut channel was more variable in its dimensions. Therefore, an extra millimetre of length was added to every channel in the droplet trap to ensure that dimensions were stable in crucial locations, like the intended trapping positions.

While this trap follows the method described in Section 5.3.1, it has a very different layout than that shown in Figure 5-1. However, its behaviour is still governed by the equivalent circuits shown in Figure 5-2 and Figure 5-3. This was the first droplet trap made following this style and was designed such that the fluid always had a net flow in one direction on the device (i.e., the fluid flowed into and out of the trap in the same direction). As the trapping channels and input and output channels required an extra millimetre of length on each channel, the bypass channels needed to flow around these dead-end channels. This led to the development of the channel layout shown in Figure 7-1.

To reduce the length of the bypass channels in future iterations of the Primary Droplet Trap, the input and output channels of the trap were oriented such that the fluid flowed in opposite directions. This led to the channel layout shown in Figure 5-1 and allowed for shorter bypass channels to be used. Shorter bypass channels allowed for channels with higher resistivities and trapping pressures to be used. This change was not implemented until the second iteration of the Primary Droplet Trap design.

As explained in Section 5.3.1, the Primary Droplet Trap functions by always directing droplets towards the trapping channels at each channel junction. This sorting is accomplished by ensuring that the flow rate towards the trapping channels is always the strongest flow rate at any given channel junction. Once the trap has been filled, subsequent droplets then flow around the trapped droplets through bypass channels. This process is explained visually in Figure 7-2, as applied to the droplet trap channel layout shown in Figure 7-1.

The droplet trap is designed such that when empty, the resistance of the trapping channels and unconstricted input/output channels ($R_T = R_{Tu} + R_{Tc}$) is less than each resistance that makes up R_B/N (i.e., R_B). Therefore, fluid will flow primarily through the trapping channel(s) (Figure 7-2A). The first droplet that encounters the droplet trap will enter the unconstricted input channel, following the flow path with the least resistance and travelling to the input side of the trapping channels. Once the droplet reaches the input side of the furthest trapping channel, it will block that trapping channel (Figure 7-2B). The first droplet will not stop at the first trapping channel that it encounters because there is no barrier to moving further towards the next trapping channel (i.e., towards Position A in Figure 7-1). With one trapping channel blocked by a droplet, the resistance of the trap (R_T) increases but is designed to be still less than each bypass resistance (R_B). Therefore, the next droplet to approach the droplet trap will also enter the unconstricted input channel, follow the flow path of least resistance, and travel to the input side of the trapping channels. This droplet will flow through the trap until it reaches the open trapping channel, at which point the droplet will block that trapping channel (Figure 7-2C). With both trapping channels blocked by droplets, the resistance of the trap, R_T, will be drastically increased, and no fluid will flow through the trapping channels. Subsequent droplets and continuous phase will flow through bypass channels rather than through the unconstricted input channel towards the trapping channels (Figure 7-2D).

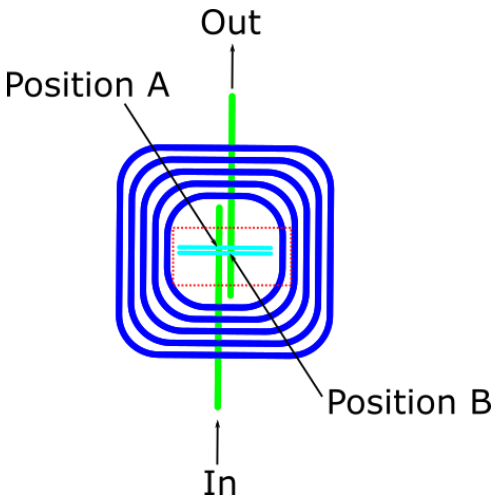

Figure 7-1 – The channel layout for the first design iteration of the Primary Droplet Trap. Green lines represent the input/output channels, blue lines represent bypass channels, and cyan lines represent trapping channels. The red dashed rectangle represents a standard framing of the Microscope when observing the droplet trap behaviour.

The dimensions of the channels involved in this design can be seen in Table 7-1, labelled with their corresponding resistivities. These dimensions resulted in trapping pressure of ΔP_{Trap} = 128 Pa and ΔP_{Vent} = 8 Pa. The channel dimensions were chosen because they could be readily estimated and achieved with the laser settings tested at the time of design. Trapping pressures were calculated assuming as an approximation that droplets would fully fill the channel cross-section. The work of Section 6.3.2 had not been performed at the time of this design.

The droplet trap was designed to trap droplets when the Droplet Generator was operated at P_d = 8.06 kPa and P_c = 8.38 kPa or any set of lower pressures. Due to unforeseen design and fabrication challenges, as discussed in Section 7.2.2, this iteration of the Primary Droplet Trap was not successful. It could not trap two droplets and hold them in contact for at least 1.5 minutes and needed to be redesigned as the second iteration of the Primary Droplet Trap.

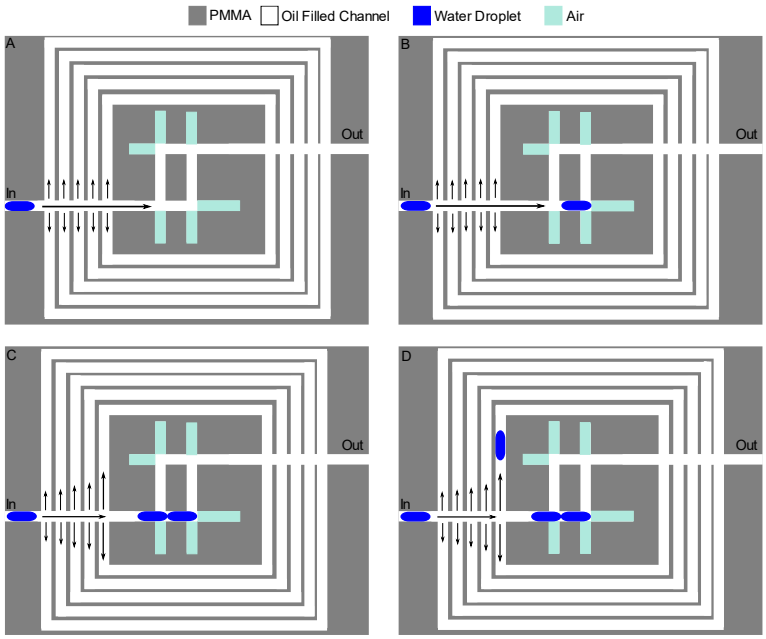

Figure 7-2 – The droplet trapping process of the first iteration of the Primary Droplet Trap design, arrows denote the fluid flow direction and relative magnitude based on their lengths. All dead-end channels are considered to be filled with air. A – A droplet approaches the droplet trap from the main channel. B – One droplet enters the trapping channel and flows until it blocks the furthest venting channel. C – With one droplet in the trapping channel, the value of R_T is still lower than the value of R_{bypass}, so a second droplet enters the trapping channel and flows until it blocks the venting channel closest to the trap entrance. D – The trapping channel contains two droplets in contact (i.e., a DIB) blocking the venting channels. R_T is large compared to R_{bypass}, so subsequent droplets flow through a bypass channel. This sketch is not drawn to scale.

Table 7-1 – A summary of all the relevant channel parameters for the channel types used in the first iteration of the Primary Droplet Trap, including the laser settings and bonded channel dimensions. Additional laser parameters common to all channel types were that the cuts were performed at 1000 Hz and focused on the material surface (z=0).

Channel Type	r_{Tc}	r_{Tu}	r_B
Laser Line Colour	Cyan	Green	Blue
Number of Passes	1 Pass	2 Pass	2 Pass
Laser Power [%]	3.5	3.5	3.1
Laser Speed [%]	0.5	0.5	0.5
Bonded Channel Depth [µm]	78 ± 1.6	215 ± 4.26	192 ± 3.84
Bonded Channel Width [µm]	161 ± 2.88	161 ± 2.88	161 ± 2.88

7.2.2 Test Results

The first iteration of the Primary Droplet Trap design (Figure 7-1) was tested and was not successful in that it was unable to trap two droplets to form a DIB. This inability to trap droplets was mainly attributed to the spacing of the trapping channels, which were only 140 µm apart. This spacing resulted in ill-defined channel dimensions due to overlapping channel profiles, as shown in Figure 7-3. Trapping channels were intended to have bonded widths of 120 µm. Therefore, it was thought that a spacing of 140 µm would be sufficient to prevent channel overlap. In preliminary testing with similar channel structures, it was found that a spacing of 140 µm resulted in minor overlap but still had a well-defined divider between the two channels. This divider was found to become sealed due to channel roof sag during the thermal bonding process. On reflection after fabrication, it was hypothesized that because the trapping channels were laser-cut

immediately after each other, the PMMA was still hot when cutting the second channel. This excess heat was thought to cause unpredictable deformation of the thin barrier between the two parallel channels, which did not occur during preliminary testing.

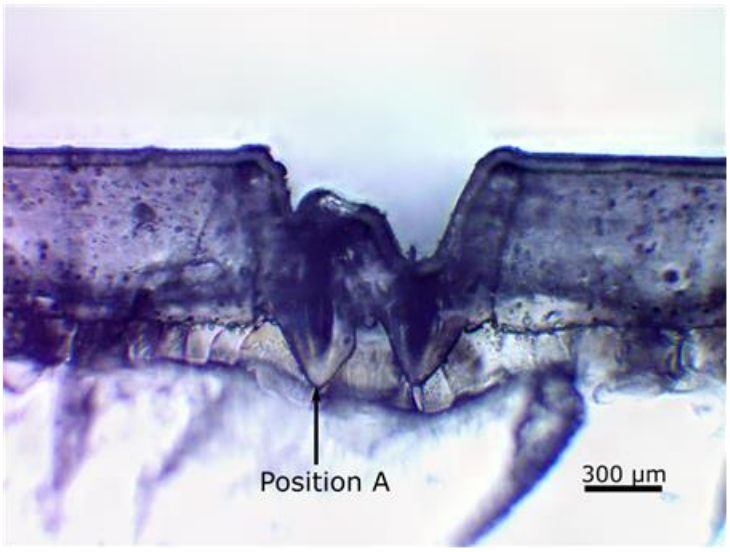

Figure 7-3 – Cross-section of the unbonded droplet trap geometry. The input main channel travels from left to right in the frame, and the trapping channels proceed into the frame. An observed trapping location (Position A) is marked for reference.

This unintended change in trapping channel dimensions prevented the droplet trap from operating effectively. However, a droplet could occasionally be trapped at Position A of the droplet trap (see Figure 7-4). A droplet could, on rare occasions, also be trapped at Position B of the droplet trap (see Figure 7-4) if it had a sufficiently small volume. Droplets trapped at Position B occupied the depression at the bottom of the channel formed by the intersection of the trapping channel and output channel. The final feature of note in Figure 7-4 is the bypass channel on the right of Figure 7-4(A) which can be seen to be filled with many small droplets. As droplets passed the bypass channels, these smaller droplets were split from the droplets approaching the droplet trap. This splitting was unforeseen and initially attributed to the small pressure barrier of the bypass channels (ΔP_{Vent} = 8 Pa). Future design iterations sought to increase this pressure barrier to address splitting. Droplet splitting at bypass channel junctions will be discussed in detail in Section 7.6.

The first design iteration of the Primary Droplet Trap was not successful due to a miscalculation of the minimum distance between trapping channels required to prevent channel overlap in the fabrication process. This miscalculation resulted in ill-defined dimensions of the trapping channels. What little "trapping" behaviour was observed was not reproducible, and therefore, the droplet trap did not perform with any degree of success. Future design iterations sought methods of improving the definition of the trapping channel dimensions and increasing the pressure barrier to bypass channels.

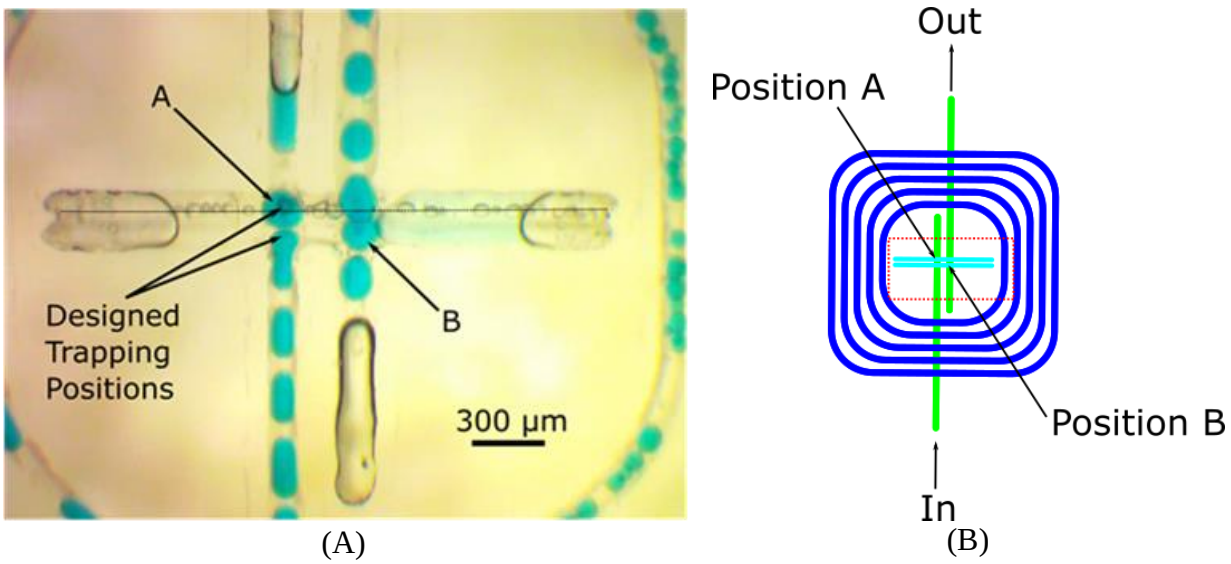

Figure 7-4 – (A) A photograph of a droplet trap holding two droplets in Position A and Position B (underneath the moving droplets). These are the locations where droplets were trapped most commonly with this design iteration. The designed trapping positions are also indicated. The dashed line denotes the barrier between the two trapping channels, which is biased towards the top of the frame. (B) The location of Figure 7-4(A) with respect to the droplet trap design is denoted by the dashed red rectangle.

7.3 Primary Droplet Trap Iteration 2

7.3.1 Design

The second design iteration of the Primary Droplet Trap used the channel geometry shown in Figure 7-5. In Figure 7-5, green lines represent unconstricted input/output channels, blue lines represent bypass channels, and cyan lines represent trapping channels. As with the first design iteration, the droplet trap includes many dead-end channels to minimize variability in channel dimensions at channel junctions. The second iteration of the Primary Droplet Trap design was also intended to function in the same manner as its first iteration (i.e., to follow the process flow depicted in Figure 7-2).

There were four main changes implemented in the second iteration of the Primary Droplet Trap design compared to the first iteration, specifically: (1) the channel layout changed to minimize the length of the bypass channels, (2) one trapping channel was cut on a 45^{o} angle with respect to the other trapping channel, (3) during fabrication, a forced wait time was included between cutting the trapping channels (i.e., one trapping channel was cut, then a pause, then the second trapping channel was cut), and (4) the channel dimensions were changed to increase the pressure barriers to the trapping and bypass channels.

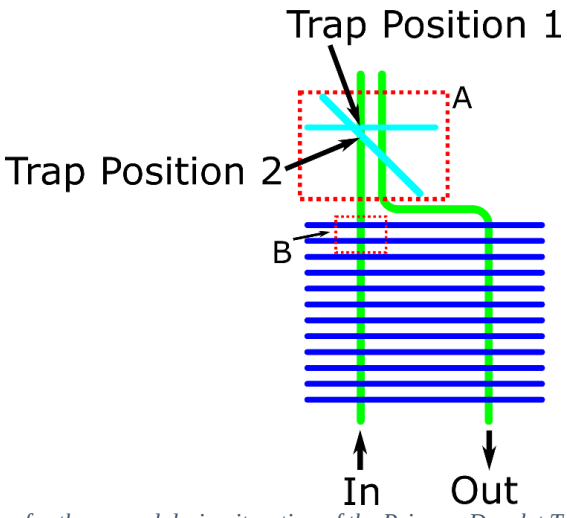

Figure 7-5 – Channel geometry for the second design iteration of the Primary Droplet Trap. Green lines represent the input/output channels, blue lines represent the bypass channels, and cyan lines represent trapping channels. The red dashed rectangles denote common framings of the Microscope used when observing droplet trap behaviour.

The layout of the droplet trap was changed to minimize its footprint and allow for shorter bypass channels, which resulted in channels with higher resistances and ΔP_{Vent} values being used. These changes were expected to improve trap performance and enable more traps to be included in an array on a single device in the future.

As discussed in Section 7.2.2, one of the main issues with the first iteration of the Primary Droplet Trap was that the trapping channels did not have well-defined profiles. These poorly-defined profiles were attributed to (1) the channel proximity and (2) the timing of laser-cutting in their fabrication. This issue was addressed by cutting one trapping channel on a 45^o angle with respect to the other trapping channel and adding a time delay in cutting the two trapping channels.

By cutting one of the trapping channels on a 45^o angle, the entrances to the trapping channels, and therefore the droplet trapping positions, were still kept 140 μm apart to ensure contact between trapped droplets to form a DIB. However, the remainder of the trapping channels were separated, preventing overlapping channel profiles and improving channel definition. This change also made the angled trapping channel slightly longer than the horizontally-oriented trapping channel in Figure 7-5, resulting in improved resistive sorting of droplets at the trapping channels. This sorting helped the first trapped droplet proceed directly to Trap Position 1, as defined in Figure 7-5. The time between cutting the trapping channels was also increased by programming the laser cutter to cut a set of sacrificial channels between cutting each trapping channel. Sacrificial channels are channels that were not connected to any part of the Droplet Generator in an unused portion of the device.

The dimensions of the channels involved in this design are described in Table 7-2, labelled with their corresponding resistivities. These dimensions resulted in trapping pressures of ΔP_{Trap} = 168 Pa and ΔP_{Vent} = 117 Pa. The channel dimensions were chosen because they could be readily estimated and achieved with the laser settings tested at the time of design. The laser settings for the r_{Tc} and r_B channel types had not yet been tested, and their dimensions were estimated. The

trapping pressures were calculated considering the droplets to fully fill the channel cross-section as an approximation, as the work of Section 6.3.2 had not been performed at the time of this design.

The droplet trap was designed to trap droplets when the Droplet Generator was operated at P_d = 8.06 kPa and P_c = 8.38 kPa or any set of lower pressures. However, due to unforeseen design and fabrication challenges (as discussed in Section 7.3.2), this droplet trap was unsuccessful and had to be redesigned in the third iteration of the Primary Droplet Trap.

Table 7-2 – The three required channel types for use in the second iteration of the Primary Droplet Trap design. Additional laser parameters common to all channel types were that the cuts were performed at 1000 Hz and focused on the material surface (z=0).

Channel Type	r_{Tc}*	r_B*	r_s **and** r_{Tu}
Laser Line Colour	Cyan	Blue	Green
Number of Passes	2 Pass	2 Pass	2 Pass
Laser Power [%]	3.1	3.3	3.5
Laser Speed [%]	1	1	0.5
Unbonded Channel Depth [μm]	73	93	249 ± 16.5
Unbonded Channel Width [μm]	143	143	161 ± 15.2
Bonded Channel Depth [μm]	70	90	240 ± 3.87
Bonded Channel Width [μm]	118	118	134 ± 3.05

7.3.2 Test Results

The second design iteration of the Primary Droplet Trap attempted to address the issues in the first iteration by cutting one of the trapping channels on an angle and adding a time delay in fabrication between cutting each trapping channel (see Section 7.3.1). However, cutting the trapping channel on an angle resulted in an unexpected change in channel dimensions, particularly the channel width, making the droplet trap ineffective.

The trapping channels were designed to be 118 μm wide, whereas, after fabrication, the horizontally-oriented trapping channels were measured to be 111 ± 3.67 μm wide. Trapping channels cut on a 45° angle were found to have widths of ~140 μm in the middle of the channel's length and ~252 μm at their entrances, directly to the right of Trapping Position 2 in Figure 7-5. The entrance became less defined because of overlapping profiles of the 45° trapping channel and the vertically-oriented input channel. This effect can be seen clearly in the unbonded channel geometry when examined as a topographical map (see Figure 7-6).

Figure 7-6(A) shows a photograph of the unbonded channel geometry composed of a stack of images taken at 20 μm height increments. Figure 7-6(B) shows the accompanying topographical map drawn by tracing the focal plane of each image in the stack used to generate Figure 7-6(A) with depths labelled in units of micrometres. The highest point was defined as 0 μm, and each line represents a decrease of 20 μm. As this was an unbonded channel geometry, a slight lip around the channels constituted the highest point.

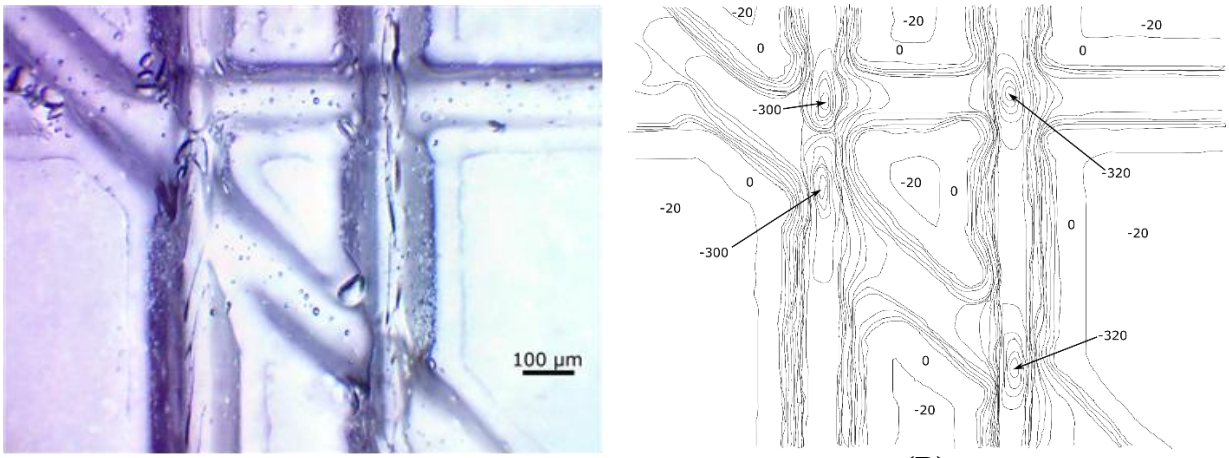

(A) (B)

Figure 7-6 – (A) A photograph of the unbonded Primary Droplet Trap Iteration 2 geometry taken with the Microscope at 10x magnification and composed of a stack of 17 photographs taken with a constant spacing of 20 µm. (B) A rough topographical map of the droplet trap was drawn by tracing the focal plane of each of the 17 photographs. The depths shown are in µm. The images are focused within position A in Figure 7-5.

Due to the much larger than intended 45^o trapping channel, the Laplace pressure barrier of that trapping channel was much lower than designed and therefore could not trap any droplets. However, the horizontally-oriented trapping channel could occasionally trap droplets, but not reproducibly. Figure 7-7 shows the droplet trap holding a single droplet at the horizontally-oriented trapping channel (Trapping Position 1 in Figure 7-5) and a second droplet entering the 45^o slanted trapping channel (Trapping Position 2 in Figure 7-5). The Droplet Generator was operated with a continuous stream of droplets at P_d = 8.06 kPa and P_c = 8.38 kPa.

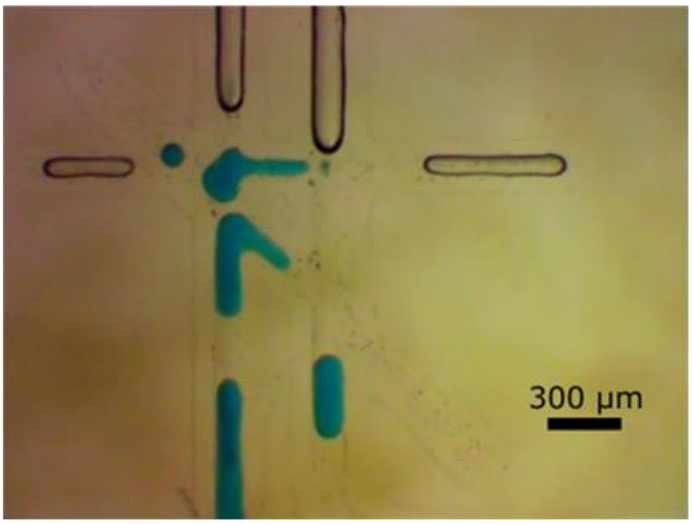

Figure 7-7 – A trapped droplet "surging" into the horizontally-oriented trapping channel as a second droplet is present in the slanted trapping channel. The photograph is framed at Position A in Figure 7-5.

The droplet in Trapping Position 1 is partially in the horizontally-oriented trapping channel while also occupying the normal trapping position. If the droplet trap had met its design specifications, the droplet in Trapping Position 1 should not have entered the horizontally-oriented trapping channel. However, the droplet in Trapping Position 2 flowed directly into the slanted trapping

channel because of that channel's lower trapping pressure, creating a spike in pressure across the droplet trap. This pressure spike caused the designed trapping pressure of the horizontally-oriented trapping channel to be exceeded temporarily. This pressure spike resulted in the droplet trapped at Trapping Position 1 "surging" into the horizontally-oriented trapping channel. This surge behaviour often resulted in the ejection of the trapped droplet and prevented the droplet trap from reproducibly demonstrating the successful trapping of even a single droplet. This pattern of behaviour was observed whenever this droplet trap was tested with these conditions.

As with the first iteration of the Primary Droplet Trap design, droplets approaching the trapping channels were observed to split at junctions of the bypass channels as they passed those channels. This splitting resulted in unpredictable droplet sizes at the trapping channels and further reduced the reproducibility of the droplet trap performance.

The bypass channels in this droplet contained minor blockages caused by the cutting order of the bypass channels and input channel to the droplet trap (see Figure 7-8). These were expected to increase the trapping pressure of the bypass channels by constricting the entrance to those channels. However, the increased trapping pressure was insufficient to prevent droplets from partially entering and splitting at the bypass channels. It was hypothesized that these blockages may have resulted in more splitting because of their short length. Once droplets pass the initial constriction, it would be energetically favourable to further continue into the bypass channel to expand and reduce surface energy. This behaviour would create competing forces at the constriction in the bypass channel entrance. There would be forces acting against the droplet entering the bypass channel and pushing the droplet further into the bypass channel. These competing forces were thought to contribute to increased droplet splitting in this trap design. The droplet splitting process is discussed in more detail in Section 7.6.

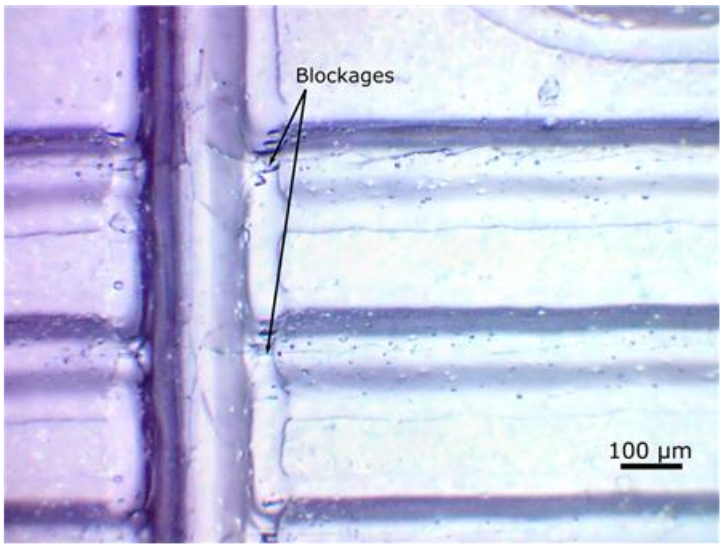

Figure 7-8 – A photograph of the unbonded bypass channel geometry of the second design iteration of the Primary Droplet Trap taken using the Microscope at 10x magnification from a stack of 21 photographs at 20 µm height intervals. Blockages to bypass channels are labelled. The image is focused at Position B in Figure 7-5.

7.3.2.1 Purge Channel Behaviour

Several Droplet Generators fabricated with this droplet trap design included a purge channel after the droplet trap to allow for the trap to be easily cleared of droplets. The complete channel geometry of this design can be seen in Figure 7-9. In Figure 7-9, light green lines represent the standard channels of the Droplet Generator, blue lines represent bypass channels, cyan lines represent trapping channels, and dark green circles represent input and output wells. The design used a large on-chip output well instead of an output syringe to collect waste from the device.

A syringe with an intact plunger was attached to the purge channel and used to apply negative pressures to the droplet trap. These negative pressures were generated by pulling on the plunger of the syringe and were sufficient to clear droplets from the droplet trap. It was predicted that the plunger only needed to be pulled to its 0.2 mL mark to generate enough negative pressure to displace droplets from the droplet trap. This prediction was confirmed during testing. However, it was found that this negative pressure was sufficient also to create droplets at the T-junction depending on how long it was applied. Before clearing droplets from the droplet trap, there had to be a sufficient amount of backflow into the dispersed phase input channel such that the Dispersed Phase was not pulled into the T-junction to form droplets. Further testing determined that allowing backflow into the dispersed phase input channel up the first long vertically-oriented channel from the T-junction was sufficient to avoid this. While the purge channel was found to be effective, it was not included in the Primary Droplet Trap Iteration 3 design because of the timing of the fabrication runs for the Iteration 2 and Iteration 3 designs.

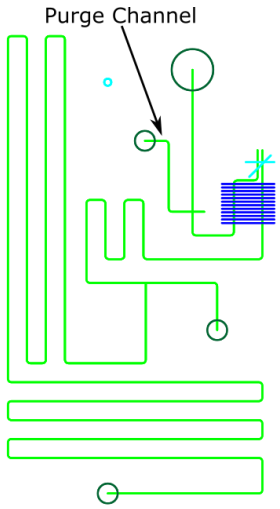

Figure 7-9 – The complete channel geometry of Droplet Generators with integrated Primary Droplet Trap Iteration 2 and a purge channel after the droplet trap.

7.4 Primary Droplet Trap – Iteration 3

7.4.1 Design

The third iteration of the Primary Droplet Trap design used the channel layout shown in Figure 7-10. In Figure 7-10, light green lines represent input/output channels part of R_s or R_{Tu}, and blue lines represent bypass channels (R_B). Dark green (grass green) lines represent type one bypass

channels (R_{B1}), grey lines represent type two bypass channels (R_{B2}), and cyan lines represent trapping channels that are part of R_{Tc}. The channel dimensions required for this droplet trap design are detailed in Table 7-3, labelled with their corresponding resistivities. Every line in Figure 7-10 has a proportional width to the targeted channel width. These dimensions resulted in the following trapping pressures: ΔP_{Trap} = 204 Pa, ΔP_{vent} = 114 Pa, $\Delta P_{vent,B1}$ = 125 Pa, $\Delta P_{vent,B2}$ = 138 Pa where ΔP_{Vent} refers to the trapping pressure of the R_B channels, $\Delta P_{vent,B1}$ refers to the trapping pressure of the R_{B1} channels and $\Delta P_{vent,B2}$ refers to the trapping pressure of the R_{B2} channel.

As with the second iteration of the Primary Droplet Trap, the third iteration design was expected to function similarly to the first iteration of the Primary Droplet Trap. Droplets were expected to be trapped following the process depicted in Figure 7-2.

The main changes to the design from the second iteration were (1) the dimensions of the trapping and bypass channels were changed, (2) the trapping channels were made parallel and spaced 300 μm apart, (3) the unconstricted output channel was slanted at the intersections with the trapping channels, and (4) more types of bypass channels were included.

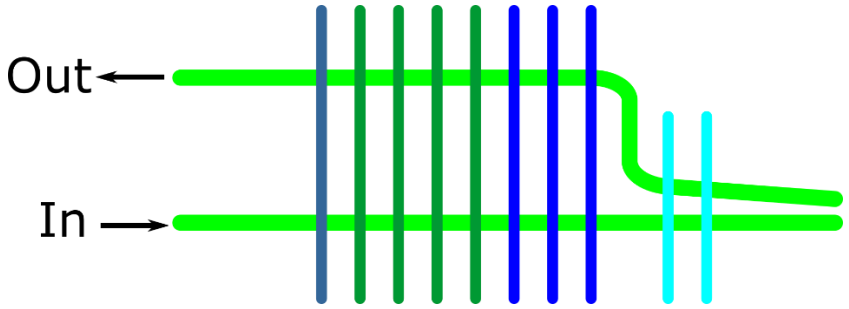

Figure 7-10 – The layout of the third design iteration of the Primary Droplet Trap, blue, dark green (grass green) and grey lines represent bypass channels, light green lines represent input/output channels, and cyan lines represent the trapping channels. The lines in this layout are proportionally as wide as the expected bonded channel widths for each channel type specified in Table 7-3.

The trapping and bypass channels were designed to have more constricted dimensions compared to the second iteration of the Primary Droplet Trap. These changes were made to be closer to the targeted dimensions that were not achieved in the second iteration of the Primary Droplet Trap and to increase the trapping pressures of all channel transitions in the droplet trap.

The trapping channels were made parallel and separated by 300 μm because droplets were produced with longer lengths (~500 μm long). Additionally, the decrease in droplet lengths when occupying the trapping positions was smaller than anticipated. This spacing also minimized distortions in channel dimensions due to the proximity of the laser-cut channels, which was an issue in both previous iterations of the Primary Droplet Trap.

As the first trapping channel that a droplet encountered entering the droplet trap was no longer cut on an angle, there was no clear distinction in the resistance of the two trapping channels. Both channels would have the same resistance, and therefore, resistive sorting may not occur. Thus, the unconstricted output channel was cut on a slight angle for the portion of its length that intersected with the trapping channels. This change ensured that the first trapping channel encountered by a droplet was slightly longer than the other, and resistive sorting would occur.

Lastly, more bypass channel types – bypass channels with different dimensions – were included in this design to equilibrate the flow rates through each bypass channel as much as possible. Equilibrating flow rates was expected to allow droplet behaviours to be predicted more easily as droplets would experience similar forces at each bypass channel junction. Therefore, the droplet trap would behave closer to the idealized model shown in Figure 5-2. However, at the channel dimensions being considered, the laser cutter could only change the depths of the channels with a resolution of ~10 μm, making optimization of the flow rates through the bypass channels fairly limited.

*Table 7-3 – The required channel types for the third design iteration of the Primary Droplet Trap. The r_B, r_{B1}, r_{B2}, and r_{Tc} are marked with *s, indicating that their laser settings were not used before this fabrication run. Channel dimensions were estimates based on previously collected data at the time the design was made. Additional laser parameters common to all channel types were that the cuts were performed at 1000 Hz and focused on the material surface (z=0).*

Channel type	r_{Tc}*	r_B*	r_{B1}*	r_{B2}*	r_s **and** r_{Tu}
Laser Line Colour	Cyan	Blue	Grass Green	Grey	Green
Number of Passes	2 Pass	2 Pass	2 Pass	2 Pass	2 Pass
Cutting Order	6	3	4	5	2
Laser Power [%]	2.7	3.2	3.1	3	3.5
Laser Speed [%]	1	1	1	1	0.5
Unbonded Channel Depth [μm]	73	122	115	104	265 ± 5.6
Unbonded Channel Width [μm]	120	124	124	124	170 ± 0.5
Bonded Channel Depth [μm]	70	120	110	100	252 ± 14
Bonded Channel Width [μm]	111	111	111	111	163 ± 14

7.4.1.1 Numerical Design of Primary Droplet Trap Iteration 3

The third iteration of the Primary Droplet Trap will be described in this Section as an example of the typical design process for Primary Droplet Traps. The design assumed that the channels of the Droplet Generator would be filled with droplets formed at a relative droplet volume ratio of 27% (i.e., a ratio of 27% of Dispersed Phase volume to total channel volume). At this relative volume ratio, droplets were expected to be created with input pressures corresponding to fluid reservoir heights of ~82.5 cm for Dispersed Phase and 1 m for Continuous Phase. This assumption was applied to all channels except trapping channels (R_{Tc}), which were not intended to be occupied by droplets. Droplets would only occupy the trapping channels if operation of the droplet trap failed or the droplet trap was being cleared of trapped droplets.

This initial design work was performed before the testing detailed in Section 6.3.2 and Section 6.3.3, resulting in the use of a droplet resistance increase factor of four. Consequently, it was found in testing that droplets were not produced at the intended 27% relative volume ratio but rather at a relative volume ratio of ~11.5%, but still had the intended droplet lengths. Similarly, the Laplace pressure difference was calculated using Equation (5-1), assuming that the droplets fully filled the channel cross-section aside from a surrounding negligibly thin Continuous Phase sheath.

At the time of design, the Droplet Generator used an r_s of 3.08 x 10^{15} Pa s m^{-4} with an L_s of 67.8 mm and a P_{Tot} of ~7.82 kPa. It was convenient to set $r_{Tu} = r_s$ and choose r_{Tc} to maximize the value of

ΔP_{Trap}. A value of r_{Tc} = 4.41 x 10^{16} Pa s m^{-4} was chosen to create a ΔP_{Trap} of 204 Pa. A value of r_B = 2.70 x 10^{16} Pa s m^{-4} was chosen to produce a ΔP_{vent} of 114 Pa. To maintain a small R_{Tc} value, an L_{Tc} of 0.426 mm was chosen. Due to the geometry of the design, L_B and L_{Tu} were dependent on each other. Therefore, L_B and L_{Tu} were simultaneously optimized to find a suitable L_B value. A suitable L_B value of 1.83 mm was determined using Equation (5-6), which resulted in L_{Tu} = 2.60 mm. The smallest distance between bypass channels was 0.3 mm, the minimum distance required to ensure each bypass channel had well-defined channel dimensions. Therefore, the length of the unconstricted channels that connected the parallel bypass channels, $L_{Tu,con}$, was equal to 0.3 mm.

Using these parameters and the resulting channel resistances, the pressure drops across a series of N bypass channels were calculated from N = 1 to N = 12 bypass channels. It was determined that N = 8 bypass channels was the optimal design parameter, based on these results (data not shown). N = 8 bypass channels ensured a design with a pressure drop across the trapping channels that was 87 Pa lower than the value of ΔP_{Trap}.

Once the droplet trap was filled with droplets, all bypass channels were expected to be accessible to subsequent droplets. The pressure drop across each bypass channel exceeded ΔP_{vent}, allowing for effective movement of excess droplets and continuous phase through the bypass channels.

At the time of design, it was thought that balancing the flow rate through each bypass channel would be advantageous. Balancing these flows would allow for droplet behaviours to be predicted more easily since droplets would experience similar forces at the junction of each bypass channel. Two additional bypass channel types, r_{B1} and r_{B2}, were introduced to optimize the flow rates through the bypass channels.

Values of r_{B1} = 3.17 x 10^{13} Pa s m^{-4} and r_{B2} = 3.81 x 10^{13} Pa s m^{-4} were chosen for bypass channels 4-7 and 8, respectively. With these changes, the average flow rate through the bypass channels was equal to 4.02 x 10^{-12} ± 8.86 x 10^{-13} m^3 s^{-1} (± 22%) when the droplet trap held one trapped droplet and 4.67 x 10^{-12} ± 6.57 x 10^{-13} m^3 s^{-1} (± 14%) when fully filled with two droplets. The use of these bypass channel types slightly changed the pressure distribution across the bypass channels. However, it did not significantly affect the operating ability of the droplet trap as the pressure drop across bypass channel 1 was still below the ΔP_{Trap} value in both states considered (see Table 7-4). The pressure drop across all bypass channels exceeded the expected ΔP_{vent} for all of the bypass channel types ($\Delta P_{vent,B}$ = 114 Pa, $\Delta P_{vent,B1}$ = 125 Pa, $\Delta P_{vent,B2}$ = 138 Pa). Therefore, droplets would not be trapped unexpectedly by the bypass channels.

Table 7-4 – The pressure drop across each bypass channel in the third design iteration of the Primary Droplet Trap. Bypass channels 1-3 had a resistivity of r_B, and bypass channels 4-7 had a resistivity of r_{B1}. Bypass channel 8 had a resistivity of r_{B2}.

Bypass Channel Number	Pressure Across Channel [Pa]	
	One Trapped Droplet	Two Trapped Droplets
1	141	195
2	156	202
3	177	217
4	204	240
5	239	270
6	280	310
7	320	346
8	379	404

Table 7-4 only considers the droplet trap when (1) it contained one trapped droplet (the "One Trapped Droplet State") and (2) it was fully filled with two trapped droplets (the "Two Trapped Droplets State"). These two states represented the highest resistance states of the trap. If the droplet trap was expected to function in these states, it was expected to successfully hold droplets stationary.

The parameters described above are represented in the channel geometry shown in Figure 7-10. The resistivities required for this droplet trap design were achieved using the channel dimensions and laser settings outlined in Table 7-3.

Based on the physics available to describe the performance of droplet traps, the third iteration of the Primary Droplet Trap was expected to function effectively. The third iteration of the Primary Droplet Trap was intended to trap droplets when the Droplet Generator was operated at pressure settings of P_d = 8.06 kPa and P_c = 8.38 kPa or any lower pressure setting. Prior iterations of the Primary Droplet Trap were numerically designed similarly and expected to function effectively but failed due to unforeseen fabrication and design issues.

At the time of the design of the third iteration of the Primary Droplet Trap, it was also decided to design an Alternate Droplet Trap to overcome the issues encountered in the behaviour of the Primary Droplet Trap, increasing the probability of constructing a successful droplet trap.

7.4.2 Test Results

The third design iteration of the Primary Droplet Trap used the channel geometry shown in Figure 7-10 and was more successful than its two predecessor design iterations. However, it still did not demonstrate reproducible trapping behaviour as it did not regularly hold two droplets stationary in the droplet trap.

In this design, trapping channels were spaced further apart to prevent channel overlap, and both trapping channels were horizontally-oriented to ensure well-defined channel dimensions. A time delay between cutting each trapping channel was included by programming the laser cutter to cut sacrificial channels in an unused area of the device. These channels created a time interval between

cutting the two trapping channels. The cutting order of the bypass channels was also changed so that no blockages were formed in those channels.

One Droplet Generator with an integrated Primary Droplet Trap Iteration 3 (Internal Chip ID: FR5.1_DT2.1) was tested at multiple pressure settings and multiple test runs and was capable of trapping two droplets in contact with each other to form DIBs. This device was the first to be tested. Droplets were held in contact initially in the position seen in Figure 7-11 but over time transitioned into the position shown in Figure 7-12. After initially being trapped, the droplet in the first trapping position slowly moved into the dead-end channel above the first trapping position. The droplet in the second trapping position slowly moved with it. However, the first droplet would slightly pull away from the second droplet before the second droplet moved to maintain contact. There were also droplets which flowed through the bypass channels after the trapping event with variable sizes due to droplet splitting (Figure 7-11). These droplets did not affect the behaviour of the trapped droplets.

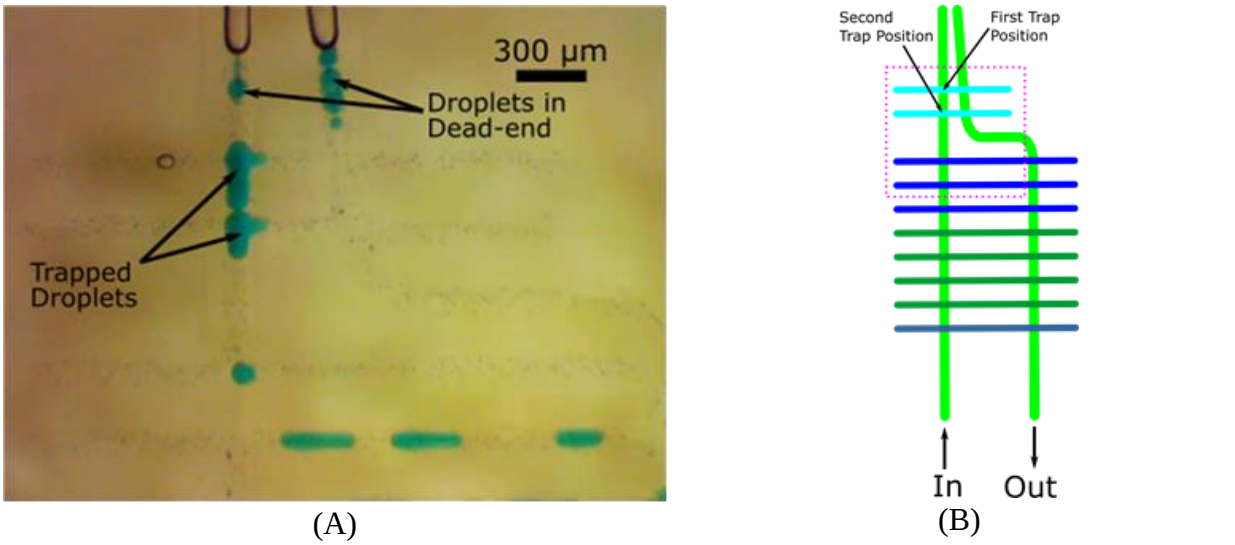

Figure 7-11 – (A) The initial position of two trapped droplets in the Primary Droplet Trap Iteration 3 (Chip FR5.1_DT2.1). The droplets were part of a continuous stream of droplets produced with pressure settings of P_d = 8.06 kPa and P_c = 8.38 kPa. A third droplet can be seen to be trapped at the entrance to bypass channel 1. Other droplets can be seen in bypass channel 2 flowing past the trap. The photograph is framed at the pink rectangle in (B).

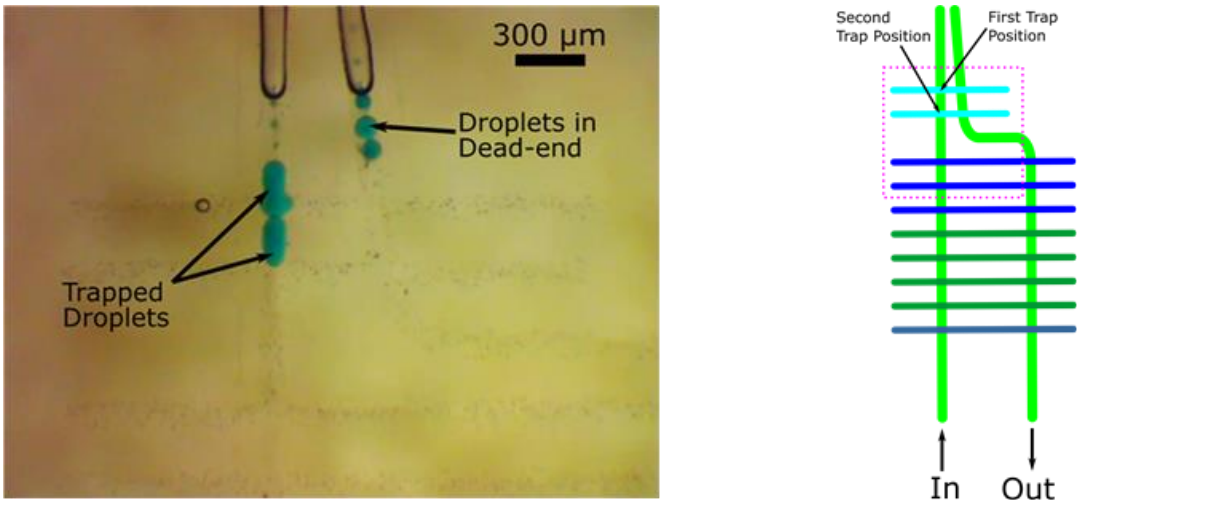

(A) (B)

Figure 7-12 – (A) The typical final position of two trapped droplets in the Primary Droplet Trap Iteration 3 (Chip FR5.1_DT2.1). The droplets were an isolated pair of droplets generated with pressure settings of P_d = 8.06 kPa and P_c = 8.38 kPa. They adopted this position 1 minute and 45 seconds after being trapped by the trapping channels. The photograph is framed at the pink rectangle in (B).

This droplet trapping behaviour was observed at various pressure settings, which are described in Table 7-5. In Table 7-5, a Y in the Successful Droplet Trapping column indicates that two droplets were successfully trapped at the first and second trapping positions of the droplet trap (see Figure 7-11(B)). An N indicates that droplets were not trapped at the designed trapping positions. The Number of Times Observed denotes the number of times the behaviour was observed in a series of consecutive tests. For example, the droplet trap was filled with droplets and then cleared at pressure settings of P_d = 8.06 kPa and P_c = 8.38 kPa with a continuous stream of droplets in five consecutively-performed tests. Successful trapping was observed four times, hence 4/5 in that column. If multiple series of consecutive tests were performed, multiple entries are listed in that column. For isolated pairs of droplets that were successfully trapped, the times taken for the droplets to merge were also recorded. There was no clear dependence on the time it took trapped droplets to merge on the test conditions. However, the results reported herein suggest that trapped droplets took longer to merge when the devices were operated at lower input pressures.

With this third iteration, as with the previous iterations, droplets approaching the droplet trap were observed to split as they passed bypass channels. In Table 7-5, a Y in the Droplet Splitting column indicates that droplet splitting was observed to occur at one or more bypass channels, and N indicates that no droplet splitting was observed. While Table 7-5 provides basic information on droplet splitting, it should be noted that droplets split at fewer bypass channels as the Droplet Generator was operated with lower input pressures. Droplet splitting occurred less frequently at lower pressures, and no droplet splitting was observed when P_c was set to 2.51 kPa, corresponding to a height of ~30 cm of the Continuous Phase reservoir.

Table 7-5 – A summary of the droplet trapping behaviours observed in the droplet trap of Chip FR5.1_DT2.1 on one day of testing. A Y in the Successful Droplet Trapping column indicates that the droplet trap trapped two droplets. A Y in the Droplet Splitting column indicates that droplets split at one or more bypass channels while approaching the trapping channels.

P_c [kPa]	P_d [kPa]	Continuous Stream or Isolated Pair	Successful Droplet Trapping (Y/N)	Number of Times Observed	Droplet Splitting (Y/N)	Time to Droplet Merge [min]
8.38	8.06	Isolated Pair	Y	3/3	Y	~3
	8.06	Continuous	Y	4/5, 2/2	Y	-
	7.94	Continuous	Y	1/1	Y	-
	7.83	Continuous	Y	1/1	Y	-
6.70	6.45	Isolated Pair	Y	3/3	Y	6-8
	6.45	Continuous	Y	2/2	Y	-
3.35	3.34	Continuous	N	1/1	Y	-
	3.22	Continuous	Y	1/1	Y	-
	3.05	Continuous	Y	1/1	Y	-
	2.98	Continuous	Y	1/1	Y	-
2.51	2.51	Isolated Pair	N	2/2	N	-
	2.51	Continuous	N	1/1	N	-

The data in Table 7-5 demonstrates that the Chip FR5.1_DT2.1, a Droplet Generator with an integrated Primary Droplet Trap Iteration 3, could be used to trap droplets in its designed trapping positions effectively (see Figure 7-11(B)). Although droplets could be consistently trapped, this behaviour was not reproducible as the trapped droplet volume was highly variable. The behaviour of the droplets approaching the trapping positions was also highly variable. This lack of reproducibility was primarily attributed to droplet splitting at the bypass channels, which was observed for almost all tested pressure settings. In the one tested pressure setting (P_c = 2.51 kPa), where droplet splitting was not observed, droplet trapping was not observed. By operating at the low-pressure settings of P_d = 2.51 kPa and P_c = 2.51 kPa, droplets would not split at its bypass channels. However, they would be moving so slowly that they would come into contact as they passed the bypass channels and merged before reaching the designed trapping positions. While droplet splitting could be avoided by operating the device at low pressures, only large single merged droplets could be trapped, which would not form DIBs.

This behaviour matched the theoretical predictions for the droplet trap. The droplet splitting model did not predict droplet splitting at these low operating pressures, as discussed later. Additionally, the two droplets would come into contact and remain stationary around bypass channel 3 until they merged and continued into the trap. This behaviour was related to the droplet length and the flow rate through the bypass channels. The cumulative flow rate through the bypass channels was expected to exceed the continuous phase flow rate at bypass channel 3. Therefore, droplet flow towards the droplet trap would be negligible until the droplets came into contact. This would result in several bypass channels being blocked at once, increasing the pressure across the bypass channels. This pressure increase occurred once two droplets merged, creating an extra-long droplet that blocked multiple bypass channels. Therefore, the behaviour of the droplet trap at this low-pressure setting was not unexpected.

When droplets became trapped in the droplet trap, they were distinct droplets in contact for at least 1.5 minutes. Therefore, if the reproducibility of droplet trapping could be increased, this might be a successful droplet trap. However, all the trapped droplets eventually merged. These merging events either immediately followed a shift in the positions of the trapped droplets, or the cause of merging could not be identified from a top-down view of the droplets.

It has been noted in the literature that DIB stability has been linked to DIB compression or rarefaction. When droplets would shift position in the droplet trap, one droplet would initially pull away, followed shortly after by the second droplet. Therefore, this shifting in droplet position could be linked to the short lifetime of the formed DIBs [76]. This droplet shifting could be caused by rearrangement of the continuous phase surrounding the droplet in the dead-end channels beside the trapping positions. It is known that droplets do not occupy the full channel cross-section (Figure 6-11). Therefore, it is possible that given the pressures applied to the trapped droplets, the continuous phase in the dead-end channels could be displaced and flow around the trapped droplets to exit the trap.

In cases where the cause of merging could not be readily identified, it is hypothesized that the droplets changed conformation or experienced contact with the channel walls. Either of these events could disrupt the monolayers on the droplet surfaces, leading to droplet merging. The fragility of droplets in contact could be explained by using Span 80 instead of a lipid, which does not form DIBs between droplets. However, similar works with droplets coated in Span 80 in contact do not report the same short droplet lifetimes [60], [70]. Therefore, it is likely that Span 80 is not the primary issue in droplet lifetime but may exacerbate another issue. Further work is required to determine the root cause of the short droplet lifetime in this droplet trap.

Chip FR5.1_DT2.1 was the first Droplet Generator with an integrated Primary Droplet Trap Iteration 3 tested, and it showed promise when operated with specific pressure settings. Four additional devices with Primary Droplet Traps Iteration 3 were tested; however, the same trapping behaviour was not observed. Two of these devices failed due to debris being introduced into and blocking specific channels of the droplet trap. In the two devices that were capable of being tested (Chip IDs: FR5.1_DT1.1 and FR5.2_DT4.2), droplets rarely reached their trapping positions, and if they did, had small droplet volumes such that the two trapped droplets did not make contact.

Both Chips FR5.1_DT1.1 and FR5.2_DT4.2 were tested as many times with as many pressure settings as was Chip FR5.1_DT2.1 but showed far more extensive droplet splitting at their bypass channels. This increased splitting was hypothesized to have severely impacted the behaviour of their droplet traps. Droplet volumes were unpredictable, and the resistance of their bypass channels was also unpredictable. Chip FR5.1_DT2.1 was thought to behave differently because of a small variation in the resistance of its bypass channel number 1, the bypass channel closest to the trapping channels. This channel was observed to trap and hold droplets in place (see Figure 7-11). This behaviour was not observed in either Chip FR5.1_DT1.1 or Chip FR5.2_DT4.2, in which most droplets simply flowed directly into and through bypass channel number 1, thereby bypassing the trapping channels. The small variation in the resistance of bypass channel number 1 could not be identified due to difficulties focusing on changes in channel dimensions when the channel was filled with the Continuous Phase. No apparent changes in the channel dimensions affecting the

channel resistance of bypass channel number 1 were found before introducing fluids into the device. Therefore, if there was an issue related to the channel resistance of bypass channel number 1, it was likely due to a piece of debris introduced into the channel during operation.

Droplet splitting at bypass channels was identified as the main issue with Primary Droplet Trap Iteration 3. The implications of and reasons for droplet splitting at bypass channels will be discussed in more detail in Section 7.6. The data shown in Table 7-5 demonstrates that although there were some device-to-device reproducibility issues, Primary Droplet Trap Iteration 3 was close to a suitable design. At least one chip could successfully trap droplets for at least 1.5 minutes and could be successful if the nuances of Chip FR5.1_DT2.1 and droplet splitting were better understood and controlled.

Chapter 8 will describe the final Primary Droplet Trap design, which sought to address these issues using a method of theoretically predicting droplet splitting at bypass channels.

7.5 Alternate Droplet Trap

7.5.1 Design

The Alternate Droplet Trap design was developed as an alternative to the Primary Droplet Trap due to the challenges encountered in implementing the first two iterations of the Primary Droplet Trap. This trap was explicitly designed to reduce the number of bypass channel junctions to reduce the possibility of droplet splitting. It was also designed to be similar to pillar-based droplet traps seen in the literature [64], [65], [68]. However, this design was made with the specific intention of addressing an issue in pillar-based droplet traps reported in the literature: that pillar-based droplet traps will eject droplets if too many droplets are sent to the trap.

Pillar-based droplet traps have been typically implemented without a bypass channel before the trapping positions in the literature. A significant pressure drop across the trap will be created without a bypass channel if another droplet is sent to the filled trap. This pressure drop will result in a trapped droplet being ejected to relieve pressure across the droplet trap. Schlicht and Zagnoni avoided this by including one channel specifically designed to eject droplets in their pillar-based droplet trap to control this ejection process [68]. However, this does not work well if droplets are continuously produced, thereby continuously ejecting droplets from the droplet trap. Therefore, in the Alternate Droplet Trap, bypass channels were placed such that after the droplet trap was full, subsequent droplets would be able to bypass the trapped droplets without ejecting them.

The design and channel layout of the Alternate Droplet Trap was discussed in Section 5.4. The specific channel layout can be seen in Figure 5-4. The droplet trap was expected to operate similarly to the first iteration of the Primary Droplet Trap shown in Figure 7-2. First, the trapping channels would be blocked by droplets and then subsequent droplets would flow around the trapped droplets through the bypass channels.

7.5.1.1 Numerical Design of Alternate Droplet Trap Iteration 1

The first design iteration of the Alternate Droplet Trap will be described in detail in this Section as an example of the numerical design process performed for this type of trap design. The design

assumed that channels contained droplets formed at a relative droplet volume ratio of 27% (i.e., a volume ratio of 27% Dispersed Phase to total channel volume). Droplets at this relative volume ratio would be created with input pressures corresponding to fluid reservoir heights of 82.5 cm for the Dispersed Phase and 1 m for the Continuous Phase. This assumption was applied to all channels except for trapping channels (R_{Tc}). Droplets would not occupy trapping channels unless operation of the droplet trap failed or the droplet trap was being purged.

This design work was performed before the testing detailed in Section 6.3.2 and Section 6.3.3, resulting in the use of a droplet resistance increase factor of four. Consequently, it was found in testing that droplets were not produced at a 27% relative volume ratio but rather at a relative volume ratio of approximately 11.5%. Similarly, the Laplace pressure difference was calculated using Equation (5-1), assuming droplets fully filled the channel cross-section and were surrounded by a negligibly thin Continuous Phase sheath.

At the time of the design, the Droplet Generator used an r_s of 3.08 x 10^{15} Pa s m^{-4} with an L_s of 67.8 mm. The droplet generation conditions detailed above provide a P_{Tot} of about 7.82 kPa when applied to the Droplet Generator design. It was convenient to set $r_{Tu} = r_s$ to simplify the design of the droplet trap. A value of r_{Tc} was then chosen to maximize the value of ΔP_{Trap} while maintaining achievable channel dimensions for the constricted trapping channels. A value of r_{Tc} = 4.41 x 10^{16} Pa s m^{-4} was chosen to create a ΔP_{Trap} of 204 Pa.

Spacing between bypass channels was 0.3 mm to prevent channel profile overlap. This spacing was also convenient for trapping channels to ensure that the trapped droplets were held in close contact to form a DIB. At the time of design, droplets could be produced with lengths of ~500 µm and were therefore expected to be in contact with that trapping channel spacing. Thus, the distance between bypass and trapping channels, $L_{Tu,1}$, was set to 0.3 mm.

The minimum channel length of the r_{Tc} channels to obtain a well-defined geometry was 0.4 mm. L_{Tc} was therefore set to 0.4 mm to minimize the resistance of the trapping channels. Large trapping channel resistances (R_{Tc}) resulted in large pressure drops and lower fluid flow rates towards the trapping channels. Minimizing R_{Tc} through minimizing L_{Tc} was therefore desirable.

As bypass channels and trapping channels were parallel to one another and in close proximity, implementing different lengths for the various bypass and trapping channels would be difficult and lead to poorly defined channel geometries. Therefore, it was convenient to set $L_B = L_{Tc}$.

Finally, to completely define the circuit shown in Figure 5-5, a value of $L_{Tu,2}$ = 1.7 mm, was chosen. This choice was made to accommodate the various requirements of the laser cutter and to produce channels with well-defined channel dimensions. This length could be increased with little to no detriment to the expected performance of the droplet trap.

Given the channel lengths and resistivities described above and the requirements determined by Equations (5-7) - (5-10), a value of r_B = 3.81 x 10^{13} Pa s m^{-4} was chosen, which resulted in ΔP_{Vent} = 138 Pa. This trapping pressure was smaller than the ΔP_{Trap} = 204 Pa and, therefore, acceptable.

The choice of r_B resulted in the values shown in Table 7-6, satisfying all of the inequalities and requirements outlined above. The value of Q_2 is smaller than Q_1, and Q_4 is smaller than Q_3 in the One Trapped Droplet State. The value of $P_A - P_B$ is smaller than ΔP_{Trap} in both the One Trapped Droplet State and Two Trapped Droplets State. The value of $P_A - P_C$ is smaller than ΔP_{Vent}, but only by 4 Pa in the Two Trapped Droplets State. Therefore, a droplet is expected to be temporarily held at a bypass channel junction and expelled once another droplet arrives and is held at the other bypass channel junction.

Table 7-6 – The values of the design parameters required for the first design iteration of the Alternate Droplet Trap. Each of the parameters is as defined in Figure 5-5.

Parameter	One Trapped Droplet	Two Trapped Droplets
Q_1 [$m^3 s^{-1}$]	8.04×10^{-12}	-
Q_2 [$m^3 s^{-1}$]	6.65×10^{-12}	8.78×10^{-12}
Q_3 [$m^3 s^{-1}$]	2.13×10^{-11}	1.76×10^{-11}
Q_4 [$m^3 s^{-1}$]	7.49×10^{-12}	9.29×10^{-12}
P_A-P_B [Pa]	130	167
P_A-P_C [Pa]	101	134

The resistivities required for the first iteration of the Alternate Droplet Trap design were expected to be achieved using the channel dimensions and laser settings detailed in Table 7-7.

*Table 7-7 – The required channel types for the first design iteration of the Alternate Droplet Trap. r_B and r_{Tc} channel types are marked with *s, indicating that they required the use of new laser parameters at the time of fabrication.*

Channel Type	r_{Tc}*	r_B*	r_s and r_{Tu}
Laser Line Colour	Cyan	Grey	Green
Number of Passes	2 Pass	2 Pass	2 Pass
Cutting Order	6	5	2
Laser Power [%]	2.7*	3*	3.5
Laser Speed [%]	1	1	0.5
Unbonded Channel Depth [μm]	73	104	265 ± 5.6
Unbonded Channel Width [μm]	120	124	170 ± 0.5
Bonded Channel Depth [μm]	70	100	252 ± 14.4
Bonded Channel Width [μm]	111	111	163 ± 14.0

Based on the physics available to describe the performance of droplet traps, the first design iteration of the Alternate Droplet Trap was expected to function effectively. It was designed to trap droplets when the Droplet Generator was operated at P_d = 8.06 kPa and P_c = 8.38 kPa but was also expected to trap droplets at any lower pressure setting. Early testing of this iteration of the Alternate Droplet Trap demonstrated that the Alternate Droplet Trap performed more consistently than the Primary Droplet Trap.

7.5.2 Test Results

The Alternate Droplet Trap Iteration 1 was developed alongside that of Primary Droplet Trap Iteration 3 and aimed to reduce the risk of droplet splitting by reducing the number of bypass channels. Reducing droplet splitting would result in more predictable droplet volumes in the

droplet trap. While this design showed a greater degree of success, it still exhibited some droplet splitting behaviour.

Two Droplet Generator devices with Alternate Droplet Trap Iteration 1 (Chips IDs: FR5.1_DT1.0 and FR5.1_DT2.0) were tested using multiple pressure settings on multiple days. They could trap droplets that were either part of a continuous stream of droplets or isolated pairs of droplets. Droplets were initially trapped in the position seen in Figure 7-13(A) but slowly moved to the position seen in Figure 7-14(A). Contact between the trapped droplets was maintained as they shifted positions. As defined in Figure 7-13(B), droplets were never observed occupying the second trapping position until the first trapping position was filled. Based on the available physics, this was the expected behaviour of the droplet trap. However, as droplets entered the droplet trap, they often split at the first set of bypass channels (as defined in Figure 7-13(B)). However, this could be avoided by operating at lower pressure settings.

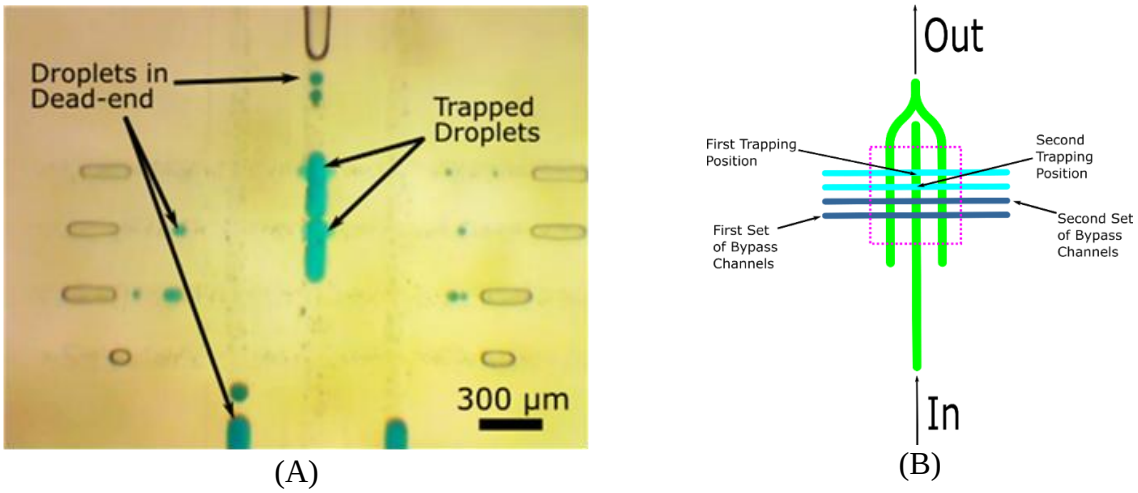

Figure 7-13 – (A) The initial position of the trapped droplets in the droplet trap of Chip FR5.1_DT2.0 produced as part of an isolated pair of droplets with the pressure settings of P_d = 7.83 kPa and P_c = 8.38 kPa. Each of the trapping positions is occupied by a droplet. Framed at the pink rectangle in (B). (B) The droplet trap channel geometry in the orientation seen in (A), with key features labelled.

After the first two droplets were trapped, a third droplet would be temporarily held at the junction of the second set of bypass channels and the input channel (as defined in Figure 7-13(B)). This droplet would then be displaced through the second set of bypass channels as a fourth droplet arrived and blocked the first set of bypass channels. This behaviour can be seen in Figure 7-15(A), where droplets trapped at the designed trapping positions can be seen to be flowing slightly into the trapping channels due to the pressure spike caused by this process. This surging indicated that as droplets flowed through the bypass channel, the pressure across the trapping channels exceeded their trapping pressure, and trapped droplets could have been ejected. However, no trapped droplets were observed to be ejected from the droplet trap because of this behaviour.

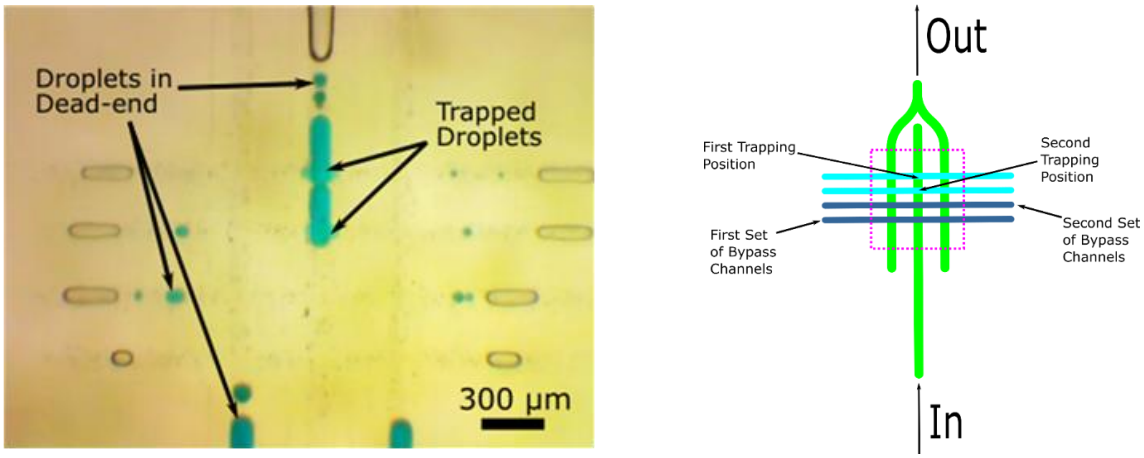

Figure 7-14 – (A) The final position of the trapped droplets in the droplet trap of Chip FR5.1_DT2.0 produced as part of an isolated pair of droplets with the pressure settings of P_d = 7.83 kPa and P_c = 8.38 kPa. Each of the trapping positions is occupied by a droplet. Framed at the pink rectangle in (B). (B) The droplet trap channel geometry in the orientation seen in (A), with key features labelled.

The droplet trapping behaviour briefly described above was observed in both Chips FR5.1_DT2.0 and FR5.1_DT1.0 for both continuous streams of droplets and isolated pairs of droplets. Droplet trapping behaviour is summarized in Table 7-8. As in Table 7-5, a Y in the Successful Droplet Trapping column of Table 7-8 indicates that two droplets were successfully trapped at the first and second trapping positions (see Figure 7-13(B)), and N indicates that two droplets were not trapped at the designed trapping positions. The Number of Times Observed denotes the number of times the behaviour was observed in a series of consecutive tests. If multiple series of consecutive tests were performed, multiple entries are provided in that column. For some of the pressure settings tested, the time taken for trapped droplets to merge was recorded. The time to merge was only recorded for some pressure settings because the procedure was concurrently developed as the testing was performed. The limited data suggested there may be a dependence of the time to merge on the operating pressures used. As there was an exceptional level of variability in the time to merge, no strong relationship could be established.

A representative droplet trapping event recording for an isolated pair of droplets can be found in Appendix E. The recording shows an isolated pair of droplets made with pressure settings of P_d = 7.83 kPa and P_c = 8.38 kPa, being made, entering and being trapped by the Alternate Droplet Trap.

In Table 7-8, it should be noted that the pressure settings of P_d = 8.06 kPa and P_d = 7.94 kPa, in each case with P_c = 8.38 kPa, did not show successful droplet trapping. Under these conditions, droplets were so long that they occupied both the first and second trapping positions and therefore, only one droplet could be trapped. This behaviour did not meet the criteria for successful droplet trapping as two droplets were not trapped. Therefore, it was labelled with an N, even though one droplet was successfully trapped.

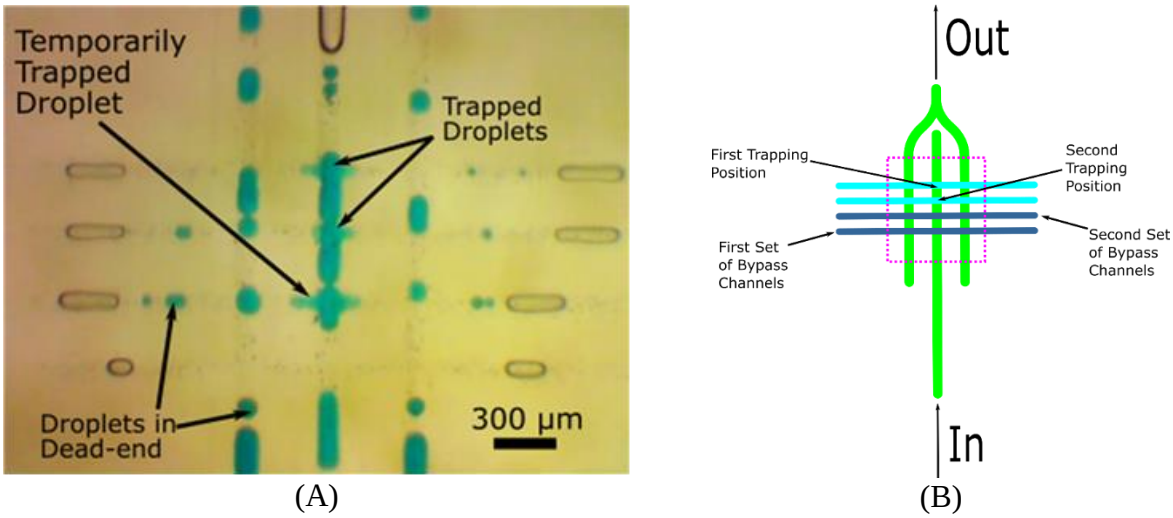

(A) (B)

Figure 7-15 – (A) The position of two trapped droplets in the droplet trap of Chip FR5.1_DT2.0 produced as part of a continuous stream of droplets with the pressure settings of P_d = 7.83 kPa and P_c = 8.38 kPa. Each of the designed trapping positions is occupied, and a third droplet can be seen to be temporarily trapped at the second set of bypass channels. Framed at the pink rectangle in (B). (B) The droplet trap channel geometry in the orientation seen in (A) with key features labelled.

Table 7-8 – A summary of the droplet trapping behaviours observed in the droplet trap of Chip FR5.1_DT1.0 and FR5.1_DT2.0 using isolated pairs or continuous streams of droplets. A Y in the Successful Droplet Trapping column indicated that the droplet trap trapped two droplets. A Y in the Droplet Splitting column indicated that droplets split at one or more bypass channels while approaching the droplet trap.

P_c [kPa]	P_d [kPa]	Continuous Stream or Isolated Pair	Successful Droplet Trapping (Y/N)	Number of Times Observed	Droplet Splitting (Y/N)	Time to Droplet Merge [min]
8.38	8.06	Continuous	N	3/3, 3/3	Y	-
	7.94	Continuous	N	1/1	Y	-
	7.83	Isolated Pair	Y	3/3	Y	3-17
	7.83	Continuous	Y	3/3, 3/3	Y	-
	7.72	Continuous	Y	3/3	Y	-
6.70	6.21	Isolated Pair	Y	3/3	Y	1-19
	6.21	Continuous	Y	3/3	Y	0.5-9
3.35	2.98	Continuous	Y	1/1, 2/2	N	>24

The droplet lifetime was typically longer for trapped droplets in the Alternate Droplet Trap compared to those in the third iteration of the Primary Droplet Trap. However, droplet lifetime was more variable. Except for two cases, the trapped droplets were held in contact without merging for at least 1.5 minutes, meeting the minimum trap time requirement.

The cause of trapped droplet merging is unclear but is thought to be related to the shift in droplet position in the trap. The droplet position shifts were caused by continuous phase redistribution around the trapped droplets. The pressures applied to the trapped droplets may have been sufficient for the continuous phase to flow through the sheath surrounding the droplets to escape the trap. Shifts in droplet position occurred more slowly at lower pressures, suggesting that they were related to the pressure applied to the droplets. Merging events were occasionally observed when these shifts in droplet position occurred.

Another possible cause of droplet merging in the Alternate Droplet Trap could be the pressure spikes caused when a third droplet is temporarily held by and then expelled through the second set of bypass channels. This pressure spike contributed to increased pressure on the trapped droplet and caused minor droplet movements. These effects may have destabilized the contact between the two droplets, resulting in droplet merging. In combination with the use of Span 80 instead of a lipid, the pressure spikes may have been sufficient to cause droplet merging in the droplet trap.

When droplet splitting was observed, incoming droplets only split at the first set of bypass channels when entering an empty droplet trap or a droplet trap containing one trapped droplet. Droplets entering a droplet trap with two droplets occupying the trapping positions always split at bypass channels as they were directed around the trapped droplets. The droplet splitting process could be avoided by operating the device at suitably low-pressure settings; specifically, P_d = 2.98 kPa and P_c = 3.35 kPa, as indicated in Table 7-8.

Alternate Droplet Trap Iteration 1 was largely successful. It reproducibly trapped droplets in its designed trapping positions and showed consistent behaviour throughout consecutive test runs and across two devices. The main design issues of the Alternate Droplet Trap were that: (1) droplets split at the bypass channels, which led to unpredictable droplet volumes and (2) trapped droplets had highly variable lifetimes before they merged. The lifetime of trapped droplets was addressed in the final design iterations of the Primary Droplet Trap and Alternate Droplet Trap, which are described in Chapter 8.

Before those design iterations could be completed, the phenomenon of droplet splitting had to be understood. A model of droplet splitting was developed and validated with test data generated using the devices with Alternate Droplet Trap Iteration 1 and devices with Primary Droplet Trap Iteration 3. This work is described in Section 7.6.

7.6 Droplet Splitting at Bypass Channel Junctions

In most literature on the design of droplet traps, the concept of droplet splitting at bypass channel junctions is not addressed in detail. Typical advice on operating droplet traps is generally limited to – do not exceed the Laplace pressure difference of the trapping channel. Models for purpose-built droplet splitting microfluidic devices were adapted to explain the droplet splitting behaviour observed during testing of droplet traps. Specifically, the model of Liang *et al.* discussed in Section 2.7 was used [105]. The main conclusion from this work was that the advice of not exceeding the Laplace pressure difference should also be applied to the bypass channels.

7.6.1.1 Verification of Droplet Splitting Model

The droplet splitting behaviour of the Alternate Droplet Trap was examined in detail to verify that the droplet splitting model described in Section 2.7 could be applied to the droplet traps in this work. Specifically, the behavioural data of isolated pairs of droplets and single droplets generated with pressure settings of P_d = 7.83 Pa and P_c = 8.38 Pa were analyzed. The volumes of droplets approaching the droplet trap and the volumes of daughter droplets in the outgoing channels past all channel junctions were measured. The behaviour of only single and isolated pairs of droplets

was examined because the resistance of the main channel could be accurately predicted in these two states but could not be for a continuous stream of droplets.

The Droplet Generator with an integrated Alternate Droplet Trap had a main channel composed of horizontally-oriented segments with depths of 249 ± 13 μm and widths of 130 ± 22 μm and vertically-oriented segments with depths of 241 ± 10 μm and widths of 154 ± 24 μm. Both orientations of the main channel had top corner angles of 75° and bottom corner radii of 14 ± 2 μm. These channel dimensions produced a main channel resistance of 1.64 x 10^{14} Pa s m^{-3} when filled with only Continuous Phase and 1.71 x 10^{14} Pa s m^{-3} considering a droplet in the vertically-oriented segment of the main channel leading up to the droplet trap.

The vertically-oriented channels in the droplet trap were found to have slightly different dimensions than other such segments of the main channel because of the intersecting channels. The channels were constricted slightly at and between the junctions of the trap (see Figure 7-16(A)). Vertically-oriented channels in the droplet trap were estimated to have depths of 223 ± 8 μm and widths of 139 ± 5 μm based on cross-sectional measurements from unbonded devices. These channels still had top corner angles of 75° and bottom corner radii of 14 ± 2 μm. The *DRIF* in these channels was calculated to be 11.8 using the method described in Section 6.3.3. The droplet trap was modelled considering unconstricted channels with these dimensions, not the dimensions of the vertically-oriented channels in the main channel. This choice was made because all unconstricted channels are short (0.3 mm long) and vertically-oriented. Additionally, they were observed to be constricted compared to the vertically-oriented channels outside the droplet trap.

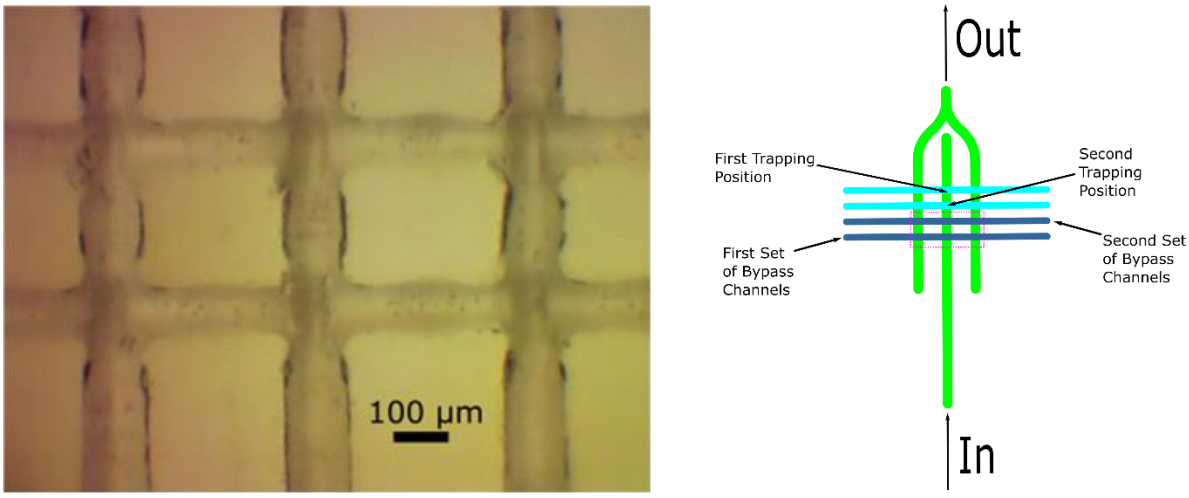

Figure 7-16 – (A) A top-down view of the bypass channel junctions of the Alternate Droplet Trap Iteration 1 in a bonded device. The center vertical channel corresponds to the input channel and can be seen to be slightly constricted at and between the bypass channel junctions. (B) The channel layout of the Alternate Droplet Trap Iteration 1 in the orientation in (A) with the location of (A) marked by the pink rectangle.

Bypass channels were found to have depths of 105 ± 8 μm, widths of 92 ± 7 μm, top corner angles of 75° and bottom corner radii of 27 μm. They were not observed to have constricted entrances as in Figure 7-8. The trapping pressure of the bypass channel was calculated using the top corner radius method based on the model of Musterd *et al.* described in Section 2.6.1 [106]. Based on the

channel dimensions used and assuming an interfacial tension of 5 mN m^{-1}, as reported by Bithi *et al.*, a trapping pressure of 116 Pa was calculated [70].

The lengths of droplets approaching the droplet trap were measured in the vertically-oriented segment of the main channel leading to the droplet trap following the standard method described in Section 4.4.2. Droplet volumes were calculated according to the method of Musterd *et al.*, as described in Section 6.3.2 with one exception [106].

The lengths of daughter droplets leaving the droplet trap were measured in the vertically-oriented outgoing collector channels after passing all channel junctions. These measurements followed the standard method described in Section 4.4.2. However, the observed daughter droplets were so small that the channel walls did not confine them, and therefore the method of Musterd *et al.* could not be applied to calculate their volumes [106]. These small daughter droplets were assumed to form spheres in the channels. Their measured radii were smaller than the critical radius required for a spherical droplet to contact an approximately isosceles-triangular channel, calculated using Equation (7-1). In Equation (7-1), w represents channel width, and h represents channel depth. Although this does not consider the actual cross-section of the channels, it predicts a smaller radius than would be predicted considering the actual cross-section. Therefore, it provides a stricter criterion for determining if a droplet was spherical. Thus, the volumes of the small daughter droplets were calculated as spheres, where measured lengths were equivalent to the diameters of the spheres.

$$r = \frac{wh}{w + 2\sqrt{\frac{w^2}{4} + h^2}} \tag{7-1}$$

The volumes of mother droplets approaching the droplet trap, the volumes of resultant daughter droplets and the ratio of these volumes produced at the pressure settings of P_d = 8.06 kPa and P_c = 8.38 kPa are summarized in Table 7-9. The data shown in Table 7-9 were collected over five test runs of each test condition; single droplets or isolated pairs approaching the trap. Two daughter droplets were generated at every splitting event. Table 7-9 shows that droplet splitting only occurred at the first set of bypass channels and never occurred at the second set of bypass channels. The volumes of mother droplets approaching the second set of bypass channels were calculated by subtracting the measured volumes of daughter droplets from the volumes of the mother droplet approaching the droplet trap.

The data in Table 7-9 was then compared to the $V_{daughter}/V_{mother}$ ratios predicted by Equation (2-22) for the first and second set of bypass channels of the Alternate Droplet Trap. When calculating the predicted $V_{daughter}/V_{mother}$ ratios, mother droplets were considered to be present in the unconstricted outgoing channel at the bypass junction. This position was the observed position of droplets when splitting events occurred. Therefore, if a single droplet was being considered when modelling, the droplet was accounted for in the unconstricted outgoing channel, and the main channel was filled only with Continuous Phase. When the first droplet of an isolated pair of droplets was being

considered, the main channel was considered only to contain one droplet. In this case, the first droplet was considered in the unconstricted outgoing channel of the channel junction.

Table 7-9 – A summary of the observed droplet splitting behaviours of Alternate Droplet Trap Iteration 1 considering single droplets and isolated pairs of droplets produced at pressure settings of P_d = 8.06 kPa and P_c = 8.38 kPa. The bypass channel number refers to the set of bypass channels, as defined in Figure 7-13(B). A droplet number of 1 denotes the first droplet to arrive at the droplet trap, and 2 denotes the second droplet to arrive at the droplet trap. All values are reported ± one standard deviation.

Test Condition	Droplet Number	Bypass Channel Number	Mother Droplet Volume [nL]	Daughter Droplet Volume [nL]	$V_{daughter}/V_{mother}$
Single Droplet	1	1	3.71 ± 0.15	0.14 ± 0.01	0.038 ± 0.004
		2	3.44 ± 0.14	0	0
Isolated Pair of Droplets	1	1	3.88 ± 0.08	0.12 ± 0.02	0.031 ±0.006
		2	3.59 ± 0.08	0	0
	2	1	3.80 ± 0.01	0.15 ± 0.01	0.038 ± 0.001
		2	3.50 ± 0.01	0	0

The model of Alternate Droplet Trap described in Section 5.4.1 predicted the $V_{daughter}/V_{mother}$ ratios shown in Table 7-10 following the assumptions stated above. Any predicted negative $V_{daughter}/V_{mother}$ ratios are simply reported as 0. The data shown in Table 7-10 demonstrates that although the droplet splitting model successfully predicts when droplet splitting would occur, the model is perhaps not as predictive as it could be. The model successfully predicted positive $V_{daughter}/V_{mother}$ values when splitting was observed. However, the predicted values did not closely match the observed values. It does provide some predictive ability as to whether droplet splitting would occur at a channel junction but could be refined further to predict the droplet splitting behaviour more accurately.

Table 7-10 – A summary of the observed and predicted $V_{daughter}/V_{mother}$ values of Alternate Droplet Trap Iteration 1 considering single droplets and isolated pairs of droplets produced at pressure settings of P_d = 8.06 kPa and P_c = 8.38 kPa. All columns are as defined in Table 7-9. All values are reported ± one standard deviation.

Test Condition	Droplet Number	Bypass Channel Number	Observed $V_{daughter}/V_{mother}$	Predicted $V_{daughter}/V_{mother}$
Single Droplet	1	1	0.038 ± 0.004	0.034
		2	0	0
Isolated Pair of Droplets	1	1	0.031 ±0.006	0.022
		2	0	0
	2	1	0.038 ± 0.001	0.034
		2	0	0

One of the major assumptions made in the model is that the interfacial tension between the Dispersed Phase and the Continuous Phase is 5 mN m^{-1} (as reported by Bithi *et al.*) [70]. Bashir *et al.* reported an interfacial tension between the Dispersed Phase and the Continuous Phase of 4.5 mN m^{-1}, indicating that the interfacial tension may not be precisely 5 mN m^{-1} [116]. The interfacial tension is an integral value in calculating trapping pressure. Therefore, if a more

accurate value could be determined, modelling droplet splitting behaviour could become more accurate. If the observed $V_{daughter}/V_{mother}$ value for the single droplet test condition is assumed to be correct, then the interfacial tension of the Dispersed Phase and Continuous Phase would be 4.93 ± 0.06 mN m^{-1}. However, based upon the $V_{daughter}/V_{mother}$ values of an isolated pair of droplets, an interfacial tension of 4.91 mN m^{-1} is a better fit for the behaviour of both droplets in the pair. Observed and predicted $V_{daughter}/V_{mother}$ values considering an interfacial tension of 4.91 mN m^{-1} can be seen in Table 7-11.

Table 7-11 – A summary of observed and predicted $V_{daughter}/V_{mother}$ values of Alternate Droplet Trap Iteration 1 considering single droplets and isolated pairs of droplets produced at pressure settings of P_d = 8.06 kPa and P_c = 8.38 kPa and an interfacial tension of 4.91 mN m^{-1}. All columns are as defined in Table 7-9. All values are reported ± one standard deviation.

Test Condition	Droplet Number	Bypass Channel Number	Observed $V_{daughter}/V_{mother}$	Predicted $V_{daughter}/V_{mother}$
Single Droplet	1	1	0.038 ± 0.004	0.040
		2	0	0
Isolated Pair of Droplets	1	1	0.031 ±0.006	0.028
		2	0	0
	2	1	0.038 ± 0.001	0.040
		2	0	0

Although the observed values do not exactly match the predicted values, they are in much closer agreement (to within ± one standard deviation) than when an interfacial tension of 5 mN m^{-1} is assumed. An interfacial tension value of 4.91 mN m^{-1} is a reasonable adjustment given the range of values (4.5 to 5 mN m^{-1}) reported in the literature. Therefore, it is believed that droplet splitting behaviours could be successfully predicted using the method described previously and an interfacial tension of 4.91 mN m^{-1}. Assuming that the same standard deviation applies to this interfacial tension as the one reported above, 4.93 ± 0.06 mN m^{-1}, the interfacial tension would be 4.91 ± 0.06 mN m^{-1}

This standard deviation was derived from the observed $V_{daughter}/V_{mother}$ value for the single droplet test condition. Determining the interfacial tension involves relating the observed $V_{daughter}/V_{mother}$ value to the one predicted by the droplet trap model and the ΔP_{LP} value. This value can then be used to calculate the interfacial tension and depends upon the Laplace pressure and the droplet's r_t value in each channel. The channel width is the primary determinant of the r_t and a significant source of error in the interfacial tension calculation. Based upon the error propagation of the measurement error in each of these values, the expected measurement error in the interfacial tension value is ~25%. This error is relatively large and is primarily due to the high degree of uncertainty in the bypass channel width (7.6%). If the channel widths could be determined with more accuracy, particularly that of the bypass channel, the accuracy of this method could be significantly improved. This method could be a powerful means of measuring the interfacial tension of a dispersed and continuous phase with further refinement.

Furthermore, following this method, it is also predicted that droplets would show splitting behaviours at all of the tested pressure settings in Table 7-8 for an isolated pair of droplets. The

one exception is the lowest pressure settings of P_d = 2.98 kPa and P_c = 3.35 kPa. At these low-pressure settings, no droplet splitting is expected, and none was observed, further indicating that the droplet splitting model is accurate.

It should be noted that this method of predicting droplet splitting at the bypass channel junctions could not be applied to predict the behaviour of the first droplet in a continuous stream of droplets. Because the Droplet Generator takes a long time to reach a steady state (see Section 6.3.4), the main channel resistance could not be accurately determined. Therefore, the pressure distribution of the droplet trap could not be determined. However, it was observed that the $V_{daughter}/V_{mother}$ ratios for the first droplet in a continuous stream of droplets were only slightly higher than the ratio for the first droplet in an isolated pair of droplets. It is thought that the behaviour of the first droplet in a continuous stream of droplets could be predicted in future designs by using the behaviour of the first droplet in an isolated pair of droplets as an approximation.

Verifying this modelling method of predicting droplet splitting with Primary Droplet Trap Iteration 3 was much more difficult, as daughter droplets spent a significant period of time in its long bypass channels. These daughter droplets affected the resistance of the bypass channels, and therefore, the pressure and fluid flow distribution through the droplet trap. Therefore, accurate modelling of pressure conditions in the droplet trap was complex. However, when a single droplet approaching the droplet trap produced at pressure settings of P_d = 8.06 Pa and P_c = 8.38 kPa was considered, the $V_{daughter}/V_{mother}$ ratio could be predicted to be 0.25, using an interfacial tension of 4.91 mN m^{-1}. The observed $V_{daughter}/V_{mother}$ value of this case was 0.19 ± 0.001 (n = 4) across two different devices. While this does not agree with the predicted value, the predicted value still indicates whether droplet splitting is expected.

The modelling method described above could be refined further to provide more accurate predictions of $V_{daughter}/V_{mother}$. Steps towards this have already been taken here by refining the interfacial tension of the Dispersed Phase and Continuous Phase. This model could be improved further by considering the local dimensions of the relevant junctions, including the locally increased depth at a junction and the slight filling of bypass channels by a droplet as it passes a bypass channel. These considerations would require extensive modelling of 3D droplet shapes, which is beyond the scope of this thesis. The predictive abilities of the modelling method described here were sufficient for designing a Primary Droplet Trap and Alternate Droplet Trap in which droplets will not split at the channel junctions. A final set of designs were developed using this predictive method to prevent droplet splitting at bypass channel junctions. Chapter 8 describes the designs of these final droplet traps.

7.7 Summary

Over the course of this project, three iterations of the Primary Droplet Trap and one iteration of the Alternate Droplet Trap were designed, built and tested. The third iteration of the Primary Droplet trap showed some promise but lacked reproducible trapping behaviour. However, the Alternate Droplet Trap was able to reproducibly trap two droplets and hold them in contact with each other for around 1.5 minutes and up to 24 minutes. The lifetime of the trapped droplets was highly variable, and the reasons behind the merging of the trapped droplets are not fully

understood. However, they are thought to be linked to (1) changes in the trapped droplet positions and (2) the pressure applied to the trapped droplets. These behaviours are linked to the compression and rarefaction of the droplet interface, which is linked to DIB stability issues [76].

In all droplet traps, droplet splitting at bypass channels was observed, which reduced the reproducibility of the trapping behaviour and resulted in unpredictable droplet volumes. A model developed by Liang *et al.* for an intentional droplet splitting device could describe the splitting behaviour observed in the tested droplet traps well [105]. This droplet splitting model was then incorporated into the droplet trap design process to design one final set of droplet traps. These droplet traps aimed to address issues with droplet splitting and droplet lifetime and will be described in Chapter 8.

Chapter 8
Final Designs of Droplet Traps

8.1 Introduction

The droplet traps discussed in Chapter 7 showed several issues which prevented the successful trapping of droplets to form DIBs. The most prevalent issues included difficulties in ensuring that trapping channels were well defined and droplet splitting at bypass channel junctions. A final set of droplet trap designs were made to address these issues, improving the consistency of droplet trapping and reducing droplet splitting. Additionally, the final designs were made to implement additional functionalities in droplet trapping, specifically the formation of 1.5D to 2D arrays of droplets of specific sizes.

8.2 Design Changes to Both Trap Designs

Droplet splitting at bypass channel junctions was a significant problem in the preceding droplet trap designs. According to the droplet splitting model discussed in Sections 2.7 and 7.6, the splitting behaviour at bypass channel junctions was affected by the trapping pressure of the bypass channels. Therefore, efforts were made to increase the trapping pressure of the bypass channels, decreasing droplet splitting by preventing droplets from entering the bypass channels.

Increasing the trapping pressure of the bypass channels was accomplished in many of the final designs described in this chapter by widening the unconstricted input channels to the droplet traps. Widening the unconstricted input channel served two purposes. A widened channel decreased the Laplace pressure of droplets in the unconstricted input channel, and it allowed droplets to expand and adopt more spherical shapes. Decreasing the Laplace pressure of droplets in the unconstricted input channel would increase the trapping pressures of both the trapping and bypass channels. Therefore, improving trapping consistency and reducing or preventing droplet splitting. Allowing droplets to expand and adopt more spherical shapes would enable more droplets to be packed into the droplet trap in a potentially ordered 1.5D or even 2D array if the droplets were small enough. Although widening laser-cut microfluidic channels is not common in the author's experience, it was chosen over deepening the unconstricted input channel for a simple reason. Deepening the channel would have little impact on the Laplace pressure of droplets compared to widening the channel, as will be discussed.

It should be noted that these widened channels would not have isosceles-triangular cross-sections and would not have perfectly rectangular cross-sections. For the initial design of these traps, it was assumed that the resistances of the widened channels could be calculated using Equation (3-6). In future work, the cross-section and resistances of these widened channels should be determined and used to verify that the designs presented here would function as intended.

Increasing the trapping pressures of the bypass and trapping channels could also be accomplished by making shallower bypass and trapping channels. However, doing so would also increase the resistance of these channels. Increasing the resistances of these channels would increase the

pressure drop across the droplet trap and may limit any improvements to the trapping pressures. Increases in channel resistance could be limited by decreasing the length of the bypass and trapping channels. However, these channels were already at their minimum length to ensure well defined channel dimensions in the Alternate Droplet Trap design. Only the trapping channels were at their minimum length in the Primary Droplet Trap iteration 3 design. Therefore, widening the input channel to the droplet trap was a much more feasible means of increasing the trapping pressures of the bypass and trapping channels.

8.2.1 Decreasing Laplace Pressure in Unconstricted Input Channel

Considering the model of Musterd *et al.*, droplets in the standard channels used for the Droplet Generator and the unconstricted input channels of the droplet traps are described by Equations (2-18) to (2-20) [106]. These equations calculate the top corner radius, r_t, the cross-sectional area of the droplet body, A_{bd}, and the length of the droplet end caps, L_{cap}.

The top corner radius, r_t, can be used to calculate the Laplace pressure of droplets in the unconstricted input channel if the droplets are longer than twice their end cap length (L_{cap}). Droplets considered in this project fit this criterion. The Laplace pressure (P_{LP}) can be calculated with Equation (2-9) using r_t considering the method described in Section 2.6.1. This method calculates the Laplace pressure of the droplet as $P_{LP} = \gamma/r_t$.

From the above relationship between P_{LP} and r_t for droplets in the unconstricted input channels of droplet traps and Equation (2-18), it can be seen that P_{LP} depends primarily on the channel width, W, and top corner angle, β. The channel depth affects the top corner angle, and therefore, Equation (2-18) could be rewritten in terms of the channel width and channel depth. However, it is important to realize that the r_t is more strongly influenced by the channel width than the channel depth.

For example, for an ideally isosceles-triangular laser-cut channel with a depth of 252 μm and a width of 163 μm, the top corner radius (r_t) would be 28.0 μm. This radius would represent a Laplace pressure (P_{LP}) of 178 Pa. Increasing the channel depth by 10 μm would result in an r_t of 28.4 μm and a P_{LP} of 176 Pa, a decrease in P_{LP} of ~1%. However, if the width were increased by 10 μm, the r_t would be 29.0 μm. This radius would result in a P_{LP} of 172 Pa, representing a 3% decrease in P_{LP}. The depth would need to be increased by 25 μm to achieve the same result. Therefore, increasing the channel width has a more significant effect on decreasing the Laplace pressure than increasing the channel depth. However, it is essential to note that this is an idealized scenario. In practice, the top corner angle β is largely independent of the channel width and depth due to the rounded bottom of the channels. Therefore, changing the depth may have even less effect on the top corner radius and Laplace pressure than in this idealized example.

Increasing the width of the unconstricted input channel would be a much more effective means of increasing the top corner radius than increasing the channel depth. Increasing this radius would decrease the Laplace pressure of the droplets. Decreasing the Laplace pressure of the droplets in the unconstricted input channel would increase the trapping pressures of the trapping and bypass channels. This change would improve droplet trapping consistency and reduce or prevent droplet splitting. Additionally, once the channel is more rectangular in cross-section, changes in depth could be used more effectively to minimize the Laplace pressure further. However, it should be

noted that the method described above is only valid for droplets with sufficient length, droplets that are at least twice as long as their end cap length, L_{cap}.

8.2.2 Reducing Droplet Length to Increase Droplet Packing

Unless droplets are split at a bypass channel junction, they flow through the Droplet Generator channels and droplet trap with a constant volume. As droplets enter a widened channel, they can adopt a more spherical shape while maintaining that constant volume. If the channel walls still constrain the droplets in the widened channel, their new length (L) can be calculated according to Equation (8-1). Equation (8-1) uses the known droplet volume (V), the expected cross-sectional area of the droplet body (A_{bd}) and the length of the droplet end caps (L_{cap}).

$$L = \frac{V}{A_{bd}} + \frac{2}{3}L_{cap} \tag{8-1}$$

If the value of L calculated using Equation (8-1) is positive, then the droplet is still constrained by the channel walls, and its length can be determined. If the value of L calculated using Equation (8-1) is negative, the droplet is no longer constrained by the channel walls and would be expected to form an ellipsoid or sphere in the channel. Therefore, if droplets with sufficiently small volumes can be produced, they will no longer be bound by the channel walls as they enter the widened input channel of a droplet trap. They can then be positioned not only along the channel length but in one and a half or two dimensions in the droplet trap, depending on the width of the channel and volume of the droplets. In other words, when droplets with a sufficiently small volume enter a widened input channel to a droplet trap, they can be positioned beside one another and not only along the length of the channel but also across the channel. These small droplet volumes would allow for the formation of 1.5D or 2D arrays of trapped droplets similar to the work of Elani *et al.* (Figure 1-7) [48].

Implementing such a system of packing droplets unconstrained by the channel walls may be challenging in a droplet trap. The droplets may be reduced to a volume where the trapping pressure of the droplet trap is significantly reduced and no longer effective. However, once the droplets form spheres in the widened input channel, their Laplace pressure becomes relatively easy to determine, and the operating conditions of the traps can be altered accordingly.

8.2.3 Changes to Design Process

The droplet traps described in this chapter followed the design processes outlined in Sections 5.3.1 and 5.4.1 closely but with one change. The droplet traps were designed such that the ratio of the droplet flow rate through a bypass channel to the flow rate entering the bypass channel junction was less than zero. This requirement was used to prevent droplet splitting, according to the droplet splitting model outlined in Section 2.7. Other than this, there were no changes to the design process of the droplet traps.

8.3 Primary Droplet Trap Final Design

The final Primary Droplet Trap Design used the channel layout shown in Figure 8-1. In Figure 8-1, light green lines represent input/output channels that are part of R_s or R_{Tu}, and blue lines represent bypass channels (R_B). Dark green (grass green) lines represent type 2 bypass channels (R_{B1}), grey lines represent type three bypass channels (R_{B2}), and cyan lines represent trapping channels that are part of R_{Tc}. The channel dimensions required for this droplet trap design are detailed in Table 8-1, labelled with their corresponding resistivities. Every line in Figure 8-1 has a proportional width to the targeted channel width.

The input and output channels of the trap (r_{Tu}) were widened to be twice as wide as the standard main channel of the Droplet Generator (r_s). Widening the channels was intended to be accomplished by cutting three parallel channels, each spaced apart by 80 μm. This method was expected to result in a channel with a similar depth to the standard main channel of the Droplet Generator but was twice as wide. This method has not been tested directly; however, preliminary testing with other laser settings indicated that channels with this width could be made by cutting multiple channels in parallel (data not shown).

These dimensions resulted in the following trapping pressures: ΔP_{Trap} = 228 Pa, ΔP_{vent} = 151 Pa, $\Delta P_{vent,B1}$ = 162 Pa, $\Delta P_{vent,B2}$ = 171 Pa where ΔP_{Vent} refers to the trapping pressure of the R_B channels, $\Delta P_{vent,B1}$ refers to the trapping pressure of the R_{B1} channels and $\Delta P_{vent,B2}$ refers to the trapping pressure of the R_{B2} channel. Compared to the third iteration of the Primary Droplet Trap, these trapping pressures increased by 24 Pa, 38 Pa, 37 Pa, and 33 Pa, respectively, because of the widened input channel.

As with the earlier iterations of the Primary Droplet Trap, the final design of the Primary Droplet Trap was expected to function in the same way as the first iteration of the Primary Droplet Trap. Droplets were expected to be trapped following the process depicted in Figure 7-2.

The main change to the design from the third iteration of the Primary Droplet Trap was the widened input and output channels for the droplet trap. The widened input and output channels increased the trapping pressures of each bypass and trapping channel and decreased the pressure drop across each channel, reducing the risk of droplet splitting. The trapping channels were also made more closely spaced to accommodate for droplets becoming shorter in the widened channels. The trapping channel spacing was decreased to 150 μm. It is thought that by including time delays between cutting each trapping channel, well-defined channel dimensions can be obtained, unlike in the first iteration of the Primary Droplet Trap (Section 7.2).

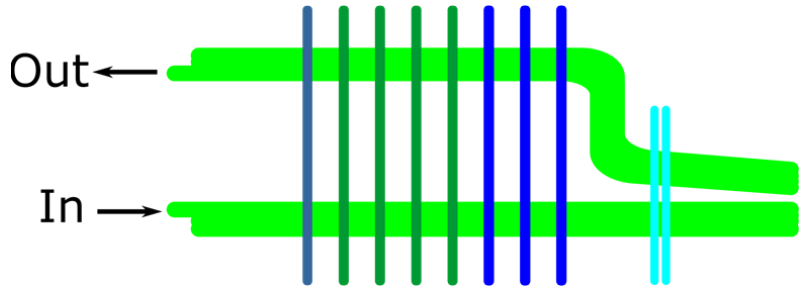

Figure 8-1 – The layout of the final design of the Primary Droplet Trap, blue, dark green (grass green) and grey lines represent bypass channels, light green lines represent input/output channels, and cyan lines represent the trapping channels. The lines in this layout are proportionally as wide as the expected bonded channel widths for each channel type specified in Table 8-1.

Table 8-1 – The required channel types for use in the final design of the Primary Droplet Trap. The r_{Tu} channels are cut with the same laser settings at the r_s channels but with three parallel lines spaced apart by 80 µm. Channel dimensions were based on previously collected data from channels cut with these laser settings. Additional laser parameters common to all channel types were that the cuts were performed at 1000 Hz and focused on the material surface (z = 0).

Channel Type	**r_{Tc}**	**r_{B1}**	**r_{B2}**	**r_{B3}**	**r_s**	**r_{Tu}**
Laser Line Colour	Cyan	Blue	Grass Green	Grey	Green	Green
Number of Passes	2 Pass	2 Pass	2 Pass	2 Pass	2 Pass	2 Pass
Cutting Order	6	3	4	5	2	2
Laser Power [%]	2.7	3.2	3.1	3	3.5	3.5
Laser Speed [%]	1	1	1	1	0.5	0.5
Unbonded Channel Depth [µm]	84 ± 6.3	119 ± 9.3	112 ± 10.9	110 ± 9.1	265 ± 5.6	265 ± 5.6
Unbonded Channel Width [µm]	108 ± 7.3	135 ± 3.8	130.3 ± 6.3	126 ± 8.6	170 ± 0.5	334
Bonded Channel Depth [µm]	81 ± 6.0	114 ± 8.9	107 ± 10.5	105 ± 8.7	252 ± 14.4	252 ± 14.4
Bonded Channel Width [µm]	90 ± 6.1	112 ± 3.2	108 ± 5.2	104 ± 7.1	163 ± 14.0	334

The droplet trap was designed to be operated at a pressure setting of P_d = 8.06 kPa and P_c = 8.38 kPa. At this setting, based on the results of testing Droplet Generators with the third iteration of the Primary Droplet Trap, droplets with lengths of ~342 ± 15 µm were expected to be produced. Once in the droplet trap, the droplets were expected to become spherical and have a radius of ~102 µm. Therefore, multiple droplets (more than three) could be trapped in the droplet trap at one time and begin to form an array of droplets. These spherical droplets are expected to have slightly lower trapping pressures, about 10 Pa lower than those detailed above. However, based on the modelling of the droplet trap, this is not expected to be an issue. Longer droplets confined by the channel walls can be made by simply increasing the dispersed phase input pressure to a point where droplets with lengths of ~480 µm in the main channel of the Droplet Generator are produced.

Eight parallel bypass channels made with three different types of bypass channels were used to maintain consistency with the third iteration of the Primary Droplet Trap design. Table 8-2 shows the pressure drop across each bypass channel, volumetric flow rate through each bypass channel and droplet flow rate ratio. Each value was calculated considering a continuous stream of droplets approaching an empty droplet trap. The values were calculated using pressures corresponding to 82.5 cm of Dispersed Phase and 1 m of Continuous Phase (P_d = 8.06 kPa and P_c = 8.38 kPa). Under these conditions, an R_s value of 2.02 x 10^{14} Pa s m^{-3} is expected. As shown in Table 8-2, no droplet splitting is expected to occur at any bypass channel junction as the droplet flow rate ratio ($Q_{B,N}/Q_{in}$) is less than zero at every bypass channel junction.

Table 8-2 – The expected pressure drops across, flow rates through, and droplet flow rate ratios of each bypass channel in the final Primary Droplet Trap design. The values were calculated considering an empty droplet trap, and a continuous stream of droplets is produced with pressures corresponding to 82.5 cm of Dispersed Phase and 1 m of Continuous Phase.

Bypass Channel Number (*N*)	**Pressure Drop [Pa]**	**Flow Rate [m^3 s^{-1}]**	$Q_{B,N}/Q_{in}$
Channel 8	128	2.76 x 10^{-12}	-0.03
Channel 7	126	3.12 x 10^{-12}	-0.03
Channel 6	123	3.12 x 10^{-12}	-0.03
Channel 5	121	3.14 x 10^{-12}	-0.04
Channel 4	119	3.17 x 10^{-12}	-0.05
Channel 3	118	3.93 x 10^{-12}	-0.05
Channel 2	117	3.89 x 10^{-12}	-0.06
Channel 1	116	3.85 x 10^{-12}	-0.08

The data presented in Table 8-2 assumes that the Droplet Generator would perform as if it was in a steady state, which may not reflect the actual performance of the droplet trap with respect to droplet splitting (see Section 7.6). Therefore, additional modeling was performed to determine whether droplet splitting would occur when a pair of isolated droplets were generated and sent to the droplet trap. An isolated pair of droplets represented a more stable Droplet Generator state which could be accurately modelled. While droplet splitting was expected to occur at the bypass channels when using pressure settings corresponding to 82.5 cm of Dispersed Phase and 1 m of Continuous Phase (data not shown), no droplet splitting was predicted when operating at slightly lower pressures. No droplet splitting was predicted when operating at pressures corresponding to ~65 cm of Dispersed Phase and ~85 cm of Continuous Phase and sending only an isolated pair of droplets to the droplet trap as all values of $Q_{B,N}/Q_{in}$ are negative in Table 8-3.

Therefore, based on the data shown in Table 8-2 and Table 8-3, the final iteration of the Primary Droplet Trap design was expected to be effective and capable of trapping two droplets at reasonable pressure settings. Additionally, should sufficiently small droplets be produced, it may be possible to trap more than two droplets in this droplet trap, leading to the development of traps that can produce arrays of DIBs.

Table 8-3 – The expected pressure drops across, flow rates through, and droplet flow rate ratios of each bypass channel in the final Primary Droplet Trap design. The values were calculated considering an empty droplet trap, and a pair of droplets is produced with pressures of ~65 cm of Dispersed Phase and ~85 cm of Continuous Phase.

Bypass Channel Number (N)	Pressure Drop [Pa]	Flow Rate [$m^3\ s^{-1}$]	$Q_{B,N}/Q_{in}$
Channel 8	154	3.33×10^{-12}	-0.01
Channel 7	151	3.76×10^{-12}	-0.008
Channel 6	148	3.77×10^{-12}	-0.01
Channel 5	146	3.79×10^{-12}	-0.01
Channel 4	143	3.83×10^{-12}	-0.02
Channel 3	142	4.75×10^{-12}	-0.01
Channel 2	140	4.69×10^{-12}	-0.02
Channel 1	139	4.65×10^{-12}	-0.02

8.4 Alternate Droplet Trap Final Design – Version 1

The first version of the final Alternate Droplet Trap designs used the channel layout shown in Figure 8-2. In Figure 8-2, green lines represent input/output channels that are part of R_S or R_{Tu}, grey lines represent bypass channels (R_B), and cyan lines represent trapping channels that are part of R_{Tc}. The channel dimensions required for this droplet trap design are detailed in Table 8-4, labelled with their corresponding resistivities. Every line in Figure 8-2 has a proportional width to the targeted channel width. With the channel dimensions shown in Table 8-4, a ΔP_{Trap} of 165 Pa and a ΔP_{vent} of 108 Pa were expected.

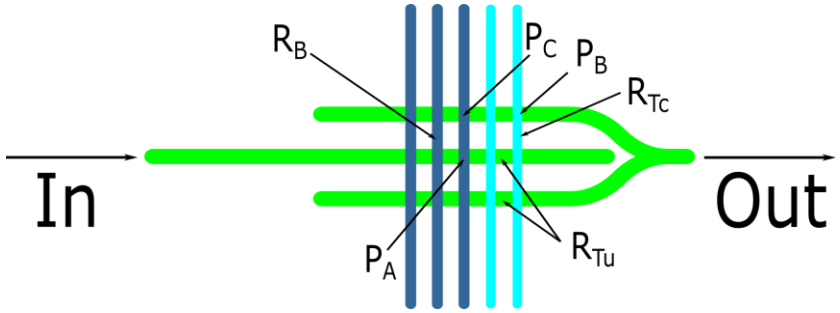

Figure 8-2 – The layout of the first version of the final Alternate Droplet Trap design. Grey lines represent bypass channels, green lines represent unconstricted channels, and cyan lines represent constricted trap channels. The lines in the layout are proportionally as wide as the expected bonded channel widths for each channel type as specified in Table 8-1. The layout is marked with relevant equivalent circuit element names.

The first version of the final set of Alternate Droplet Trap designs included one extra bypass channel to minimize pressure spikes across the trapped droplets when a third droplet was temporarily trapped at a set of bypass channels. Otherwise, the design is the same as that presented in Section 7.5.1.

The trap was designed following the model described in Section 5.4 but adapted to account for an additional bypass channel. The extra set of bypass channels would allow the temporarily trapped droplet to be displaced without blocking all bypass channels and causing a spike in the pressure across the trapped droplets. The performance of droplet traps with several additional bypass

channels was also modelled. However, it was found that performance gains were minimal beyond having three sets of bypass channels.

Table 8-4 – The three required channel types for use in the first version of the final Alternate Droplet Trap design. Channel dimensions were based on previously collected data from channels cut with these laser settings. Additional laser parameters common to all channel types were that the cuts were performed at 1000 Hz and focused on the material surface (z = 0).

Channel Type	r_{Tc}	r_B	r_s **and** r_{Tu}
Laser Line Colour	Cyan	Grey	Green
Number of Passes	2 Pass	2 Pass	2 Pass
Cutting Order	6	5	2
Laser Power [%]	2.7	3	3.5
Laser Speed [%]	1	1	0.5
Unbonded Channel Depth [µm]	84 ± 6.3	110 ± 9.1	265 ± 5.6
Unbonded Channel Width [µm]	108 ± 7.3	126 ± 8.6	170 ± 0.5
Bonded Channel Depth [µm]	81 ± 6.0	105 ± 8.7	252 ± 14.4
Bonded Channel Width [µm]	90 ± 6.1	104 ± 7.1	163 ± 14.0

The droplet trap was modelled considering the Droplet Generator operating at a pressure setting of P_d = 8.06 kPa and P_c = 8.38 kPa and producing droplets at a 14% volume ratio. The modelling results can be seen in Table 8-5. In Table 8-5, even-numbered flow rates correspond to the flow through a trapping or bypass channel. Odd-numbered flow rates correspond to the flows between trapping or bypass channel junctions, following the same numbering convention seen in Figure 5-5. It can be seen in Table 8-5 that in all trapping states, No Trapped Droplets, One Trapped Droplet and Two Trapped Droplets, the ratios of $Q_{2,droplet}/Q_3$, $Q_{4,droplet}/Q_5$, $Q_{6,droplet}/Q_7$ and $Q_{8,droplet}/Q$ are negative. These results indicate that no splitting will occur at any bypass channels. Additionally, the flow rate towards the trapping channels is always the strongest at any bypass channel junction, guaranteeing resistive sorting.

In all trapping states, the pressure across the trapping channels (P_A - P_B) and the pressure across the bypass channels (P_A - P_C) are lower than ΔP_{Trap} and ΔP_{vent}, respectively. Therefore, droplets will be successfully trapped at the constricted trapping channels though they will also be temporarily trapped at the bypass channels. However, it is expected that any droplets held up at the bypass channels will be ejected before any droplet would be ejected through a constricted trapping channel. This behaviour was observed in the previous iteration of the Alternate Droplet Trap.

As with the final Primary Droplet Trap design, the data presented in Table 8-5 considers the Droplet Generator operating at a steady state which may not be the most accurate representation of the droplet splitting behaviour. Therefore, the droplet trap performance was also examined, considering an isolated pair of droplets approaching the trap.

Table 8-5 – The values of the parameters necessary to judge the droplet trap's effectiveness. All values were calculated assuming the droplet trap only contained the continuous phase aside from droplets held in trapping positions.

Parameter	No Trapped Droplets	One Trapped Droplet	Two Trapped Droplets
Q_1 [m^3 s^{-1}]	4.69 x 10^{-12}	-	-
Q_2 [m^3 s^{-1}]	2.04 x 10^{-12}	2.66 x 10^{-12}	-
Q_3 [m^3 s^{-1}]	8.76 x 10^{-12}	5.32 x 10^{-12}	-
Q_4 [m^3 s^{-1}]	4.19 x 10^{-12}	5.19 x 10^{-12}	6.01 x 10^{-12}
Q_5 [m^3 s^{-1}]	1.72 x 10^{-11}	1.59 x 10^{-11}	1.20 x 10^{-11}
Q_6 [m^3 s^{-1}]	4.59 x 10^{-12}	5.37 x 10^{-12}	5.96 x 10^{-12}
Q_7 [m^3 s^{-1}]	2.63 x 10^{-11}	2.63 x 10^{-11}	2.39 x 10^{-11}
Q_8 [m^3 s^{-1}]	5.78 x 10^{-12}	6.52 x 10^{-12}	6.94 x 10^{-12}
$Q_{2,droplet}/Q_3$	-0.75	N/A	N/A
$Q_{4,droplet}/Q_5$	-0.48	-0.46	N/A
$Q_{6,droplet}/Q_7$	-0.30	-0.27	-0.27
$Q_{8,droplet}/Q$	-0.18	-0.16	-0.12
P_A - P_B [Pa]	45	61	71
P_A - P_C [Pa]	36	45	52

When producing an isolated pair of droplets at the pressure settings P_d = 8.06 kPa and P_c = 8.38 kPa, corresponding to 82.5 cm of the Dispersed Phase and 1 m of the Continuous Phase, droplet splitting might occur at the first bypass channel encountered by the droplets (see Table 8-6). This splitting could be easily avoided by operating at a slightly lower pressure setting, like pressures corresponding to ~65 cm Dispersed Phase and ~85 cm Continuous Phase. Therefore, the first version of the final set of Alternate Droplet Trap designs was expected to be effective and trap two droplets at conditions close to those normally used to operate Droplet Generators.

Table 8-6 – The predicted droplet splitting ratios for the first version of the Final Droplet Trap considering an isolated pair of droplets approaching the droplet trap, one of which is present in the first channel junction produced with pressures corresponding to 82.5 cm of Dispersed Phase and 1 m of Continuous Phase.

Parameter	No Trapped Droplets	One Trapped Droplet
$Q_{2,droplet}/Q_3$	-0.24	N/A
$Q_{4,droplet}/Q_5$	-0.08	-0.23
$Q_{6,droplet}/Q_7$	-0.03	-0.02
$Q_{8,droplet}/Q$	0.01	0.03

8.5 Alternate Droplet Trap Final Design – Version 2

The second version of the final Alternate Droplet Trap design used the channel layout shown in Figure 8-3. In Figure 8-3, green lines represent input/output channels that are part of R_S or R_{Tu}, grey lines represent bypass channels (R_B), and cyan lines represent trapping channels that are part of R_{Tc}. The channel dimensions required for this droplet trap design are detailed in Table 8-7, labelled with their corresponding resistivities. Every line in Figure 8-3 has a proportional width to the targeted channel width.

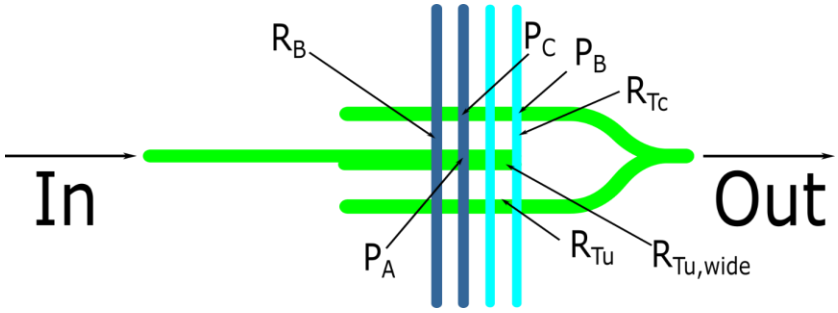

Figure 8-3 – The layout of the second version of the final Alternate Droplet Trap design, grey lines represent bypass channels, green lines represent unconstricted channels, and cyan lines represent constricted trap channels. The lines in the layout are proportionally as wide as the expected bonded channel widths for each channel type as specified in Table 8-7. The layout is marked with relevant equivalent circuit element names.

The second version of the final set of Alternate Droplet Trap designs was identical to the Alternate Droplet Trap described in Section 7.5 but had a widened input channel and no dead-end channels at the trapping positions. The input channel was widened to increase the Laplace pressure differences of the bypass and trapping channels to prevent droplet splitting and improve trapping reproducibility. The dead-end channel was removed to prevent droplets from shifting their positions once trapped to improve the lifetime of trapped droplets. The trap was designed following the model described in Section 5.4 but adapted for a widened input channel.

The input channel width was increased to 1.5 times the width of a standard channel by cutting two channels in parallel but separated by 80 µm. This method was expected to result in a channel width of 254 µm rather than 163 µm (Table 8-7). This widened input channel resulted in a ΔP_{Trap} of 212 Pa and a ΔP_{vent} of 156 Pa, which were much higher than the trapping pressures in the version of the design with a regularly sized channel (Section 8.4).

When operating the Droplet Generator at pressures of P_d = 8.06 kPa and P_c = 8.38 kPa, corresponding to 82.5 cm of Dispersed Phase and 1 m of Continuous Phase, droplets were expected to have lengths of 342 ± 15 µm. As they entered the widened input channel of the droplet trap, they were expected to shrink slightly to a length of approximately 276 µm. The trapping channel spacing was kept constant at 300 µm. Therefore, droplets may or may not make contact depending on the final droplet positioning as they arrive in the trap. This spacing was not thought to be an issue, but if it is found to be, slightly larger droplets can be made by increasing the dispersed phase input pressure without compromising the trap performance.

Table 8-7 – The required channel types in the second version of the final Alternate Droplet Trap design. The r_{Tu} channels are cut with the same laser settings at the r_s channels but with two parallel lines separated by 80 μm. Channel dimensions were based on previously collected data from channels cut with these laser settings. Additional laser parameters common to all channel types were that the cuts were performed at 1000 Hz and focused on the material surface (z = 0).

Channel Type	**r_{Tc}**	**r_B**	**r_s and r_{Tu}**	**$r_{Tu,wide}$**
Laser Line Colour	Cyan	Grey	Green	Green
Number of Passes	2 Pass	2 Pass	2 Pass	2 Pass
Cutting Order	6	5	2	2
Laser Power [%]	2.7	3	3.5	3.5
Laser Speed [%]	1	1	0.5	0.5
Unbonded Channel Depth [μm]	84 ± 6.3	110 ± 9.1	265 ± 5.6	265 ± 5.6
Unbonded Channel Width [μm]	108 ± 7.3	126 ± 8.6	170 ± 0.5	254
Bonded Channel Depth [μm]	81 ± 6.0	105 ± 8.7	252 ± 14.4	252 ± 14.4
Bonded Channel Width [μm]	90 ± 6.1	104 ± 7.1	163 ± 14.0	254

As with the first version of the final set of Alternate Droplet Trap designs, the droplet trap was modelled considering a pressure setting of P_d = 8.06 kPa and P_c = 8.38 kPa and producing droplets at a 14% volume ratio. The results of this modelling can be seen in Table 8-8. It can be seen that in all trapping states, No Trapped Droplets, One Trapped Droplet and Two Trapped Droplets, the ratios of $Q_{2,droplet}/Q_3$, $Q_{4,droplet}/Q_5$ and $Q_{6,droplet}/Q$ are negative. Therefore, no splitting will occur at any bypass channels. As in Table 8-5, the even-numbered flow rates in Table 8-8 correspond to the flow through a trapping or bypass channel, and odd-numbered flow rates correspond to the flows between trapping or bypass channel junctions. The numbering followed the same numbering convention seen in Figure 5-5. In all trapping states, no droplet splitting is predicted as all the flow rate ratios are negative, and the flow rate towards the trapping channels is the strongest at every channel junction.

In all trapping states, the pressure across the trapping channels (P_A - P_B) and the pressure across the bypass channels (P_A - P_C) are much lower than ΔP_{Trap} and ΔP_{vent}, respectively. Therefore, droplets will be successfully trapped at the constricted trapping channels, but another droplet will be temporarily trapped at the bypass channels. It is expected that any droplets held by the bypass channels will be ejected before any droplet would be ejected through a constricted trapping channel.

As with the previous two designs discussed in this chapter, the data presented in Table 8-8 considers the Droplet Generator operating at a steady state which may not be the most accurate representation of the droplet splitting behaviour. Therefore, the droplet trap performance when an isolated pair of droplets approached the trap was also examined.

Table 8-8 – The values of the parameters necessary to judge the second version of the final set of Alternate Droplet Trap's effectiveness. All values were calculated assuming the droplet trap only contained the continuous phase aside from droplets held in trapping positions.

Parameter	No Trapped Droplets	One Trapped Droplet	Two Trapped Droplets
Q_1 [m^3 s^{-1}]	6.78×10^{-12}	-	-
Q_2 [m^3 s^{-1}]	3.03×10^{-12}	3.76×10^{-12}	-
Q_3 [m^3 s^{-1}]	1.28×10^{-11}	7.53×10^{-12}	-
Q_4 [m^3 s^{-1}]	6.18×10^{-12}	7.58×10^{-12}	9.51×10^{-12}
Q_5 [m^3 s^{-1}]	2.52×10^{-11}	2.27×10^{-11}	1.90×10^{-11}
Q_6 [m^3 s^{-1}]	6.12×10^{-12}	7.36×10^{-12}	9.15×10^{-12}
$Q_{2,droplet}/Q_3$	-0.62	N/A	N/A
$Q_{4,droplet}/Q_5$	-0.47	-0.46	N/A
$Q_{6,droplet}/Q$	-0.32	-0.25	-0.21
P_A - P_B [Pa]	67	82	101
P_A - P_C [Pa]	54	66	79

When considering an isolated pair of droplets approaching the second version of the final set of Alternate Droplet Trap designs produced with pressure settings of P_d = 8.06 kPa and P_c = 8.38 kPa, no droplet splitting is predicted to occur at any bypass channels (Table 8-9). Therefore, the droplet trap is expected to perform well at these settings without splitting any droplets and trap two droplets at the trapping channels. Additionally, droplets with lengths of 242 μm are expected to take on nearly spherical shapes in the widened input channel, and arrays of droplets in the droplet trap may be produced with droplets of this length.

Table 8-9 – The predicted droplet splitting ratios for the second version of the final set of Alternate Droplet Trap designs considering an isolated pair of droplets approaching the droplet trap, one of which is present in the first channel junction produced with pressures corresponding to 82.5 cm of Dispersed Phase and 1 m of Continuous Phase.

Parameter	No Trapped Droplets	One Trapped Droplet
$Q_{2,droplet}/Q_3$	-0.31	N/A
$Q_{4,droplet}/Q_5$	-0.20	-0.22
$Q_{6,droplet}/Q$	-0.16	-0.11

8.6 Alternate Droplet Trap Final Design – Version 3

The third version of the final Alternate Droplet Trap design used the channel layout shown in Figure 8-4. In Figure 8-4, green lines represent input/output channels that are part of R_s or R_{Tu}, grey lines represent bypass channels (R_B), and cyan lines represent trapping channels that are part of R_{Tc}. The channel dimensions required for this droplet trap design are detailed in Table 8-10, labelled with their corresponding resistivities. Every line in Figure 8-4 has a proportional width to the targeted channel width.

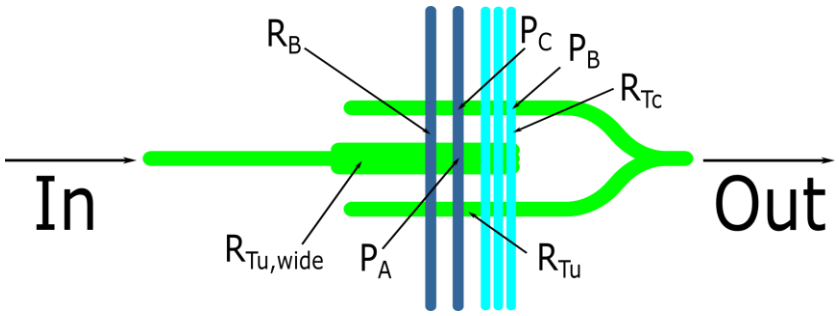

Figure 8-4 – The layout of the droplet trap design, grey lines represent bypass channels, green lines represent unconstricted channels, and cyan lines represent constricted trap channels. The lines in the layout are proportionally as wide as the expected bonded channel widths for each channel type, as specified in Table 8-10. The layout is marked with relevant equivalent circuit element names.

The third version of the final set of Alternate Droplet Trap designs was identical to the second version of the final set of Alternate Droplet Traps described in Section 8.5 except for two changes. The input channel was made even wider, and a third trapping channel was added to the design.

The input channel was made twice as wide as the standard channels by cutting three channels in parallel but separated by 80 µm. This method was expected to result in a channel width of 334 µm rather than 163 µm (Table 8-10). This wider input channel resulted in a ΔP_{Trap} of 228 Pa and a ΔP_{vent} of 171 Pa, which was much higher than the trapping pressures in the version of the design with a regularly sized channel (Section 8.4).

With such a wide channel, droplets entering the input channel were expected to become dramatically shorter. Therefore, a third input channel was added to ensure contact between trapped droplets. The spacing between the trapping channels was also reduced to 150 µm. It is thought that by including time delays between cutting each trapping channel, well-defined channel dimensions can be obtained, unlike in the first iteration of the Primary Droplet Trap (Section 7.2).

Droplets produced at P_d = 8.06 kPa and P_c = 8.38 kPa, corresponding to 82.5 cm of the Dispersed Phase and 1 m of the Continuous Phase, were expected to have lengths of 342 ± 15 µm before entering the widened input channel of the droplet trap. Once in the droplet trap, the droplets were expected to become spherical and have a radius of ~102 µm. Therefore, multiple droplets (more than three) could be trapped in the droplet trap at one time and begin to form an array of droplets. These spherical droplets are expected to have slightly lower trapping pressures, about 10 Pa lower than those detailed above. However, based on the modelling of the droplet trap, this is not expected to be an issue. Longer droplets confined by the channel walls can be made by simply increasing the dispersed phase input pressure to a point where droplets with lengths of ~480 µm in the main channel of the Droplet Generator are produced.

Table 8-10 – The required channel types in the third version of the final Alternate Droplet Trap design. The r_{Tu} channels are cut with the same laser settings at the r_s channels but with three parallel lines separated by 80 μm. Channel dimensions were based on previously collected data from channels cut with these laser settings. Additional laser parameters common to all channel types were that the cuts were performed at 1000 Hz and focused on the material surface (z = 0).

Channel Type	**r_{Tc}**	**r_B**	**r_s and r_{Tu}**	**$r_{Tu,wide}$**
Laser Line Colour	Cyan	Grey	Green	Green
Number of Passes	2 Pass	2 Pass	2 Pass	2 Pass
Cutting Order	6	5	2	2
Laser Power [%]	2.7	3	3.5	3.5
Laser Speed [%]	1	1	0.5	0.5
Unbonded Channel Depth [μm]	84 ± 6.3	110 ± 9.1	265 ± 5.6	265 ± 5.6
Unbonded Channel Width [μm]	108 ± 7.3	126 ± 8.6	170 ± 0.5	334
Bonded Channel Depth [μm]	81 ± 6.0	105 ± 8.7	252 ± 14.4	252 ± 14.4
Bonded Channel Width [μm]	90 ± 6.1	104 ± 7.1	163 ± 14.0	334

The behaviour of the droplet trap was modelled considering it to be integrated into the Droplet Generator producing a continuous stream of droplets at P_d = 8.06 kPa and P_c = 8.38 kPa (corresponding to 82.5 cm of Dispersed Phase and 1 m of Continuous Phase) with a 14% relative volume ratio. The results of this modelling can be seen in Table 8-11. It can be seen that no droplet splitting is predicted to occur in any of the trapping states and that all $P_A - P_B$ values are lower than ΔP_{Trap}. Additionally, the $P_A - P_C$ values are lower than the value of ΔP_{vent}. These results indicate that droplets will be successfully trapped at the constricted trapping channels, although some will be temporarily trapped at the bypass channels. As with the previous versions of the Alternate Droplet Trap, this is not expected to be an issue.

The data presented in Table 8-11 considers the droplet trap performance when the Droplet Generator operates at a steady state. As mentioned previously, this condition is not the most accurate predictor of droplet splitting behaviour. Therefore, the behaviour of the droplet trap when an isolated set of three droplets is made and sent to the droplet trap at P_d = 8.06 kPa and P_c = 8.38 kPa was also modelled. The results of this modelling can be seen in Table 8-12 and provide the same conclusions as stated regarding the data shown in Table 8-11. Therefore, the third version of the final set of Alternate Droplet Trap designs was expected to be successful and suitable for droplet trapping experiments. Additionally, this droplet trap design shows promise and progress towards generating an ordered array of trapped droplets and DIBs.

Table 8-11 – The values of the parameters necessary to judge the effectiveness of the third version of the final set of Alternate Droplet Trap designs. All values were calculated assuming the droplet trap only contained the continuous phase aside from droplets held in trapping positions. A continuous stream of droplets approached the droplet trap made with pressures corresponding to 82.5 cm of Dispersed and 1 m of Continuous Phase was also assumed.

Parameter	No Trapped Droplets	One Trapped Droplet	Two Trapped Droplets	Three Trapped Droplets
Q_1 [m^3 s^{-1}]	5.95×10^{-12}	-	-	-
Q_2 [m^3 s^{-1}]	2.79×10^{-12}	3.80×10^{-12}	-	-
Q_3 [m^3 s^{-1}]	1.15×10^{-11}	7.60×10^{-12}	-	-
Q_4 [m^3 s^{-1}]	2.64×10^{-12}	3.59×10^{-12}	3.83×10^{-12}	-
Q_5 [m^3 s^{-1}]	1.68×10^{-11}	1.48×10^{-11}	7.67×10^{-12}	-
Q_6 [m^3 s^{-1}]	5.33×10^{-12}	7.78×10^{-12}	7.69×10^{-12}	1.34×10^{-11}
Q_7 [m^3 s^{-1}]	2.74×10^{-12}	3.14×10^{-11}	2.31×10^{-11}	2.68×10^{-11}
Q_8 [m^3 s^{-1}]	5.14×10^{-12}	7.47×10^{-12}	7.36×10^{-12}	1.28×10^{-11}
$Q_{2,droplet}/Q_3$	-0.79	N/A	N/A	N/A
$Q_{4,droplet}/Q_5$	-1.22	-1.24	N/A	N/A
$Q_{6,droplet}/Q_7$	-0.53	-0.38	-0.52	N/A
$Q_{8,droplet}/Q$	-0.39	-0.32	-0.29	-0.11
P_A - P_B [Pa]	57	78	83	141
P_A - P_C [Pa]	46	67	67	116

Table 8-12 – The predicted droplet splitting ratios for the third version of the final set of Alternate Droplet Trap designs considering an isolated set of three droplets approaching the droplet trap, one of which is present in the first channel junction produced with pressures corresponding to 82.5 cm of Dispersed Phase and 1 m of Continuous Phase.

Parameter	No Trapped Droplets	One Trapped Droplet	Two Trapped Droplets
$Q_{2,droplet}/Q_3$	-0.48	-	-
$Q_{4,droplet}/Q_5$	-0.75	-0.79	-
$Q_{6,droplet}/Q_7$	-0.31	-0.22	-0.30
$Q_{8,droplet}/Q$	-0.24	-0.19	-0.16

8.7 Summary

Chapter 8 provides an overview of four droplet trap designs meant to address the issues encountered in the droplet trap designs tested as part of this project. The most common change was to widen the input channel of the droplet trap. This change increased the trapping pressures of the trapping and bypass channels which was predicted to prevent droplet splitting at bypass channel junctions.

The final Primary Droplet Trap design was expected to be more effective than previous designs. However, it could not be operated at the standard pressure setting of P_d = 8.06 kPa and P_c = 8.38 kPa, but was expected to operate satisfactorily at a slightly lower pressure setting.

Three versions of the Alternate Droplet Trap design were also discussed, each expected to be effective. The addition of an extra bypass channel to the Alternate Droplet Trap was expected to allow it to be operated effectively at a pressure setting just below P_d = 8.06 kPa and P_c = 8.38 kPa.

In contrast, the widening of the input channel was expected to allow the Alternate Droplet Trap to be operated effectively at this pressure setting and even allow the formation of arrays of trapped droplets. While these designs were never fabricated and tested, they represent a logical next step to create an ordered array of trapped DIBs.

Chapter 9
Conclusions and Future Work

9.1 Thesis Summary

This thesis describes the development of T-junction droplet generators (Droplet Generators), which incorporated Primary Droplet Traps or Alternate Droplet Traps. These devices were designed for the automated formation of droplet interface bilayers. They can serve as a platform to study transmembrane proteins in conditions representative of their *in vivo* environments. Devices were constructed using low-cost materials and fabrication methods and can be operated with little specialized training. They have been designed to be simple, time-efficient and cost-effective alternatives to the traditionally-used methods of forming lipid bilayers, which can be time-consuming and require specialized equipment, extensive training and large quantities of reagents. Future development of these devices intends to add more functionality to these devices, including creating large ordered arrays of DIBs.

The work began by establishing the fluid properties necessary to design and fabricate microfluidic devices (Chapter 2 and Chapter 3). Then models of (1) microfluidic droplet generators operated using pressure-driven fluid flows (Chapter 4) and (2) droplet trapping behaviours (Chapter 5) were developed. A Droplet Generator was then designed, tested and determined to be suitable for the formation of DIBs in a microfluidic droplet trap (Chapter 6). Several iterations of droplet traps were designed and tested in an iterative process. This process led to refinements in the model of droplet trapping behaviours to prevent the splitting of droplets entering the droplet traps (Chapter 7). Final versions of the droplet traps were designed using these refinements. They were expected to address issues affecting previous droplet traps, namely droplet splitting and inconsistent DIB lifetimes (Chapter 8). Additionally, these final designs laid the groundwork for creating ordered arrays of DIBs in laser-cut microfluidic devices. Although not directly demonstrated in this project, these are thought to be capable of reliably producing DIBs for future use in the study of transmembrane proteins.

In Chapter 2, the physics required to understand the behaviour of designed microfluidic devices was established. These physics included explanations of fluid flows through channel-based microfluidic devices, fluidic resistance of channels and the role of Laplace pressure. This analysis guided the materials and fabrication choices discussed in Chapter 3. It also determined which fluid and materials properties needed to be determined before device design.

In this thesis, devices were fabricated by laser cutting channels into layers of PMMA using a CO_2 laser. Devices were designed to be operated using gravity to generate the necessary fluid flows and blue-dyed deionized water and mineral oil loaded with 2 wt% Span 80 to form droplets. The surface properties of PMMA, viscosities and densities of the fluids and fluidic resistances of the laser-cut channels were verified through testing. Verifying these properties allowed the behaviours of the designed devices to be accurately predicted. This testing required the development of a simple purpose-built viscometer and the adaptation of previously-made microfluidic devices to

determine the channel resistance of laser-cut microfluidic channels. No analytical solutions for the resistance of a laser-cut channel have been reported in the literature. Therefore, determining a method of predicting the resistance of these channels was particularly important.

Chapter 4 introduced the refinements to the theoretical approach used to model the behaviours of microfluidic T-junction droplet generators, and Chapter 5 described the refinements to the theory of droplet traps. Droplet Generators in this project were based on a T-junction design because of the author's familiarity with this design through their previous work [83]. A model of a T-junction droplet generator using pressure-driven fluid flow was developed based primarily on the work of Glawdel and Ren [85]. This model was used to ensure the reliable production of droplets suitable for droplet trapping applications. This design process required serious consideration as channel resistances in droplet generators inherently fluctuate as droplets are produced, which necessitated a balance of design parameters and input pressures.

A Droplet Generator without an integrated droplet trap was then designed, fabricated and tested that was capable of reliably producing droplets that were (1) twice as long as they were wide and (2) varied in volume by no more than 10%. Droplet Generators reliably produced droplets that were 342 ± 15 μm long, ~106 μm wide and had volumes of 2.52 ± 0.24 nL. These droplets varied run to run by no more than 5% at a dispersed phase input pressure (P_d) of 8.06 kPa and a continuous phase input pressure (P_c) of 8.38 kPa. Droplet Generators with an integrated droplet trap reliably produced droplets that were 313 ± 28 μm long, ~97 μm wide and had volumes of 2.11 ± 0.21 nL. These droplet volumes varied between devices by no more than 10% at the pressure settings of P_d = 8.06 kPa and P_c = 8.38 kPa. Therefore, the designed Droplet Generators met the critical success criteria related to droplet length and droplet volume and were suitable for droplet trapping applications.

During testing, the droplet generator model was refined based on the observed behaviour of the devices. Specifically, using a predictive model of droplet shape developed by Musterd *et al.*, a new method was developed for approximating the effect a droplet has on channel resistance [106]. To the best of the author's knowledge, a predictive method for the resistance effects of droplets in microfluidic channels based on their cross-sectional shape, like the one described in Chapter 6, has not been described previously in the literature.

Once it was established that Droplet Generators reliably produced droplets suitable for droplet trapping applications, a series of droplet traps were designed and tested, as described in Chapter 7. Several early design iterations suffered from unforeseen fabrication and design issues related to maintaining well-defined channels and unexpected operational issues. Operational issues were primarily droplets splitting as they entered the droplet traps and inconsistent DIB lifetimes.

Droplet splitting behaviour is not often discussed in the literature in the context of droplet trapping. Models of intentional droplet splitting microfluidic devices were therefore adapted to predict droplet splitting behaviour in droplet traps. This adapted model was applied to new channel geometries and was validated using the observed behaviours of droplets in the designed droplet traps. While droplet splitting was frequently observed when droplets entered the droplet traps, reproducible trapping of two droplets in contact with each other was observed for the Alternate

Droplet Trap. Experimentation with various pressure settings resulted in identifying appropriate values for P_d and P_c to avoid droplet splitting and trap droplets. However, these pressure settings were much lower than the settings at which the droplet traps were designed to operate. The last iterations of the droplet traps described in Chapter 7 did have some measure of success in holding two droplets stationary and in contact with one another to form precursor DIB structures.

Based on the observed behaviours and identified issues of the droplet traps described in Chapter 7, a final set of droplet traps was designed and described in Chapter 8. In addition to addressing the issues identified in testing previous versions of the droplet trap, these droplet traps potentially incorporated additional functionality. These droplet traps might allow the formation of 1.5D or 2D ordered arrays of droplets of specific sizes and improve the lifetime of trapped droplets.

This work demonstrated that the designed microfluidic platform could successfully generate DIBs for the study of transmembrane proteins. Improvements could still be made to result in more consistent device performance and progress towards creating an ordered array of DIBs and studying complex transmembrane proteins. This platform could be developed further in several exciting ways to improve its applicability and versatility in studying transmembrane proteins. The immediate next steps would be to test the final designs proposed in Chapter 8 and demonstrate the formation of actual DIBs using lipids. The only change necessary in the operating procedure to form actual DIBs would be to use an amphiphilic lipid instead of, or in addition to, the surfactant (Span 80) in the Continuous Phase.

9.2 Contributions

This thesis made several unique contributions to the field of microfluidics.

This thesis relied on laser-cut microfluidic channels and required the determination of their fluidic resistance. No analytical solutions exist for the fluidic resistance for channels with the near isosceles-triangular geometry of laser-cut channels. Therefore, a method of calculating the fluidic resistance was determined based on existing standard approximations of fluidic resistance for channels with arbitrary geometries (Section 3.7). This work resulted in the development of Equation (3-6). This method may be helpful to other researchers using microfluidic devices with laser-cut channels. Further work should be done to verify that Equation (3-6) is valid for a wide range of channel dimensions.

Typically, Laplace pressure has been calculated for droplets in channels with standard cross-sections, most frequently rectangular cross-sections. The principal radii of curvature can therefore be analytically determined. Laser-cut channels do not have standard cross-sections. Consequently, a different approach was required to calculate Laplace pressure in laser-cut microfluidic channels. Specifically, a method was developed for calculating the Laplace pressure difference between two channels based on the change in surface energy of a droplet (Section 5.2). This method provided a more versatile means for calculating the trapping pressure, i.e., the Laplace pressure difference, of a droplet trap and accounted for the changes in channel wall contact.

A droplet generating device was designed, mainly following the model of Glawdel and Ren, that could successfully produce droplets with volumes that varied by less than 5%. This performance

was not compromised when a droplet trap was incorporated into the droplet generator. The model of Musterd *et al.* for the cross-sectional shape of a droplet in a microfluidic channel was verified using this device and used to calculate droplet volume from top-down measurements [106]. That model was then applied to approximate the effects of droplets on the resistance of a microfluidic channel. The application of this model helped demonstrate that the droplet generator model agreed with the observed droplet generating behaviour (Section 6.3.3). To the best of the author's knowledge, such an approximation of the resistive effects of droplets has not been reported in the literature.

A model of droplet splitting at channel junctions with asymmetrical dimensions was verified by comparing its predictions to the behaviour of droplet traps in this thesis. This model, proposed by Liang *et al.*, had not been verified previously with junctions of asymmetrical dimensions. It was subsequently adapted to improve the design of droplet traps to prevent droplet splitting [105]. Droplet traps were designed with this model incorporated into the design process, which were expected to trap droplets and form preliminary arrays of droplets successfully; however, these designs were not tested.

9.3 Future Work

There are a number of ways that this work could be extended further to (1) further refine the new models of droplet behaviour proposed in this thesis or (2) be more applicable to the study of transmembrane proteins.

A less complicated droplet generator could be designed and tested to focus solely on more accurate measurement of increases in channel resistance. Such a design would further refine the approximation of the droplet resistance increase factor discussed in Section 6.3.3. For example, a device with a main channel composed of one long straight channel with a constant orientation would allow the droplet resistance increase factor to be determined without considering the contributions of droplets in channels with different orientations and dimensions. The resistance behaviour of individual droplets could be studied by measuring the average flow rate through the device's main channel containing only one droplet. This method would eliminate potential variations in the droplet resistance increase factor because of droplets with inconsistent sizes, although this was not a significant factor in this work.

Further, a device with simpler channel geometries than the complex droplet trap geometries used in this project could be used to test the model of droplet splitting at channel junctions. Such a device would allow for more well-defined channel geometries and, therefore, better-defined droplet shapes to be considered, potentially increasing the model's accuracy.

Most importantly, droplet generators with integrated droplet traps should be tested with lipids capable of forming DIBs. Doing so would verify that (1) DIBs are indeed formed by droplets in contact with one another within the droplet trap and (2) the lifespan of the DIBs is sufficiently long to allow the study of transmembrane proteins. Performing this experiment is the logical next step to test the fabricated devices, considering the targeted study of transmembrane proteins.

The most commonly used lipids in the study of DIBs are 1,2-dioleoyl-sn-glycero-3-phosphocholine ("DOPC") and 1,2-diphytanoyl-sn-glycero-3-phosphocholine ("DPhPC"), although, DPhPC is less biologically relevant than DOPC and other less commonly used lipids [6], [42], [46], [48], [58]. Either DOPC or DPhPC could be used with the Dispersed Phase and Continuous Phase used in this project and would be expected to form lipid bilayers. The lipids would displace the Span 80 in the Continuous Phase at the interface between two trapped droplets to form DIBs [40].

One of the advantages of using DIBs to create lipid bilayers to study transmembrane proteins is their ability to form asymmetrical lipid bilayers. Creating asymmetrical bilayers would be accomplished using the lipid-in technique of forming DIBs in microfluidic systems (see Section 1.1.3). The lipid-in technique would require a droplet generator capable of creating two types of droplets, one containing each variety of lipid to be used [46], [47]. The existing Droplet Generators with their integrated droplet traps could easily be adapted to achieve this by arranging two Droplet Generators in parallel.

Adapting the Droplet Generator to produce two types of droplets would involve a design where the output end of the main channels of each device are combined and flow into a third combined output channel. Preliminary modelling of this design (data not shown) suggests that the stability of the individual Droplet Generators would not be significantly affected as long as each device is designed using the methods described in Chapter 2 and Chapter 4 of this thesis. The only additional requirement would be that the resistance of the combined output channel is smaller than the resistance of the main channel of each device, respectively. A droplet trap could then be integrated into the combined output channel. Droplets produced by each device providing input into the combined output channel could be trapped to form DIBs. This design would also enable the creation of asymmetric DIBs or DIBs with a chemical stimulant for a transmembrane protein on only one side of the bilayer [34], [42], [44], [46]–[48], [50], [64]. This capability could be a valuable technique for the directional stimulation of transmembrane proteins in DIBs. Alternatively, on-chip valving could be included to simplify the process of making droplets of two types by simply switching specific dispersed phase input channels to generate and order droplets of different types.

To provide more functionality to droplet generators with integrated droplet traps in studying transmembrane proteins, interaction with the formed DIBs would be beneficial. If electrophysiological responses of transmembrane proteins are of interest, then electrodes could be added to the device. These would allow for electrical signals to be sent to the DIBs. Electrodes could be incorporated using through-holes in the well layer of the droplet trapping devices. Agar-coated silver electrodes could be inserted into the through-holes to contact the droplets forming DIBs of interest [46], [47], [64]. Alternatively, if a suitable fabrication method is determined, planar electrodes could be incorporated onto the surface of the well layer of the droplet trapping devices. These would be able to contact droplets involved in forming DIBs [6], [60], [77], [88]. These are more difficult to use in the context of DIBs, as they require droplets to contact the channel wall. However, alternating current signals could be used to capacitively couple with

droplets across an insulating layer of the continuous phase. Hybrid bilayer structures could also be formed to allow direct contact of droplets with the planar electrodes [60], [139]–[141].

An optical method of interrogating transmembrane proteins could also be used, either with or without an electrical interrogation method. There are a vast number of optical detection methods that have been used in microfluidic devices for a variety of applications. Part of the initial motivation for this thesis was to study heme-containing proteins related to mitochondrial functions (e.g., cytochromes) using Raman spectroscopy. Certain heme groups, like those in cytochrome bc1, exhibit Raman spectra related to the spin of the iron atoms in the hemes. When excited with a 532 nm laser, these related spectra have increased signal levels due to resonance effects [82], [142]–[144]. It is thought that these proteins could be studied with the equipment available in the Backhouse Lab, a Raman spectroscopy system with a 532 nm laser, at temperatures close to physiologically-relevant temperatures due to this increase in signal strength. One potential limitation of the current Droplet Generators is that they have been fabricated with PMMA, which has strong Raman signatures that could interfere with correct characterization. Similar polymer-based microfluidic devices have been shown to reduce Raman signals by about a factor of four [73]. However, this potential drawback of using a polymer device could be addressed by fabricating devices in glass or using glass instead of PMMA as the well layer of the devices. Alternatively, other signal-enhancing Raman techniques could be used, which would likely be necessary to study quantum biological effects.

One such technique would be surface-enhanced Raman spectroscopy ("SERS"), which has been used previously in microfluidic devices [73], [139], [145]. The operating principle of SERS is relatively simple; molecules within ~15-25 nm of a nanostructured noble metal surface. Such a SERS active surface, typically gold or silver, enhances Raman signals with localized surface plasmon resonances created when an excitation laser strikes the SERS active surface [82], [139], [142]. This technique generally enhances the Raman signals by a factor of $10^4 – 10^8$, allowing even minuscule Raman signals to be detected [139], [146]. While this technique requires close proximity with a nanostructured noble metal surface, this could be addressed by forming a hybrid bilayer system on an integrated noble metal electrode [60], [139]–[141]. However, this may impact the physiological relevance of the bilayer. Perhaps a better way of introducing a SERS active surface to a DIB would be to put a SERS active metal colloid into one of the droplets of an asymmetrical DIB. If the colloid has been functionalized to selectively bind to a lipid membrane or target protein, the surface of the interface might become decorated in colloid particles [73]. This coating on a bilayer would allow for the SERS active surface to be in close proximity to the target protein without compromising the integrity of the DIB or requiring the integration of electrodes into the device.

Any of the above methods, integration of electrodes or optical detection systems, would allow for the practical study of the behaviour of transmembrane proteins. The integration of electrodes to measure electrophysiological behaviours of transmembrane proteins can be applied to discovering new drugs required to interact with transmembrane proteins or the selective mixing of droplets for chemical production [47], [60]. Raman spectroscopy could allow for the structure of transmembrane proteins to be better understood, aiding in developing novel drugs and

understanding unique protein functions. This knowledge could then be applied to other novel biomaterials and the development of novel diagnostic tools for disease detection [146]–[150]. Regardless of the method of interrogation used, it is clear that the microfluidic platform designed in this thesis has the potential for further exciting developments and future work for the study of transmembrane proteins. Eventually, even quantum biological effects of proteins may be studied with future versions of the device in a low-cost and automated manner in physiologically representative environments.

References

[1] J. McFadden and J. Al-Khalili, *Life on the Edge: The Coming of Age of Quantum Biology*. London: Bantam Press, 2014.

[2] N. Lambert, Y. Chen, Y. Cheng, C. Li, G. Chen, and F. Nori, "Quantum biology," *Nat. Phys.*, vol. 9, pp. 10–18, 2012, doi: 10.1038/nphys2474.

[3] J. C. Brookes, "Quantum effects in biology: golden rule in enzymes, olfaction, photosynthesis and magnetodetection," *Proc. R. Soc. A*, vol. 473, pp. 1–28, 2017.

[4] L. Tiefenauer and S. Demarche, "Challenges in the Development of Functional Assays of Membrane Proteins," *Materials (Basel).*, vol. 5, pp. 2205–2242, 2012, doi: 10.3390/ma5112205.

[5] J. Xu, T. K. Vanderlick, and P. A. Beales, "Lytic and Non-Lytic Permeabilization of Cardiolipin- Containing Lipid Bilayers Induced by Cytochrome c," *PLoS One*, vol. 8, no. 7, pp. 1–9, 2013, doi: 10.1371/journal.pone.0069492.

[6] M. Nguyen, B. Srijanto, C. P. Collier, S. T. Retterer, and S. A. Sarles, "Hydrodynamic trapping for rapid assembly and in situ electrical characterization of droplet interface bilayer arrays," *Lab Chip*, vol. 16, pp. 3576–3588, 2016, doi: 10.1039/c6lc00810k.

[7] E. Romero, V. I. Novoderezhkin, and R. Van Grondelle, "Quantum design of photosynthesis for bio-inspired solar-energy conversion," *Nature*, vol. 543, pp. 355–365, 2017, doi: 10.1038/nature22012.

[8] F. Pichierri, "A quantum mechanical analysis of the light-harvesting complex 2 (LH2) from purple photosynthetic bacteria: Insights into the electrostatic effects of transmembrane helices," *BioSystems*, vol. 103, no. 2, pp. 132–137, 2011, doi: 10.1016/j.biosystems.2010.08.006.

[9] J. D. Roscioli, S. Ghosh, A. M. Lafountain, H. A. Frank, and W. F. Beck, "Quantum Coherent Excitation Energy Transfer by Carotenoids in Photosynthetic Light Harvesting," *J. Phys. Chem. Lett.*, vol. 8, pp. 5141–5147, 2017, doi: 10.1021/acs.jpclett.7b01791.

[10] A. Ishizaki and G. R. Fleming, "Theoretical examination of quantum coherence in a photosynthetic system at physiological temperature," *Proc. Natl. Acad. Sci.*, vol. 106, no. 41, pp. 17255–17260, 2009.

[11] M. Ben-Nun, F. Molnar, H. Lu, J. C. Phillips, T. J. Marinez, and K. Schulten, "Quantum dynamics of the femtosecond photoisomerization of retinal in bacteriorhodopsin," *Faraday Discuss.*, vol. 110, pp. 447–462, 1998.

[12] G. Panitchayangkoon *et al.*, "Direct evidence of quantum transport in photosynthetic light-harvesting complexes," *Proc. Natl. Acad. Sci.*, vol. 108, no. 52, pp. 1–5, 2011, doi: 10.1073/pnas.1105234108.

[13] D. J. Heyes, M. Sakuma, S. P. De Visser, and N. S. Scrutton, "Nuclear Quantum Tunneling in the Light-activated Enzyme," *J. Biol. Chem.*, vol. 284, no. 6, pp. 3762–3767, 2009, doi: 10.1074/jbc.M808548200.

[14] H. W. Rathbone, J. A. Davis, K. A. Michie, S. C. Goodchild, N. O. Robertson, and P. M. G. Curmi, “Coherent phenomena in photosynthetic light harvesting: part one — theory and spectroscopy,” *Biophys. Rev.*, vol. 10, pp. 1427–1441, 2018.

[15] H. W. Rathbone, J. A. Davis, K. A. Michie, S. C. Goodchild, N. O. Robertson, and P. M. G. Curmi, “Coherent phenomena in photosynthetic light harvesting: part two — observations in biological systems,” *Biophys. Rev.*, vol. 10, pp. 1443–1463, 2018.

[16] R. Akiyama, A. Yoshimori, T. Kakitani, and Y. Shichida, “Analysis of the temperature dependence of femtosecond excited state dynamics of bacteriorhodopsin by spin-boson model,” *Chem. Phys. Lett.*, vol. 4, no. 256, pp. 165–171, 1996.

[17] R. F. Dallinger, J. R. Nestor, and T. G. Spiro, “Resonance Coherent Anti-Stokes Raman Scattering Evidence for Out-of-Plane Heme Iron Displacement within 6 ns of CO Dissociation in CO Hemoglobin,” *J. Am. Chem. Soc.*, vol. 100, no. 19, pp. 6251–6252, 1978, doi: 10.1021/ja00487a058.

[18] L. Ujj, G. H. Atkinson, M. Sheves, N. Livnah, and M. Ottolenghi, “Vibrational Spectrum of K-590 Containing 13 C 14 , 15 Retinal : Picosecond Time-Resolved Coherent Anti-Stokes Raman Spectroscopy of the Room Temperature Bacteriorhodopsin Photocycle,” *J. Phys. Chem.*, no. 96, pp. 12066–12075, 1996, doi: 10.1021/jp961131i.

[19] J. Terner, D. F. Vom, C. Paddock, R. B. Miles, and T. Spiro, “Picosecond Resonance Raman Spectrum of the Oxyhemoglobin Photoproduct. Evidence for an Electronically Excited State,” *J. Phys. Chem.*, vol. 86, no. 6, pp. 859–861, 1982, doi: 10.1021/j100395a001.

[20] R. Lingle, X. Xu, H. Zhu, S. Yu, and J. B. Hopkins, “Picosecond Raman Study of Energy Flow in a Photoexcited Heme Protein,” *J. Phys. Chem.*, vol. 95, no. 23, pp. 9320–9331, 1991, doi: 10.1021/j100176a053.

[21] D. Carbonera, “Optically detected magnetic resonance (ODMR) of photoexcited triplet states,” *Photosynth. Res.*, vol. 102, pp. 403–414, 2009, doi: 10.1007/s11120-009-9407-5.

[22] T. Yang *et al.*, “Zero-field magnetic resonance of the photo-excited triplet state of pentacene at room temperature Zero-field magnetic resonance of the photo-excited triplet state of pentacene at room temperature,” *J. Chem. Phys.*, vol. 113, no. 24, pp. 11194–11201, 2000.

[23] S. Santabarbara *et al.*, “Chlorophyll triplet states associated with Photosystem I and Photosystem II in thylakoids of the green alga Chlamydomonas reinhardtii,” *Biochim. Biophys. Acta*, vol. 1767, pp. 88–105, 2007, doi: 10.1016/j.bbabio.2006.10.007.

[24] R. H. Clarke, W. R. Leenstra, and W. G. Hagar, “Observation of a triplet state in chlorophyll protein 668 via optically detected magnetic resonance,” *FEBS Lett.*, vol. 99, no. 1, pp. 207–209, 1979, doi: 10.1016/0014-5793(79)80280-X.

[25] H. A. Frank, M. B. Mclean, and K. Sauer, “Triplet States in Photosystem I of spinach chloroplasts and subchloroplast particles,” *Proc. Natl. Acad. Sci.*, vol. 76, no. 10, pp. 4464–4468, 1979.

[26] D. Carbonera, G. Giacometti, and G. Agostini, “FDMR of Carotenoid and Chlorophyll Triplets in Light-Harvesting Complex LHCII of Spinach,” *Appl. Magn. Reson.*, vol. 3, pp. 859–872, 1992.

[27] E. L. Frankevich, A. I. Pristupa, and V. I. Lesin, “Magnetic Resonance of Short-Lived Triplet Exciton Pairs Detected by Fluorescence Modulation at Room Temperature,” *Chem. Phys. Lett.*, vol. 47, no. 2, pp. 304–308, 1977.

[28] D. Mishra, T. Z. Markus, R. Naaman, M. Kettner, B. Göhler, and H. Zacharias, “Spin-dependent electron transmission through bacteriorhodopsin embedded in purple membrane,” *Proc. Natl. Acad. Sci.*, vol. 110, no. 37, pp. 14872–14876, 2013, doi: 10.1073/pnas.1311493110/-/DCSupplemental.www.pnas.org/cgi/doi/10.1073/pnas.1311493110.

[29] T. Kitagawa, Y. Kyogoku, and M. I. Saitoib, “Nature of the Iron-Ligand Bond in Ferrous Low Spin Hemoproteins Studied by Resonance Raman Scattering,” *J. Am. Chem. Soc.*, vol. 98, no. 17, pp. 5169–5173, 1976, doi: 10.1021/ja00433a019.

[30] M. Allen-benton, H. E. Findlay, and P. J. Booth, “Probing membrane protein properties using droplet interface bilayers,” *Exp. Biol. Med.*, vol. 244, pp. 709–720, 2019, doi: 10.1177/1535370219847939.

[31] L. C. M. Gross, A. J. Heron, S. C. Baca, and M. I. Wallace, “Determining Membrane Capacitance by Dynamic Control of Droplet Interface Bilayer Area,” *Langmuir*, vol. 27, pp. 14335–14342, 2011, doi: 10.1021/la203081v.

[32] P. Mueller, D. O. Rudin, H. T. Tien, and W. C. Wescott, “Methods for the Formation of Single Bimolecular Lipid Membranes in Aqueous Solution,” *J. Phys. Chem.*, vol. 67, pp. 534–535, 1963.

[33] M. Montal and P. Mueller, “Formation of Bimolecular Membranes from Lipid Monolayers and a Study of their Electrical Properties,” *Proc. Natl. Acad. Sci.*, vol. 69, no. 12, pp. 3561–3566, 1972.

[34] H. Bayley *et al.*, “Droplet interface bilayers,” *Mol. Biosyst.*, vol. 4, no. 12, pp. 1191–1208, 2008, doi: 10.1039/b808893d.Droplet.

[35] M. Traikia, D. E. Warschawski, O. Lambert, J. Rigaud, and P. F. Devaux, “Asymmetrical Membranes and Surface Tension,” *Biophyscial J.*, vol. 83, pp. 1443–1454, 2002.

[36] P. F. Devaux, “Static and dynamic lipid asymmetry in cell membranes,” *Biochemistry*, vol. 30, no. 5, pp. 1163–1173, 1991, doi: 10.1021/bi00219a001.

[37] S. E. Horvath and G. Daum, “Lipids of mitochondria,” *Prog. Lipid Res.*, vol. 52, no. 4, pp. 590–614, 2013, doi: 10.1016/j.plipres.2013.07.002.

[38] I. Köper, “Insulating tethered bilayer lipid membranes to study membrane proteins,” *Mol. Biosyst.*, vol. 3, no. 10, pp. 651–657, 2007, doi: 10.1039/b707168j.

[39] I. K. Vockenroth, D. Fine, A. Dodobalapur, A. T. A. Jenkins, and I. Köper, “Tethered bilayer lipid membranes with giga-ohm resistances,” *Electrochem. commun.*, vol. 10, no. 2, pp. 323–328, 2008, doi: 10.1016/j.elecom.2007.12.018.

[40] D. Jeong, H. Jang, S. Q. Choi, and M. C. Choi, “Enhanced stability of freestanding lipid bilayer and its stability criteria,” *Sci. Rep.*, vol. 6, no. 38158, pp. 1–7, 2016, doi: 10.1038/srep38158.

[41] Y. Tsuji, R. Kawano, T. Osaki, K. Kamiya, N. Miki, and S. Takeuchi, “Droplet-based lipid bilayer system integrated with microfluidic channels for solution exchange,” *Lab Chip*, vol. 13, no. 8, pp. 1476–1481, 2013, doi: 10.1039/c3lc41359d.

[42] M. J. Booth, V. R. Schild, F. G. Downs, and H. Bayley, “Functional Aqueous Droplet Networks,” *Mol. Biosyst.*, vol. 13, pp. 1658–1691, 2017, doi: 10.1039/c7mb00192d.

[43] P. Mruetusatorn, J. B. Boreyko, G. A. Venkatesan, S. A. Sarles, D. G. Hayes, and C. P. Collier, “Dynamic Morphologies of Microscale Droplet Interface Bilayers,” *Soft Matter*, vol. 10, pp. 2530–2538, 2014, doi: 10.1039/c3sm53032a.

[44] M. A. Holden, D. Needham, and H. Bayley, “Functional Bionetworks from Nanoliter Water Droplets,” *J. Am. Chem. Soc.*, vol. 129, no. 27, pp. 8650–8655, 2007, doi: 10.1021/ja072292a.

[45] M. A. Czekalska, T. S. Kaminski, K. Makuch, and P. Garstecki, “Passive and parallel microfluidic formation of droplet interface bilayers (DIBs) for measurement of leakage of small molecules through artificial phospholipid membranes,” *Sensors Actuators B Chem.*, vol. 286, pp. 258–265, 2019.

[46] M. A. Czekalska, T. S. Kaminski, M. Horka, S. Jakiela, and P. Garstecki, “An Automated Microfluidic System for the Generation of Droplet Interface Bilayer Networks,” *Micromachines*, vol. 8, no. 93, pp. 1–11, 2017, doi: 10.3390/mi8030093.

[47] M. A. Czekalska, T. S. Kaminski, S. Jakiela, K. T. Sapra, H. Bayley, and P. Garstecki, “A droplet microfluidic system for sequential generation of lipid bilayers and transmembrane electrical recordings,” *Lab Chip*, vol. 15, pp. 541–548, 2015, doi: 10.1039/c4lc00985a.

[48] Y. Elani, A. J. DeMello, X. Niu, and O. Ces, “Novel technologies for the formation of 2-D and 3-D droplet interface bilayer networks,” *Lab Chip*, vol. 12, pp. 3514–3520, 2012, doi: 10.1039/c2lc40287d.

[49] J. L. Poulos, S. A. Portonovo, H. Bang, and J. J. Schmidt, “Automatable lipid bilayer formation and ion channel measurement using sessile droplets,” *J. Phyriscs Condens. Matter*, vol. 22, pp. 1–6, 2010, doi: 10.1088/0953-8984/22/45/454105.

[50] G. Villar, A. J. Heron, and H. Bayley, “Formation of droplet networks that function in aqueous environments,” *Nat. Nanotechnol.*, vol. 6, pp. 803–808, 2011, doi: 10.1038/nnano.2011.183.

[51] G. Villar, A. D. Graham, and H. Bayley, “A Tissue-Like Printed Material,” *Science (80-.).*, vol. 340, no. 6128, pp. 48–52, 2013.

[52] S. Ma, N. Mukherjee, E. Mikhailova, and H. Bayley, “Gel Microrods for 3D Tissue Printing,” *Adv. Biosyst.*, vol. 1, pp. 1–11, 2017, doi: 10.1002/adbi.201700075.

[53] Y. Xia and G. M. Whitesides, “Soft Lithography,” *Annu. Rev. Mater. Sci.*, vol. 28, pp. 153–184, 1998.

[54] B. K. Gale *et al.*, “A Review of Current Methods in Microfluidic Device Fabrication and Future Commercialization Prospects,” *Inventions*, vol. 3, no. 60, pp. 1–25, 2018, doi: 10.3390/inventions3030060.

[55] S. Park *et al.*, “Silicones for Stretchable and Durable Soft Devices: Beyond Sylgard-184,” *Appl. Mater. Interfaces*, vol. 10, pp. 11261–11268, 2018, doi: 10.1021/acsami.7b18394.

[56] Y. Lin, C. Gao, D. Gritsenko, R. Zhou, and J. Xu, “Soft lithography based on photolithography and two-photon polymerization,” *Microfluid. Nanofluidics*, vol. 22, no. 9, pp. 1–11, 2018, doi: 10.1007/s10404-018-2118-5.

[57] A. K. Au, W. Huynh, L. F. Horowitz, and A. Folch, “3D-Printed Microfluidics,” *Angew. Chemie - Int. Ed.*, vol. 55, pp. 3862–3881, 2016, doi: 10.1002/anie.201504382.

[58] N. E. Barlow, G. Bolognesi, A. J. Flemming, N. J. Brooks, M. C. Barter, and O. Ces, “Multiplexed droplet interface bilayer formation,” *Lab Chip*, vol. 16, pp. 4653–4657, 2016, doi: 10.1039/C6LC01011C.

[59] D. Wong and C. L. Ren, “Microfluidic droplet trapping, splitting and merging with feedback controls and state space modelling,” *Lab Chip*, vol. 16, pp. 3317–3329, 2016, doi: 10.1039/c6lc00626d.

[60] C. Priest, S. Herminghaus, and R. Seemann, “Controlled electrocoalescence in microfluidics: Targeting a single lamella,” *Appl. Phys. Lett.*, vol. 89, no. 134101, pp. 1–3, 2006, doi: 10.1063/1.2357039.

[61] C. Priest, S. Herminghaus, and R. Seemann, “Generation of monodisperse gel emulsions in a microfluidic device,” *Appl. Phys. Lett.*, vol. 88, pp. 1–3, 2006, doi: 10.1063/1.2164393.

[62] J. H. Kim, J. Choi, J. Y. Sim, W. C. Jeong, S. Yang, and S. Kim, “Ordered Packing of Emulsion Droplets toward the Preparation of Adjustable Photomasks,” *Langmuir*, vol. 30, pp. 5404–5411, 2014, doi: 10.1021/la5007692.

[63] A. C. Hatch *et al.*, “1-Million droplet array with wide-field fluorescence imaging for digital PCR,” *Lab Chip*, vol. 11, pp. 3838–3845, 2011, doi: 10.1039/c1lc20561g.

[64] P. H. King, G. Jones, H. Morgan, M. R. R. De Planque, and K. Zauner, “Interdroplet bilayer arrays in millifluidic droplet traps from 3D-printed moulds,” *Lab Chip*, vol. 14, pp. 722–729, 2014, doi: 10.1039/c3lc51072g.

[65] P. Carreras, Y. Elani, R. V Law, N. J. Brooks, J. M. Seddon, and O. Ces, “A microfluidic platform for size-dependent generation of droplet interface bilayer networks on rails,” *Biomicrofluidics*, vol. 9, pp. 1–7, 2015, doi: 10.1063/1.4938731.

[66] T. Nisisako, S. A. Portonovo, and J. J. Schmidt, “Microfluidic passive permeability assay using nanoliter droplet interface lipid bilayers,” *Analyst*, vol. 138, pp. 6793–6800, 2013, doi: 10.1039/c3an01314f.

[67] J. Wang, M. Jin, T. He, G. Zhou, and L. Shui, “Microfluidic Induced Controllable Microdroplets Assembly in Confined Channels,” *Micromachines*, vol. 6, pp. 1331–1345, 2015, doi: 10.3390/mi6091331.

[68] B. Schlicht and M. Zagnoni, “Droplet-interface-bilayer assays in microfluidic passive networks,” *Sci. Rep.*, vol. 5, pp. 1–8, 2015, doi: 10.1038/srep09951.

[69] P. M. Korczyk, L. Derzsi, S. Jakiela, and P. Garstecki, “Microfluidic traps for hard-wired

operations on droplets," *Lab Chip*, vol. 13, pp. 4096–4102, 2013, doi: 10.1039/c3lc50347j.

[70] S. S. Bithi and S. A. Vanapalli, "Behavior of a train of droplets in a fluidic network with hydrodynamic traps," *Biomicrofluidics*, vol. 4, pp. 1–10, 2010, doi: 10.1063/1.3523053.

[71] C. H. J. Schmitz, A. C. Rowat, S. Köster, and D. A. Weitz, "Dropspots: A picoliter array in a microfluidic device," *Lab Chip*, vol. 9, no. 1, pp. 44–49, 2009, doi: 10.1039/b809670h.

[72] C. E. Stanley *et al.*, "A microfluidic approach for high-throughput droplet interface bilayer (DIB) formation," *Chem. Commun.*, vol. 46, no. 10, pp. 1620–1622, 2010, doi: 10.1039/b924897h.

[73] I. J. Jahn *et al.*, "Surface-enhanced Raman spectroscopy and microfluidic platforms: challenges, solutions and potential applications," *Analyst*, vol. 142, pp. 1022–1047, 2017, doi: 10.1039/c7an00118e.

[74] C. Iliescu, H. Taylor, M. Avram, J. Miao, and S. Franssila, "A practical guide for the fabrication of microfluidic devices using glass and silicon," *Biomicrofluidics*, vol. 6, pp. 1–16, 2012.

[75] D. N. Freitas, A. Mongersun, H. Chau, and I. E. Araci, "Tunable soft lithography molds enable rapid-prototyping of multi-height channels for microfluidic large-scale integration," *J. Micromechanics Microengineering*, vol. 29, pp. 1–13, 2019.

[76] A. P. Debon, R. C. R. Wootton, and K. S. Elvira, "Droplet confinement and leakage: Causes, underlying effects, and amelioration strategies," *Biomicrofluidics*, vol. 9, pp. 1–16, 2015, doi: 10.1063/1.4917343.

[77] M. Zagnoni, G. Le Lain, and J. M. Cooper, "Electrocoalescence Mechanisms of Microdroplets Using Localized Electric Fields in Microfluidic Channels," *Langmuir*, vol. 26, no. 18, pp. 14443–14449, 2010, doi: 10.1021/la101517t.

[78] F. Adar and M. Erecinska, "Resonance Between Membrane-Bound complex Hemes: Raman spectra of mitochondrial cytochrome b-c1 complex as a function of redox potential," *FEBS Lett.*, vol. 80, no. 1, pp. 195–200, 1977.

[79] C. Johannessen, P. C. White, and S. Abdali, "Resonance Raman Optical Activity and Surface Enhanced Resonance Raman Optical Activity Analysis of Cytochrome c," *J. Phys. Chem. A*, vol. 111, no. 32, pp. 7771–7776, 2007, doi: 10.1021/jp0705267.

[80] S. Berezhna, H. Wohlrab, and P. M. Champion, "Resonance Raman Investigations of Cytochrome c Conformational Change upon Interaction with the Membranes of Intact and Ca 2+ -Exposed Mitochondria," *Biochemistry*, vol. 42, no. 20, pp. 6149–6158, 2003, doi: 10.1021/bi027387y.

[81] T. G. Spiro and T. C. Strekas, "Resonance Raman Spectra of Heme Proteins. Effects of Oxidation and Spin State," *J. Am. Chem. Soc.*, vol. 96, no. 2, pp. 338–345, 1974, doi: 10.1021/ja00809a004.

[82] N. A. Brazhe *et al.*, "Probing cytochrome c in living mitochondria with surface-enhanced Raman spectroscopy," *Sci. Reports*, vol. 5, pp. 1–13, 2015, doi: 10.1038/srep13793.

[83] Z. Strike, K. Ghofrani, and C. Backhouse, “CO2 Laser-Based Rapid Prototyping of Micropumps,” *Micromachines*, vol. 9, no. 215, pp. 1–14, 2018, doi: 10.3390/mi9050215.

[84] K. W. Oh, K. Lee, B. Ahn, and E. P. Furlani, “Design of pressure-driven microfluidic networks using electric circuit analogy,” *Lab Chip*, vol. 12, pp. 515–545, 2012, doi: 10.1039/c2lc20799k.

[85] T. Glawdel and C. L. Ren, “Global network design for robust operation of microfluidic droplet generators with pressure-driven flow,” *Microfluid. Nanofluidics*, vol. 13, pp. 469–480, 2012, doi: 10.1007/s10404-012-0982-y.

[86] A. K. Au, B. R. Utela, and A. Folch, “Microvalves and MicroPumps for BioMEMS,” *Micromachines*, vol. 2, pp. 179–220, 2011, doi: 10.3390/mi2020179.

[87] K. W. Oh and C. H. Ahn, “A review of microvalves,” *J. Micromechanics Microengineering*, vol. 16, no. 5, 2006, doi: 10.1088/0960-1317/16/5/R01.

[88] M. G. Simon and A. P. Lee, “Microfluidic Droplet Manipulations and Their Applications,” in *Microdroplet Technology: Principles and Emerging Application in Biology and Chemistry*, P. Day, A. Manz, and Y. Zhang, Eds. Springer Science & Business Media, 2012, pp. 23–51.

[89] D. J. Laser and J. G. Santiago, “A review of micropumps,” *J. Micromechanics Microengineering*, vol. 14, pp. 35–64, 2004, doi: 10.1088/0960-1317/14/6/R01.

[90] G. F. Christopher and S. L. Anna, “Microfluidic methods for generating continuous droplet streams,” *J. Phys. D. Appl. Phys.*, vol. 40, pp. 319–336, 2007, doi: 10.1088/0022-3727/40/19/R01.

[91] W. Zeng, I. Jacobi, S. Li, and H. A. Stone, “Variation in polydispersity in pump- and pressure-driven micro-droplet generators,” *J. Micromechanics Microengineering*, vol. 25, pp. 1–4, 2015, doi: 10.1088/0960-1317/26/3/039501.

[92] N. Mavrogiannis, M. Ibo, X. Fu, F. Crivellari, and Z. Gagnon, “Microfluidics made easy: A robust low-cost constant pressure flow controller for engineers and cell biologists,” *Biomicrofluidics*, vol. 10, pp. 1–12, 2016, doi: 10.1063/1.4950753.

[93] B. E. Rapp, *Microfluidics: Modelling, Mechanics and Mathematics*, First. Amsterdam: William Andrew, 2017.

[94] H. Babahosseini, T. Misteli, and D. L. Devoe, “Microfluidic on-demand droplet generation, storage, retrieval, and merging for single-cell pairing,” *Lab Chip*, vol. 19, no. 3, pp. 493–502, 2019, doi: 10.1039/c8lc01178h.

[95] H. Bruus, *Theoretical Microfluidics*. Oxford: Oxford University Press, 2008.

[96] M. S. Razavi, E. Shirani, and M. R. Salimpour, “Development of a general method for obtaining the geometry of microfluidic networks,” *AIP Adv.*, vol. 4, pp. 1–15, 2016, doi: 10.1063/1.4861067.

[97] T. Glawdel, C. Elbuken, and C. Ren, “Passive droplet trafficking at microfluidic junctions under geometric and flow asymmetries,” *Lab Chip*, vol. 11, no. 22, pp. 3774–3784, 2011,

doi: 10.1039/c1lc20628a.

[98] L. A. Godwin, K. S. Deal, L. D. Hoepfner, L. A. Jackson, and C. J. Easley, "Measurement of Microchannel Fluidic Resistance with a Standard Voltage Meter," *Anal. Chim. Acta*, vol. 758, pp. 101–107, 2013, doi: 10.1016/j.aca.2012.10.043.Measurement.

[99] S. A. Vanapalli, A. G. Banpurkar, D. Van Den Ende, M. H. G. Duits, and F. Mugele, "Hydrodynamic resistance of single confined moving drops in rectangular microchannels," *Lab Chip*, vol. 9, pp. 982–990, 2009, doi: 10.1039/b815002h.

[100] K. Loizou, V.-L. Wong, and B. Hewakandamby, "Examining the Effect of Flow Rate Ratio on Droplet Generation and Regime Transition in a Microfluidic T-Junction at Constant Capillary Numbers," *Inventions*, vol. 3, no. 54, pp. 1–17, 2018, doi: 10.3390/inventions3030054.

[101] N. Tarchichi, F. Chollet, and J.-F. Manceau, "New regime of droplet generation in a T-shape microfluidic junction," *Microfluid. Nanofluidics*, vol. 14, pp. 45–51, 2013, doi: 10.1007/s10404-012-1021-8.

[102] S. Bashir, J. M. Rees, and W. B. Zimmerman, "Simulations of microfluidic droplet formation using the two-phase level set method," *Chem. Eng. Sci.*, vol. 66, no. 20, pp. 4733–4741, 2011, doi: 10.1016/j.ces.2011.06.034.

[103] M. Tress, S. Karpitschka, P. Papadopoulos, J. H. Snoeijer, D. Vollmer, and H. J. Butt, "Shape of a sessile drop on a flat surface covered with a liquid film," *Soft Matter*, vol. 13, no. 20, pp. 3760–3767, 2017, doi: 10.1039/c7sm00437k.

[104] T. Satoh, K. Kodama, K. Hattori, S. Ichikawa, S. Sugiura, and T. Kanamori, "Pressure-Driven Microfluidic Device for Droplet Formation with Minimized Dead Volume," *J. Chem. Eng. Japan*, vol. 47, no. 11, pp. 841–847, 2014, doi: 10.1252/jcej.14we103.

[105] P. Liang, J. Ye, D. Zhang, X. Zhang, Z. Yu, and B. Lin, "Controllable droplet breakup in microfluidic devices via hydrostatic pressure," *Chem. Eng. Sci.*, vol. 226, p. 115856, 2020, doi: 10.1016/j.ces.2020.115856.

[106] M. Musterd, V. Van Steijn, C. R. Kleijn, and M. T. Kreutzer, "Calculating the volume of elongated bubbles and droplets in microchannels from a top view image," *RSC Adv.*, vol. 5, no. 21, pp. 16042–16049, 2015, doi: 10.1039/c4ra15163a.

[107] H. Wong, C. J. Radke, and S. Morris, "The Motion of Long Bubbles in Polygonal Capillaries. Part 1. Thin Films," *J. Fluid Mech.*, vol. 292, pp. 71–94, 1995, doi: 10.1017/S0022112095001455.

[108] C. N. Baroud, F. Gallaire, and R. Dangla, "Dynamics of microfluidic droplets," *Lab Chip*, vol. 10, no. 16, pp. 2032–2045, 2010, doi: 10.1039/c001191f.

[109] D. R. Link, S. L. Anna, D. A. Weitz, and H. A. Stone, "Geometrically Mediated Breakup of Drops in Microfluidic Devices," *Phys. Rev. Lett.*, vol. 92, no. 5, p. 4, 2004, doi: 10.1103/PhysRevLett.92.054503.

[110] A. Carlson, M. Do-Quang, and G. Amberg, "Droplet dynamics in a bifurcating channel," *Int. J. Multiph. Flow*, vol. 36, no. 5, pp. 397–405, 2010, doi:

10.1016/j.ijmultiphaseflow.2010.01.002.

[111] G. F. Christopher, J. Bergstein, N. B. End, M. Poon, C. Nguyen, and S. L. Anna, "Coalescence and splitting of confined droplets at microfluidic junctions," *Lab Chip*, vol. 9, no. 8, pp. 1102–1109, 2009, doi: 10.1039/b813062k.

[112] Z. Li, L. Li, M. Liao, L. He, and P. Wu, "Multiple splitting of droplets using multi-furcating microfluidic channels," *Biomicrofluidics*, vol. 13, no. 2, pp. 1–6, 2019, doi: 10.1063/1.5086716.

[113] B. Verbruggen *et al.*, "Design of a flow-controlled asymmetric droplet splitter using computational fluid dynamics," *Microfluid. Nanofluidics*, vol. 15, no. 2, pp. 243–252, 2013, doi: 10.1007/s10404-013-1139-3.

[114] D. Zaremba, S. Blonski, M. J. Marijnissen, and P. M. Korczyk, "Fixing the direction of droplets in a bifurcating microfluidic junction," *Microfluid. Nanofluidics*, vol. 23, no. 4, pp. 1–18, 2019, doi: 10.1007/s10404-019-2218-x.

[115] K. Trinavee, N. S. K. Gunda, and S. K. Mitra, "Anomalous Wetting of Underliquid Systems: Oil Drops in Water and Water Drops in Oil," *Langmuir*, vol. 34, no. 39, pp. 11695–11705, 2018, doi: 10.1021/acs.langmuir.8b02569.

[116] S. Bashir, X. C. I. Solvas, M. Bashir, J. M. Rees, and W. B. J. Zimmerman, "Dynamic wetting in microfluidic droplet formation," *Biochip J.*, vol. 8, no. 2, pp. 122–128, 2014, doi: 10.1007/s13206-014-8207-y.

[117] J. R. Rumble, Ed., *CRC Handbook of Chemistry and Physics*, 100th ed. Boca Raton: CRC Press, 2019.

[118] K. Chemicals, "Water Tracing Dye - Standard Blue Products Technical Data Bulletin." 2021, [Online]. Available: https://www.kingscotechemicals.com/wp-content/uploads/2020/07/TD-Std-Blue.pdf.

[119] Sigma-Aldrich, "M5904 Mineral Oil Safety Data Sheet," 2020, [Online]. Available: https://us.vwr.com/assetsvc/asset/en_US/id/16490607/contents.

[120] Sigma-Aldrich, "Span 80 Safety Data Sheet." 2020, [Online]. Available: https://us.vwr.com/assetsvc/asset/en_US/id/16490607/contents.

[121] J. C. Bowman and A. Hammerlindl, "Asymptote: A vector graphics language." Community TeX Users Group, pp. 288–294, 2008.

[122] S. A. M. Shaegh *et al.*, "Rapid prototyping of whole-thermoplastic microfluidics with built-in microvalves using laser ablation and thermal fusion bonding," *Sensors Actuators B. Chem.*, vol. 255, pp. 100–109, 2018, doi: 10.1016/j.snb.2017.07.138.

[123] A. Pourmand, S. Ali, M. Shaegh, H. Badri, E. Najafi, and M. Remzi, "Fabrication of whole-thermoplastic normally closed microvalve, micro check valve, and micropump," *Sensors Actuators B. Chem.*, vol. 262, pp. 625–636, 2018, doi: 10.1016/j.snb.2017.12.132.

[124] S. A. M. Shaegh *et al.*, "Plug-and-play microvalve and micropump for rapid integration with microfluidic chips," *Microfluid. Nanofluidics*, vol. 19, pp. 557–564, 2015, doi:

10.1007/s10404-015-1582-4.

[125] C. De Marco *et al.*, “Surface Properties of Femtosecond Laser Ablated PMMA,” *Appl. Mater. Interfaces*, vol. 2, no. 8, pp. 2377–2384, 2010, doi: 10.1021/am100393e.

[126] D. G. Waugh, J. Lawrence, D. J. Morgan, and C. L. Thomas, “Interaction of CO2 laser-modified nylon with osteoblast cells in relation to wettability,” *Mater. Sci. Eng. C*, vol. 29, no. 8, pp. 2514–2524, 2009, doi: 10.1016/j.msec.2009.07.020.

[127] M. J. T. Vargas, M. Nieuwoudt, R. M. Yong, F. Vanholsbeeck, D. E. Williams, and M. C. Simpson, “Excellent quality microchannels for rapid microdevice prototyping: direct - CO2 laser writing with efficient chemical postprocessing,” *Microfluid. Nanofluidics*, vol. 23, no. 124, pp. 1–13, 2019, doi: 10.1007/s10404-019-2291-1.

[128] H. Qi, T. Chen, L. Yao, and T. Zuo, “Hydrophilicity modification of poly(methyl methacrylate) by excimer laser ablation and irradiation,” *Microfluid. Nanofluidics*, vol. 5, pp. 139–143, 2008, doi: 10.1007/s10404-007-0234-8.

[129] D. G. Waugh and J. Lawrence, “On the use of CO2 laser induced surface patterns to modify the wettability of poly(methyl methacrylate) (PMMA),” *Opt. Lasers Eng.*, vol. 48, no. 6, pp. 707–715, 2010, doi: 10.1016/j.optlaseng.2010.01.005.

[130] J. Lawrence and L. Li, “Modification of the wettability characteristics of polymethyl methacrylate (PMMA) by means of CO2, Nd:YAG, excimer and high power diode laser radiation,” *Mater. Sci. Eng. A*, vol. 303, pp. 142–149, 2001.

[131] C. T. Rueden *et al.*, “ImageJ2: ImageJ for the next generation of scientific image data,” *BMC Bioinformation*, vol. 18, p. 529, 2017.

[132] M. G. C. Peiris and K. Tennakone, “Simple method for determination of the viscosity of a liquid,” *Am. J. Phys.*, vol. 48, no. 6, pp. 497–498, 1980, doi: 10.1119/1.12071.

[133] F. Malloggi, H. Gu, A. G. Banpurkar, S. A. Vanapalli, and F. Mugele, “Electrowetting - A versatile tool for controlling microdrop generation,” *Eur. Phys. J. E*, vol. 26, no. 1–2, pp. 91–96, 2008, doi: 10.1140/epje/i2007-10252-x.

[134] DDBST GmbH, “Liquid Dynamic Viscosity Calculation by Vogel Equation (Water).” http://ddbonline.ddbst.de/VogelCalculation/VogelCalculationCGI.exe?component=Water (accessed Oct. 19, 2020).

[135] X. Wang, A. Riaud, K. Wang, and G. Luo, “Pressure drop-based determination of dynamic interfacial tension of droplet generation process in T-junction microchannel,” *Microfluid. Nanofluidics*, vol. 18, pp. 503–512, 2015, doi: 10.1007/s10404-014-1449-0.

[136] P. Roura, “Thermodynamic derivations of the mechanical equilibrium conditions for fluid surfaces: Young’s and Laplace’s equations,” *Am. J. Phys.*, vol. 73, no. 12, pp. 1139–1147, 2005, doi: 10.1119/1.2117127.

[137] A. Sommers and A. M. Jacobi, “Calculating the Volume of Water Droplets on Aluminum Surfaces,” in *International Refrigeration and Air Conditioning Conference*, 2008, pp. 1–8.

[138] V. Labrot, M. Schindler, P. Guillot, A. Collin, and M. Joanicot, “Extracting the

hydrodynamic resistance of droplets from their behavior in microchannel networks," *Biomicrofluidics*, vol. 3, no. 1, pp. 1–16, 2009, doi: 10.1063/1.3109686.

[139] I. Bruzas, W. Lum, Z. Gorunmez, and L. Sagle, "Advances in surface-enhanced Raman spectroscopy (SERS) substrates for lipid and protein characterization: sensing and beyond," *Analyst*, vol. 143, pp. 3990–4008, 2018, doi: 10.1039/c8an00606g.

[140] R. W. Taylor *et al.*, "Watching individual molecules flex within lipid membranes using SERS," *Sci. Rep.*, vol. 4, no. 5940, pp. 1–6, 2014, doi: 10.1038/srep05940.

[141] A. L. Plant, "Supported Hybrid Bilayer Membranes as Rugged Cell Membrane Mimics," *Langmuir*, vol. 15, no. 15, pp. 5128–5135, 1999, doi: 10.1021/la981662t.

[142] R. Bohme *et al.*, "Characterizing cytochrome c states - TERS studies of whole mitochondria," *Chem. Commun.*, vol. 47, pp. 11453–11455, 2011, doi: 10.1039/c1cc15246g.

[143] D. D. Hobbs, A. Kriauciunas, S. Guner, D. B. Knaff, and M. R. Ondrias, "Resonance Raman spectroscopy of cytochrome bc1 complexes from Rhodospirillum rubrum: initial characterization and reductive titrations," *Biochim. Biophys. Acta*, vol. 1018, pp. 47–54, 1990.

[144] N. A. Brazhe, M. Treiman, B. Faricelli, J. H. Vestergaard, and O. Sosnovtseva, "In Situ Raman Study of Redox State Changes of Mitochondrial Cytochromes in a Perfused Rat Heart," *PLoS One*, vol. 8, no. 8, 2013, doi: 10.1371/journal.pone.0070488.

[145] S. Yan *et al.*, "Rapid, one-step preparation of SERS substrate in microfluidic channel for detection of molecules and heavy metal ions," *Spectrochim. Acta Part A Mol. Biomol. Spectrosc.*, vol. 220, p. 117113, 2019, doi: 10.1016/j.saa.2019.05.018.

[146] B. Sharma, R. R. Frontiera, A.-I. Henry, E. Ringe, and R. P. Van Duyne, "SERS: Materials, applications, and the future," *Mater. Today*, vol. 15, no. 1–2, pp. 16–25, 2012, doi: 10.1016/S1369-7021(12)70017-2.

[147] Y. Wang *et al.*, "Highly Sensitive and Automated Surface Enhanced Raman Scattering-based Immunoassay for H5N1 Detection with Digital Microfluidics," *Anal. Chem.*, vol. 90, pp. 5224–5231, 2018, doi: 10.1021/acs.analchem.8b00002.

[148] M. R. Willner, K. S. Mcmillan, D. Graham, P. J. Vikesland, and M. Zagnoni, "Surface-Enhanced Raman Scattering Based Microfluidics for Single-Cell Analysis," *Anal. Chem.*, vol. 90, pp. 12004–12010, 2018, doi: 10.1021/acs.analchem.8b02636.

[149] I. M. White, S. H. Yazdi, and W. W. Yu, "Optofluidic SERS: synergizing photonics and microfluidics for chemical and biological analysis," *Microfluid. Nanofluidics*, vol. 13, pp. 205–216, 2012, doi: 10.1007/s10404-012-0962-2.

[150] F. Domenici, A. R. Bizzarri, and S. Cannistraro, "Surface-enhanced Raman scattering detection of wild-type and mutant p53 proteins at very low concentration in human serum," *Anal. Biochem.*, vol. 421, no. 1, pp. 9–15, 2012, doi: 10.1016/j.ab.2011.10.010.

Appendix A
Derivations of T-junction Generator Model

This appendix aims to provide a somewhat detailed description of the math involved in deriving Equation (2-11), Equation (2-12), Equation (2-13), Equation (2-14), and Equation (4-1).

A.1 Deriving Equation (2-11)

Following electric circuit principles, analyzing the fluidic circuit presented in Figure 2-4 can be used to obtain Equation (2-11) by applying Ohm's Law (Poiseuille's Equation for fluidic analysis) to the R_d resistor.

$$Q_d = \frac{P_d - P_j - P_{LP}}{R_d}$$

A.2 Deriving Equation (2-12)

A similar process to deriving Equation (2-11) can be applied to the circuit in Figure 2-4 to obtain an equation for the continuous fluid flow rate (Equation (2-12)).

$$Q_c = \frac{P_c - P_j}{R_c}$$

A.3 Deriving Equation (2-13)

Using the Ohm's Law fluidic analogy again provides an equation for P_j in terms of the main channel resistance and total fluid flow rate:

$$P_j = Q_m R_m$$

By applying Kirchoff's current law to the fluidic circuit, it can be seen that $Q_m = Q_d + Q_c$. This relationship can be used to derive Equation (2-13); see below.

$$P_j = (Q_d + Q_c)R_m$$

$$P_j = \left(\frac{P_d - P_j - P_{LP}}{R_d} + \frac{P_c - P_j}{R_c}\right) R_m$$

$$P_j \left(1 + \frac{R_m}{R_d} + \frac{R_m}{R_c}\right) = \left(\frac{P_d - P_{LP}}{R_d}\right) R_m + \frac{P_c R_m}{R_c}$$

$$P_j(R_d R_c + R_m R_c + R_m R_d) = (P_d - P_{LP})R_m R_c + P_c R_m R_d$$

$$P_j = \frac{(P_d - P_{LP})R_m R_c + P_c R_m R_d}{R_d R_c + R_m R_c + R_m R_d}$$

A.4 Deriving Equation (2-14)

Equation (2-14) is an inequality for P_d where the lower bound is defined by the case of $Q_d = 0$, and the upper bound corresponds to the case of $Q_c = 0$. First, the calculation of the lower bound will be performed.

As discussed in the derivation of Equation (2-13), the following equation for the junction pressure can be written:

$$P_j = (Q_d + Q_c)R_m$$

If Q_d is equal to zero, P_j can be combined with Equation (2-12) to write P_j in terms of P_c, R_c, and R_m.

$$P_j = \frac{P_c - P_j}{R_c} R_m$$

$$P_j \left(1 + \frac{R_m}{R_c}\right) = \frac{R_m}{R_c} P_c$$

$$P_j(R_c + R_m) = R_m P_c$$

$$P_j = \frac{R_m}{R_c + R_m} P_c$$

If $Q_d = 0$ for a long time and no backflow has occurred, then R_m equals the main channel resistance when filled only with the continuous phase (R_{mcp}).

$$P_j = \frac{R_{mcp}}{R_c + R_{mcp}} P_c$$

Using P_j as defined by P_c, R_{mcp}, and R_c, the required P_d to prevent backflow can be calculated by solving for P_d using Equation (2-11) and the requirement $Q_d > 0$.

$$Q_d = \frac{P_d - P_j - P_{LP}}{R_d} > 0$$

$$P_d > P_j + P_{LP}$$

$$P_d > \frac{R_{mcp}}{R_c + R_{mcp}} P_c + P_{LP}$$

A similar procedure considering $Q_c = 0$ can be used to determine the upper limit of the P_d operating range.

$$P_j = (Q_d + Q_c)R_m$$

$$P_j = \frac{P_d - P_j - P_{LP}}{R_d} R_m$$

$$P_j \left(1 + \frac{R_m}{R_d}\right) = \frac{R_m}{R_d}(P_d - P_{LP})$$

$$P_j(R_d + R_m) = R_m(P_d - P_{LP})$$

$$P_j = \frac{R_m}{R_m + R_d}(P_d - P_{LP})$$

In the case where $Q_c = 0$ for a long period and no backflow has occurred, then R_m is equal to the main channel resistance when filled with the dispersed phase (R_{mdp}).

$$P_j = \frac{R_{mdp}}{R_{mdp} + R_d}(P_d - P_{LP})$$

Using P_j as defined by P_d, P_{LP}, R_{mdp} and R_d, the required P_d to not create backflow can be calculated by solving for P_d using Equation (2-12) and the requirement $Q_c > 0$.

$$Q_c = \frac{P_c - P_j}{R_c} > 0$$

$$P_c > P_j$$

$$P_c > \frac{R_{mdp}}{R_{mdp} + R_d}(P_d - P_{LP})$$

$$P_d < \left(1 + \frac{R_{mdp}}{R_d}\right) P_c + P_{LP}$$

Combining the inequalities derived for the cases of $Q_d = 0$ and $Q_c = 0$ with respect to P_d results in Equation (2-14).

$$P_c \left(\frac{R_{mcp}}{R_c + R_{mcp}}\right) + P_{LP} < P_d < P_c \left(1 + \frac{R_d}{R_{mdp}}\right) + P_{LP}$$

A.5 Deriving Equation (4-1)

Equation (4-1) calculates the value of $\delta Q_d/\delta R_m$ by applying the Chain rule to Equation (2-13) and Equation (2-11). The derivatives involved in Equation (4-1) are presented here, but it is left to the reader to perform the derivatives themselves if desired.

$$\frac{\delta Q_d}{\delta P_j} = -\frac{1}{R_d}$$

$$\frac{\delta P_j}{\delta R_m} = \frac{\big((P_d - P_{LP})R_c + P_c R_d\big)R_d R_c}{[(R_c + R_d)R_m + R_d R_c]^2}$$

Appendix B
Preliminary Gravity Fed Droplet Generator

Before the design and fabrication of the devices discussed in the thesis above, a set of preliminary pressure-driven microfluidic droplet generators with integrated droplet traps was fabricated. These devices were not designed according to the method outlined in Section 2.5 and were operated with a slightly different operating procedure from that described in Section 4.4. However, these devices provided a baseline for the design of the Droplet Generator. Therefore, they are described in some detail here.

B.1 Preliminary Test Device Fabrication

The preliminary test devices were fabricated using the same method as all other devices in this thesis (Section 3.3) and consisted of two layers of PMMA. Two types of channels were used to design these devices, which are characterized by the colour of their lines in the Asymptote design files (Table B. 1). Green lines were used to cut most channels of the test droplet generators, and blue lines were used in parts of the integrated "droplet trap". All channels were cut with two passes of the corresponding laser line.

Table B. 1 - The targeted dimensions of the channel types intended for use in the preliminary test droplet generator devices.

Asymptote Line Colour	Depth [µm]	Width [µm]
Blue	207	156
Green	272	156
Red	Throughcut	Throughcut
Dark Green (Forest Green)	Throughcut	Throughcut

B.2 Gravity Fed Device Design

The preliminary droplet generator devices were designed using the resistive network shown in Figure 2-4 but without the accompanying model to predict operating range and droplet production stability. Instead, the layout of the device was based around the layout of droplet generators using the author's previous work on micropump-based droplet generators [83]. The layout of the device can be seen in Figure B. 1, where the blue section represents an integrated droplet trap.

The resistances of all channels involved in the T-junction droplet generator are detailed in Table B. 2. The resistance of each channel was calculated using Equation (2-7) and assuming the channels had an isosceles triangular cross-section.

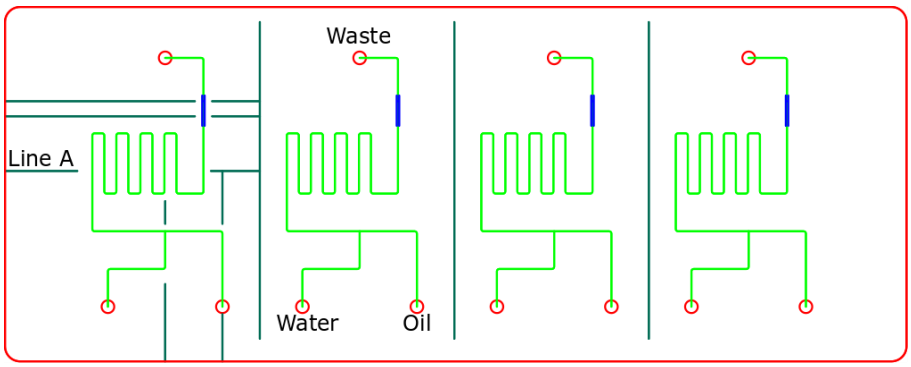

Figure B. 1 - A microfluidic master chip design for fabrication in the Backhouse fabrication method. The designs for layers 1 and 2 are stacked for convenience. The red circles represent well to connect brass fittings for syringes, the dark green lines are throughcuts to separate chips and examine channels and the green, and blue lines represent fluidic channels.

Table B. 2 - The channel resistances for the droplet generator design are shown in Figure B. 1. All channels are considered to be filled with the Continuous Phase except for the Dispersed Phase Input Channel, which is considered filled with the Dispersed Phase.

Channel	$R_{fluidic}$ [Pa s m^{-3}]
Dispersed Phase Input Channel	6.12×10^{11}
Continuous Phase Input Channel	9.79×10^{12}
Main Channel	6.78×10^{13}

B.3 Gravity Fed Device - Droplet Trap Design

The droplet trap was designed to use intentionally overlapping channels to create a structure to hold droplets in place. This was similar to a rail-based trap and took advantage of the unique profile of laser-cut channels (Figure B. 2). Barriers were expected to be formed between the overlapping channels, which would hold droplets in place while allowing the continuous phase separating the droplets to flow around the trapped droplets. This trap is similar to the metering droplet trap designed by Korczyk et al. shown in Figure 1-10 but relies on two side channels to vent the oil between the droplets rather than a wide shallow region [69].

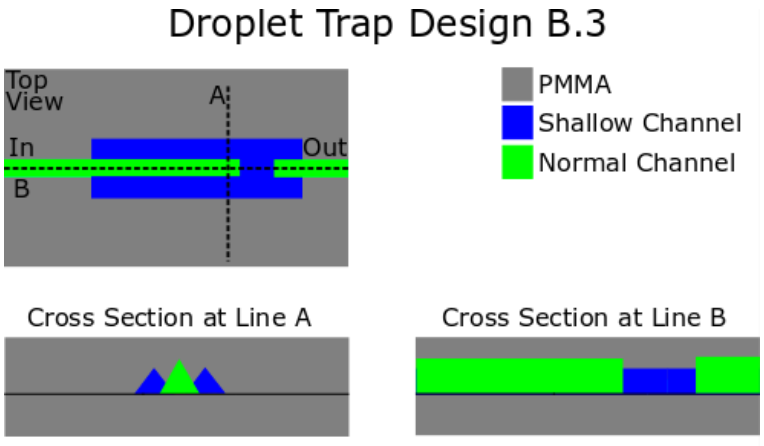

Figure B. 2 - A rail-based droplet trap designed for fabrication by the in-house method and use in a gravity-fed microfluidic chip.

The droplet trap generated a Laplace pressure difference by varying the depth of the input and side channels of the trap. When this trap was designed, droplets were assumed to form cylindrical plugs in the laser-cut channels whose radii could be calculated according to Equation (7-1). Then, Equation (2-17) could calculate the Laplace pressure difference of the channel transitions. The droplet trap was fabricated such that the input channel to the trap was 272 μm deep. The surrounding shallow channels were 207 μm deep, resulting in a Laplace pressure difference of only 15 Pa. Based on the expected resistance of the trapping structure, the flow rate through the droplet trap could not exceed 16 nL s^{-1} without ejecting the trapped droplets. This flow rate was calculated using Equation (2-21), considering a known trapping pressure and trap resistance.

B.4 Calculation of Operating Conditions

As this was preliminary work performed before developing the droplet generator model, precise operating conditions were not predicted theoretically but rather determined through experiment. It was found through initial testing that droplets could be easily formed using this droplet generator as long as the ratio between the dispersed phase input pressure (P_d) and continuous phase input pressure (P_c), P_d/P_c was between 0.96 and 1.01.

B.5 Initial Gravity Fed Device Testing and Results

The goal of initial testing with gravity-fed microfluidic devices was to establish working procedures for pressure-driven microfluidic devices to form droplets and evaluate a basic droplet trapping structure. First, droplet trapping structures were evaluated using crack test chips (Section 3.3.2) and then on-chip using droplets.

Devices were operated according to the procedure described in Section 4.4 but with one change. Before priming the device with the Dispersed and Continuous Phases, the droplet generators were first manually flushed with a 70% ethanol solution introduced from the output of the device. This step was required to clear air bubbles from the channels and prevent air bubbles from becoming trapped in the droplet trap.

B.6 Gravity Fed Device Initial Testing Results

Initial examination of unbonded channels from a crack test chip showed that the two channel types had different dimensions than intended (Table B. 3). The channels cut with the blue laser line were much shallower than intended when unbonded and could not be measured accurately once bonded. The channels cut with the green laser line were much shallower and narrower than intended once bonded.

Table B. 3 – The measured unbonded and bonded channel dimensions for the crack test chips produced with the preliminary test droplet generators. The bonded channel dimensions of channels cut with the blue laser line could not be measured.

Asymptote Channel Colour	Unbonded Channel Depth [μm]	Unbonded Channel Width [μm]	Bonded Channel Depth [μm]	Bonded Channel Width [μm]
Blue	162 ± 18	166 ± 14	-	-
Green	291 ± 58	150 ± 6	181 ± 13	118 ± 9

The bonded channels had cross-sections similar to those discussed in Section 3.3.3, but the orientational dependence of the channel dimensions was not discovered at this time in the project. The more interesting discovery was related to the droplet trap itself. The unbonded droplet trap had a cross-section close to what was intended (i.e., depicted in Figure B. 2) with well-defined barriers between the central and side channels of the droplet trap (Figure B. 3). However, after thermal bonding, the roof of the top layer of PMMA sags into the droplet trap, and the barriers between the central and side channels became far less distinct (Figure B. 4). This was thought to be caused by the reflow of PMMA during thermal bonding and the lack of droplet trap roof support. The droplet trap had a total width of ~500 μm, and therefore, channels that are this wide may experience significant changes in dimensions due to the roof "sagging" during thermal bonding.

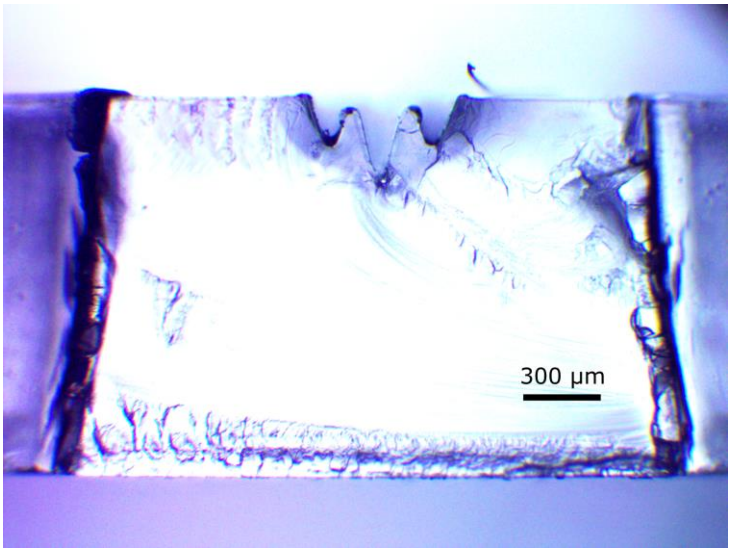

Figure B. 3 - A perpendicular cross-section of the droplet trap geometry on the crack test chip whose channel dimensions are shown in Table B. 3. The channels were made with two passes of the green laser line along the central channel and the side channels separated from the central channel at 0.2 mm.

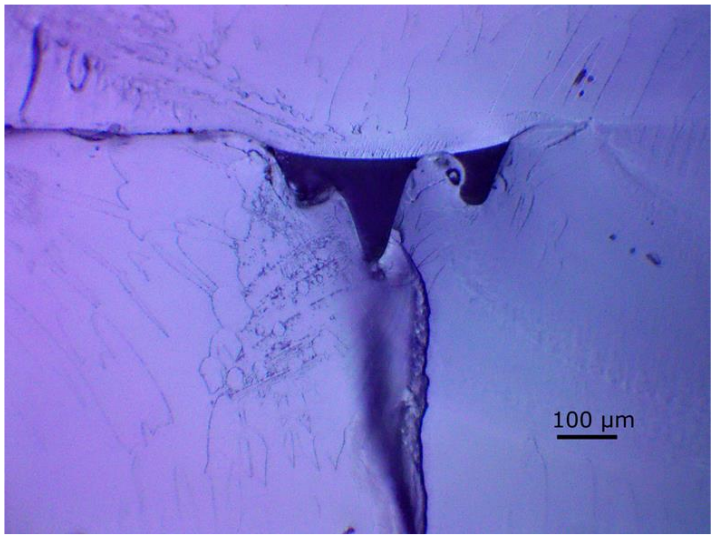

Figure B. 4 - A cross-section of a bonded droplet trap structure at 10x magnification from the same bonded chip as the channels shown in Figure B. 3.

Following examinations of the crack test chips, the preliminary test droplet generators were tested for their droplet generating capabilities. Due to the timing of the testing, which was immediately before the Covid-19 lockdown, the droplet trapping capabilities of these devices could not be tested. However, the droplet generating capabilities were tested at a total of 6 pressure combinations, three with P_c = 8.76 kPa and three with P_c = 9.89 kPa. The dispersed phase input pressure was set to P_d = 8.38 kPa, 8.53 kPa and 8.82 kPa for the former and P_d = 9.46 kPa, 9.56 kPa and 9.68 kPa. The flow rate ratios (Q_d/Q_c) at these settings were expected to range from 0.154 to 0.162 at these settings.

At the tested pressure settings, it was found that droplets could be produced with lengths ranging from ~280 μm to ~1628 μm, corresponding to droplet volumes of 3.22 ± 0.36 nL to 18.20 ± 1.47 nL. This range of produced droplets included those considered suitable for droplet trapping applications as they were about twice as long as they were wide. However, an unacceptable level of variation in the droplet volume was found. In most tested cases, the variation in droplet volume exceeded 10%. Therefore, a droplet generator model was developed to improve the design of the droplet generator to maintain a suitable level of variability in the droplet volume. When the droplet generator model described in Section 2.5 was applied to this droplet generator design, it was found that there was only one way for the model to describe the observed behaviour accurately. This required that the droplets increased the resistance of the microfluidic channels by a factor of four compared to when they were just filled with the Continuous Phase.

These preliminary test droplet generators served as a means to investigate both the basic operating procedures of pressure-driven droplet generators and the fabrication method used to make them. The work described in the thesis used these preliminary test devices as a starting point from which to design improved devices and droplet traps.

Appendix C
Surface Energy Approach to Laplace Pressure

Trapping droplets based on the transition between two channels with different dimensions requires the accurate prediction of the energy cost of the droplet making that transition. This energy cost can be determined by considering a droplet partway through the transition between two channels of arbitrary dimensions, Channel 1 and Channel 2. This approach will consider a droplet made of water and a continuous phase of oil; both are assumed to be incompressible. The change in energy required to push a droplet through an arbitrary channel transition based on the dimensions of the two channels involved in the transition will be determined and converted into the pressure required to push the droplet through the transition.

The surface energy of a droplet in a microfluidic channel can be described by Equation (C-1), where Γ is the surface energy, γ is the surface tension, and SA is the surface area of the droplet.

$$\Gamma\,[J] = \gamma\left[\frac{J}{m^2}\right] * SA\,[m^2] \tag{C-1}$$

As the surface tension for a given fluidic system is constant (ignoring fast surfactant dynamics), the change in surface energy, or energy cost of a transition, can be described by Equation (C-2).

$$\Delta\Gamma = \gamma\,\Delta\,SA \tag{C-2}$$

The surface area of the dx length of a droplet in Channel 1 (SA_{c1}) is simply $SA_{c1} = U_{c1}*dx$, where U_{c1} is the perimeter of the droplet in Channel 1. On moving length dx into Channel 2, due to the incompressible nature of the droplet, the length of the transitioning segment will be extended. As the volume of the droplet must remain constant, it can be determined that a length dx in Channel 1 will be equivalent to a length of $(A_{cs1}/A_{cs2})dx$ in Channel 2, where A_{cs1} and A_{cs2} represent the cross-sectional area of the droplet in Channel 1 and Channel 2, respectively. This means that the surface area of the droplet section entering Channel 2 (SA_{c2}) becomes $SA_{c2} = U_{c2}*(A_{cs1}/A_{cs2})*dx$. The change in surface area can be described by Equation (C-3).

$$\Delta SA = dx\left(U_{c2}\left(\frac{A_{cs1}}{A_{cs2}}\right) - U_{c1}\right) \tag{C-3}$$

Equation (C-3) can be substituted into Equation (C-2) to write Equation (C-4). In Equation (C-4), γ_{c1} and γ_{c2} are the interfacial tensions of the fluid front in Channel 1 and Channel 2, respectively.

$$\Delta\Gamma = dx\left(\gamma_{c2}U_{c2}\left(\frac{A_{cs1}}{A_{cs2}}\right) - \gamma_{c1}U_{c1}\right) \quad \text{(C-4)}$$

Equation (C-4) can then be converted into pressure by dividing by the length the droplet moves (*dx*) and the area to which the resulting force is applied. In this scenario, the force would be being applied to the back end of the droplet still in Channel 1. Therefore the cross-sectional area of the droplet still in Channel 1 (A_{cs1}) will be used. The required pressure to push a droplet through a transition from Channel 1 to Channel 2 can be written as Equation (C-5). This pressure is equivalent to the trapping pressure preventing a droplet from entering a constricted channel when coming from a non-constricted channel.

$$\Delta P_{trap} = \frac{\Delta\ \Gamma}{dxA_{cs1}} = \frac{\left(\gamma_{c2}U_{c2}\left(\frac{A_{cs1}}{A_{cs2}}\right) - \gamma_{c1}U_{c1}\right)}{A_{cs1}} = \left(\frac{\gamma_{c2}U_{c2}}{A_{cs2}} - \frac{\gamma_{c1}U_{c1}}{A_{cs1}}\right) \quad \text{(C-5)}$$

C.1 Verifying Surface Energy Approach to Trapping Pressure

The surface energy approach to determining the trapping pressure resulted in Equation (C-5), which depends entirely on the channel dimensions rather than the principal radii of a fluid front. Solutions for the Laplace pressure difference method of determining the trapping pressure of a channel transition have been reported in the literature for both circular and rectangular channels. A channel transition in a circular channel has a Laplace pressure difference that can be described by Equation (2-9). In contrast, a rectangular channel transition has a Laplace pressure difference that can be described by Equation (C-6) [6], [70]. In Equation (C-6), w_2 and h_2 are the width and height of Channel 2, respectively, and w_1 and h_1 are the width and height of Channel 1, respectively. Equation (C-6) assumes a constant interfacial tension throughout the transition and that the droplet fully fills the channel.

$$\Delta P_{LP,rectangular\ channel} = 2\gamma\left[\left(\frac{1}{w_2} + \frac{1}{h_2}\right) - \left(\frac{1}{w_1} + \frac{1}{h_1}\right)\right] \quad \text{(C-6)}$$

The generalized equation for the required pressure to push a droplet through a channel transition with arbitrarily shaped channels described above (Equation (C-5)) can be used to arrive at the same final equation as the Laplace pressure approach for both circular and rectangular channels.

For a circular channel, the cross-sectional droplet area is $A = \pi r^2$, and the droplet perimeter is $U = 2\pi r$, where *r* is the radius of the droplet. Assuming the droplet in Channel 2 has a radius of r_2 and the droplet in Channel 1 has a radius of r_1, values for U_{c1}, U_{c2}, A_{cs1} and A_{cs2} can be substituted into Equation (C-5) to generate Equation (C-7). This assumes a constant interfacial tension of $\gamma = \gamma_{c1} = \gamma_{c2}$. It can be seen that Equation (C-7) matches Equation (2-9), and therefore the surface energy approach detailed above matches the Laplace pressure difference approach for circular channels.

$$\Delta P_{trap,ciruclar\ channels} = \frac{\gamma\left(2\pi r_2\left(\frac{r_1^2}{r_2^2}\right) - 2\pi r_1\right)}{\pi r_1^2} = 2\gamma\left(\frac{1}{r_2} - \frac{1}{r_1}\right) \quad \text{(C-7)}$$

For a rectangular channel, the cross-sectional area is $A = wh$, and the channel perimeter is $U = 2w + 2h$, where w and h are the width and height of the channel, respectively. Assuming Channel 2 has a width of w_2 and a height of h_2 and Channel 1 has a width of w_1 and a height of h_1. If the droplet completely fills the channel, values for U_{c1}, U_{c2}, A_{cs1} and A_{cs2} can be substituted into Equation (C-5**)** to generate Equation (C-8**)** and Equation (C-9**)**, assuming a constant interfacial tension of $\gamma = \gamma_{c1} = \gamma_{c2}$. It can easily be seen that Equation (C-9**)** matches Equation (C-6**)**. Therefore, the surface energy approach detailed above matches the Laplace pressure difference approach for rectangular channels.

$$\Delta P_{trap,rectangular\ channels} = \frac{\gamma\left((2w_2 + 2h_2)\left(\frac{w_1 h_1}{w_2 h_2}\right) - (2w_1 + 2h_1)\right)}{w_1 h_1} \quad \text{(C-8)}$$

$$\Delta P_{trap,rectangular\ channels} = 2\gamma\left(\left(\frac{1}{h_2} + \frac{1}{w_2}\right) - \left(\frac{1}{h_1} + \frac{1}{w_1}\right)\right) \quad \text{(C-9)}$$

For both cases, the surface energy approach to calculating the trapping pressure of a channel transition agrees with the Laplace pressure difference method. Therefore, the surface energy approach described above can be used to determine the trapping pressure of a channel transition for droplets of an arbitrary shape.

Appendix D
Video of Droplet Generation

This appendix is a video file of droplets being produced with a Droplet Generator at pressure settings of P_d = 8.06 kPa and P_c = 8.38 kPa. The video is a five-minute test run to determine if droplets could be reproducibly made with these settings. The Droplet Generator used has no integrated droplet trap in its main channel. Before testing, the main channel of the Droplet Generator was completely filled with the Continuous Phase.

The droplet generation process begins 10 seconds into the video. The video is focused on the T-junction of the droplet generator, with the dispersed phase input channel coming up from the bottom of the screen, the continuous phase input channel coming from the left of the screen and the main channel proceeding to the right of the screen. The channels have a speckled appearance, as explained in Section 3.3.3, and did not affect device performance. The droplets produced in this video had an average length of 342 ± 15 μm and were ~106 μm wide.

The file name of this video file is “DropletGenerationPd806kPaPc838kPa.mp4”.

Appendix E
Video of Droplet Trapping

This appendix is a video file of an isolated pair of droplets approaching and trapped by the Alternate Droplet Trap. This work aimed to observe the production and behaviour of an isolated pair of droplets in the Alternate Droplet Trap. The droplets were produced at pressure settings of P_d = 7.83 kPa and P_c = 8.38 kPa. The droplets in the video both have lengths of 400 μm. Before testing, the Droplet Generator and Alternate Droplet Trap were completely filled with the Continuous Phase except for droplets in the dead-end channels of the droplet trap.

The video is initially focused on the T-junction of the Droplet Generator to observe the production of the droplets. The droplets are produced after 24 seconds. The focus is then shifted onto the droplets as they flow through the main channel of the Droplet Generator and enter the droplet trap (timestamp ~1:02). The droplets are successfully trapped and held in the droplet trap for the remainder of the video. The droplets were observed after the video ended; they did not merge until they had been held in the trap for 17 minutes.

The channels have a speckled appearance explained in Section 3.3.3 and did not affect device performance. It should also be noted that there are some droplets in the dead-end channels of the droplet trap. These could not be cleared when the trap was purged and did not affect the performance of the droplet trap.

The file name of this video file is “AltTrapIsolatedPairPd783kPaPc838kPa.mp4”.